

DEVELOPMENT OF EXPERIMENTAL FACILITIES FOR INVESTIGATIONS OF
VORTEX MACHINING

by

Stephen Christopher Howard

A dissertation submitted to the faculty of
The University of North Carolina at Charlotte
in partial fulfillment of the requirements
for the degree of Doctor of Philosophy in
Mechanical Engineering

Charlotte

2014

Approved by:

Dr. Stuart T. Smith

Dr. Brigid A. Mullany

Dr. Faramarz Farahi

Dr. Russell G. Keanini

Dr. Thomas G. Lucas

ABSTRACT

STEPHEN CHRISTOPHER HOWARD. Development of experimental facilities for investigations of Vortex Machining. (Under direction of DR. STUART T. SMITH and DR. BRIGID A. MULLANY)

This dissertation presents work done in investigation of a novel polishing process called Vortex Machining. Vortex Machining uses an oscillating probe to induce vortices in a polishing slurry above a workpiece, thereby removing material in regions measuring micrometers laterally. The probe features a high-aspect ratio geometry that enables it to reach into (and potentially polish) complex geometries such as small holes and deep channels. The probe can also be used for force and displacement feedback, providing potential for in situ measurement. Throughout this research two test facilities have been developed; a low-power facility utilizing a 7 μm diameter probe oscillating at 32.7 kHz with amplitudes in the tens of micrometers, and a high-power facility utilizing a 500 μm diameter probe oscillating at several kHz with amplitudes of several hundred micrometers. The facilities control probe position to 0.5 μm , slurry depth to 10 μm , and probe phase to 2.5° ; and have demonstrated machining capabilities used in preliminary studies of the process. Analysis software was developed to characterize process footprints. While substantial variability in footprints is observed, material removal rates of the order 10^{-8} and $10^{-4} \text{ mm}^3 \cdot \text{hr}^{-1}$ have been measured on silicon. Surface finish values of footprints are typically sub-nanometer and thus comparable to traditional polishing.

TABLE OF CONTENTS

CHAPTER 1: INTRODUCTION	1
1.1 Motivation and Goals	1
1.2 Background of Vortex Machining	2
1.3 Dissertation Layout	4
CHAPTER 2: LITERATURE REVIEW	5
2.1 Theory of Fluid Flow	5
2.1.1 Analytical Solutions	6
2.1.2 Particle Energy Derivations	8
2.1.3 Visualization of Theory	12
2.2 Comparable Processes	17
2.2.1 Magnetorheological Finishing	18
2.2.2 Computer Controlled Polishing	21
2.2.3 Elastic Emission Machining	24
2.2.4 Fluid Jet Polishing	27
2.2.5 Ion Beam Figuring	39
2.2.6 Comparison to Vortex Machining	31
2.3 Measurement Tools	34
2.3.1 Non-contact Methods	36
2.3.2 Contact Methods	37

	v
2.3.3 Summary and Relation to Vortex Machining	41
2.4 Analysis Tools	43
2.4.1 Filtering	43
2.4.2 Surface Characterization	48
2.4.3 Summary and Relation to Vortex Machining	52
CHAPTER 3: DESIGN OF LOW-POWER EXPERIMENTAL FACILITY	55
3.1 Overview of Design	55
3.2 Tooling	58
3.3 Mechanical Systems	62
3.3.1 Machine frame	63
3.3.2 Indexable Platform	63
3.3.3 Sensor Bank	64
3.3.4 Translation Stages	66
3.4 Instrumentation Systems	68
3.4.1 Probe Lock-in and Phase-locked Loop	68
3.4.2 Slurry Depth Compensation	70
3.4.3 Probe-to-workpiece Automated Referencing	74
3.5 Control Systems	76
3.5.1 FPGA Lock-in and Phase-locked Loop	77
3.5.2 Translation Systems	79

	vi
3.5.3 Slurry Depth	82
3.5.4 Experimental Automation	83
3.6 Testing Procedure	84
3.6.1 Pre-experimental Preparation	85
3.6.2 Probe-to-Workpiece Referencing	86
3.6.3 Initiation of Experiment	87
3.6.4 Ending the Experiment	88
3.6.5 Post-experimental Analysis	88
CHAPTER 4: DESIGN OF HIGH-POWER EXPERIMENTAL FACILITY	90
4.1 Overview of Design	91
4.2 Tooling	92
4.2.1 High-Frequency Flexure	92
4.2.2 Machining Probes	94
4.2.3 High-Power Capacitive Amplifier	95
4.2.4 In situ Tool Measurement System	97
4.3 Machine Frame	99
4.4 Translation Stages	100
4.5 Testing Procedure	103
4.5.1 Pre-experimental Preparation	104
4.5.2 Probe-to-Workpiece Referencing	104

	vii
4.5.3 Ending the Experiment	105
4.5.4 Post-Experimental Analysis	105
CHAPTER 5: DATA ANALYSIS PACKAGE	106
5.1 Features	106
5.1.1 Plane Fitting	109
5.1.2 Outlier Elimination	110
5.1.3 Sectional Data Elimination	112
5.1.4 Volumetric Removal Estimation	113
5.1.5 Filtering	115
5.1.6 Parametric Characterization	117
5.2 Program Verification	118
5.2.1 Volumetric Estimation Algorithm	118
5.2.2 Filtering	119
5.2.3 Parameters	120
CHAPTER 6: RESULTS AND DISCUSSION	121
6.1 Low-Power Experimental Facility	122
6.1.1 Footprint Volume and Machining Time	122
6.1.2 Footprint Volume and Probe Amplitude	124
6.1.3 Evaluation of Footprint Roughness	126
6.1.4 Process Automation	127

	viii
6.2 High-Power Experimental Facility	129
6.2.1 Material Removal Rate and Stand-off Distance	131
6.2.2 Material Removal Mechanism	132
6.2.3 Forced Contact Machining Mode	136
6.2.4 Material Removal Rate and Process Roughness	137
6.2.5 Evaluation of Process Roughness	138
6.3 Conclusions of Preliminary Results	139
CHAPTER 7: CONCLUSIONS	140
7.1 Experimental Implementation	140
7.2 Material Removal Mechanisms	142
7.3 Process Viability	145
7.4 Advisable Future Work	146
REFERENCES	149
APPENDIX A: LIST OF PAPERS AND CONFERENCE PROCEEDINGS FROM THESES STUDIES	155
APPENDIX B: MATLAB CODE FOR FLUID STREAMING SOLUTION	156
APPENDIX C: PRELIMINARY VALIDATION OF FLUID FLOW THEORY	162
APPENDIX D: ZYGO NEWVIEW 5000 SPECIFICATIONS	171
APPENDIX E: VEECO AFM SPECIFICATIONS	172
APPENDIX F: CIRCUIT DIAGRAMS	174
APPENDIX G: VORTEX MACHINING OPERATIONAL GUIDELINES	182

CHAPTER 1: INTRODUCTION

1.1 Motivation and Goals

In this research, investigations of a novel, sub-aperture material removal method called Vortex Machining have been undertaken. As will be discussed further in section 2.2, many sub-aperture processes currently exist but each has specific attributes and limitations. Sub-aperture processes are differentiated from traditional polishing in that the tool is smaller than the workpiece. To finish an entire surface, a map of the material removal profile is used to determine a tool path and corresponding dwell times of the tool as it rasters across the entire surface. These methods are ordinarily used to produce workpiece shapes that are difficult for traditional polishing techniques, such as producing aspheres for optical lenses. Many sub-aperture processes are designed for quickly shaping a workpiece to its desired form, while others are suited for slower finishing operations that provide optimal surface roughness characteristics. These processes are required in many industrial applications; from manufacture of custom optical lenses, telescope mirrors, or even lens micro-arrays – to final finishing of molds used to produce optical components in mass quantities. With exponential growth of certain technologies (such as cellphone cameras) and their use in the world – as well as an increasing demand for quality products – manufacturing techniques such as these have never been more important and in demand. Due to its high-aspect ratio tooling and low-roughness finishing capability, Vortex Machining has the potential to be another useful polishing

process. In addition to analyzing the mechanisms of the process, this research has allowed other areas to be investigated. Machine design and its implementation, fluid flow theory, particle tracking, measurement analysis, and polishing theory have been just a few of the fields of study utilized during the course of research. In this account, a review of theory applied to Vortex Machining and related processes will be given; followed by a detailed presentation of the experimental design and analysis procedures. In conclusion, results from the analysis will be presented along with their implications to Vortex Machining and related polishing processes. For publications made during this research, see Appendix A.

1.2 Background of Vortex Machining

Before proceeding into the literature review of related theory and polishing processes, it is important to provide context by briefly describing the background and principles of operation in Vortex Machining. Less than five years old, the process was first investigated by Nowakowski in which he showed that it was capable of nanometer-level material removal over lateral areas of tens of micrometers in scale [1]. In the process, a $\varnothing 7 \mu\text{m}$ cylindrical rod (hereafter referred to as the probe) is submerged in polishing slurry with the probe tip located at a fixed distance above a silicon workpiece, see Figure 1-1(a). A footprint representative of the process is shown in Figure 1-1(b). When the probe is oscillated in a linear trajectory, stationary vortices are developed which are hypothesized to be responsible for material removal. After Nowakowski's initial characterization, further research commenced in late 2010. The goal of this research was to determine the principle mechanisms of removal and also critical process parameters for estimating the size, geometry, and roughness of the resultant footprints. Removal mechanisms have been investigated through comparisons of machining tests

using different experimental process parameters. In addition to analysis of process footprints, theoretical models [2] have been investigated to estimate the effect of process parameters on energy density for further context in understanding how the effect of each parameter influenced the process. Since the models are currently limited to the prediction of two dimensional flows, only probe diameter, amplitude, and frequency are included in this analysis. Additional parameters such as probe stand-off distance and slurry concentration were investigated solely through analysis of footprints from experimental testing.

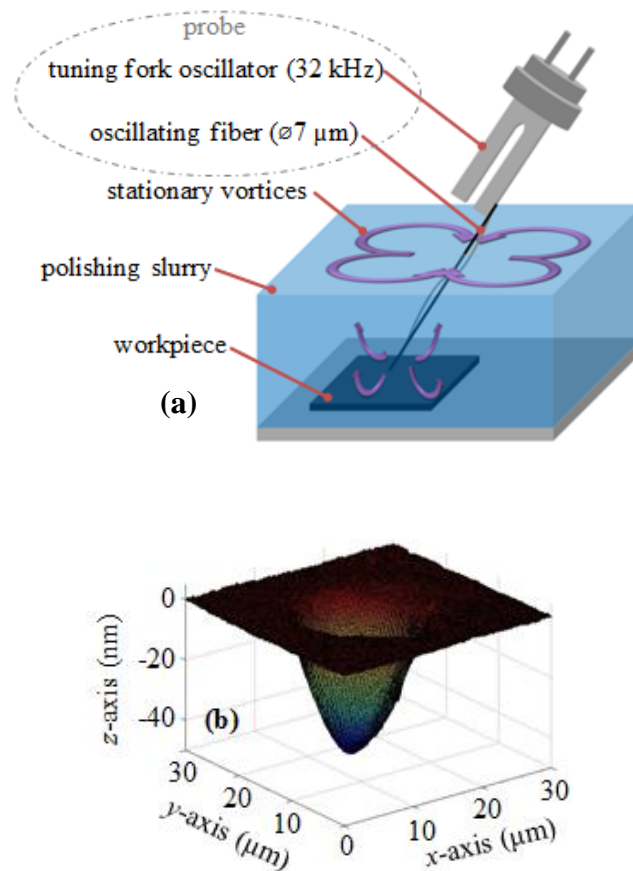


Figure 1-1: Schematic displaying main features and principle of operation of the Vortex Machining process (a) and footprint representative of the process (b). Modified from [3].

1.3 Dissertation Layout

This section will outline the layout of the dissertation. In Chapter 2, theories of fluid flow resulting from the principle of operation of Vortex Machining will be discussed. To provide a reference for this process, selected sub-aperture processes will be discussed individually and in relation to Vortex Machining. Measurement and Analysis tools relevant to this dissertation will also be covered. Chapter 3 will detail the development of the low-power experimental facility and Chapter 4 will detail the development of the high-power facility. The software analysis package used that was designed for investigating Vortex Machining footprints will be discussed in Chapter 5. Chapter 6 will discuss preliminary results from each of the processes. Chapter 7 will summarize these results, discuss the viability of Vortex Machining, and provide ideas for future work to investigate the process.

CHAPTER 2: LITERATURE REVIEW AND BACKGROUND TO THE VORTEX MACHINING CONCEPT

In order to adequately describe the evolution of research and development into Vortex Machining, it is useful to give a review of background relating to the process. This review will include; a brief introduction into the theory of fluid flow resulting from the process, a description of similar material removal processes and how Vortex Machining is differentiated, existing material removal theories that are relevant to the process, and measurement and analysis tools that were used to investigate footprints resulting from experimental research that was completed. This review will not only provide a broader insight into where Vortex Machining fits into the world of sub-aperture polishing, but also provide background detail of accepted polishing mechanisms for removal of material.

2.1 Theory of Fluid Flow

As stated in the introduction, Vortex Machining is postulated to remove material through a process of fluid flow (specifically vortex streaming induced by an oscillating probe) interacting with a workpiece. As a result, it was envisaged early into the project that a basic understanding of the fluid flow theory governing the process would aid in experimental studies and analysis of the corresponding results. A review of related literature turned up work that had been done on solving analytically the resulting fluid streaming in the region of an oscillating cylinder, not dissimilar to Vortex Machining [2]. In addition, work was done by Dr.'s Stuart Smith and Russell Keanini of UNCC on

estimating the energy resulting from particulates within such fluid flow. The analytical solutions were implemented as numerical software code to visualize the effects of probe diameter, frequency, and amplitude.

2.1.1 Analytical Solutions

The main analytical theory of the fluid flow induced in Vortex Machining is based on solutions derived from Holtsmark et al. [2]. The solutions were initially derived to mathematically explain the fluid flow experimentally recorded by Andrade [4] in which smoke was vibrated in a tube around a cylindrical obstacle. While the cylinder is oscillated in Vortex Machining, in theory the flow resulting from either configuration should be identical, see Figure 2-1. Working directly from the Navier-Stokes equation, the authors were able to derive a second-order approximation for the steady-state streaming flow resultant from oscillations of a cylinder in a fluid medium. In addition to the flow only being described in the lateral dimensions, there are some notable limitations to the theory. The derivations rely on assumptions of either an infinitely large fluid reservoir or a cylindrically bounded reservoir, and an infinitely long cylinder (or probe). Also, it is assumed that the oscillation trajectory will be strictly linear which in reality is somewhat difficult to achieve in practice. While the complete solution can be found in the article [2], notable relationships that resulted from the derivations are extracted here. The dimensionless frequency, R , can be described by Equation 2-1,

$$R = D \left(\frac{\omega}{\eta} \right)^{1/2} \quad \text{Equation 2-1}$$

where

D , diameter of the cylinder (probe)

ω , oscillation frequency

η , kinematic viscosity

It has been found that as the dimensionless frequency approaches a value of approximately 20, the size of the inner vortices of the stationary flow, see Figure 2-1, approach the size of the radius of the cylinder. As this number decreases, the thickness of the inner vortices shrinks rapidly. In addition to the dimensionless frequency, it can be easily shown that the square of the maximum oscillation velocity, or maximum energy of the probe, is represented by

$$U_0 = A^2 \omega^2 \quad \text{Equation 2-2}$$

where

U_0 , maximum oscillation velocity

A , amplitude of oscillation

Clearly the energy imparted into the flow depends on the square of both the amplitude and oscillation frequency. Lastly it is worth making a few brief statements on the implications of the flow pattern displayed in Figure 2-1. This flow pattern is the most common resulting from linear oscillation of a cylindrical tool in a fluid medium. In most cases, the inner and outer vortices are rotating in counter directions, with the inner vortices at much higher absolute velocities. This has been verified from the derived analytical equations as well as experimental investigations that are detailed in Appendix C. It is at this time theorized that the high-velocity inner vortices are responsible for much of the probe to surface interaction by way of bringing slurry particulates into contact with the workpiece surface, with the slower outer vortices responsible for bulk transport of slurry particulates into and out of the high velocity inner vortices.

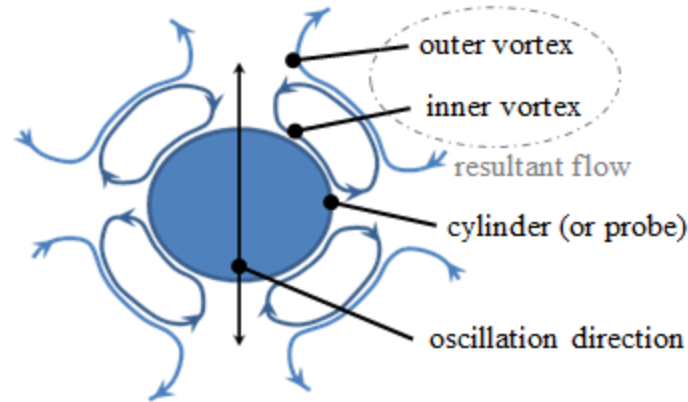


Figure 2-1: Schematic diagram displaying stationary flow resultant from an oscillating cylinder (or probe) in a fluid medium. Modified from [5].

2.1.2 Particle Energy Derivations

The analytical theory presented by Holtsmark describes fluid flow resultant from the process, but does not address how the trajectories of particulates in such flow would be influenced. Since in Vortex Machining the polishing solutions consist of particulates suspended in a fluid, it was of interest to investigate mathematically how the particles would be affected by such flows. In order to address this, Dr.'s Russell Keanini and Stuart Smith derived equations to estimate this effect on the particles [6]. In order to present their derivations it is first necessary to define several terms:

M_p , mass of the abrasive particle (kg)

D_p , diameter of the abrasive particle (m)

c_d , drag coefficient for the abrasive particle (typically 3π , dimensionless)

ρ_p , density of the abrasive particle ($\text{kg}\cdot\text{m}^{-3}$)

ρ_f , density of the fluid ($\text{kg}\cdot\text{m}^{-3}$)

v_p , velocity of the abrasive particle ($\text{m}\cdot\text{s}^{-1}$)

v_f , velocity of the fluid ($\text{m}\cdot\text{s}^{-1}$)

η , kinematic viscosity of the fluid (for water, approximately $1\cdot 10^{-6} \text{ m}^2\cdot\text{s}^{-1}$)

Since the particulate size in polishing mediums used for Vortex Machining are in general small ($<100 \text{ nm}$), a low Reynold's number (i.e. Stokes flow) can be assumed. Using Newton's laws governing motion of a particle in a fluid flow the following equation can be derived,

$$M_p \frac{dv_p}{dt} = \mu D_p \rho_f c_d \left(v_f(r, \theta) - v_p(r, \theta, t) \right) \quad \text{Equation 2-3}$$

Equation 2-3 can be further rewritten in terms of a characteristic time constant, τ , and a first-order linear differential equation, see Equations 2-4 and 2-5 respectively. Note that in Equation 2-4 the expression is simplified in part by assuming a drag coefficient of 3π .

$$\tau = \frac{M_p}{\eta D_p \rho_f c_d} = \frac{\frac{\pi}{6} \rho_p D_p^3}{\eta D_p \rho_f c_d} = \frac{\rho_p D_p^2}{18 \eta \rho_f} \quad \text{Equation 2-4}$$

$$\tau \dot{v}_p + v_p = v_f \quad \text{Equation 2-5}$$

Equation 2-5 can be rearranged to give the following expression between the particle and fluid flow velocities,

$$\frac{v_p}{v_f} = \frac{1}{1 + i\omega\tau} \quad \text{Equation 2-6}$$

In addition to this, it can also be shown that the kinetic energy of the abrasive particle can be estimated as

$$T \propto \frac{1}{2} M_p v_p^2 \propto \frac{1}{2} M_p \frac{v_f^2}{(1 + (\tau\omega)^2)} \propto \frac{\pi D_p^3 A^4 \omega^3 \rho_p \rho_f}{12 \mu (1 + (\tau\omega)^2)} F^2(R, \theta) \quad \text{Equation 2-7}$$

where $F(R, \theta)$ is a function normalizing the kinetic energy to its cylindrical coordinates and is derived in [2].

Examining Equations 2-4 through 2-7, there are a few implications that can be made. Considering first the derivation for the time constant in Equation 2-4, it is clear that as the time constant of the abrasive particle decreases linearly with its density and with the square of its diameter. Figure 2-2 shows a plot of the time constant of an alumina particle in a water-based fluid. As will be discussed in Chapter 6, the primary slurry used in Vortex Machining investigations to date has been Alumina based. Also, the maximum oscillation frequency of the probes used in these studies was approximately 32 kHz. Assuming homogeneous Alumina particulates in a water-based solution, it is clear from the figure that for particulates smaller than 10 μm in diameter the time constant will be smaller than the period of oscillation of the probe. From this consideration and the assumption that the particulate and fluid mixture behaves as a kind of low-pass filter as described in Equations 2-5 and 2-6, particulates smaller than 10 μm in diameter should follow the fluid flow field. This derivation thus gives more validity to the use of the work of Holtmark [2], in which only homogeneous fluids were considered in estimating the flows of particulate-based slurries as is required for estimation of the flows in the Vortex Machining process.

It has been theorized that higher energy particulates incident on the workpiece will correlate to more material removal. Therefore, it is useful to consider the derivation for the kinetic energy of the particulates in Equation 2-7. However, before moving on it will help to simplify the analysis by taking another look at Equation 2-6 and its low-pass filter behavior. For studies presented in this thesis, in general only one type of slurry was used. Early on, it became clear that 0.05 μm diameter Alumina slurry provided the most repeatable results and was therefore chosen as the standard for all subsequent

investigations. In later investigations involving the high-power facility, there was some investigation into the affect of different concentrations ranging from 2.5% to 50% slurry-to-water ratio, see section 6.2. However, for most investiations the same the same slurry type was used. Considering this, the calculated time constant is approximately 0.5 ns, and thus the denominator involving τ can be effectively ignored simplifying Equation 2-7 to yield,

$$T \propto \frac{\pi D_p^3 A^4 \omega^3 \rho_p \rho_f}{12\mu} F^2(R, \theta) \quad \text{Equation 2-8}$$

Looking at the simplified expression for kinetic energy of the Alumina particles in Equation 2-8, some general notes can be made. Assuming a constant slurry composition (constant particulate diameter and density, and fluid density), the kinetic energy will increase with the fourth power of amplitude of the probe oscillation and to the third power of the probe frequency.

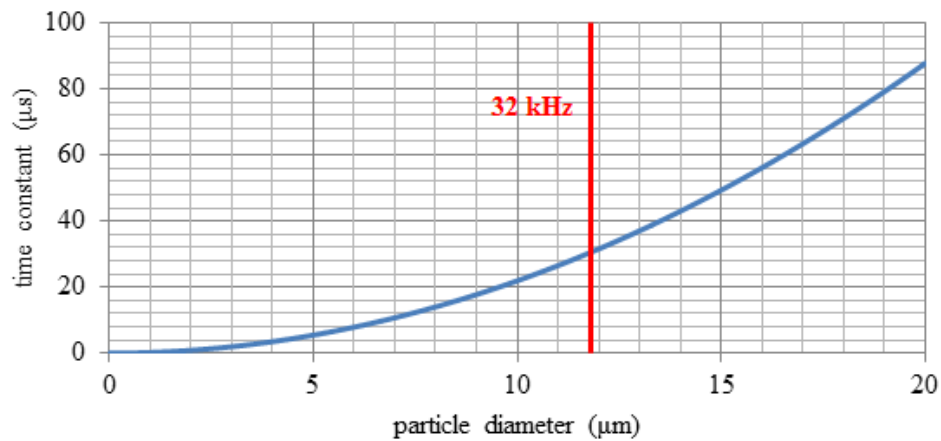


Figure 2-2: Plot of time constant derivation from Equation 2-4 assuming $\rho_p = 3950 \text{ kg}\cdot\text{m}^{-3}$ (Alumina), $\eta = 1\cdot 10^{-6} \text{ m}^2\cdot\text{s}^{-1}$ (water), $\rho_f = 1 \text{ kg}\cdot\text{m}^{-3}$ (water), and $c_d = 3\pi$. Using a 32 kHz frequency probe, the period of oscillation for the fluid flow will be approximately 30 μs as indicated by the vertical line. As a result, for Alumina particles (used primarily in slurries for testing) it can be assumed that for diameters less than 10 μm they should follow the flow field.

2.1.3 Visualization of Theory

In the previous sections, an analytical theory of fluid flow [2] has been discussed and derivations estimating particle tracking and energy have been utilized to estimate the particulate trajectories and energies in Vortex Machining. While the theory derived from Holtsmark [2] was discussed and a general figure showing the flow was given in Figure 2-1, it is difficult to show the implications of the theory without graphical representations. Due to this, utilizing the help of Dr.'s Bethany Woody, Stuart Smith, and Phanindra Tallapragada, the solution was coded into a MATLAB script so that the fluid flow field (i.e. streamlines) could be plotted given initial conditions. These conditions include the diameter of the probe, its amplitude, and its frequency. Two cases are chosen to show these flow fields and are displayed in Figure 2-3 and Figure 2-4. As discussed in 2.1.1, as the Reynold's number approaches a value of around 20 the thickness of the inner vortex is approximately the radius of the probe, see Figure 2-3. As the Reynold's number decreases this thickness decreases rapidly until it is no longer visible, see Figure 2-4. While Figure 2-3 was plotted based on parameters used in Holtsmarks original paper [2], Figure 2-4 illustrates parameters characteristic of the low-power Vortex Machining facility.

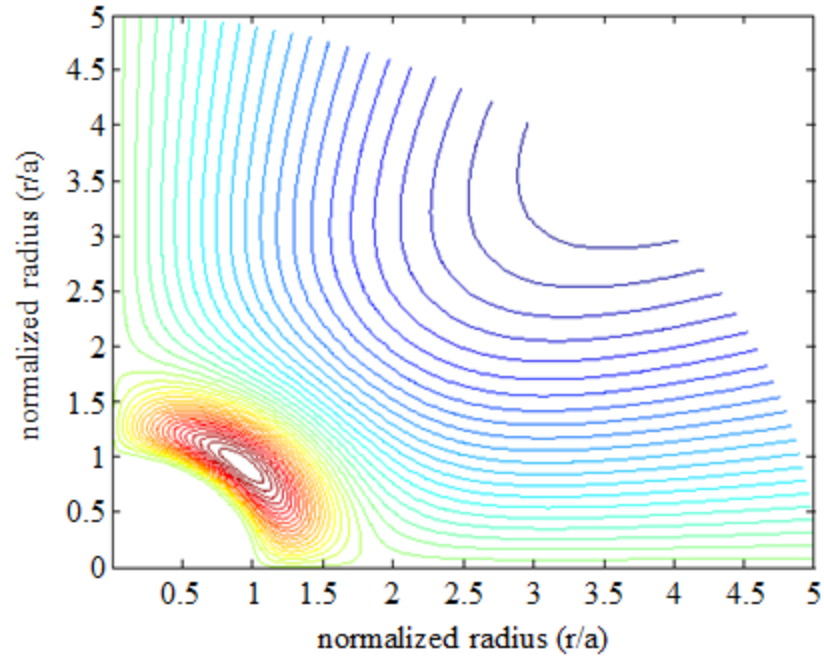


Figure 2-3: Flow field streamlines plotted using code derived from Holtmark theory [2]. Parameters used are $a = 0.0011$ m (probe radius), $f = 200$ Hz, $\eta = 15 \cdot 10^{-6} \text{ m}^2 \cdot \text{s}^{-1}$, and $A = 20 \text{ } \mu\text{m}$. $R = 20$.

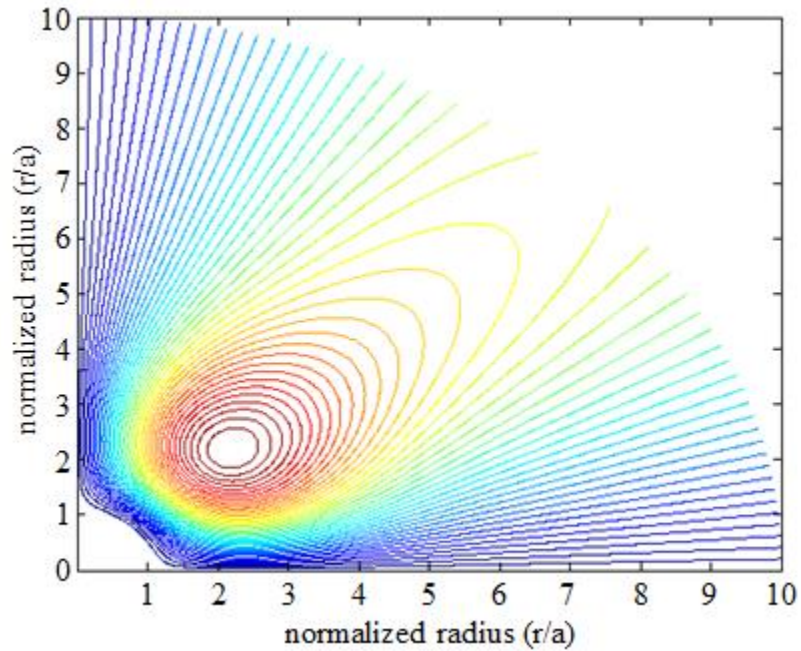


Figure 2-4: Flow field streamlines plotted using code derived from Holtmark theory [2]. Parameters used are $a = 3.5 \text{ } \mu\text{m}$ (probe radius), $f = 32.7 \text{ kHz}$, $\eta = 1 \cdot 10^{-6} \text{ m}^2 \cdot \text{s}^{-1}$, and $A = 20 \text{ } \mu\text{m}$. Parameters are characteristic to those used in low-power Vortex Machining facility. $R = 1.6$.

In addition to plotting the streamlines, the program was modified to enable plotting the energy density of the flow characterized as the square of the velocity of the flow field. It was thought that energy density would be a much more useful parameter in estimating flows in that it could be used to compare and predict testing using different experimental configurations. Shown in Figure 2-5 is a plot of the energy density with the same parameters used for plotting the streamlines in Figure 2-4. As was shown in Equation 8, increasing amplitude should increase the energy by the fourth power. Doubling the amplitude to 40 μm yielded an approximate 16 times increase in the peak energy as expected, see Figure 2-6. Further plots have shown that increasing frequency increases the energy density to the third power approximately as well. While interesting, this increase in the energy of flow should be considered carefully. While we can in theory code an amplitude for the 7 μm diameter probe (low-power facility tooling), in reality the amplitude will be damped significantly when inserted into the slurry and be very difficult to predict. This fact is due to the probe dynamics being changed and a full mathematical analysis was beyond the scope of these investigations. However, more information on probe dynamics will be discussed in section 3.2.

These limitations ultimately led to the design and implementation of a high-power experimental facility, see Chapter 4. This high-power system was designed to use larger diameter probes (100 to 500 μm diameter) which could be oscillated at larger amplitudes (up to 500 μm) at a range of frequencies up to 10 kHz. While limitations exist, the premise of the design was based on reliably comparing energy density derivations. The larger diameter probes were not damped as significantly and thus the assumption that their amplitudes stayed relatively constant when submerged into polishing slurry could be

made. While increasing the diameter of the probe and decreasing its frequency undoubtedly decreased its potential energy density of flow, this was mostly offset by the actual amplitude in the slurry being increased significantly. For brevity, only Figure 2-7 is shown to give the reader an idea of the potential using higher-power tooling. As can be seen, much higher energy densities are possible by increasing the amplitude of the probe. The MATLAB program used to plot both the streamlines and energy density is in Appendix B.

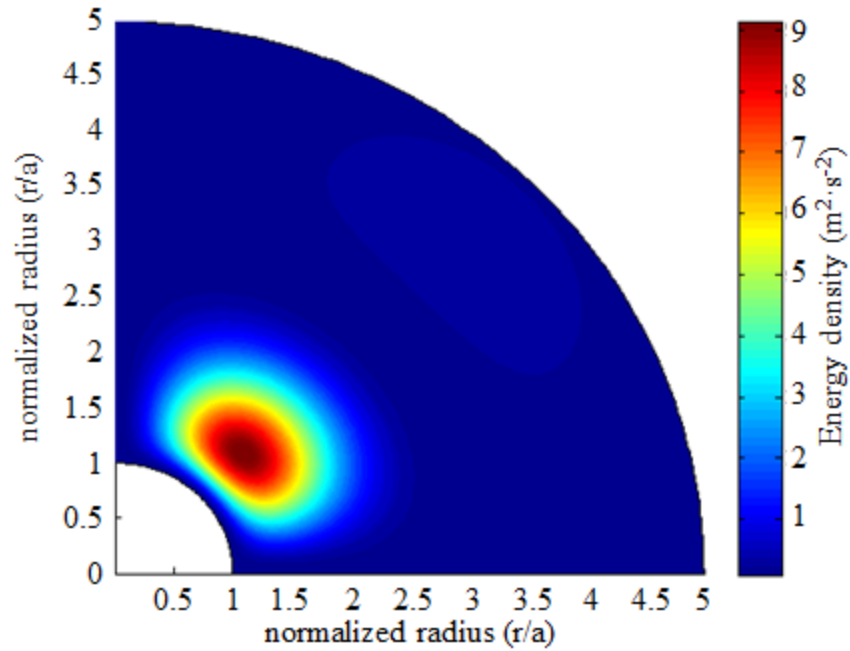


Figure 2-5: Energy density plotted using code derived from Holtmark theory [2]. Parameters used are $a = 3.5 \mu\text{m}$ (probe radius), $f = 32.7 \text{ kHz}$, $\eta = 1 \cdot 10^{-6} \text{ m}^2 \cdot \text{s}^{-1}$, and $A = 20 \mu\text{m}$. Parameters are characteristic to those used in low-power Vortex Machining facility.

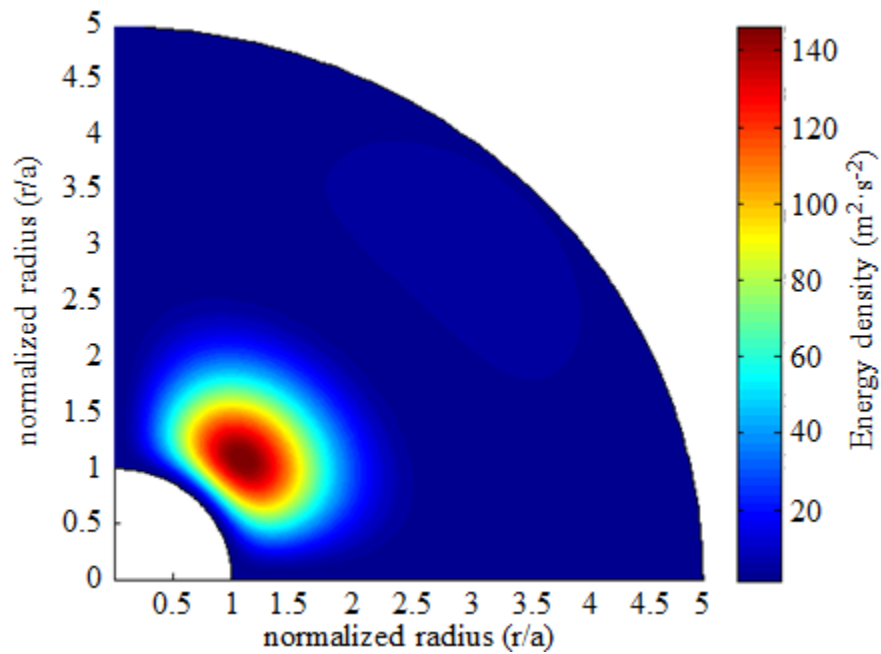


Figure 2-6: Energy density plotted using code derived from Holtmark theory [2]. Parameters used are $a = 3.5 \mu\text{m}$ (probe radius), $f = 32.7 \text{ kHz}$, $\eta = 1 \cdot 10^{-6} \text{ m}^2 \cdot \text{s}^{-1}$, and $A = 40 \mu\text{m}$.

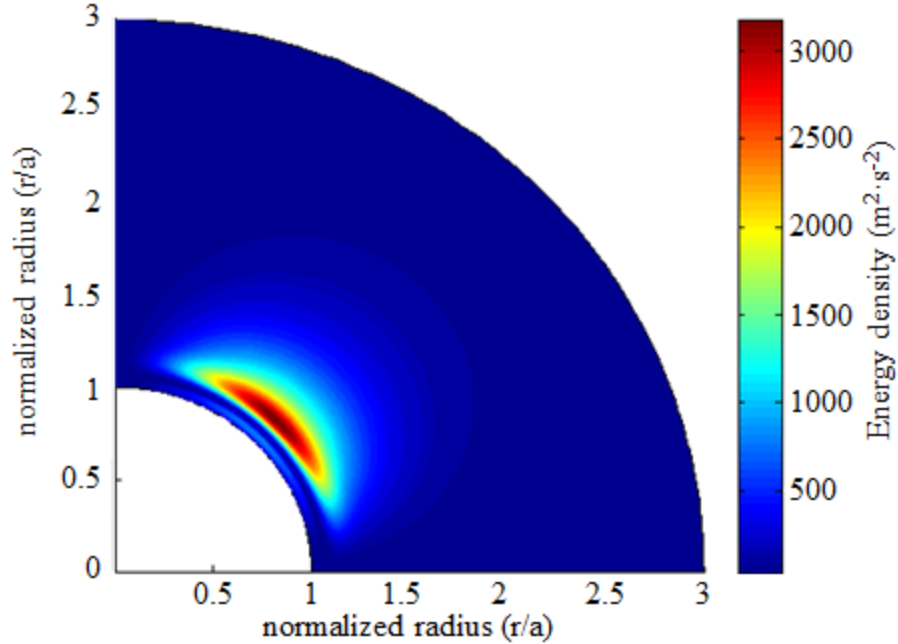


Figure 2-7: Energy density plotted using code derived from Holtmark theory [2]. Parameters used are $a = 250 \text{ } \mu\text{m}$ (probe radius), $f = 3 \text{ kHz}$, $\eta = 1 \cdot 10^{-6} \text{ m}^2 \cdot \text{s}^{-1}$, and $A = 1 \text{ mm}$. Parameters are characteristic to those used in high-power Vortex Machining facility.

2.2 Comparable Processes

Since the time of Newton, traditional optics polishing was typically performed using a pitch-based (highly viscous polishing medium) polishing wheel that extended beyond the diameter of the workpiece being finished. While this has been the primary polishing mechanism for hundreds of years, the process is still not fully understood in its details and generally considered to be more of an art than a science. This is not to say that the process has not been studied and the interested reader is referred to [7] and [8] where many of the remaining issues are discussed.

Vortex Machining fits into a category of polishing techniques known as sub-aperture processes. In contrast to traditional polishing, sub-aperture techniques are characterized by tooling that is smaller in scale than the workpiece and therefore has to

be scanned across the entire surface primarily for modifying the workpiece form. These techniques have only become prevalent recently, potentially due to the increase in computing power necessary to determine and control the tool trajectory. Using these methods, it is possible to produce more complex surface geometries than previously possible.

In this new age of polishing, the goal is to establish more deterministic methods that can be used to facilitate rapid manufacture of complex workpiece shapes (usually non-planar or non-spherical shapes such as aspheres) which cannot be finished by traditional full-aperture techniques. A variety of processes which have achieved this goal are discussed herein. While many of them offer superior attributes to the traditional methods, there are still gaps in terms of feature size and geometry in which new processes are needed for finishing applications. By examining these processes, Vortex Machining will be compared against these other state of the art techniques. Additionally, the novel and advantageous characteristics of the process will be more clearly discriminated.

2.2.1 Magnetorheological Finishing

Magnetorheological finishing (MRF) is a process in which a workpiece (usually of glass composition) is modified using a magnetorheological fluid (MR fluid) consisting of both magnetic particles (carbonyl iron) and polishing abrasives (typically cerium oxide or diamond) [9]. The principle of operation of MRF is shown in Figure 2-8. By use of a moving boundary, often facilitated by a drum, a ribbon of MR fluid is generated and the workpiece is brought into contact with the MR fluid. The novelty of this process is that a continuously renewed finishing tool (ribbon of MR fluid) is generated. A magnetic field,

often facilitated by an electromagnet, is used to stiffen the MR fluid in a localized region. Since the fluid has effectively zero yield strength when no magnetic field is applied, material is removed only in the region where the field is induced thus allowing localized finishing of centimeter-scale lateral footprints with a characteristic D-shape [9], see Figure 2-9. In this process, the amount of material removed is controlled by determining a dwell time based on the removal function of the setup. This removal function is dependent on a number of factors: the slurry composition, ribbon speed, workpiece material, and submersion depth of the workpiece to name a few[10]. Material removal rates ranging from 2 to 12 $\mu\text{m}\cdot\text{min}^{-1}$ and volumetric removal rates ranging from 10 to 100 $\text{mm}^3\cdot\text{hr}^{-1}$ are characteristic of the process depending on workpiece material (for these values: fused silica to F7, respectively) [10]. Additionally, tests have shown that independent of starting roughness, workpiece surfaces can generally be finished down to the 1 nm RMS region with sub-surface damage virtually undetectable using optical profiler measurement techniques [10].

It is useful to note that the millimeter scale and orientation between the tooling and workpiece is similar to many traditional sub-aperture polishing techniques. However, the ability to adjust the local viscosity of the MR fluid allows more control of the tool contact geometry without the need for making and storing specific lapping heads. Also, there has been work on variant designs utilizing fluid jets that in general offer the same removal rate and roughness characteristics, while offering the ability to polish more complex workpiece structures [11]. The material removal in MRF has been often attributed to shear mechanisms. This is supported by the linear relationship between the drag force (due to induced viscosity from magnetic field) between the MR fluid and

workpiece, but there is also evidence of an effect when using different polishing abrasives thus not ruling out chemical and other mechanical components [9].

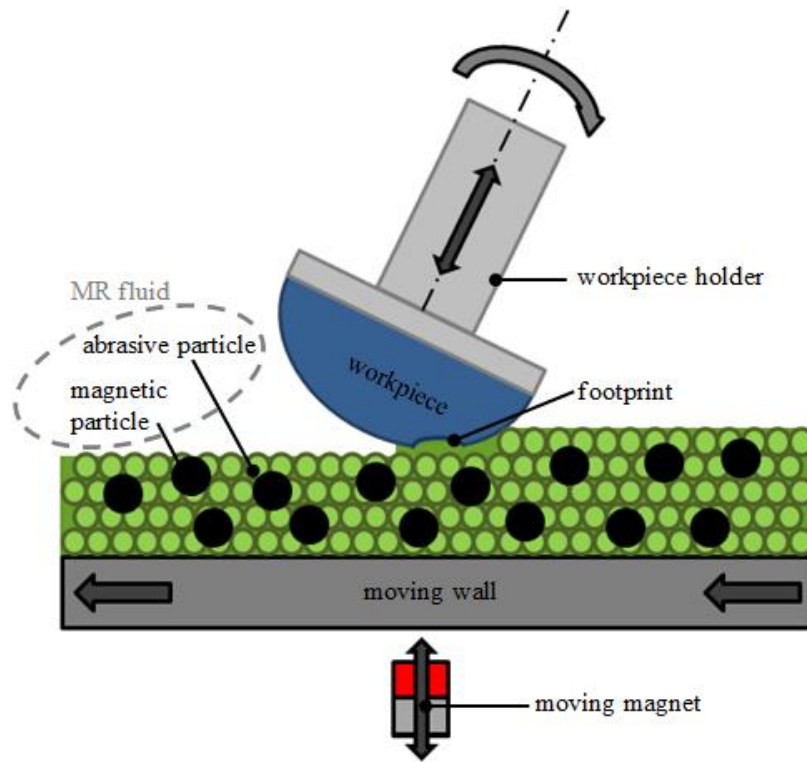


Figure 2-8: Schematic diagram showing close-up view of principles of operation in magnetorheological finishing (MRF). Note that slurry particles (represented by circles in MR fluid schematic) are not to scale.

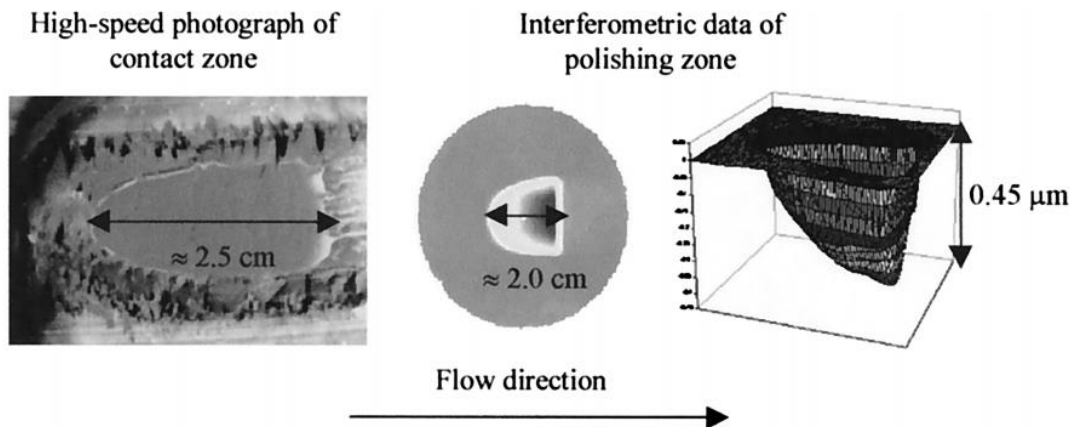


Figure 2-9: Figure reproduced from [9] depicting contact region and measurement of footprint resulting from MRF.

2.2.2 Computer Controlled Polishing

In many ways similar to conventional pitch polishing techniques dating back centuries, computer controlled polishing (CCP) utilizes traditional polishing methodology combined with modern day computational control to yield more deterministic results. As can be seen in Figure 2-10, CCP is a three-body process utilizing a rotating polishing head to apply pressure between the polishing pad, slurry, and workpiece. In many CCP processes, the polishing pad is normal to the workpiece. However, some commercial versions of the process (for instance Zeeko machines) allow the polishing pad orientation to the workpiece to be adjusted, so that the removal function can be optimized for certain applications such as creating millimeter Gaussian footprint shapes [12]. Note that in CCP the tool is rotated while the workpiece is fixed, an obvious differentiation between this process and MRF. As stated previously, CCP is an extrapolation of conventional polishing techniques which, while they have been in use for centuries, are also possibly one of the least well understood material removal processes [13].

Where MRF removes material due to a build-up of shear stresses, CCP removes material by application of compressive stress between the abrasive particles in the slurry and the workpiece. One formulation that has been used to predict material removal in conventional polishing is the Preston equation [14],

$$MRR = k \times P \times v \quad \text{Equation 2-9}$$

where

MRR , material removal rate of the process

k , constant depending on process parameters being used

P , pressure applied by the polishing pad

v , velocity of the polishing pad

Equation 2-9 implies a proportional relationship between the applied pressure and velocity of the polishing pad. The process constant usually depends on a number of factors, including the workpiece material, slurry composition and concentration, and tool-to-workpiece orientation and geometry.

There have been multiple theories of material removal mechanisms for conventional pad-slurry-workpiece processes. Possibly the earliest theory, Newton stipulated material is removed through brittle fracture by abrasive particles. Also a mechanical explanation, others have theorized frictional heating between the particle-workpiece interaction to cause the workpiece to plastically deform or flow [13]. Some models are based on chemical affinity and attraction between slurry components and the workpiece atoms. If the attraction is large enough and the bonds between the workpiece atoms weak enough, the slurry particles can potentially pull the workpiece atoms from the surface [13]. These competing theories are often subdivided into ‘mechanical tooth’ and ‘chemical tooth’ explanations that are combined to develop more complete theories and models to explain and/or predict how material is removed. The specific characterization often combines both mechanical and chemical explanations (sometimes denoted tribochemical). For example, chemical-mechanical polishing (CMP) and in general traditional polishing of glass usually attribute a strong chemical component to the removal process [13]. It is not uncommon for traditional methods used in CCP to produce surfaces with RMS roughnesses of 1 nm. Additionally, values of 0.2 nm and lower have been reported [15].

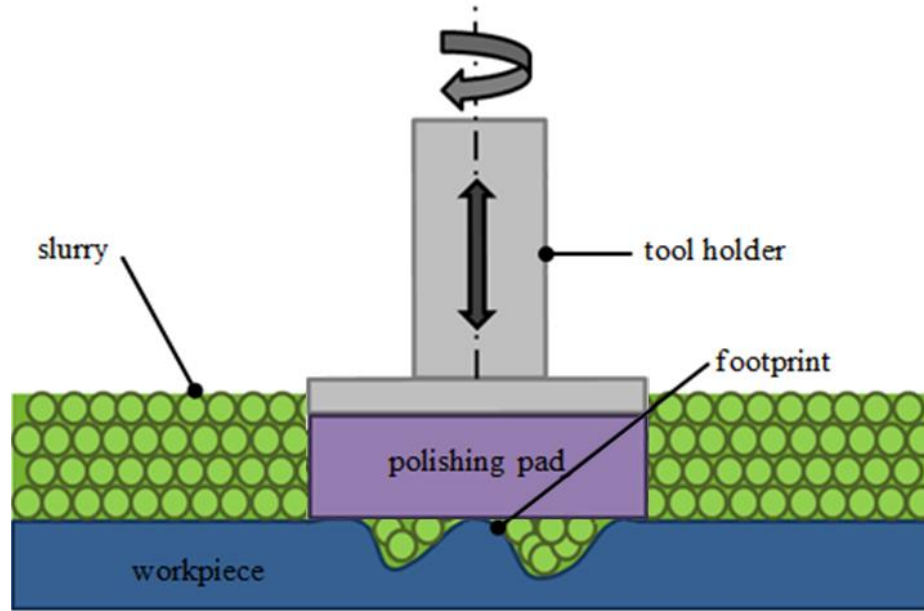


Figure 2-10: Schematic diagram showing principle of operation of a sub-aperture, computer controlled polishing (CCP) process. Note that slurry particles (represented by circles in slurry) are not to scale.

2.2.3 Elastic Emission Machining

Where the principle of operation of many polishing processes look foreign when compared to Vortex Machining, elastic emission machining (EEM) exhibits several noteworthy similarities, see Figure 2-11. There are two versions of EEM currently in use; one which utilizes a rotating sphere normal to the workpiece [16] and another which uses a jet nozzle [17]. The principle of either approach is to accelerate polishing slurry across a workpiece, thereby removing material. This is a mechanism previously postulated for Vortex Machining that also proposes material is removed through an acceleration of slurry across the workpiece surface. Since both methods use non-contact methods for material removal, EEM was of specific interest early on in these investigations. Additionally, EEM was often studied with respect to silicon workpieces which, due to its homogeneity, is the primary choice of specimen material for Vortex Machining studies.

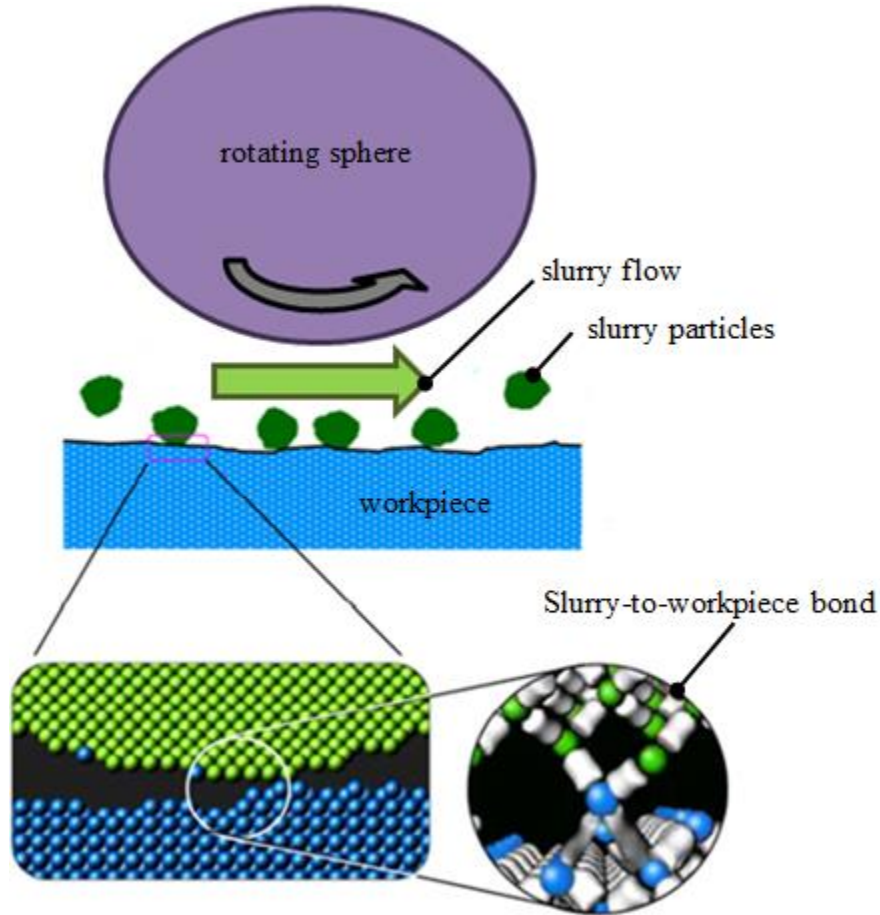


Figure 2-11: Schematic diagram showing close-up view of principle of operation in rotating sphere version of elastic emission machining (EEM). Note inset showing bonding between slurry and workpiece atoms. Note that slurry particles are not to scale. Modified from [18].

The mechanism of removal in EEM has been theorized to be primarily chemical. According to Yamauchi *et al* [18], the slurry particles may form hydrogen bonds with workpiece atoms through interaction of hydroxide species terminating from both. Workpiece atoms are then pulled from the bulk material as the slurry is accelerated away from the surface [19]. As such, it would seem that the principle parameter governing the rate of material removal would be the number of slurry particles interacting with the

workpiece. One investigation revealed that spherical slurry particles yielded slower material removal than agglomerated particles which have more surface area. However, it was also observed that smoother surfaces were produced with the spherical particles [20].

Notwithstanding the chemical effect, it has also been theorized that a significant mechanical component involving shear-stress being enacted by the fluid on the slurry atoms is required to produce removal. The theory states that while slurry atoms are atomically bonding to the workpiece atoms, a threshold shearing force is required or no material will be pulled from the workpiece surface. In addition, the same studies showed some peculiar relationships between the process parameters and material removal rate. While increasing the force between the rotating ball (hydrodynamically floating over the workpiece) increases removal rates, increasing the speed of the ball produces the reverse (less removal) [21]. While this disagrees with predictive models for other polishing processes such as the Preston equation (shown in Equation 2-9), investigations have shown that increasing rotational speeds likely produce extra lift force on the slurry particles preventing them from making contact with the workpiece surface [18].

EEM is macroscopically similar in operation to Vortex Machining. However, comparisons of the mechanisms of material removal between the two processes cannot be made at this time. However, it is also worth examining the footprints resulting from each process. While Vortex Machining produces small, localized footprints (see section 6.1), EEM, like most other material removal methods, produces footprints with millimeter scale lateral dimensions due to the dimensional scale of the tooling. Additionally, like many other sub-aperture processes EEM's low-aspect ratio tooling confines it to processing of relatively low-curvature, non-complex workpiece geometries. It has also

been shown that the process is only capable of comparatively slow depth removal rates of around $30 \text{ nm} \cdot \text{min}^{-1}$ [21] and volume removal rates of approximately $1 \cdot 10^{-4} \text{ mm}^3 \cdot \text{hr}^{-1}$ [16]. However, EEM has been shown to produce ultra-smooth surfaces with roughness values less than 0.1 nm RMS [16] and also no detectable surface damage [20].

2.2.4 Fluid Jet Polishing

Fluid jet polishing (FJP) is a process in which a pressurized jet of slurry is directed towards a workpiece, see Figure 2-12. Since this is a two-body process using a non-contacting tool, at first glance it may seem to resemble EEM. However, in FJP material is removed through erosion by mechanical collision of slurry particles and subsequent shearing of workpiece atoms from the bulk material [22]. Differentiated from fluid jet machining (FJM), in which material is removed quickly using high pressure slurry jets, FJP is generally uses pressures below 10 bars similar to those seen in processes such as EEM [23]. The first FJP systems utilized high pressures at low impinging angles with the workpiece to achieve less catastrophic removal than in FJM. Recent variations have switch to much lower pressures at angles closer to normal to the workpiece. In addition to achieving less catastrophic, smoother, and slower material removal, low pressure FJP is also characterized by relatively insignificant tool (nozzle) wear [24].

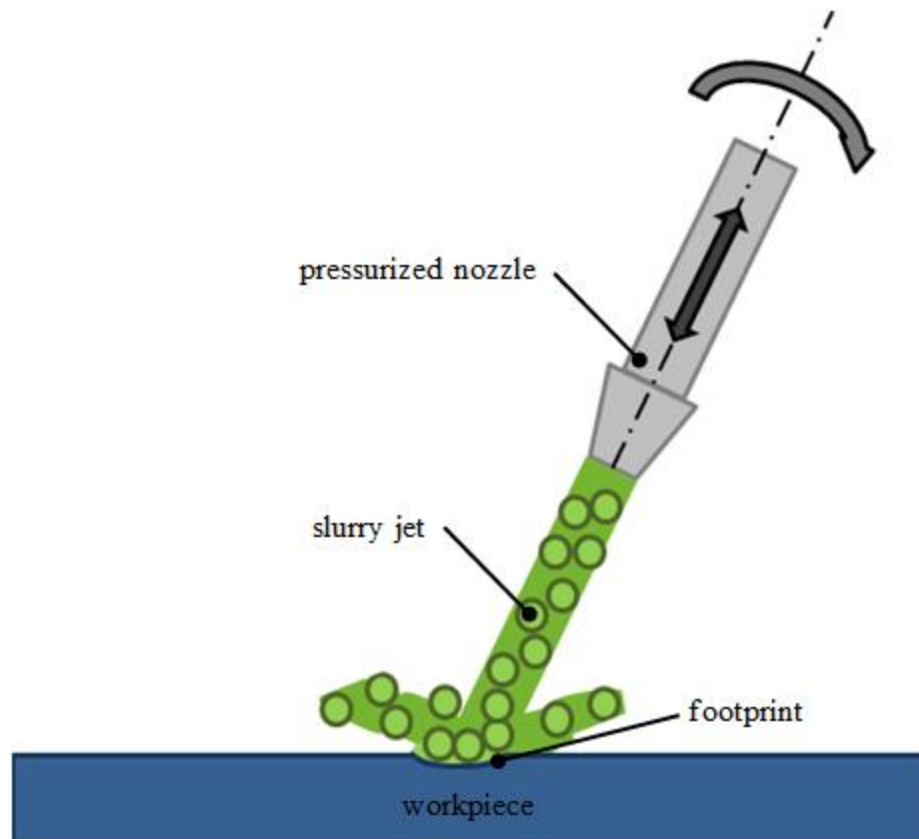


Figure 2-12: Schematic diagram showing principle of operation of fluid jet polishing (FJP) process. Note that slurry particles are not to scale.

As mentioned previously, material is removed primarily through action of mechanical erosion in FJP. It is postulated that this is facilitated through brittle removal phenomena, where cracks are initiated and propagated through the workpiece, and ductile removal, where the particles do not have sufficient energy to crack the surface but remove material through plowing across the surface. Also, while brittle materials are usually subject to the brittle removal regimes, it has been shown that there is a critical depth that can be achieved by the slurry abrasives where ductile removal will be predominant (as a rule of thumb, ductile removal usually results in smoother surfaces) [25]. In further validation and characterization, it has also been shown that material removal is linearly proportional to particle concentration, thereby implying that material

removal depends on the number of particles impacting and eroding the workpiece surface. Also, material removal has been shown to be proportional to the kinetic energy of the impacting particles, with a minimum threshold needed for removal to be initiated [25].

Depending on a number of factors, including nozzle size and orientation, footprint dimensions can range from 1 mm [25] to over 10 mm [26] laterally. Also heavily dependent on process factors as well as types of workpiece, final finished roughness values have been shown to range from close to 1 μm down to almost 1 nm RMS [23,24]. Pitting of workpiece surfaces has been shown to occur and is usually minimized by using smaller abrasive particles in the slurry solutions [22]. Additionally, this process can be configured to remove material at variable rates, from 1 $\text{nm}\cdot\text{min}^{-1}$ ($\sim 1\cdot 10^{-4} \text{ mm}^3\cdot\text{hr}^{-1}$) to as fast as 1 $\mu\text{m}\cdot\text{min}^{-1}$ ($\sim 0.1 \text{ mm}^3\cdot\text{hr}^{-1}$) [25]. Utilizing these wide ranging characteristics and versatile, non-contact tooling, FJP can be used to polish more complex surfaces than most other processes.

2.2.5 Ion Beam Figuring

In contrast to all other sub-aperture processes previously discussed, ion beam figuring (IBF) does not use slurry. It also doesn't rely on mechanical or chemical tooth means of material removal. Beginning in the 1960's, it was discovered that through sputtering of ion beams material could be removed from a workpiece [27]. Since this time, the process has been refined to the point where an ion source is used to focus a near Gaussian shaped ion beam onto a workpiece, see Figure 2-13. Material is removed through energetic ions (gallium for focused beams and Argon for broad beams) impinging on the surface and removing workpiece atoms. The process is advantageous in

that it is non-contact, can remove material at relatively high rates, is highly deterministic, and also does not exhibit edge effects common to most processes [28]. While many of these advantageous are attractive, the process has to be used in a vacuum environment, and, while often debated, has been shown to impart significant damage and surface roughening into certain materials. Polycrystalline materials are especially susceptible to these effects and initial surface quality can strongly influence how well the process can figure a surface [29].

In IBF, the ion beam is usually directed normally towards the workpiece surface. Complex algorithms for factoring in the effect of minor slopes on the surface have been employed to increase determinism of the process [30]. Depending on the type of grid optics and masking used, the ion beam can range in size from less than 0.5 mm to near 100 mm in diameter (full width at half maximum) with corresponding footprint sizes [29,30]. While IBF is a precision figuring process, it is often used to correct longer wavelength errors (up to 10 cm). Corrections using this process have resulted in figure errors less than 1 nm, and roughness errors as low as 0.2 nm have been reported [30]. Some of the extremely low roughness tolerances are achieved through variations of the process known as ion beam smoothing (IBS) and ion beam planarization (IBP). Without getting into the specific details, IBS utilizes inherent relaxation mechanisms and IBP a sacrificial deposited layer. A short, but thorough review of these techniques can be found in [30].

Due to the wide range of ion beam sizes and energies that can be utilized, the depth removal rate can range from approximately 20 to 200 nm·min⁻¹ with the volumetric removal ranging from approximately 0.01 to 1 mm³·hr⁻¹ [29]. Even with the mentioned

limitations, IBF has been of significant interest in many industries. Its use has been applied to lithography-based optics [31] and due to its immunity to edge effects its application has been used in large-scale astronomy-based optics as well [32].

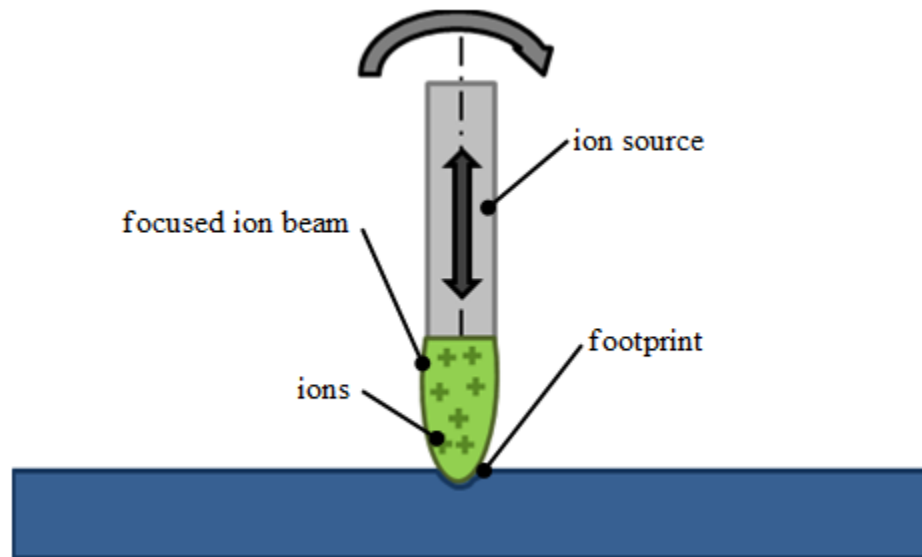


Figure 2-13: Schematic diagram showing principle of operation of ion beam figuring (IBF).

2.2.6 Comparison to Vortex Machining

While the specifics of Vortex Machining have not yet been covered, its principle of operation has been briefly discussed in sections 1.1 and 1.2, and a schematic is shown in Figure 1-1. Similar to EEM and FJP, it is postulated that in Vortex Machining material is removed through action of accelerating polishing slurry across a workpiece. At this point but it is worth comparing Vortex Machining to the other sub-aperture processes to understand where it fits in among the various polishing techniques.

Table 2-1 compares Vortex Machining and the other discussed polishing processes using seven general categories. First, it is interesting to consider how long each

process has been in development. While all processes have been under investigation for at least 20 years, Vortex Machining was only first realized in 2009 with full-time studies beginning in late 2010 (less than 5 years). Hence this is the youngest of all these processes, a fact that should guide the perspective concerning the understanding that can be expected for such a new and novel process.

Table 2-1: Tabulated processing properties of Vortex Machining (VM) against magnetorheological finishing (MRF), computer controlled polishing (CCP), elastic emission machining (EEM), fluid jet polishing (FJP) and ion beam figuring (IBF).

	VM	MRF	CCP	EEM	FJP	IBF
Machining Orientation	normal or parallel	normal	normal	normal	adjustable angle	normal
Footprint Size	10 to 600 μm	10 or more mm	5 or more mm	2 or more mm	1 to 10 mm	0.5 to 100 mm
Footprint Shape	Gaussian	'D' shape	variable; Gaussian	Planar or flat	variable; 'W' shape	Gaussian
Achievable Roughness	0.25 to 5 nm	1 nm	0.2 to a few nm	0.1 to 1 nm	1 nm	nm to sub-nm
Depth Removal Rate	1 to 100 $\text{nm} \cdot \text{min}^{-1}$	2 to 12 $\mu\text{m} \cdot \text{min}^{-1}$	100 nm to 10 $\mu\text{m} \cdot \text{min}^{-1}$	30 $\text{nm} \cdot \text{min}^{-1}$	1 to 1000 $\text{nm} \cdot \text{min}^{-1}$	20 to 200 $\text{nm} \cdot \text{min}^{-1}$
Volumetric Removal Rate	10^{-8} to $10^{-4} \text{mm}^3 \cdot \text{hr}^{-1}$	10 to 100 $\text{mm}^3 \cdot \text{hr}^{-1}$	0.1 to 10 $\text{mm}^3 \cdot \text{hr}^{-1}$	$10^{-4} \text{mm}^3 \cdot \text{hr}^{-1}$	10^{-4} to 0.1 $\text{mm}^3 \cdot \text{hr}^{-1}$	0.01 to 1 $\text{mm}^3 \cdot \text{hr}^{-1}$
Time in Development	5 years	30 years	30 years	40 years	20 years	50 years

Given the above considerations it is clear that Vortex Machining has a number of unique attributes, including;

- Small aperture and near Gaussian footprint
- Stationary specimen and self-contained machining probe
- High aspect ratio probe

Most of the sub-aperture processes can only remove material in an orientation with the tooling normal to the workpiece. This adds significant limitations to the complexity of shapes that can be finished. While in FJP the tooling can be adjusted significantly, it cannot be used to figure surfaces parallel to the tooling as is the case with Vortex Machining. This parallel configuration provides potential for finishing of sidewalls and deep channels that would not be possible with any other technique.

The footprint size of the sub-aperture processes is in general at least in the millimeter scale, while Vortex Machining is capable of producing features down to 10 μm in lateral dimensions or less. Most of the processes have relatively limited range in footprint sizes. The tooling in Vortex Machining can be adjusted to enable polishing of features up to 0.5 mm in length. Note that this wide range of adjustability in tooling is also possible with IBF. It is also interesting to consider the footprint shapes produced from each process. Most, including Vortex Machining, are in general Gaussian, but this is heavily dependent on the process parameters. FJP has an interesting 'W' shape when the nozzle is positioned normally and MRF tends to produce 'D' shaped spots. However, the shape is usually not as critical considering the availability of advanced algorithms used to convolute the specific footprint shape into a tool path.

All of the processes are, in general, capable of producing surfaces with nanometer to sub-nanometer roughness. EEM is generally known to be the best for producing

potentially atomically smooth surfaces with negligible subsurface damage. IBF and its related technologies can also produce very smooth surfaces under certain circumstances, but care must be taken or significant surface roughening or even damage can occur. To date, surfaces with measured roughness close to the precision of EEM have been produced using Vortex Machining.

The last two categories to compare are the volumetric and depth removal rates. First considering the volumetric removal rate, it is shown that, as of the time of writing, the fastest rates for Vortex Machining ($10^{-4} \text{ mm}^3 \cdot \text{hr}^{-1}$) are comparable to EEM, the slowest of the other sub-aperture processes. MRF can remove material the fastest – however, such fast removal rates are usually reserved for rough shaping in which surface finish isn't of significant concern. While these comparisons are interesting, it is much more useful to compare the depth removal rates since the lateral dimensions of the footprints vary significantly. Considering depth per unit time, Vortex Machining is more comparable to the other processes. Its removal rates are faster than EEM and even similar to slow CCP finishing. MRF is again capable of producing the quickest removal.

Providing these comparisons are useful to understand the scale of Vortex Machining when related to other sub-aperture processes and also specific niches that it could potentially fill. It is also worth considering the mechanisms of each process. Some are almost purely chemical tooth, such as EEM, whereas others are facilitated through predominantly mechanical abrasion. While the results of investigations will be presented in Chapter 6, it can be said that Vortex Machining likely fits in between these extremes as do most polishing processes, involving both chemical and mechanical phenomena to remove material.

2.3 Measurement Tools

There are many of different instruments that have been used to measure surface features on a workpiece. These instruments can be broadly separated into contact (tactile) and non-contact categories – each offering specific advantages and disadvantages. Some have quicker processing times while others may return more significant or accurate data. In investigating Vortex Machining, it is especially critical to determine suitable measuring instruments since the process is new and the resulting footprint topographies have not before been documented nor analyzed. This section will review literature related to measurement methods and pertinent information for assessing each method's applicability to measurement and analysis in Vortex Machining. Correlation between various methods will also be investigated.

As measurement specifications are highly dependent on the feature geometry and shape, it is worth reiterating some of the general points of Vortex Machining presented in Table 2-1. The footprints can range significantly in size, from approximately ten micrometers (low-power) to hundreds of micrometers (high-power) in lateral dimensions with depths typically less than one hundred nanometers to several micrometers [3,5,33,34,35]. Also, since the footprints in general exhibit Gaussian-like geometries with modest depth-to-width ratios (usually less than 1:100), large surface gradients are usually not found. Realizing this, multiple measurement tools can be categorized in terms of their suitability for measuring Vortex Machining footprints.

As previously stated, contact methods, such as stylus or AFM, and non-contact methods, such as optical techniques will be discussed. Before going into the individual methods, it is useful to consider the Stedman diagram [36] displaying the limitations of each in terms of lateral and vertical feature measurement capability, see Figure 2-14. As

can be seen, the AFM is capable of measuring the shortest vertical and lateral dimensions, and the stylus is capable of measuring the largest vertical and lateral dimension (optical techniques are in the middle). Additionally, it has been noted that there is an inherent range-to-resolution ratio (approximately 10,000:1) for most of these techniques [37]. As such, in general as the range of measurement increases the fineness of resolution decreases.

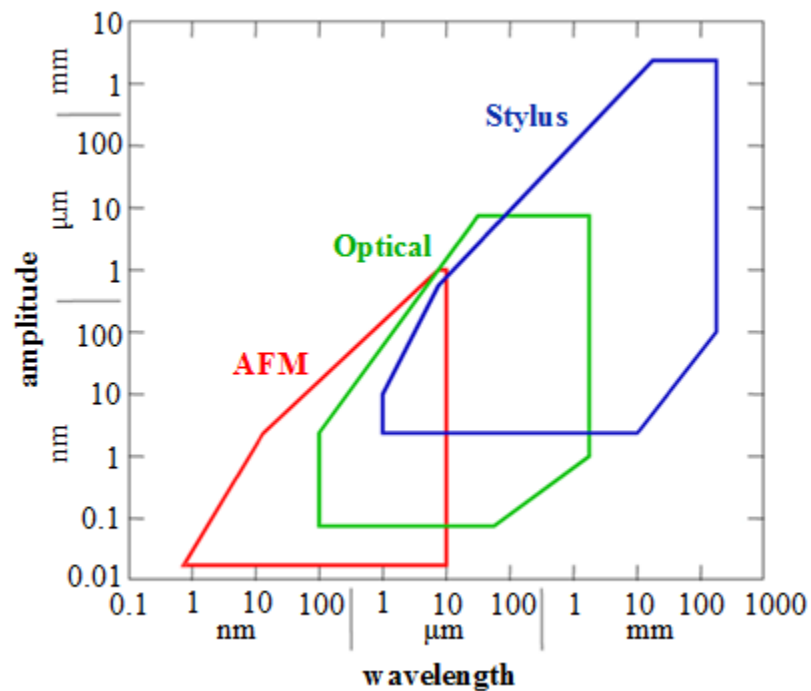


Figure 2-14: Stedman diagram showing general limitations of AFM, optical, and stylus measurement techniques. Modified from [36].

2.3.1 Non-contact Methods

As stated by Thomas, all surface measurements can be generalized as either looking at them or touching them [37]. Non-contact methods are usually characterized as the former. There are a variety of optical techniques that are in use such as optical profilometers, where focused light is reflected off and rastered across a surface, interferometers, where interference patterns are used to measure deviations in a surface, and even parametric methods in which large scale scattering of light is used to estimate surface roughness or other qualities [37]. Due to the available resources at UNCC and also applicability to the project, the method of interest to this research was the scanning white light interferometer (SWLI).

2.3.1.1 Scanning White Light Interferometer

The SWLI operates by using a low coherence, white light source usually in conjunction with Mirau or Michelson-type objective. At a certain stand-off distance from the workpiece, the recombined light produces strong interference patterns. By scanning the objective and measuring the interference patterns in each pixel, a surface map can be generated.

SWLIs offer the immediate advantage of being non-contact, thus workpiece deflection or even damage (such as from tactile techniques) are not an issue. Additionally, measurements are made of an area relatively quickly, from a few seconds to under a minute depending on the parameters that are used. Sub-nanometer vertical resolution and lateral resolution less than $0.5\text{ }\mu\text{m}$ is achievable with high-magnification objectives. However, there are noteworthy limitations. Gao et al. studied several commercial SWLIs and found that errors commonly occur near surface discontinuities or

large surface gradients (not an issue in the studies of this thesis). Also, SWLIs often overestimate surface roughness as a result of multiple scattering. The authors of this research study warn that care must be taken for nanometer resolution of complex structures [39].

2.3.2 Contact Methods

Perhaps the easiest to visualize and understand, contact or tactile measurement is characterized by measurement through touching, or contacting, the surface of interest. This is usually embodied by a sharp stylus connected to a cantilever being scanned in a raster path across the surface of interest. Motion of the stylus is then either transferred mechanically to recording paper, or, more recently, recorded electronically. As with the non-contact techniques, there is also an array of obscure methods used in the past to indirectly determine surface properties; one such interesting example is measuring the time a ball takes to roll across a workpiece [37]. In this section, focus will be put on the mechanical stylus and also the atomic force microscope (AFM) as potential techniques for measuring Vortex Machining footprints.

2.3.2.1 Stylus Profilometer

Probably one of the oldest quantitative measuring methods, the stylus profilometer is also relatively easily to conceptualize. In this method, a stylus is dragged across a surface, following the deviations of the workpiece being measured. Unlike the SWLI or AFM, the stylus profilometer is traditionally used to measure single line profiles across a sample. In its initial conception, innovative ways of recording these measurements included a system of levels that recorded the stylus displacement on a smoked-glass plate [40] and even a method of focusing light via a mirror onto

photosensitive film [41]. The next step was to integrate a transducer and electrically transmit the measurement to a recording instrument such as a chart recorder [42]. In current form, the profilometer signal is usually data logged on a computer (digitally) so that the measurement can be plotted and manipulated using software. The history of stylus instruments is both interesting and insightful, and a good review of this (as well as other measurement techniques) is given by Thomas [37].

Unlike optical methods which can produce artificial features, mechanical methods are generally regarded as more stable since a stylus is used to make physical contact with the surface of interest. That being said, some disadvantages of stylus techniques are only single line profiles are usually measured at a time and the dynamics of the stylus have to be considered as sometimes a resonance or mechanical damage can cause artificial features to be present or original features to be absent [37]. Contacting methods also pose the risk of damaging the measured specimen [37] and sequential measurement also gives way to potential long-spatial range errors [43] due to effects such as thermal gradients (longer measurement times than optical techniques). In addition, the stylus tip geometry is critical to the spatial resolution of mechanical profilers, with the tip radius acting as a type of low-pass filter. The tip radius value is, in general, the upper spatial frequency cutoff wavelength for this filtering effect [43]. While the majority of tips have radii ranging from 2 to 10 μm [43], some are as small as 100 nm [44]. Vertical resolutions for stylus measurements have been cited as low as 0.05 nm [44].

2.3.2.2 Atomic Force Microscope

The AFM is essentially a type of mechanical profilometer in which the stylus is manufactured onto a small cantilever using microelectronic processing methods. When

operated in a non-contact mode, the tip is maintained at separations of 10 to 100 nm from the workpiece due to attractive forces (molecular and electrostatic). As a result the tip ‘floats’ and indirectly measures the surface topography. More often the repulsive ‘contact’ forces between the tip and specimen surface are measured. In practice AFMs are often operated either in a contact mode, in which the cantilever connected to the stylus tip is elastically deformed according to Hooke’s law, or in tapping mode, where the tip is oscillated near a resonance frequency. In tapping mode, height of the stylus tip is controlled in order to stay at a fixed resonance state. Due to the strong relationship between the tip-to-surface distance, the surface shape is measured by controlling the height of the stylus tip. In either method, the tip is rastered laterally in order to measure an area map of the surface. In addition to surface shape, the AFM has also been used to investigate an array of other properties including friction forces, and elastic and plastic deformations [45].

While the AFM is characterized by high vertical and lateral resolution, there are some notable disadvantages. Since this measurement is recorded by rastering a stylus across the sample, the process can take a significant amount of time (at least a few to tens of minutes). Due to this, the process is relatively susceptible to environmental disturbances such as temperature changes and gradients, and also vibrations. These disturbances can introduce artifacts into the measurement. Additionally, while the AFM can potentially (at best) have atomic level vertical resolution, this is not always the case. According to Lin and Meier, who tested a TopoMetrix TMX 2000 AFM in variable force mode, AFMs do not necessarily have atomic resolution (but close to it). It is important to realize that the size of the AFM tip governs the interaction with the measured specimen.

The tip used in this study had an estimated radius of curvature of 100-400 Å (10 Å = 1 nm). With their configuration, the authors concluded that atomic spacing could only be resolved if atoms were separated by at least 2.5 Å [46]. Such resolutions are typically measured under very controlled laboratory and specimen surface conditions, with super-smooth surfaces. Additionally, the repeated contacts of this method make tip wear a significant issue, particularly with the sharpest tips necessary to achieved these high lateral resolutions.

2.3.3 Summary and Relation to Vortex Machining

In summary of the measurement methods, the SWLI and stylus profilometer can offer significant vertical resolution, but only the AFM offers both high vertical and lateral resolution. Additionally, when measurements from the different methods are evaluated together inconsistencies can arise. Comparisons between SWLIs and stylus profilometers have shown that when measuring sinusoidal gratings, the arithmetic mean between these two methods can differ by as much as 80 nm. This was measured independently of bandwidth, and may have something to do with slope-related errors in the SWLI [44]. Comparisons between AFMs and profilometers found that arithmetic mean, root-mean-square, and peak-to-valley were measured to be greater with the AFM, probably a result of the inherent filtering in stylus methods due to larger tip radii and therefore less spatial resolution [47]. For the studies presented in this thesis, the footprints machined using the low-power and high-power facilities were measured and analyzed using a Zygo NewView 5000 SWLI and a Veeco AFM located at UNCC. Datasheets for the SWLI and AFM can be found in Appendix D and Appendix E, respectively.

In initial studies, Vortex Machining footprints were measured using a SWLI. Most footprints were investigated using a 50X objective and 2X zoom (50 μm by 70 μm measured area) which yielded near 0.5 μm spatial resolution. While this method was quick and relatively easy to use, for the small footprints machined using the low-power Vortex Machining facility (approximately 10 μm in diameter) the lateral resolution was not high enough to evaluate much more than the general form of the features. As a result, due to its higher lateral resolution, the AFM was considered to be most suitable for investigating the surface roughness of these features. Figure 2-15 shows a comparison of two footprints measured with both the SWLI and AFM that displays the resolution differences between the two instruments. With the AFM's max scan size near 80 μm , the full footprint could be measured. This is not the case for the much larger footprints (up to 500 μm dimensions) machined with the high-power facility. Thus these features were primarily measured using the SWLI.

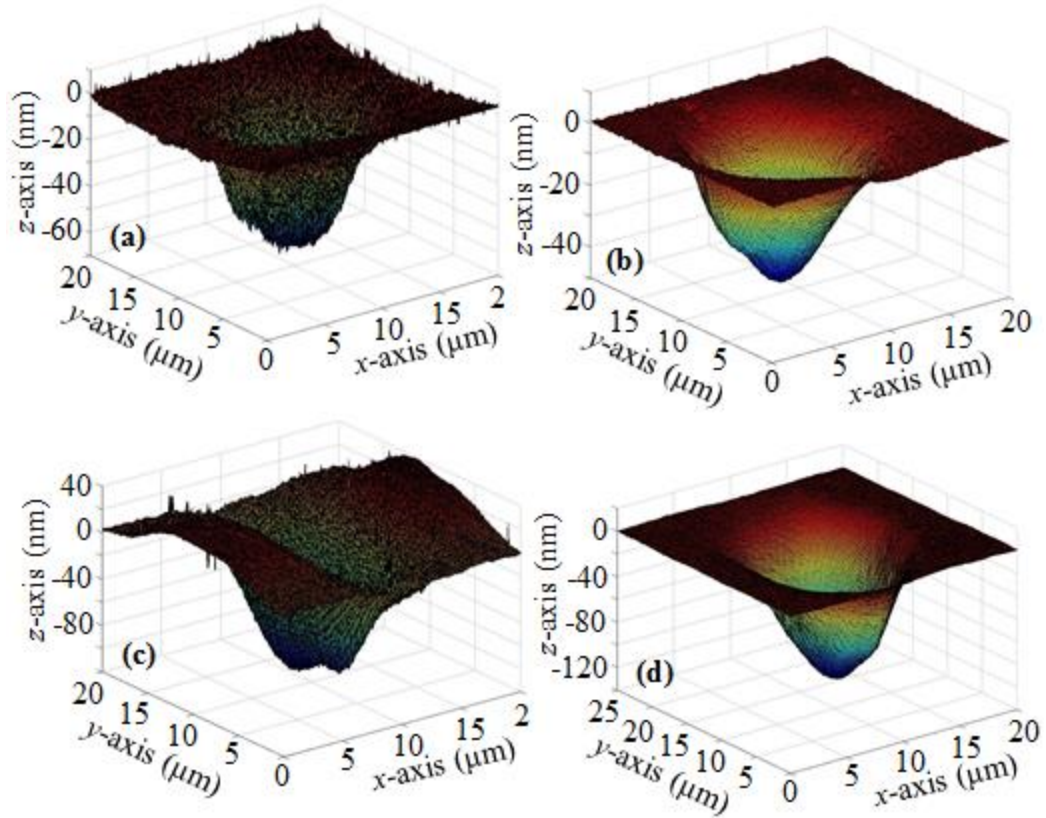


Figure 2-15: Surface plots of two Vortex Machining footprints measured with an AFM ((a) and (c)) and SWLI ((b) and (d)). For clarity, (a) and (b) are one footprint, and (c) and (d) are one footprint.

2.4 Analysis Tools

In terms of analysis, considerable post measurement analysis is necessary. To effectively make quantitative comparisons – as is necessary for any material removal method – the results need to be characterized. Characterization of surface geometries is a wide-ranging topic that has been covered significantly by others in the past [37,48]. In the following sections a brief review of topics related to this research is presented. In order to effectively examine surface properties, measurement data is often split into different spatial regimes. Such regimes are often denoted as form (low frequency, long wavelength), waviness (mid frequency, mid wavelength), and roughness (high frequency, short wavelength). To split the data into these regimes it must be filtered. Additionally, the data is usually characterized using mathematical formulas to provide single or dual number parameters that help to describe the surface properties thus enabling more effective comparisons. These parameters are almost always made relative to a specific spatial regime. Due to differences in filtering, it is wise (though often not practiced) to include the specific filters and cut-off wavelengths used for the analysis. These topics and their relation to Vortex Machining will be explained in this section.

2.4.1 Filtering

In early implementation of studies into surface texture, many interesting methods were used to filter a measurement into different spatial regimes. Filtering was often utilized to separate out the high spatial frequencies. This was accomplished sometimes with a mechanical skid or even electrical resistance-capacitance (RC) filters [37]. As mentioned previously, the use of large sized stylus radius could be used to isolate the low spatial frequencies in a form of mechanical filtering. There are some inherent shortcomings to these approaches such as the original surface measurement being lost.

Also, standardization of stylus radii and even skid types can be cumbersome, especially considering the large number of instrument designs that have been put in use [49] therefore making comparisons difficult. Electronic RC filters could solve some of these problems; however, their roll-off characteristics were often gradual – a disadvantage when trying to concisely separate spatial regimes. In addition, RC filters have an inherent phase shift thus distorting the actual measurement [37]. Much of these problems have been overcome with the advent of digital recording and processing. Since measurements are often stored in digital arrays on computers, this data can be digitally filtered allowing a much wider array of filter types – specifically ones utilizing regression algorithms. Only a few will be covered here, but the reader is encouraged to refer to works by Thomas [37] as well as Raja and Muralikrishnan [50] for extensive historical and practical reviews of the subject. The latter in particular provides many examples of filter implementation and has been of great help in the development of tools for the analysis of Vortex Machining footprints.

2.4.1.1 Gaussian and Related Filters

The Gaussian filter is a widely used technique which utilizes a symmetric Gaussian window for filtering data while not imparting any phase shift. It is advantageous that the filter is specified by the International Organization for Standardization (ISO). However, it is not necessarily the most convenient filter for this research that is specified by ISO [51]. Problems with the Gaussian filter include significant edge effects – specifically edge roll off – which therefore require the filtered profile to be truncated. Also, significant deviations of the mean can occur when filtering

profiles with deep valleys [50,51]. It was noticed that some Vortex Machining footprints exhibited deep valleys, therefore presenting the need for a more appropriate filter.

There are several alternatives to the Gaussian filter that do not exhibit its previously mentioned shortcomings. The R_k filter eliminates much of the effect of deep valleys by first fitting a mean line to the profile and then replacing data points below the mean line with the mean line's value. A Gaussian filter is then applied to the new data yielding a considerably more conformant profile, but having the same edge effects. It seems that the Gaussian regression filter attacks both problems successfully [50]. This is accomplished by applying the Gaussian regression filter, which is robust against end effects, on the original profile and then repeating this filtering process on the subsequent profile. This filtering process can be applied multiple times and often yields a filtered profile that is robust against deep valleys and end effects [52]. One thing to note, however, is the R_k filter is in the ISO standards while, as of the writing of this thesis, the robust Gaussian regression filter is not.

Implementation of the filter will be covered more fully in a later section, but in this section it should be mentioned that usually a low-spatial frequency profile is extracted by implementing the basic algorithm as it takes a form similar to the common boxcar filter. However, it is not necessary to apply a separate high-pass filter to obtain roughness. Since Gaussian-type filters specify the spatial cutoff at 50% transmission, the high-frequency portion of the profile can be obtained by subtracting the low-pass filtered profile from the raw data. By performing this operation sequentially, multiple spatial regimes can be isolated [52]. An important limitation is that when the initial filtering

operation does not fully capture the intended spatial frequencies, this information is lost to subsequent operations [50]. As a result, the spatial cutoffs must be carefully specified.

2.4.1.2 Spatial Cut-offs

Spatial cut-offs define where each specific regime will be separated. In terms of application, this means that the long and short wavelength cutoff should correspond to the wavelength limits on the filtered region of interest. As such, this initial definition can have significant impact on the resulting analysis of form or roughness, and it is important to both specify and be consistent when applying cut-off limits. According to Thomas, the wavelength cut-offs between form, waviness, and roughness are usually specified arbitrarily as this characterization depends on the surface being measured. However, he does report that DIN 4760 (a German metrology standard) suggests the length to amplitude ratio of form to be 1000:1. There is a similar ratio specification for waviness as well. An important note is that he emphasizes that these cut-offs, especially the roughness cutoff, are “a matter of subjective assessment” [37]. The standards as well as historical comments on cutoffs separating different spatial wavelengths should be kept in mind and consulted in reference to filtering operations.

It is also worth considering the widely recognized ISO standards. ISO 4287-1997, as is specifically stated in its title (Geometrical Product Specifications – Surface texture: Profile method – Terms, definitions and surface texture parameters), applies to profiling methods. The cutoffs separating form, waviness, and roughness are defined in this standard [53]. In ISO 4288-1996, it is stated that parameters should be calculated from each sampling length and then values from each sampling length can be averaged for an average of parameter estimate. There should be five sampling lengths, with the smallest

recommended length of 0.08 mm. If less than five sampling lengths are used, an equation is given to calculate the modified standard deviation that can be appropriately compared to the standard deviation calculated using the previous techniques [54]. Relating this back to the research presented in this dissertation, in many cases this minimum cutoff of 80 μm is considerably larger than the feature size of the material removal footprints produced by Vortex Machining.

2.4.1.3 Comments on Area Filtering

Historically, line profiles have been the most widely investigated measurements and thus many of the filters, cutoffs, and respective standards apply to such data. In addition, filtering of any area-based measurement was not possible until the advent of digital processing and filtering techniques. However, area measurements are becoming more widely used and offer a much greater amount of data available on surface topography. For research presented in this dissertation, it is not conceivable to have produced the same amount of analysis on Vortex Machining without being able to analyze, filter, and process data on three-dimensional measurements of the process footprints. Also, if desired, profiles can be easily extracted from area data. In terms of applications to filtering, most of the methods mentioned can be easily transferred to area data. Most digital filtering consists of a convolution of a ‘filter map’ with the data array. Extending this to another dimension, a ‘filter matrix’ can be convoluted with the three-dimensional data for area filtering. Muralikrishnan and Raja give examples using Gaussian filtered techniques for three-dimensional data [52]. Similar steps could be taken to apply other filters in three dimensions as well.

2.4.2 Surface Characterization

While separating surface components into different spatial regimes is necessary, the data is still left in a graphical form that is inconvenient for direct comparison. Technicians often utilize these graphs to understand the properties of surfaces, but when comparing a large number of workpieces this can become tedious and subjective. As a result, it has become standard to assign numerical values to quantify surface characteristics. In order to effectively compare the results of Vortex Machining to other polishing processes, this characterization is necessary and a background is covered in this section.

2.4.2.1 Parameterization of Surface Roughness

In most polishing processes, surface roughness is of primary interest. After separating out the high frequencies from the raw surface data (roughness), the next step is to characterize the surface. A number of mathematical formulas have been designed for such characterization. Before proceeding in this section, it is noted that there are too many parameters available to cover here, and the reader is advised to consult Thomas [37] or Whitehouse [48] for further reading on this topic. In fact, it has been noted before that there are so many of these parameters that many of them do not make mathematical sense or are redundancies of earlier basic parameters already defined. This large and unnecessary number of parameter definitions was aptly denoted as the “parameter rash” by Whitehouse [55].

Some of the most common and easily understood are the amplitude parameters, of which the name implies that parameters are used to describe the distribution of amplitudes of the data, typically from a mean line. Probably some of the first to be used

were the extreme value characterizations such as R_t , which is the length from the highest peak from the lowest valley.

$$R_t = R_{peak} - R_{valley} \quad \text{Equation 2-10}$$

where

R_{peak} , highest peak from profile mean

R_{valley} , deepest valley from profile mean

Deficiencies in R_t are abundant, such as the fact that only two points out of all the data are considered thus making it a very poor representation of the surface. Originally an American standard convention, the root mean square average, or RMS roughness (R_q) takes into account the average of the squared deviations from the mean line.

$$R_q = \sqrt{\frac{1}{n} \sum_{i=1}^n y_i^2} \quad \text{Equation 2-11}$$

where

n , total number of data points

i , current data point

y , profile value

It is still sensitive to peaks to valleys, but obviously returns a more useful representation than a simple extreme value. While the RMS roughness is a significant improvement, it can be readily demonstrated that surfaces which appear very different can have the same RMS value. Due to this, another set of variables defining the asymmetry in the distribution of surface points (skewness, R_{sk}) and also the sharpness of the distribution (kurtosis, R_{ku}) have been defined [37].

$$R_{sk} = \frac{1}{nR_q^3} \sum_{i=1}^n y_i^3 \quad \text{Equation 2-12}$$

$$R_{ku} = \frac{1}{nR_q^4} \sum_{i=1}^n y_i^4 \quad \text{Equation 2-13}$$

In fact, these three parameters can be represented as the second, third and fourth moments of the probability densities of the surface heights. Each of these parameters can be used to describe profile or area data. Usually an ‘R’ is used in front of the parameter when applied to a profile and an ‘S’ for a surface (for example R_q and S_q , respectively).

Spatial parameters are also sometimes used to describe surfaces. Thomas gives the analogy that sometimes “it is useful to know that the average height of the surrounding terrain is 1000 metres, but it is more important to know how quickly the height changes with position” [37]. One parameter is used to measure the correlation or randomness of adjacent data points through the autocorrelation function (ACF). It can be also thought of as measuring any periodicities in the data. Another parameter would be the power spectral density function (PSD) which returns information about both the amplitude and spatial characteristics in a single graph. In fact these both contain the same information and can be derived from one to the other through the Fourier transform pair. The PSD can be helpful in identifying and isolating information about specific spatial frequencies and their dominance in the data. For more information on these parameters and others, see [37,52]. These relations are mathematically more advanced, but can be of use in further characterizing complex surfaces.

2.4.2.2 Calculation of Removal Volumes

In addition to surface roughness, calculating the material removal rate is an important parameter for quantifying polishing processes. Calculating the depth removal

rate (length per time) is most often reported and is relatively simple to calculate. The volumetric removal rate can yield much more information, yet is significantly more difficult to implement. Due to this, background research on techniques to accurately perform such volumetric calculations was conducted.

McBride et al. discuss several techniques for calculating volume. One of the simplest is the three dimensional linear approximation method which is very similar to the trapezoidal technique. Other techniques such as the average-of-points method and three dimensional Simpson's rule have been discussed and applied by other researchers for calculating volumes of small-scale electrical contact bumps. It is interesting to note that comparison of the relatively simple linear approximation method and more complicated Simpson's rule show small deviations. The authors suggest the application should gauge which algorithm to use, as the shape and geometry of the volume can affect how well each method will work [56]. After a series of trials, the linear approximation method was chosen for use in analyzing Vortex Machining footprints. It was simple to implement, easily verified (see section 5.2.1), and showed consistent results.

In the approximation methods discussed in the previous paragraph, any deviation in the data will factor into the calculation. Defining the footprint boundaries is often difficult, however optimal selection could provide more accurate estimates of volume. Jiang et al. developed a technique to define footprint boundaries by identifying several slope parameters and a critical height parameter to determine when a point could be considered a boundary [57]. While interesting, this technique could pose problems in actual implementation. They provide some implementation discussion using two dimensional examples, but translation to real surfaces may be more difficult. For Vortex

Machining, most footprints were machined on atomically flat silicon substrates. As a result, footprint boundaries were not required since surrounding surface data averaged out of these measurements.

In performing volume calculations, it is often assumed that the measured footprint is a deviation from a perfect plane. As a result, calculations are made in reference to a nominal plane. While this method is convenient, it is likely not optimal in terms of its accuracy. Schöfer and Santner introduce possibly one of the most robust ways to accurately estimate volumes. A sample is secured to a platform which is kinematically placed under an AFM for measurement. After an indentation is made, the same area is measured again. Cross-correlation and linear regression algorithms are used to align the two sets of measurement data. Once aligned, one can be subtracted from another, with the new data yielding the deviation from the two. Numeric integration is subsequently used to calculate volume [58]. While this method is probably the most accurate that was identified in background research, it is also the most difficult to implement and could not be adopted for these studies.

2.4.3 Summary and Relation to Vortex Machining

Within each analysis tool that was presented, there are a myriad of different designs and implementations. While a full review could not be conveyed in this thesis, the above provides the reader with a sense of what is available. A variety of filtering methods are available, many designed to be specifically applicable for certain types of surfaces that have been encountered. For Vortex Machining, it was determined that the zero-order Gaussian regression filter was optimal and was used as the standard for all analysis reporting of resulting removal footprint data. It is relatively robust against end

effects and against deep valleys which are encountered in the process. Additionally, the filter is relatively common and easy to implement.

For many processes, the resulting surfaces will be split into three regimes (form, waviness, and roughness) for analysis. However, since Vortex Machining is so new and there is no standard for what the footprint should look like, it was decided to only use two regimes; form and roughness. This was convenient for the preliminary analyses that will be presented in this thesis. However, for readers practiced in studying surfaces it should be noted that as a result of only using two regimes some components normally considered to be waviness may be observed in the form profile. Also, due to the process being new and many of its footprints exhibiting lateral dimensions below cutoff standards presented by ISO, custom spatial cutoffs were specified for analysis of Vortex Machining footprints. It is conceivable that ISO standards could be applied to the footprints resultant from the high-power facility. However, this conformity to spatial cutoffs was not considered of critical importance in preliminary investigations and thus not employed.

While many robust volumetric estimation techniques were mentioned, the simple linear approximation method was used for calculating the volume of Vortex Machining footprints. Alternate, more sophisticated algorithms were shown to have limited deviations from the linear approximation method. It was found in implementation that the largest variability arose from other operations such as the plane fitting routine. While other methods such as those employed by Schöfer and Santner would likely be more accurate and robust, the implementation would require development of a further test facility and there were not sufficient resources to consider this for the presented analyses.

Lastly, in terms of characterization the roughness was specified by an RMS value along with its accompanied cutoff. Tribologically, other parameters may be of importance. However, since there is not a specific application for Vortex Machining any focus on these parameters would be speculation at this point.

CHAPTER 3: DESIGN OF LOW-POWER EXPERIMENTAL FACILITY

To provide a testing platform for conducting experiments into Vortex Machining using known process parameters, the low-power facility was designed and fabricated. Before this, the only evidence of the process capability was random removal spots created using a fixed tool experimental design [1]. With unstable testing, it was not possible to investigate specific details of how the process was removing materials and which parameters played a significant role in the removal. The low-power facility has gone through many iterations in pursuit of constructing an experimental test bed that is repeatable enough for these investigative studies. While instabilities are still present, the process has improved considerably as discussed in section 6.1. The design and early results of this facility have been outlined before and for further reference the reader is advised to look at [3,5,33,34,35].

3.1 Overview of Design

In early studies [1], erratic footprint removal volumes and geometries alerted the principle researchers into Vortex Machining that significant instabilities were present in the process. Due to the fixed position of the probe, the lack of controls in the initial experimental setup, and long testing intervals, it was realized that effects of the environment caused significant shifts in the position of the tooling relative to the workpiece. Environmental influences such as temperature instability caused expansion of test components causing relative locations to change and also significant evaporation of

the polishing medium caused meniscus effects on the probe resulting in not only a change in its location but also the machining dynamics. The problems with evaporation and slurry particle settlement lead to a new design that used a steadily flowing slurry stream. While it was possible to demonstrate materials removal with this set-up, the instabilities remained and precluded further study.

In an effort to improve the stability and repeatability of the process, a new facility was designed to maintain a relatively constant probe-to-workpiece position. A block diagram of this design and a photograph of the physical system is shown in Figure 3-1 and Figure 3-2, respectively.

This system comprises a bridge-type frame with a vertical axis supporting the machining probe and an X-Y stage attached to the instrument based and located under the vertical stage. As can be seen from Figure 3-2, attached to the machine frame is a high-precision single axis stage which is used to position the probe vertically relative to the workpiece. A sensor bank is attached near to the probe to minimize the measurement loop and machining loop. The workpiece is positioned laterally using an additional set of X-Y axes located below the frame. In addition to the translation mechanisms and sensors already discussed, the hardware for controlling the polishing slurry depth is shown as the auto syringe and reflective sensor. These components were implemented to maintain the slurry height and thereby further stabilize the probe's machining dynamics. Also, by ensuring relatively constant meniscus and fluid forces the probe location relative to the workpiece was stabilized more effectively.

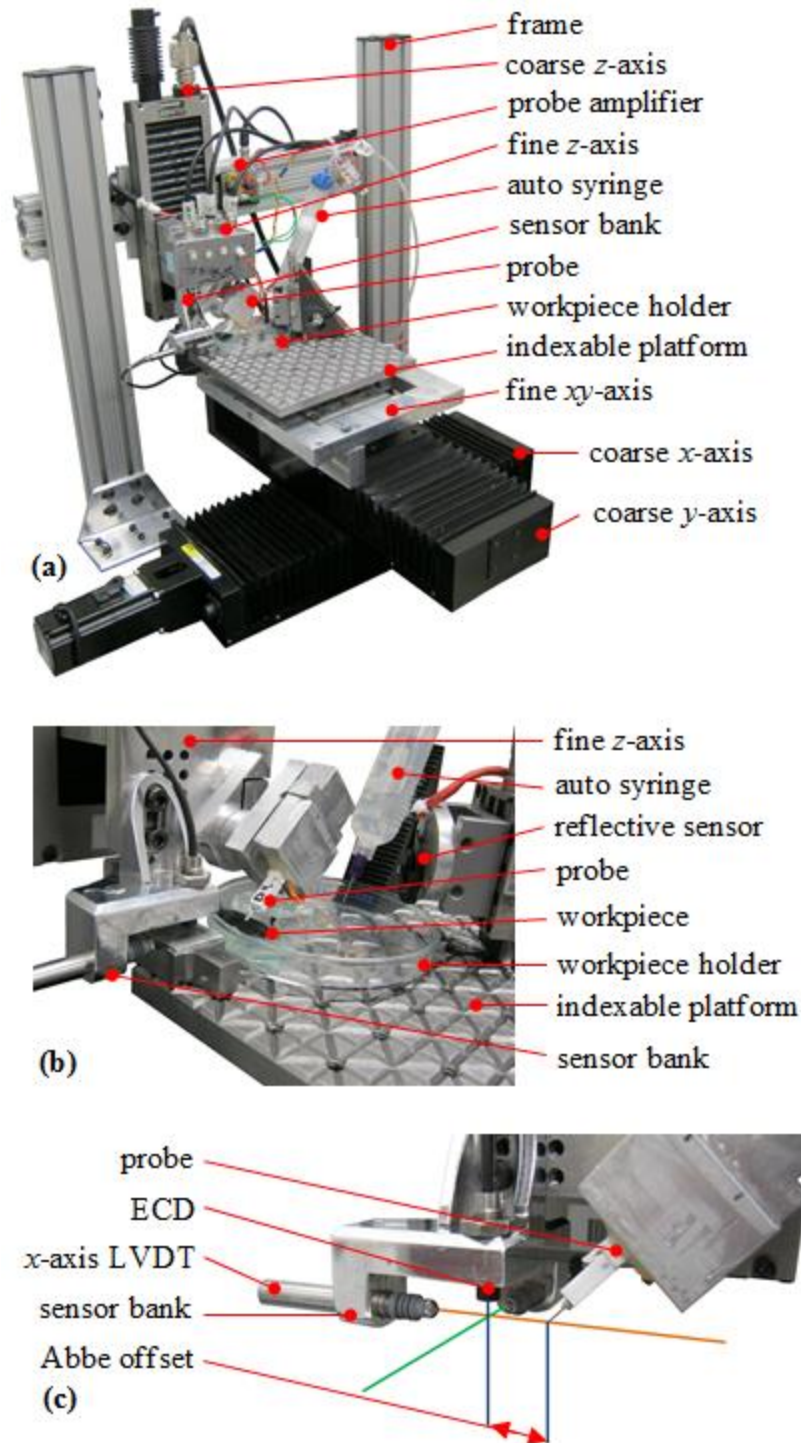


Figure 3-1: Image of complete low-power Vortex Machining experimental facility (a), close-up view of machining area (b), and close-up view of sensor bank showing Abbe offset of measurement axes and machining loop. Modified from [3].

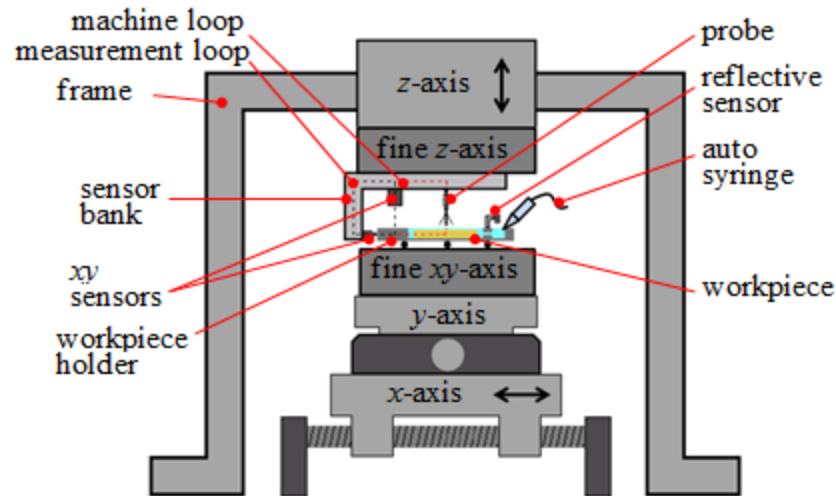


Figure 3-2: Schematic diagram of low-power experimental facility for Vortex Machining [3].

3.2 Tooling

In Vortex Machining a dynamic, high-frequency probe is used for the tooling. The probe is embodied by a cylindrical rod attached to a high-frequency actuator. As the rod is oscillated, it is inserted into the polishing slurry to induce vortices which are thought to be a primary method of material removal in the process, see Figure 2-1. As is represented in Figure 1-1, the probe for the low-power facility is embodied by a quartz crystal crystal tuning fork oscillator (Fox Electronics, model # NC38LF-327) with an attached 7 μm diameter, 3.5 mm long carbon fiber (Goodfellows, model #C006560). These types of probes have been commercialized by Insitutech, Inc. and used in a variety of applications including micro-scale manipulation [59] and also as force and touch sensors for measurement of localized surface features [60]. For the low-power facility, the probe is oscillated near 32.7 kHz inducing a 4th mode resonance into the attached fiber. This mode shape gives the probe the required rigidity for inserting in a highly viscous fluid such as polishing slurry while also allowing fiber amplitudes of 50 μm or more. In addition, the

near 500-to-1 aspect ratio of the probe could enable it to reach into complex or localized geometries [3].

Due to the widespread use of tuning forks in the microelectronics industry, these actuators are highly repeatable and also inexpensive. The high elasticity carbon fibers are also manufactured in large batches and exhibit significant repeatability of geometry and mechanical properties. Despite this, many issues have arisen in assembling probes causing variability in operation. In current practice, the probes are assembled in the Instrumentation Group laboratory by attaching the fork and fiber via ultra-violet cured glue (Norland™ Optical Adhesive 61), see Figure 3-3. The fiber is held in place while the tuning fork is moved into position using a manual translation stage. After the glue is cured, the fiber is trimmed using a sharp razor blade until a stable 4th mode resonance with relatively large oscillation amplitude (20 μm or more) is reached [35]. In practice, it is difficult to manufacture probes with variability in resonance frequency typically around 50 Hz in frequency and maximum amplitude variations being around 10 μm . However, it is still debatable how relevant these inconsistencies are to machining performance. In preface to the discussion in section 6.1, there have been limited correlations between amplitude and the resulting footprints. Due to the probe frequencies being around 32 kHz, it is unlikely that inconsistencies of tens of Hertz in the resonant frequency would impact the process significantly. This is verified by empirical evidence as well. In practice, much of the probe variability may be minimized due to significant damping from the polishing slurry reducing the amplitude at the tip. A study in which a machining probe was submersed in water showed the amplitude diminished by 50% or more depending on its depth. It is possible that while dynamics may show significant

differences when measured in air, the viscous polishing medium will variability between different probes to be minimized when machining.

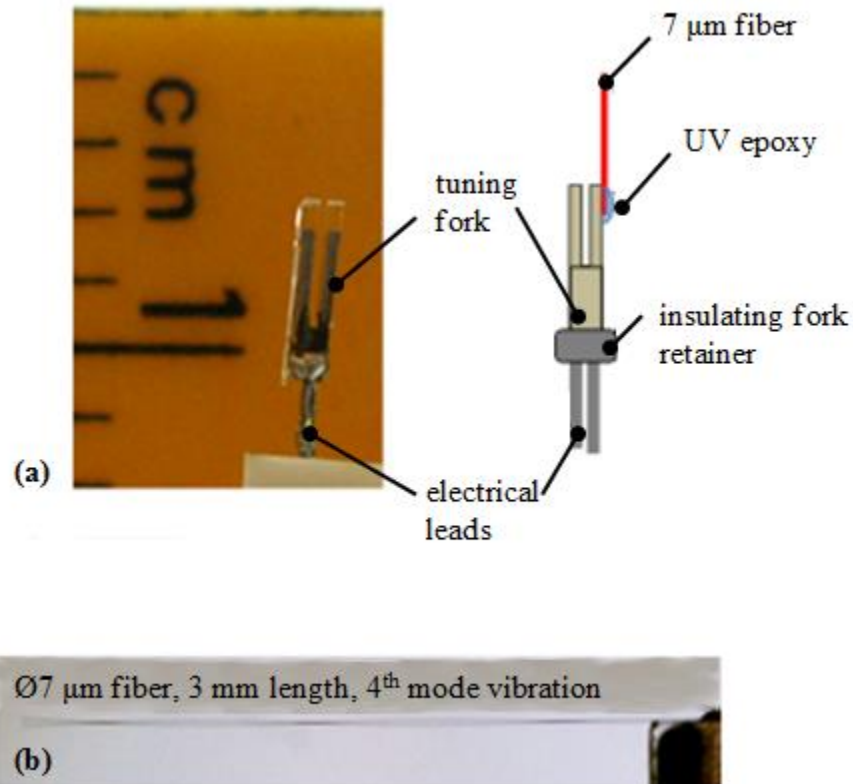


Figure 3-3: Image of tuning fork actuator and diagram (a) and probe in operation with a 4th mode resonance (b). Modified from [35].

While the effect of probe dynamics in the low-power facility is not yet fully understood, other instabilities in probe operation have shown to affect repeatability of the process significantly. Variables such as the parallelism of the fiber and tuning fork, amount of glue, and curing dose can affect the operation of the probe. Some generalizations of these effects have been made up to this point. Non-parallel misalignment between the fiber and tuning fork axes often results in resonance trajectories that are elliptical in nature and not limited to two dimensional motions. While

not necessarily a bad thing, these trajectories are not represented by the relevant fluid flow theory presented in section 2.1. It has been observed qualitatively that these elliptical motions tend to cause fluid flows that travel in a near circular trajectory around the probe instead of showing multiple vortices. Also, when the glue is not cured properly multiple modes near the resonance have been noticed and shifts between these modes have been observed, see Figure 3-4. This ‘mode hopping’ is often erratic in nature and can occur during machining operations, leading to inconsistent results as each mode often exhibits significantly different dynamics and, by implication, resulting fluid flows. For the reader interested in nonlinear dynamics, this behavior is reminiscent of strain hardening response. These issues are one of the reasons that a second, high-power facility using an alternate type of tooling was designed.

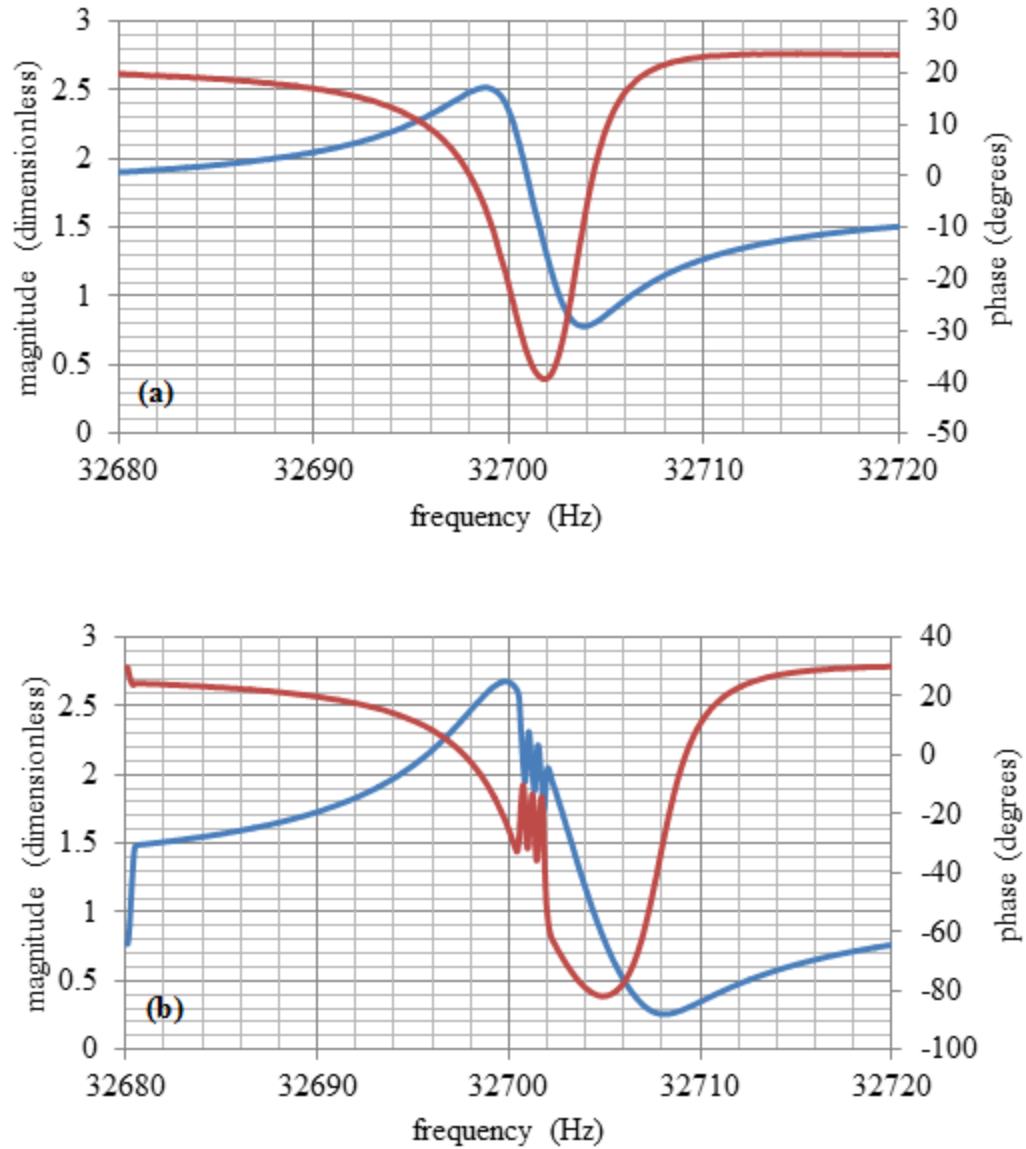


Figure 3-4: Plot of normal (a) and irregular (b) low-power probe dynamic response. Irregular response displays multiple modes or ‘mode hopping’ behavior. Blue lines are magnitude and red lines are phase.

3.3 Mechanical Systems of the Low-Power Experimental Facility

Keeping with the philosophy of Occam’s razor, the low-power facility’s design was simplified to reduce complexity of controls and also modeling of errors induced by

environmental disturbances. Specific performance goals and attributes of several of the main mechanical features of this facility are discussed in this section.

3.3.1 Machine frame

The machine frame utilized for the low-power facility is a variant of the fixed bridge construction often used in precision coordinate measuring machines (CMM's). This design is more rigid than many others due to the fixed overhead frame and is also less susceptible to component temperature induced expansion distortions as a result of its symmetry. In other machining centers, the vertical axis is often extended over the workpiece using a cantilever. This provides an open space for large workpieces and easy access, but results in a correspondingly large bending moment and lower resonances and stiffness of the vertical axis. Another variant, the moving bridge machining center can accept large workpiece weights, but suffers from non-repeatable motions and less rigidity due to the moving overhead frame [61]. Since Vortex Machining is used for polishing of micrometer scale footprints on small-scale workpieces, the use of the more stable fixed bridge machining center was employed.

3.3.2 Indexable Platform for Sensor Targets, Workpiece, and Slurry Controls

The indexable platform, see Figure 3-1(a), is a unique feature of the system that was integrated to enable easier cleaning of the experimental facility and also machine re-configuration. The platform is essentially a steel plate with a network of vee-grooves machined at incremental angles of 120° . Spheres and magnets are attached to the bottom of components to provide a kinematic location, allowing them to be snapped repeatably into place. In addition, the components can be spaced at regular intervals. As is shown in

the figure, the workpiece holder, auto syringe, and reflective sensor are all attached to the indexable platform using this method.

3.3.3 Sensor Bank

After initially constructing the machine frame there was some doubt over whether positional feedback and compensating control would be required for this application. The original plan for the experimental facility was to simply locate individually controlled translation stages that would hold the probe and workpiece in a constant position. To investigate the stability of such an uncompensated system, a laser interferometer was fastened to the machine frame to measure any motions in the vertical axis. Tests showed a positional drift of $6\text{ }\mu\text{m}$ over 24 hours that eventually settled out as well as an ongoing, cyclical variation of $0.5\text{ }\mu\text{m}$ with a period of approximately 15 minutes, see Figure 3-5. After investigation of the data and experimental setup, it was determined that this long-term drift can be most likely attributed to operator-induced thermal instability (i.e. the presence of the operator). The short-term cyclical behavior had been noticed before in other systems, and is mostly due to on-off cycles of the laboratory air conditioning system. In an effort to reduce the effects due to the air conditioning system, the system was mounted to a vibration isolation table and moved to a separate laboratory with temperature stability of $20 \pm 0.1^{\circ}\text{C}$ and a controlled humidity of less than 40%. During early designs, the size of the machining footprints was thought to be in the range of hundreds of micrometers and this performance was deemed adequate for the purpose of these studies. However, as machining process stability improved the size of the footprints reduced by a factor of ten and at this time, these instabilities were re-evaluated as unacceptable.

To reduce these instabilities, a metrology system for measuring the relative position between the probe and workpiece was designed. The sensor bank, see Figure 3-1(c), contains two linear variable differential transformer (LVDT) sensors (Solarton Metrology, model #M922500A36-01; Fowler, model #M922608A503-02) for measuring the lateral axes and an eddy current sensor (ECD; Lion Precision, model #ECD140) for measuring the vertical position. The sensors offer ranges of 1.5 mm, 1.5 mm, and 2 mm, respectively; and resolutions of 0.5 μm , 0.5 μm , and 0.1 μm , respectively. The sensor bank holding the sensors is attached to the vertical axis and measurements are made in reference to a monolithic rectangular steel block that is mounted on the fine-motion lateral axis next to the workpiece.

While the sensor ranges limit the controllable working volume of the system, even at millimeter scale there is enough room to machine tens to hundreds of micrometer scale footprints that are characteristic of the low-power Vortex Machining process. The design allows both the measurement loop and potential Abbe offsets to be minimized, see Figure 3-1(c). While the x -axis measurement offset was nearly eliminated, a minimal offset of 25 mm was allowed in the y -axis for viewing with a high-magnification camera (Sony, model #XCD-SX910). A 25 mm offset in the vertical axis was also required as the sensor cannot intersect with the machining location. Another feature is that the machine axes are governed by the precision of the monolithic reference block, which was implemented using a precision gage block bonded to the indexable platform. All of these features provide an effective, but inexpensive and easily implemented metrology system for the experimental facility [3].

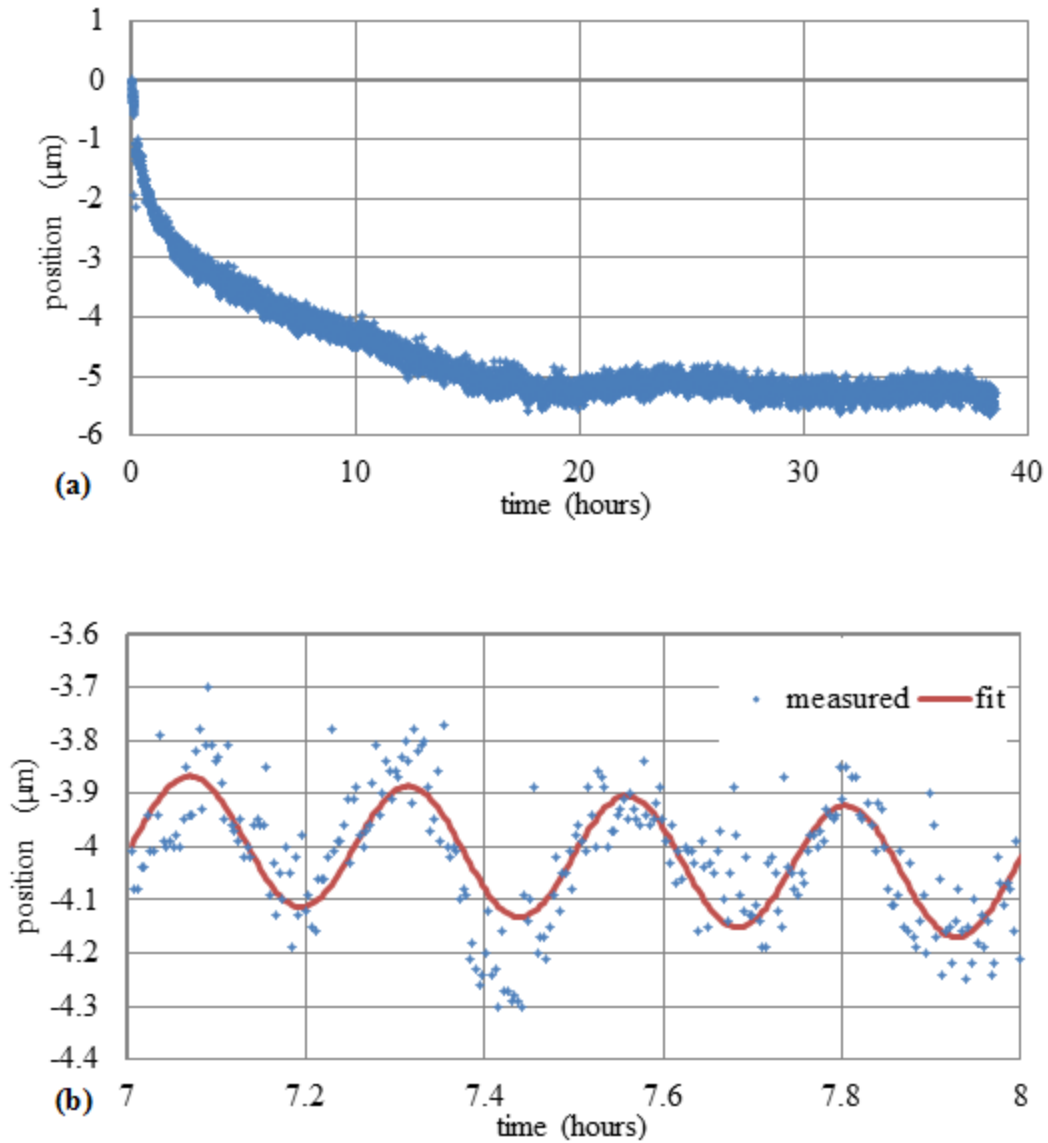


Figure 3-5: Graphs of measured long-term drift (a) and short term cyclical (b) position variance in the uncompensated machine frame [3].

3.3.4 Translation Stages

In order to take advantage of the metrology system, a mechanism for position compensation was required. Initially, UNCC manufactured, ball-screw driven translation stages were used to position the workpiece and probe relative to each other. These stages offered positional compensation below 10 μm which was considered adequate for the

material removal footprints initially expected to have lateral dimensions of 100 – 500 μm [1]. After preliminary tests yielded footprints with lateral features 10 μm in scale, a need was apparent for a more precise positioning system. It was predicted that coarse-axis and fine-axis stages coupled together could produce positional compensation reliably below 1 μm . In addition, this type of setup would allow adequate range for retracting the workpiece and probe away from each other so there would be a comfortable working space for setting up new experiments subsequent to testing. This also provides post-testing cleaning operations which are a necessity with any process that uses polishing slurry.

To accomplish this new design for lateral positioning, two commercial ball-screw stages (Parker Daedel, model #081-6107) driven by AC servo-motors (Yaskawa, model #SGMAH-02BA41) were integrated for the coarse axes. These stages offered a best-case 2.5 μm control resolution. In order to increase the precision to the sub-micrometer scale, a fine xy -stage driven by stacked piezoelectric actuators (Tokin, model #AE0505D16F) and having a positioning range of 15 μm was placed on top of the coarse axes, see Figure 3-1(a).

Background research indicated a need to produce a vertical axis with even better control than the lateral axes. According to Qi, who studied fluid flow resulting from actuators similar to those used in the low-power facility, the flow energy is more highly correlated with the probe-to-workpiece vertical position when compared to other process parameters [62]. This full relationship has not been determined, but can be understood by noting that the workpiece represents the only major boundary condition within the flow. Independent of the reasons, a more stable vertical axis was implemented to combat

instabilities resultant to the probe-to-workpiece position variation. The z -axis stage construction is similar to the lateral axis with a coarse-axis stage (Klinger Scientific, serial #6638) for long range control and a piezoelectrically actuated fine-axis stage mounted on top, see Figure 3-1(a).

The total range for the x , y , and z -axes is 300 mm, 300 mm, and 100 mm, respectively. In addition, the fine-axis stages offer total displacements 15 μm , 15 μm , and 30 μm in each axis. Note that while the large range for each axis is critical for machine re-configuration and cleaning, the precision controllable range is localized to the working volume of the metrology sensors. The long-range axes can be controlled manually or by way of rotary encoder feedback on the servo-motors outside of this volume [3].

3.4 Instrumentation Systems

It was advantageous to categorize and describe the dimensional metrology sensors in section 3.3.3. However, there are a variety of additional instrumentation systems that were critical for stabilizing the Vortex Machining process. While the controls of each system will be covered in section 3.5, this section will outline attributes of the instrumentation sensors and details on their implementation.

3.4.1 Probe Lock-in and Phase-locked Loop Implementation

Issues with probe repeatability and also dynamic instabilities have been outlined in section 3.2. Even when properly working, the machining probes offer an interesting problem in controls. Tuning fork oscillators have a high quality factor with a resonance that is sensitive to environmental changes such as temperature and humidity. Due to this, applying a fixed frequency during testing is not sufficient. As shown in Figure 3-6, the fiber amplitude (or energy) varies significantly depending on where it is on the resonance

curve. Since this resonance can shift by several Hertz during the course of a test, a more robust method of control was required.

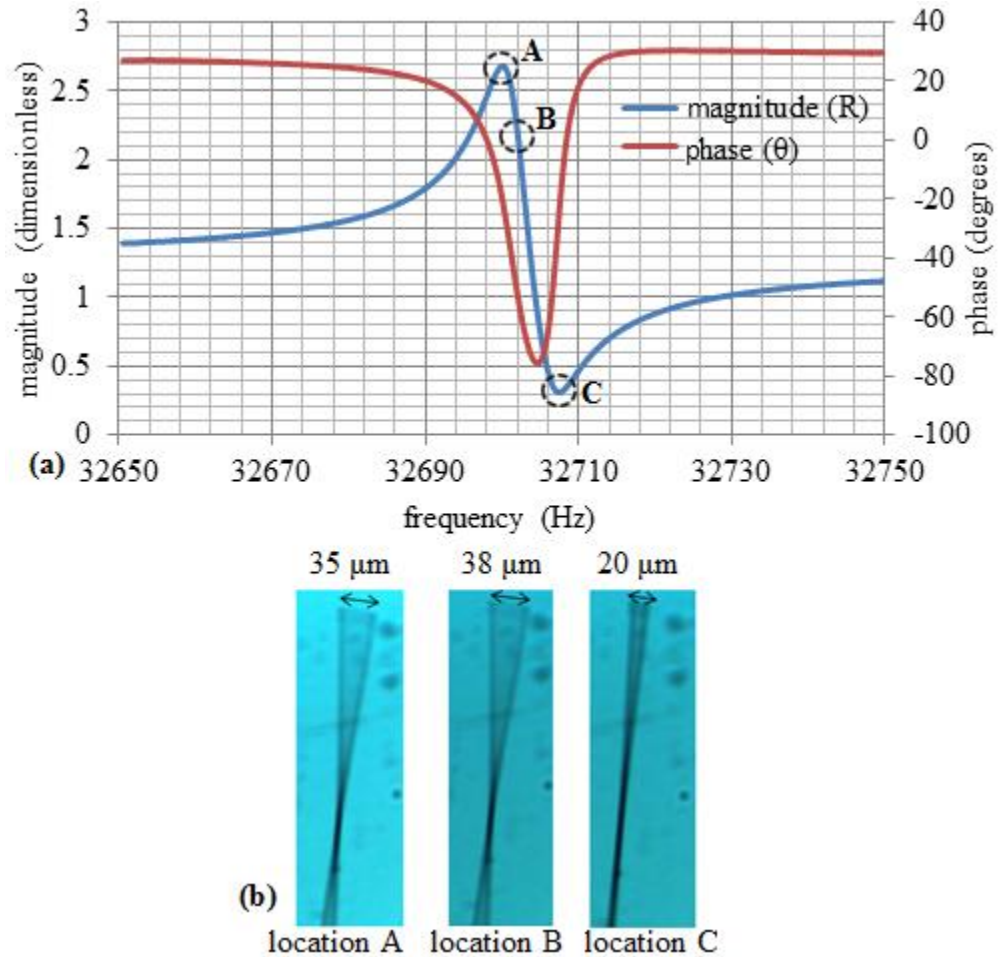


Figure 3-6: Typical probe response curve (a) showing amplitude variability (b) at different places in the dynamic response [35].

A schematic diagram of the amplified bridge circuit used to control the probe is shown in Figure 3-7. While a less complex version could be used to simply drive the probe oscillations, quantitative process feedback can be derived through the balancing bridge after which the signal is amplified using a differential integrated circuit. This

signal is then demodulated using a lock-in for real-time measurement of the gain and phase of the dynamic response. While a commercial lock-in was used initially, an FPGA-based (National Instruments PXIe-1073) lock-in was programmed into the control hardware for a later evolution of this process [3]. Additionally, the in situ lock-in provided the ability to integrate a custom phase-locked loop for controlling the probe to a constant phase (which more closely follows a single resonance) and therefore enabling it to induce consistent flow energy to the polishing slurry. Further details will be covered in section 3.5.1.

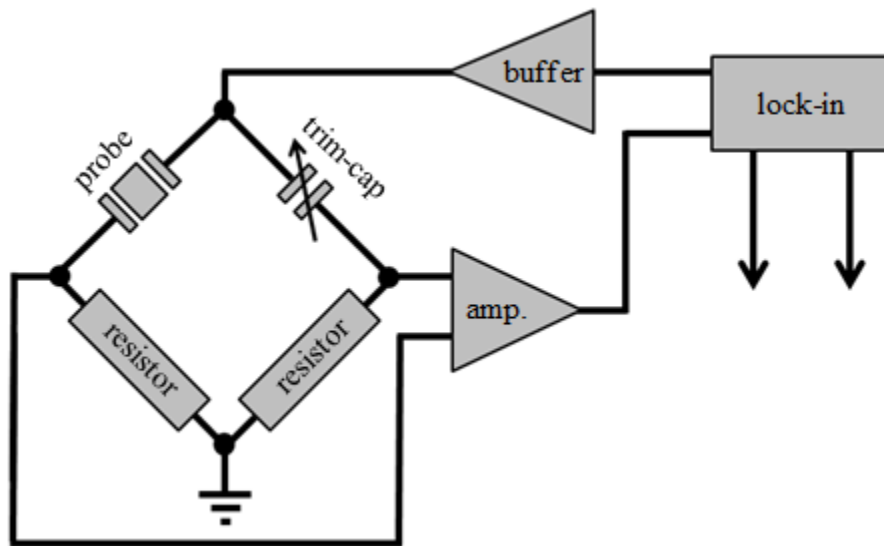


Figure 3-7: Schematic diagram of balanced bridge amplifier circuit for real-time measurement of probe gain (R) and phase (θ) response [3].

3.4.2 Slurry Depth Compensation

The high aspect-ratio, slender tooling in the low-power facility is susceptible to environmental effects – most significant being the polishing slurry meniscus forces. During the testing procedure, the workpiece holder is filled to a specific depth of

polishing slurry prior to the probe being lowered into position. The polishing slurry forms a meniscus around the probe and this meniscus generates a significant force, causing a 'virtual' node to be formed where it is incident on the fiber. When this virtual node is incident at the fiber's 'natural' node, the energy of oscillations is at a maximum. When incident on a natural antinode, the energy is at a minimum [3]. During the course of the experiment, the slurry will begin to evaporate at a rate typically near to 200 μm per hour causing the virtual node to move down the length of the fiber and this varies the probe's oscillation amplitude. Additionally, this change in meniscus will drag the fiber laterally in position, causing the machining location of the oscillating probe tip relative to the workpiece surface to change. Out of all the effects, slurry depth evaporation was observed to have the most significant impact on the process. Footprints with unrepeatable, irregular, and sometimes 'streaked' geometries were produced as can be seen in Figures 6-1 and 6-2.

In response to these problems, a system for compensating the changes in the slurry depth was developed, see Figure 3-8. This comprises a reflective sensor for measuring the slurry surface height and an autosyringe that is used to replenish evaporation. The reflective sensor (Fairchild Semiconductor, model #QRB1133) directs radiant, infrared-wavelength light at a small angle to the slurry surface. The light reflects and travels back to the photodiode sensor which measures its intensity. The circuit for this sensor uses a simple current driver for the light emitting diode (LED) and the emitter voltage of the phototransistor for measuring height variation. Overall this simple circuit works well providing a high signal to noise (around 40 mV of noise) that can be

amplified significantly to vary by around 3 V (i.e. signal to noise value of 75:1 or less than 2%). For a circuit diagram, see Appendix F.

In addition to measuring the slurry surface level, an automatically controlled syringe (Nordson EFD Ulitimus III) is used to replenish purified water into the slurry solution as the evaporation occurs. By sending an impulse signal to the syringe, it will pump 0.4 μL volumes of liquid. This pumping is achieved through a pressurized system in which a piston is used to push the liquid through a small syringe. The syringe is placed beneath the slurry surface and the pressure level was optimized to minimize disturbances to the slurry during this injected pulse of a water droplet. Utilizing the syringe as a compensating mechanism, the nonlinear sensor output is nulled to a highly sensitive region for micrometer level slurry depth control at which it has a sensitivity of approximately $1000 \text{ V}\cdot\mu\text{m}^{-1}$, see Figure 3-9 [3]. However, due to the fact that optical methods were used to measure the slurry depth, this sensitivity was subject to change depending on the slurry type and concentration. To simplify this matter, a null-control routine was used to stabilize the slurry depth, see section 3.5.3.

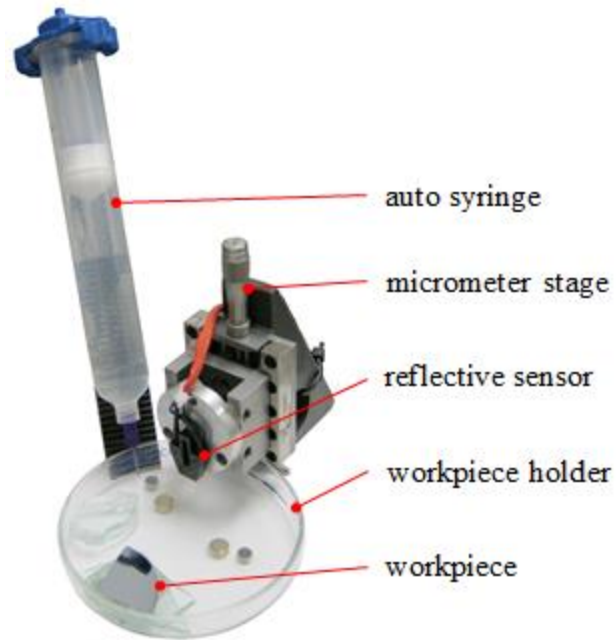


Figure 3-8: Image identifying components of the slurry depth compensation system [3].

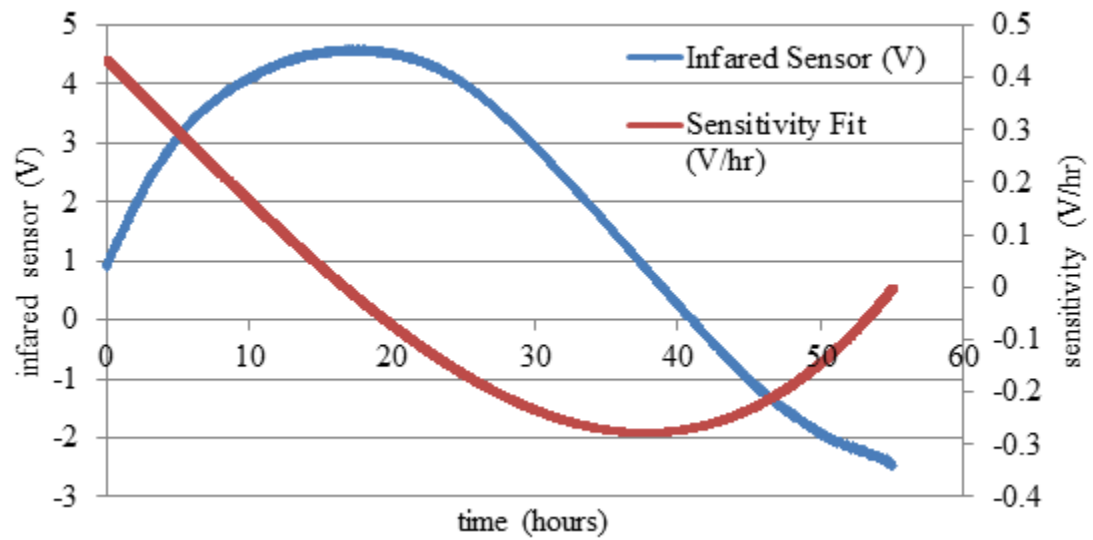


Figure 3-9: Plot of reflective sensor voltage output over two days as the slurry evaporates. Circle indicates the voltage in which the null-output routine is applied [3].

3.4.3 Probe-to-workpiece Automated Referencing

As will be discussed in section 3.6.2, one of the more time consuming parts of the experimental procedure is establishing a reference height between the probe and workpiece. This not only reduces efficiency in testing, but since the current procedure entails the operator manually finding and marking the position where the probe and workpiece make contact, it is also is potentially prone to human-induced variability. In an attempt to alleviate these issues, a system for automatically finding this reference for each machining location was designed and constructed. The automated referencing system is still in prototype phase and there remain issues that need to be worked out. As such, it is not currently in use. However, because of its potential to increase repeatability and save time in the Vortex Machining process, its design will be described for future users of the process.

To begin, probes similar to those used in Vortex Machining have been used previously as high-resolution contact sensors [60]. In many of these applications, the probe is used to detect proximity to a relatively rough and ‘sticky’ surface such as aluminum or steel. By using the circuitry shown in Figure 3-7, contact between the probe and workpiece can be identified by noticing a significant amplitude and phase change in the probe dynamics. In Vortex Machining, the primary workpiece is single crystal silicon which is nearly atomically smooth. For this material, contact between the probe and workpiece could not be detected reliably using the conventional circuitry. To remedy this, a high-sensitivity nulling circuit was employed to enable small changes in probe dynamics to be amplified, see Figure 3-10. A more complete diagram of the circuit is given in Appendix F. The circuit works by first attempting to balance the probe with a

trimming capacitor. Since the probe exhibits significant parallel resistance and inductance in addition to around 12 pF of capacitance, it is, in practice, difficult to null a circuit bridge to much better than a few hundred millivolts. In this new design, two identical frequency signals are sent to the probe and trim capacitor. By adjusting the amplitude and relative phase of these two signals, the circuit can be nulled to effectively less than a couple millivolts. The nulled signal is then amplified and demodulated after which any form of contact causes a high-sensitivity spike in the amplitude and phase of the measurement. By programming a microcontroller (Digilent Max32 chipKIT) to interface with two direct digital synthesis (DDS) IC's (Analog Devices AD9833), an algorithm was developed for reliably nulling the probe output.

While a step in the right direction, the automated referencing system still has a few issues to be worked out. The nulled output is actually so sensitive that any change in air current or temperature can produce significant spikes in the output. Mostly, adequate control routines need to be developed to discriminate between environmental noise and probe-to-workpiece contact.

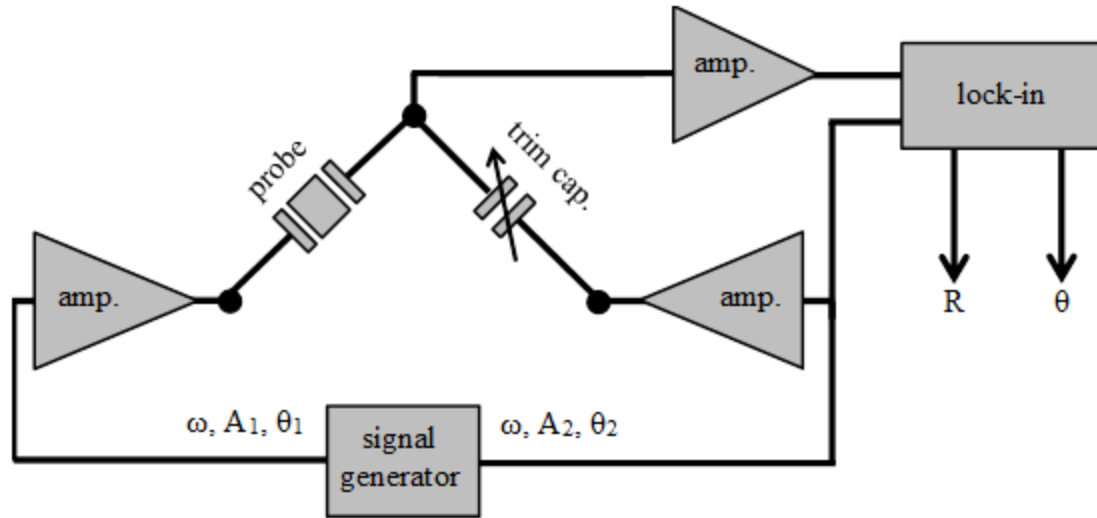


Figure 3-10: Schematic diagram of high-sensitivity nulling bridge circuit. A signal generator is used for sending two identical frequency (ω) signals with independently adjustable amplitudes (A_1, A_2) and relative phases (θ_1, θ_2). Magnitude of probe gain (R) and phase (θ) can then be measured [1].

3.5 Control Systems

As with any mechatronic system, design is not complete until adequate controls are in place. By investing significant time into developing a robust experimental platform, relatively simple controls were adequate for implementing the process. In addition, Vortex Machining is a comparatively slow material removal technique requiring stability ranging from minutes to hours with many process controls. To simultaneously control all process conditions and enable automated test procedures, a National Instruments, LabVIEW-based control system was developed. The system consists of a host control panel on a desktop computer, with a real-time computer for fast computation and control of most of the system hardware. An FPGA is also used for real-time control of the high frequency probe. The operator interfaces with the experiment through the host computer and the host connects to the real-time computer and FPGA for the bulk of

hardware control. A full description of the software code would be tedious and unnecessary to the goal of this these. However, the control algorithms for several of the main systems will be discussed.

3.5.1 FPGA Lock-in and Phase-locked Loop

In order to implement a lock-in and phase-locked loop that could be integrated with the rest of the Vortex Machining hardware controls, a lock-in algorithm was first programmed into the FPGA. The LabVIEW coding language allows a DDS signal to be generated with over ten points per cycle for a 32 kHz waveform. This signal was then filtered using a third-order active Sallen-Key filter to remove quantization before being applied to the balanced bridge circuit for driving the probe oscillations, see Figure 3-7. The reference signal from the probe measuring circuit was then measured into the FPGA using an analog input. By multiplying the reference signal with the original signal and then summing the products using a set of ten shift registers, the gain and phase of the probe's dynamic response could be measured in real-time. Also, by controlling the frequency, swept-sine frequency response tests could be generated and measured on demand. This functionality proved invaluable for in situ probe characterization before, during, and after experimental studies.

In addition to the real-time measurement of dynamics, a phase-locked loop was also implemented digitally into the real-time computer code. By using an integrator and differentiator to servo the generated probe frequency, the probe could be locked to a defined phase. Before integration of the phase-locked loop, the probe phase could change by 30 degrees or more through the course of a 30 minute test. As is shown in Figure 3-11, the control of probe dynamics have been significantly improved since the system has

been implemented with RMS deviations of 0.2 lock-in amplifier units on magnitude and 2.5 degrees in phase. During this period the frequency showed a steady drift of around 0.2 Hz. While relatively small, this drift appears to continue for days and even months. As will be explained in section 6.1, the probe control routine also contributed significantly towards stabilizing and improving repeatability of low-power Vortex Machining footprints.

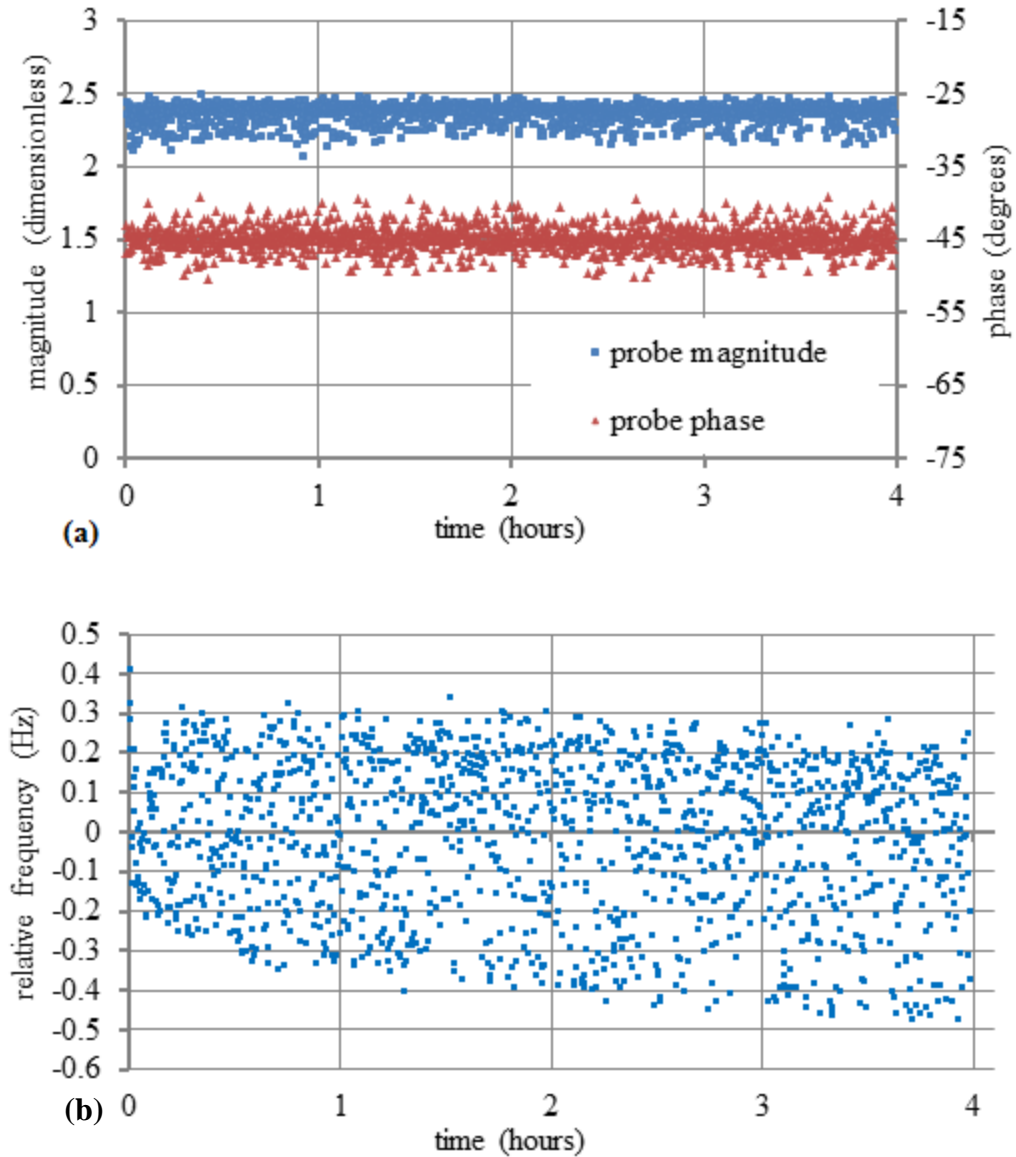


Figure 3-11: Plots of measured probe responses under close loop control of phase; (a) probe magnitude and phase, (b) frequency under phase-locked loop control. Relative frequency (b) shows probe frequency deviation from 32.178 kHz. Frequency is adjusted using the algorithm to stabilize phase to a setpoint of -45° [3].

3.5.2 Translation Systems

Each translation stage is composed of a long-range servo controlled stage and a short-range piezoelectrically actuated flexure stage. The long-range stages are controlled by sending a step and direction signal to the proprietary driver interfaces. The

piezoelectric actuator in the short-range axis is driven using a high-voltage (0 – 150 V) amplifier (Thorlabs, model #MDT693A) that is controlled using a digital-to-analog converter (DAC, 0 – 10 V) from the real-time computer. Comparing the corresponding sensor measurement to the desired position, an error signal is sent to a modified proportional plus integral controller, see Figure 3-13. As seen from the figure, the difference between the piezoelectric actuator voltage and its midpoint voltage is used to drive the long-range stage. In this fashion, the network of long and short-range stages is servoed to the appropriate position while keeping the short-range stage within range and near its midpoint. This keeps the faster short-range stages in an effective position for correcting high-frequency disturbances that can occur during testing. For this system, independent controller updating rates of 50 samples per second (sps) and 1000 sps are used for the long and short-range translation axes. In addition to this, controls for manually jogging the stages during experimental setup procedures have also been implemented. Figure 3-12 shows position errors for all three axes and indicates that after integration of this control strategy the positional controller error is better than $\pm 2 \mu\text{m}$ for all three orthogonal axes over a 17.5 hour period [3].

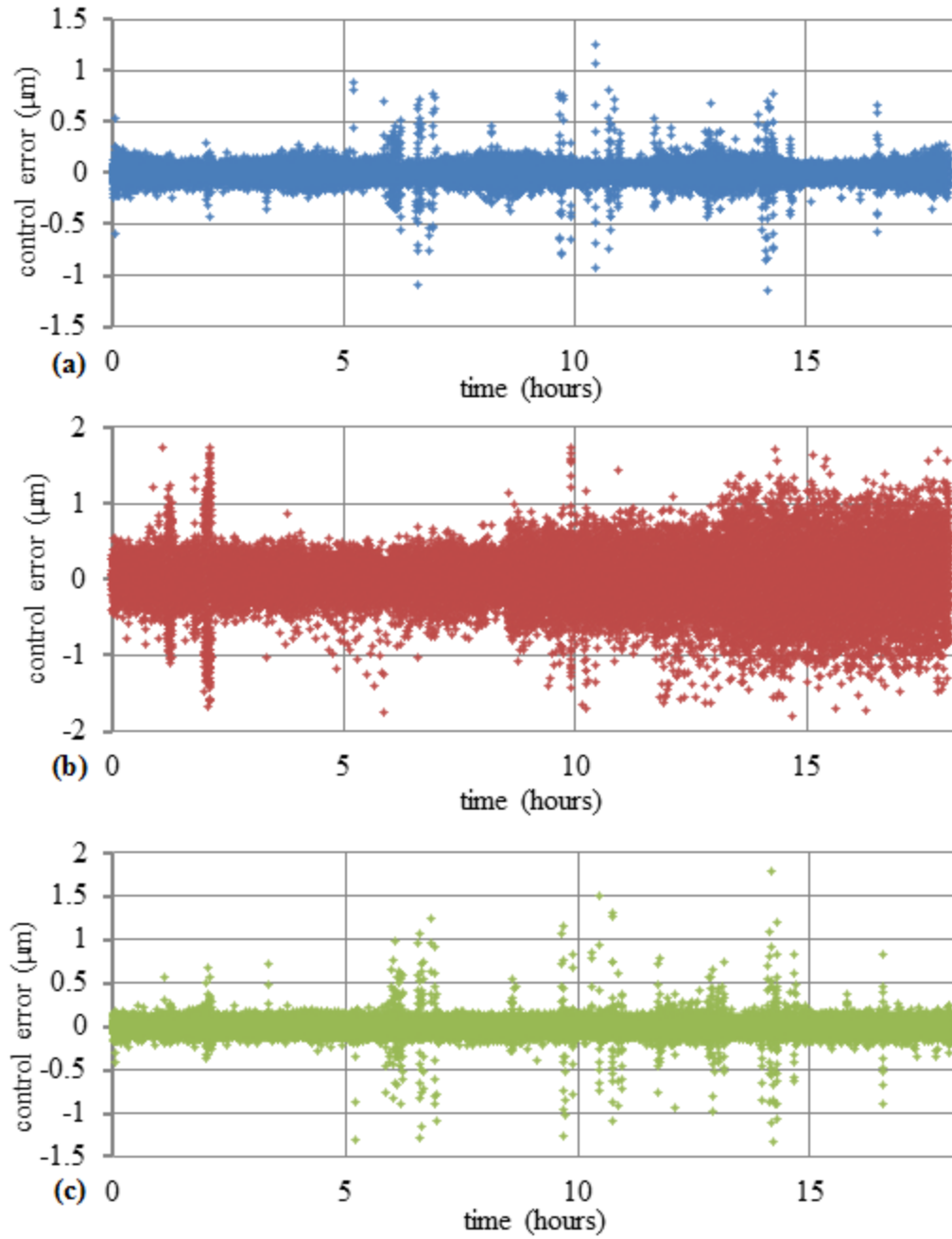


Figure 3-12: Control error in the x (a), y (b), and z (c) axes over an approximately 17.5 hour testing period while positioning to a total of 52 different locations over a $600\text{ }\mu\text{m}$ by $300\text{ }\mu\text{m}$ lateral area [3].

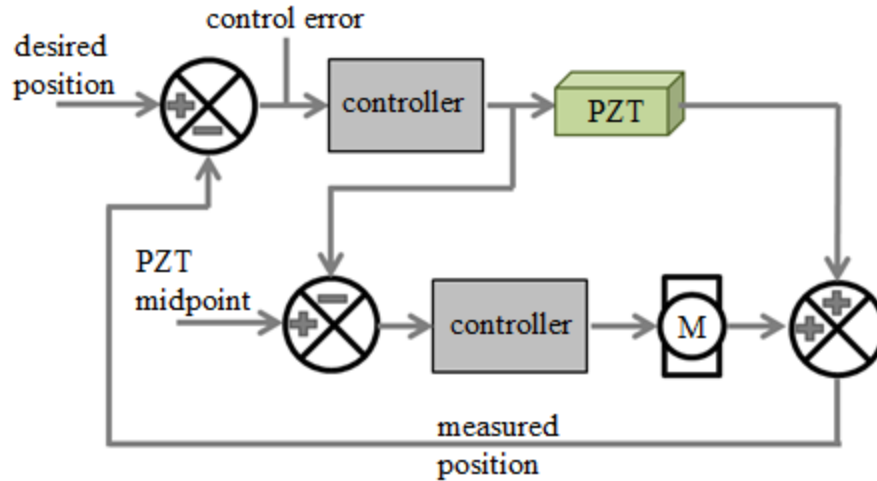


Figure 3-13: Block diagram of proportional plus integral controller algorithm for long-range and short-range translation stages. Position error is used to drive the piezoelectric actuators (PZT) and the PZT voltage difference from its midpoint is used to drive the servo motors (M) [1].

3.5.3 Slurry Depth

Because evaporation is unidirectional, a simplified ‘bang-bang’ controller was implemented for regulation of the slurry depth compensation system, see Figure 3-14. After the reflective sensor was nulled to its sensitive region, see Figure 3-9, the output was amplified and calibrated. If the sensor output is less than the user-defined target slurry depth, an impulse signal is sent to the automated syringe adding a precision amount of fluid ($\sim 0.4 \mu\text{L}$) to the slurry reservoir. Since the dynamics of the fluid reservoir are often slow in terms of the time delay between injecting the fluid and observing the resultant change in slurry height, speed controls were implemented to prevent overfilling. While simple, the controller has enabled slurry depth control with controller errors maintained within $10 \mu\text{m}$, see Figure 3-15.

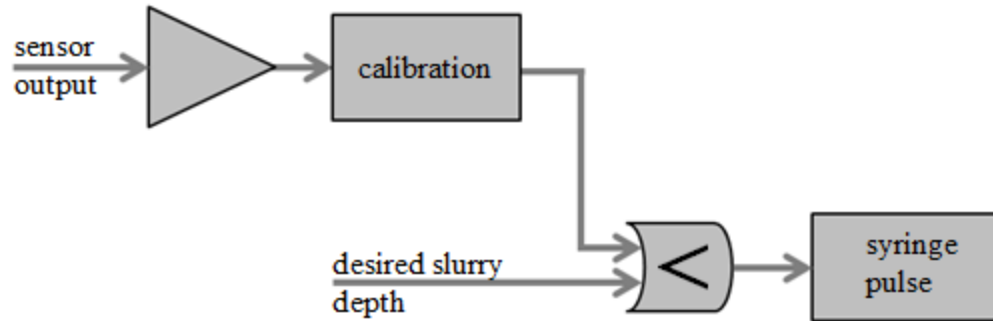


Figure 3-14: 'Bang-bang' control algorithm for slurry depth compensation system [3].

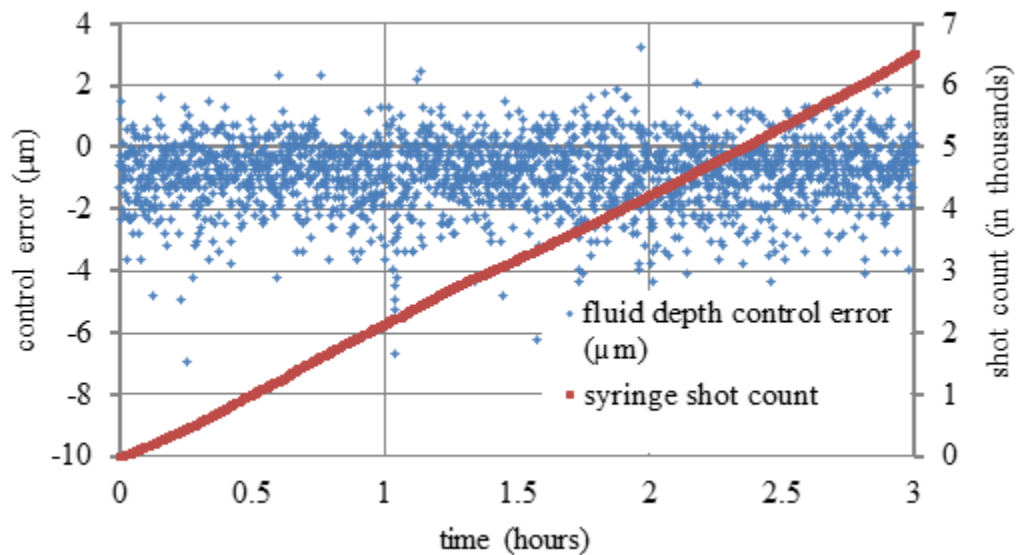


Figure 3-15: Plot of slurry depth controller error and syringe shot count for slurry depth compensation system [3].

3.5.4 Experimental Automation

For much of the development of Vortex Machining, an operator has been integral in setting up machining parameters and conducting experiments. Operator-induced variability is a significant concern, especially since multiple research endeavors headed by separate individuals have investigated the process. In its initial state, the low-power facility was used to conduct single polishing experiments in series, with an operator required to set up each experiment. This not only led to errors but was also time-

consuming. Since then efforts have been invested in automating many parts of the process.

Thus far, a mechanism for computer numeric control (CNC) of multiple machining tests has been implemented. After the operator determines the coordinates for a set of testing locations, he or she can upload these coordinates and the corresponding dwell times to a spreadsheet. The spreadsheet is read by the control hardware, controlling the probe and workpiece relative positions. In addition, the program has checks to ensure machining does not begin until the specific location is reached to within a target setpoint controller error (usually 1 μm). Implementation of the CNC automation control has enabled machining of arrays of footprints, see Figure 6-6, with set up times considerably reduced as well as minimizing operator-induced errors. This system is also capable of retaining precision positioning – Figure 3-12 shows control errors for all three axes after the translation stages were commanded to a total of 52 different positions over a 600 μm by 300 μm lateral area over a time period of 17.5 hours [3].

3.6 Testing Procedure

In order to better convey the Vortex Machining process as well as give guidance to future researchers of the process, the general testing procedure used in these studies is outlined. An operational manual detailing this procedure for the low-power facility is reproduced in Appendix G. The procedure will be subdivided into sections describing the pre-experiment setup, setup of the experiment, running a series of machining tests, and post-experiment analysis.

To clarify the discussion of the procedure, a few of the specific setup parameters used throughout these studies need to be explained. While the low-power facility has a rotary mount for positioning the probe in virtually any orientation relative to the

workpiece, the studies presented in this thesis have been performed with the probe positioned 45° relative to the surface with the oscillation trajectory of the probe tip directed along the surface plane (i.e. not into the workpiece). Due to its homogeneity and near atomic flatness, un-doped, polished silicon wafers with a lattice of $\langle 100 \rangle$ have been used as the workpiece. Also, a mixture of 50% water and 50 nm colloidal Alumina slurry (Allied High Tech Products, model #180-30000) has been employed for the polishing medium. The probe orientation, workpiece material, and polishing slurry were chosen as their combination produced optimally repeatable results in early investigations. Since most studies to date have focused on identification of the process roughness and repeatability, these variables have not yet been fully investigated.

3.6.1 Pre-experimental Preparation

Prior to setting up an experiment, several things should be taken care of. The workpiece should be chosen and, if needed, cut to a desirable size to fit in the experimental facility. The silicon workpieces are usually separated into smaller pieces (about 10 mm by 10 mm) by starting a small scratch with a diamond scribe and then bending along this fracture line. If done correctly, the workpiece will separate along a straight line started by the initial scratch. The workpiece is then fastened to the workpiece holder using a 5 minute epoxy and allowed to cure for a minimum of 24 hours. Even though 5 minute epoxies often set quickly, a full cure will often take half a day or more. Epoxy cures in a brittle state, making it optimal for rigidly holding the workpiece and also being relatively easy to break off using a sharp razor blade when machining is finished.

Next, a probe is chosen and its frequency response is measured. This response will be compared to a measurement after the test to assess whether or not the probe dynamics have changed significantly during the course of a test. It has been noticed that significant slurry particulates can accumulate on the probe's fiber during the course of a test. This can slowly change the dynamics of the probe, affecting repeatability in testing. However, no mechanical wear to the probe has been measured when studied by observation using an SEM before and after extensive machining [63].

3.6.2 Probe-to-Workpiece Referencing

Discussed briefly in section 3.3.4, a critical parameter for consistent polishing of Vortex Machining footprints is the probe-to-workpiece vertical stand-off distance. Throughout investigations, the probe stand-off has been set to 20 μm above the workpiece surface. Once again, this was found to be an optimal setting for reliably producing footprints. In order to establish this stand-off distance, the probe tip must be referenced to the workpiece surface.

The probe is oscillated near its resonance and slowly rastered towards the workpiece surface. As the probe approaches the workpiece its phase changes rapidly. Viewing the probe through the high-magnification camera, it can be seen to go from steady-state oscillation to becoming visibly unstable as the oscillation begins to interact with the sample surface. Through a combination of visual inspection and monitoring the phase change, the contact position can be established by a trained operator. Repeatability studies by individual operators have shown that this contact position can be referenced to $\pm 1 \mu\text{m}$. After establishing contact, the vertical machining position can be set to 20 μm above this reference.

Since integration of the automated CNC software for performing multiple Vortex Machining tests in a single test setup, the operator has to perform this referencing procedure for each machining location. The operator rasters the stages to the lateral coordinates of each machining location and references the vertical contact position. The coordinates are then uploaded to a spreadsheet (along with the dwell times) to be used by the control program.

3.6.3 Initiation of Experiment

After the pre-setup procedures are complete and the machining location spreadsheet has been generated, the experiment can be initiated. Using the probe tip as a measurement reference, the polishing slurry is filled to a specific level above the workpiece surface (usually 1 mm). The probe is then lowered into its starting position. The slurry depth sensor is set into place and set to its null height using the micrometer stage it is attached to, see Figure 3-8. The syringe is also set into place and the slurry depth control routine is initiated.

Prior to starting the experiment, the dynamic response of the probe is measured using a frequency sweep to identify the location of its resonance. The resonant phase is then used as the controller set-point and locked using the phase-locked loop. The experiment can then be initiated. The program will use the CNC spreadsheet to identify the probe location and dwell time for each machining location. The operator will leave the environmentally controlled lab – in order to reduce the affect of disturbances – and return after the appropriate amount of time for all machining tests to have been conducted.

3.6.4 Ending the Experiment

After machining the final location, the probe will retract itself from the slurry bath in order to prevent further machining. The operator will conduct another frequency response of the probe in order to measure any degradation in performance. The probe is then cleaned by holding it at resonance and then dipping it into a bath of distilled water for a short period of time.

After all hardware is turned off and the control program is stopped, the operator will remove the workpiece holder and dispose of the slurry. Any remnant slurry on the experimental facility will also be cleaned. The operator will then remove the workpiece from the holder and clean it in preparation for subsequent measurement.

3.6.5 Post-experimental Analysis

Once the machining is finished, the analysis procedure begins. The first step is to evaluate the stability of the experimental testing. The positional control errors, slurry depth control error, temperature, as well as probe magnitude, phase, and frequency are recorded for subsequent analysis. If any major instability occurred during the course of an experiment they should be observable in this data. In practice, actions as subtle as opening the laboratory door can be noticed through temperature rises and probe variability.

Additionally, the probe dynamics can be evaluated using data saved from frequency sweeps before and after the testing procedure. If significant changes are observed, footprints with non-repeatable geometries often follow. Finally, after evaluation of the experimental test, the footprint array is measured using the SWLI. If further resolution is required, the sample will also be measured using the AFM. Surface

measurement data is saved and analyzed using the data analysis package described in Chapter 5.

CHAPTER 4: DESIGN OF HIGH-POWER EXPERIMENTAL FACILITY

After two years of development, testing, and analysis, a low-power facility for machining repeatable arrays of Vortex Machining footprints has been developed [3,5,34,35]. System repeatability was a critical first step towards investigations into the process. However, some limitations are inherent to its design. The slender aspect-ratio of the tooling makes it highly susceptible to environmental instability. The probe's dynamics are damped by the viscous polishing medium, thus preventing investigations into machining with higher amplitudes observed with a probe oscillating in air. Also, the probe has a fixed power and size limiting testing to a narrow band of frequencies and a single fiber diameter. Reception by the scientific community – while positive – indicated an interest in scaling the process for higher removal rates. In response to this, an additional high-power facility was designed and constructed for parallel investigations into the process. In addition to providing a platform for investigation of a broader range of operating parameters, the process has demonstrated material removal rates well over 1000 times that of the low-power facility [33].

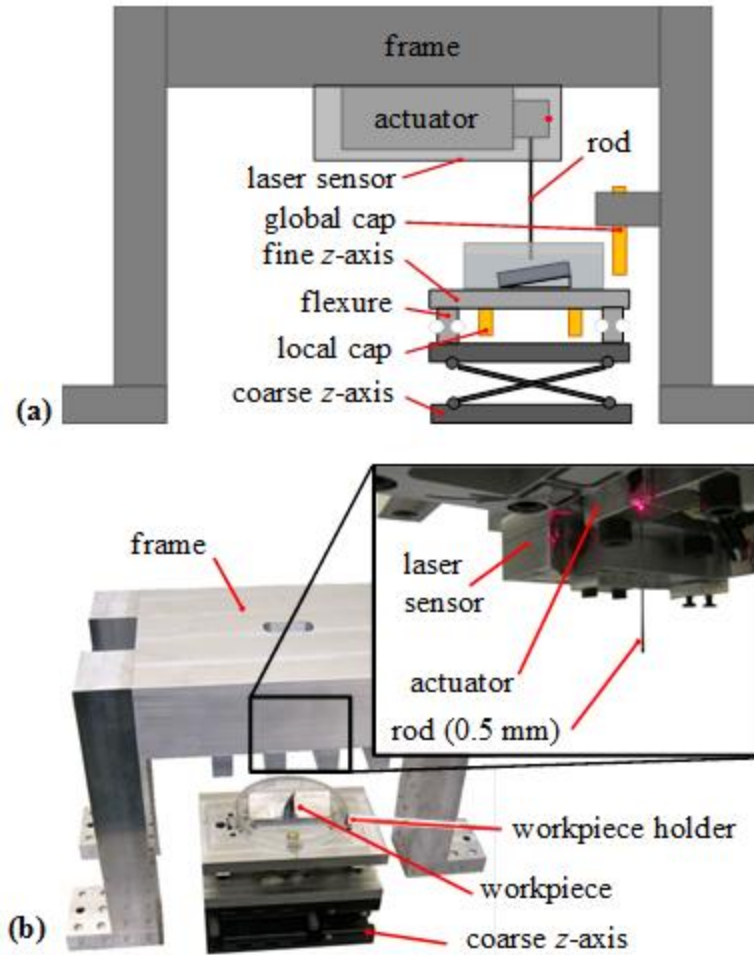


Figure 4-1: Schematic (a) and image (b) of high-power facility showing subsystems used in its design. Inset box in (b) displays subcomponents of the tooling. Since implementation, a manual xy -axis translation stage has been added below the z -axis [33].

4.1 Overview of Design

Due to the higher power machining capabilities of the experimental facility, a sturdier, more simplified design was employed. The original design, shown in Figure 4-1, comprises a heavy bridge-type frame structure to support the high-power actuator, with a z -axis stage for positioning the workpiece vertically relative to the workpiece. The workpiece holder is mounted using a magnetic kinematic clamp to the top of the z -axis stage. Since the original design, a manual xy -axis translation stage (Phase II, model #

260-512) has also been added below the z -axis for more repeatable lateral translations that were necessary to enable location of the probe tip relative to the workpiece surface. With this facility in its current implementation, positioning requirement limit its use to one machining location per test. While the design is simple, considerable effort went into minimizing the metrology loop for holding an accurate machining location, stabilizing the support structure to reduce disturbances from the actuator, and developing hardware and methodologies for repeatably referencing the probe and workpiece. The following sections describe the subcomponents of the high-power facility.

4.2 Tooling

In comparing the low and high-power facilities, the main differentiating factor is the tooling used to facilitate material removal. Where the low-power facility uses a tuning fork oscillator with a relatively fixed operating frequency (~ 32 kHz) and micrometer scale amplitudes, the high-power facility uses a millimeter scale tool in which the probe diameter is capable of a wide variation of oscillation frequencies and amplitudes. This ability not only enables a large variability of machining parameters, but also applications requiring a dynamic control of material removal with the potential of removing material at high rates. Subcomponents of the tooling are the high-frequency flexure, machining probes, and real-time tool measurement system.

4.2.1 High-Frequency Flexure

A broad-bandwidth flexure mechanism was designed for constraining the motion of the machining probe and providing a linear freedom for the piezoelectric actuator, see Figure 4-2. The flexure design consists of a symmetric array of four leaf springs to constrain motion to one degree of freedom. Evaluation using mobility analysis reveals

that the design is overconstrained. In practice the design works well with small oscillation amplitudes relative to the flexure dimensions (tens of micrometers). From FEA analysis in SolidWorks, the desired linear mode at 10 kHz is separated by several hundred Hz from parasitic modes such as torsion of the leaf springs. The combination of the high leaf spring stiffness (approximately $450 \text{ N}\cdot\text{mm}^{-1}$ for one spring; $1800 \text{ N}\cdot\text{mm}^{-1}$ total) and light central mass produced a design capable of elastic displacement of $15 \text{ }\mu\text{m}$ with a linear first mode natural frequency of 10 kHz. Due to its range and high-stiffness, a piezoelectric element (Tokin, model #AE0505D16F) was chosen to actuate the mechanism, see Figure 4-2. The piezoelectric actuator provided a maximum of approximately $15 \text{ }\mu\text{m}$ displacement when 150 V was applied. In practice, the assembled flexure actuator produced large-oscillations well past 10 kHz [33]. To increase controllability of the actuator, silicon gel (Sylgard 184) was added in between the central mass and base structure to provide shear-based damping, see Figure 4-2. Further details into the dynamic response of the complete system will be covered in section 4.2.3. While the flexure was designed using a combination of fine element modal analysis and analytical theory, readers are cautioned as computational estimates often deviated significantly from actual results. Useful references for design and flexures and consideration of mechanical mobility can be found in [64,65,66].

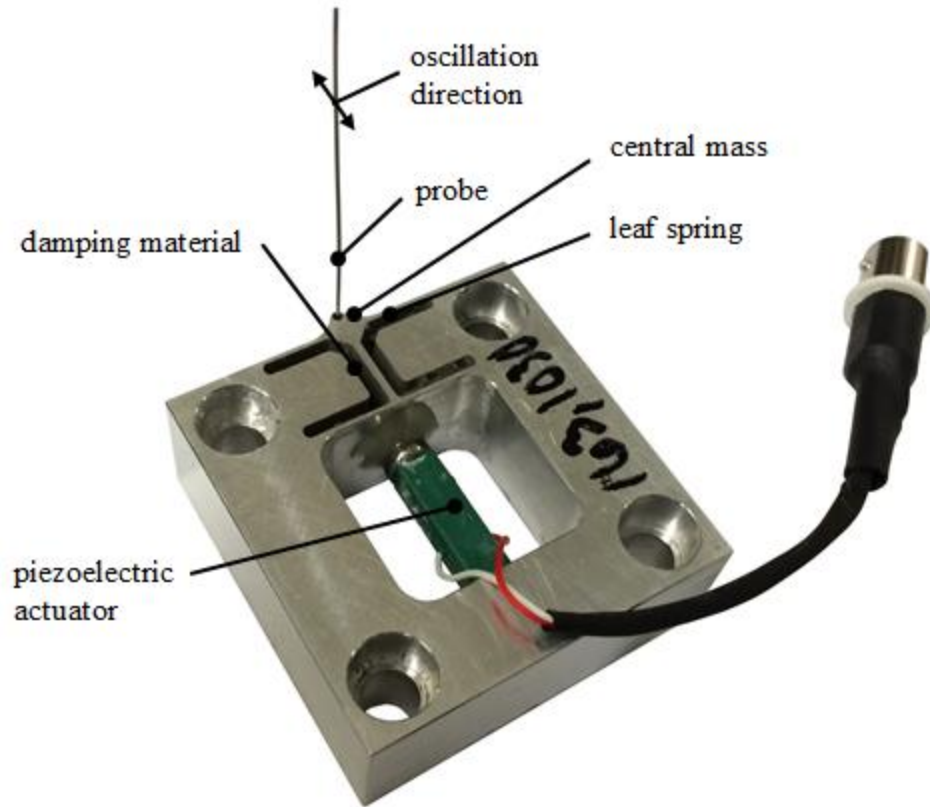


Figure 4-2: Image of high-frequency, flexure-actuated probe for high-power experimental facility.

4.2.2 Machining Probes

At the tip of the central mass in the high-frequency flexure, see Figure 4-2, is the machining probe. The probe consists of a molybdenum rod of cylindrical geometry. By drilling a precision hole in the central moving platform of the high frequency flexure (Figure 4-2) the rod was securely fastened using a thin film of high-strength Loctite 30 minute epoxy. In addition, for fastening smaller diameter probes into place, sets of hypodermic tubing were used to step down the hole's diameter. In this way, many flexures were manufactured (with identical geometries) and were assembled with varying probe diameters and lengths. In similarity to the probes from the low-power facility,

correctly fastening the probes to the flexure is critical to the resulting dynamic response. Studies tracking oscillation trajectories have shown that even with careful assembly, probe oscillations can become elliptical near resonance.

Comparatively, the high-power probes are in general easier to assemble and characterize. While the high-power tooling can technically be oscillated at any frequency, it has been beneficial to operate the probes near resonant frequencies to produce high amplitudes and thus more energetic slurry flows. By choosing the diameter and cutting them to specific lengths using precision scissors, probes of known 1st through 3rd mode resonances as high as 3 kHz have been cataloged and used in investigations so far. As an example, a 0.5 mm diameter probe with a second mode frequency near 2 kHz was desired for a series of machining tests. After calculating the appropriate length using dynamic theory, the probe was trimmed to approximately 33 mm. This resulted in a measured resonant frequency of 2050 Hz with 200 μm in amplitude at the probe tip.

4.2.3 High-Power Amplifier Capable of Driving Capacitive Loads

Aside from designing a broad-bandwidth flexure, development of an amplifier for driving the piezoelectric actuator to high frequencies was necessary to facilitate the high-power tool. Piezoelectric actuators are dominated by a capacitive impedance which reduces inversely with increasing frequency. By using Ohm's law, it can be easily shown that the power required to drive this type of load will thus be in square proportion to increasing frequency. To make matters worse, most design handbooks for high-power amplifiers are focused on voice-coil (inductance dominated) actuators for which the impedance increases with frequency and is, therefore, inherently more stable. However,

inductance-based actuators are limited by their large volume, heat generation and were not selected for this application.

Before designing a custom amplifier, many commercial versions were considered but most offered signal bandwidths of lower than 250 Hz and higher power amplifiers cost tens of thousands of dollars while still being limited to drive currents ranging from 100 up to 400 mA (see for example the high voltage power amplifiers manufactured by Trek Inc.). Due to this, an amplifier based on a simple open-loop, hybrid class-AB architecture was designed and constructed. The simple design was found to be much more effective than more complex, closed-loop versions which would exhibit oscillatory instability with even small changes in loading conditions. Field-effect transistors (FET's) are used to source and sink the capacitive load. A 50 ohm power resistor placed in parallel with the load was also found to significantly improve the stability of the design. For a diagram of the amplifier circuit, see Appendix F. From the large signal frequency response shown in Figure 4-3, the system is capable of bandwidths of approximately 10 kHz.

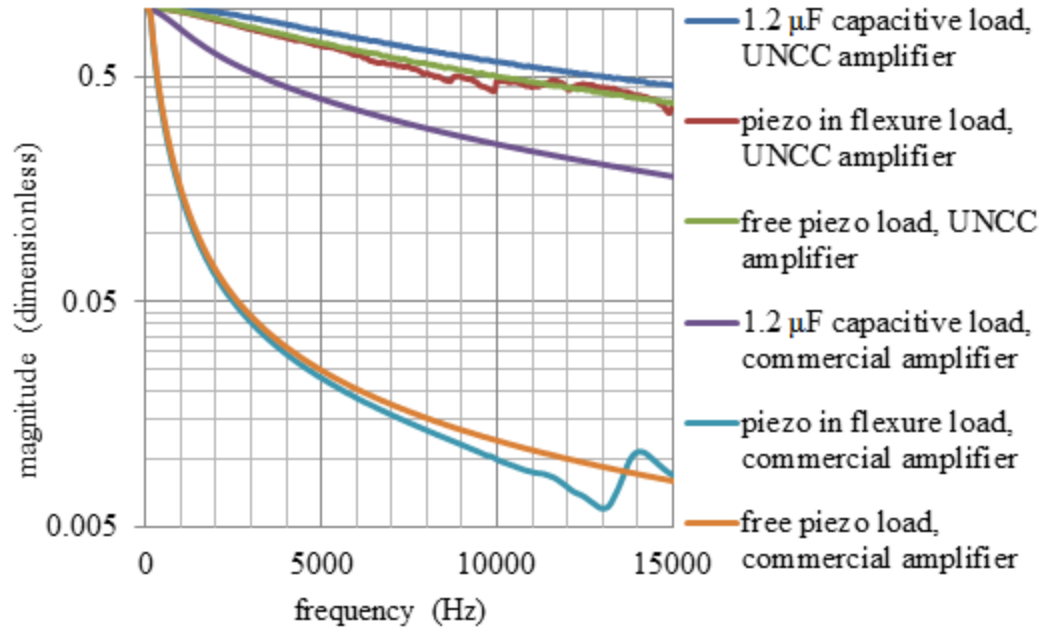


Figure 4-3: Comparison of frequency response of UNCC amplifier and commercial amplifier (Thorlabs, model #MDT691). Frequency response was measured using large signal ($90\text{ V}_{\text{pk-pk}}$) signal amplitude [5].

4.2.4 In situ Tool Measurement System

To measure the frequency response and real-time dynamics of the high-frequency probe, an in situ measurement system was developed. The measurement system, see Figure 4-4, uses the tip of the moving central mass on the flexure to block a focused laser beam and thereby measure the oscillations. The laser module (Thorlabs, model #CPS198) and photodiode (Thorlabs, model #FDG03) are not shown in the photograph in Figure 4-4(a) but are located inside as is shown schematically in Figure 4-4(b). The module and photodiode are mounted in tubes drilled through the measurement system's body which are parallel to the flexure actuator's motion. The laser beam is reflected off a 45° mirror, focused onto the tip of the flexure, and reflected back into the second tube to be measured by the photodetector. The photodetector circuit is given in Appendix F. As the flexure is

oscillated, the laser beam path to the photodetector is selectively blocked, generating a change in voltage in the photodetector circuit. Effectively, the vee structure of the moving platform acts like a knife edge that cuts across the focal spot of the laser. Hence as the platform oscillates it periodically blocks or lets through the light with the resultant intensity arriving at the detector being nearly proportional to the displacement of the platform. In this fashion the oscillations can be tracked using the modular measurement system. Additionally, using a set of machined spacers, the laser spot location can be adjusted vertically so that it is incident directly on the edge of the probe to measure the probe oscillations. By measuring the probe oscillation using a laser beam, changes in magnitude and phase can be demodulated by comparing the photodiode voltage and driving voltage. By using this method to monitor probe dynamics, the natural frequency of the probes can be characterized in situ and contact between the probe and workpiece can also be measured, as will be discussed in section 4.5.2.

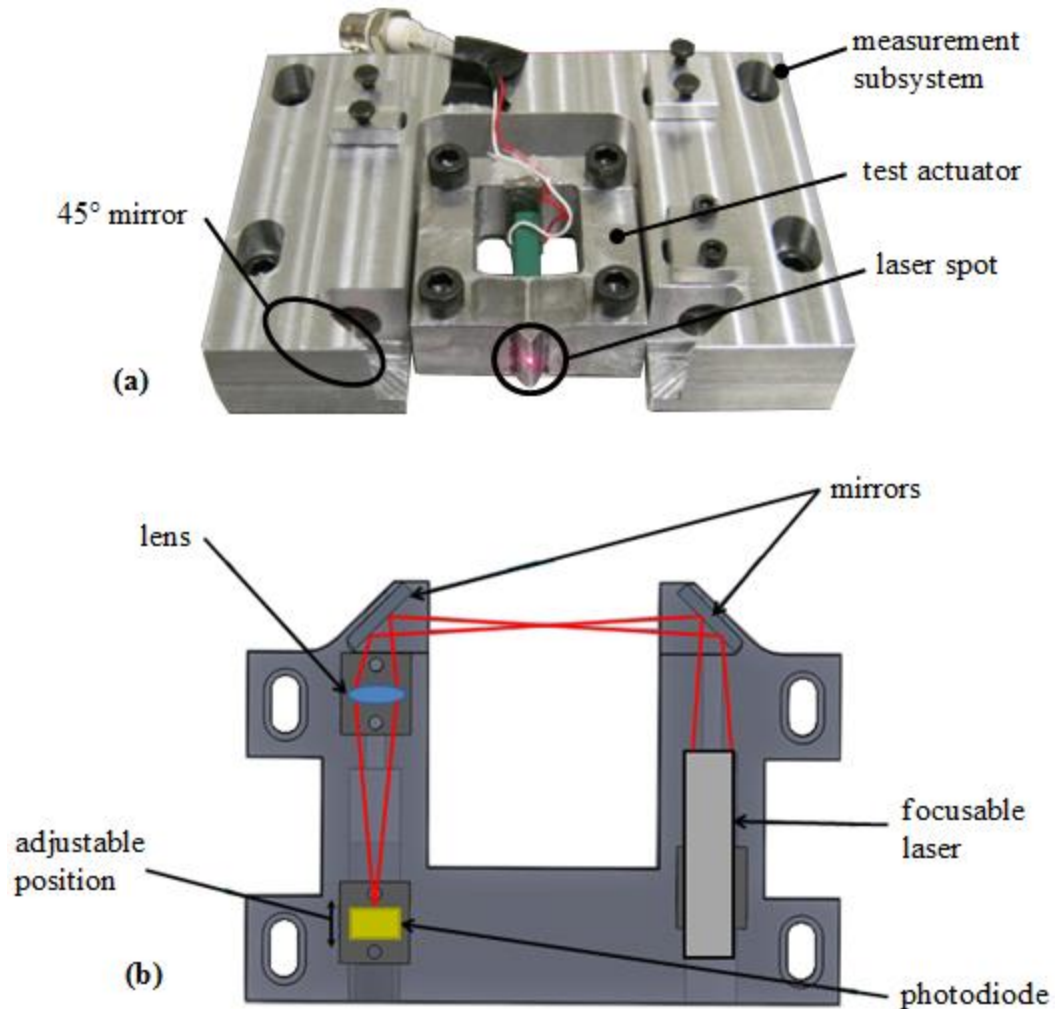


Figure 4-4: Shown above is (a) image of a test actuator being measured using the in situ tool measurement system and (b) schematic diagram of the in situ measurement system. A laser spot is reflected off the tip of the flexure actuator's moving central mass and intensity of the laser is monitored using a photodetector in order to track movement of the flexure actuator.

4.3 Machine Frame

The machine frame for the high-power facility consists of a sturdy set of modular pieces, each machined out of 6061 aluminum stock, see Figure 4-1(b). The frame is bolted together, and then fastened to an optical breadboard table using $\frac{1}{4}$ -20 fasteners. On the underside of the frame, integrated toe clamps are used to securely fasten the tooling to

the structure. The tooling can be adjusted and a second machining probe can be added. This capability for a second machining probe is not necessary for Vortex Machining, but was added for use in Particle Manipulation studies for investigating fluid streaming using multiple oscillating probes. While bulky, the frame was designed to resist high frequency disturbances and with sufficient mass to attenuate excitations forces from the tooling, and to provide a stable global reference point for the metrology sensors. Attached to the frame is an LVDT (Fowler, model #M922608A503-01) used for measuring the vertical position of the workpiece relative to the machining probe. Local capacitive gaging on the z -axis of the specimen support platform is used for measuring angular tilt.

4.4 Translation Stages

As mentioned in the overview of the high-power facility, section 4.1, the workpiece is attached to the z -axis stage and is translated via a manual xy -axis positioner and a custom z -axis positioner. The manual xy -axis is used for rough positioning with no feedback. Also, it is employed for part of the probe-to-workpiece referencing procedure as will be discussed in section 4.5.2. Due to the larger scaling of this process, it was determined that precision lateral control was not necessary to the experimental facility. In contrast, a precise and controllable vertical axis was required for both stability during the test and also for repeatable collocation of the probe and workpiece.

The z -axis stage, see Figure 4-1, is composed of a coarse and fine axis. The coarse axis is a commercial scissor-type positioner (Newport lab jack, model #270) that was chosen for its high-load capability. It can be manually adjusted over a range of more than 50 mm, with positional resolution in the tens of micrometers using external feedback. Mounted above the coarse positioner is a fine positioning stage consisting of two custom, two-bar level type flexures driven by piezoelectric actuators (Tokin, model

#AE0505D16F), see Figure 4-5(a). The lever type flexures shown in Figure 4-5 are located at either side of the fine stage. Two serially connected piezoelectric actuators (approximately 30 μm total range) are horizontally mounted into lever flexures that amplify this motion to a maximum of 140 μm of displacement. The combination of these two actuators mounted on either side of the platform enables both tilt and vertical motion capability. For the purpose of these experiments, the tilt capability was not used. In addition, two custom capacitance gages that were designed and constructed by UNCC student Feilong Lin are integrated into the stage for local tilt measurement [67]. The capacitance gages consist of a cylindrical probe and shield and a flat target that are both manufactured from oxygen-free copper stock, see Figure 4-5(b). For relevant theory in designing custom cap gages, see [68]. The capacitance gage instrumentation circuit consists of a precision 1 kHz sinusoidal oscillator source, which is buffered with a balanced line driver (Texas Instruments DRV134) for sending two 180° signals to either sides of a balanced bridge. On one side of the bridge is the capacitance probe and target (gage) and the other side is a precision trim capacitor that is adjusted in order to null the bridge. Using an instrumentation amplifier (Analog Devices AD711), the bridge output is amplified and sent to a separate demodulation circuit. The diagram for this capacitance gage driver is given in Appendix F. In practice, the magnitude of the demodulated signal is approximately linear with the distance between the capacitance probe and target. Using these capacitance gages the heights of each side and, therefore, tilt of the z -axis stage can be locally measured.

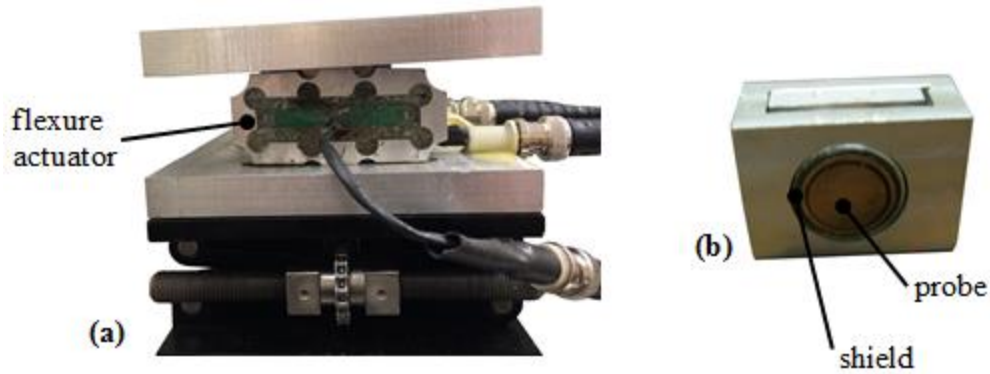


Figure 4-5: Images of side of z -axis stage for high-power experimental facility (a) and UNCC capacitive gage manufactured by Feilong Lin (b). Two-bar, amplifying flexure actuator (a) and capacitive gage components (b) are displayed.

To control the height and tilt of the z -axis, a dual loop, modified proportional plus integral controller was implemented using a LabVIEW real-time desktop system and 16 bit NI-series DAQ. The control error between the desired position and global LVDT measurement is used to drive the right side of the stage, see Figure 4-1, to the correct height. Simultaneously, the positional error between the two local capacitance gages is used to drive the left side of the stage. In this way, the right side of the stage is servo controlled to the correct vertical height, with the left side of the stage ‘chasing’ to minimize the tilt error. The reason that two-actuators were used instead of one where a simpler controller could have been employed is that the dual actuator system allows greater control and future angular tilts of up to 10 mrad to be deterministically employed. In addition, with this feedback the coarse-fine combination stage is effectively stiffened, making the system robust against the larger incidental forces imposed by the larger scale probing of the high-power facility. Translation and angular control errors for the z -axis are better than approximately 80 nm and 1 μ rad, see Figure 4-6.

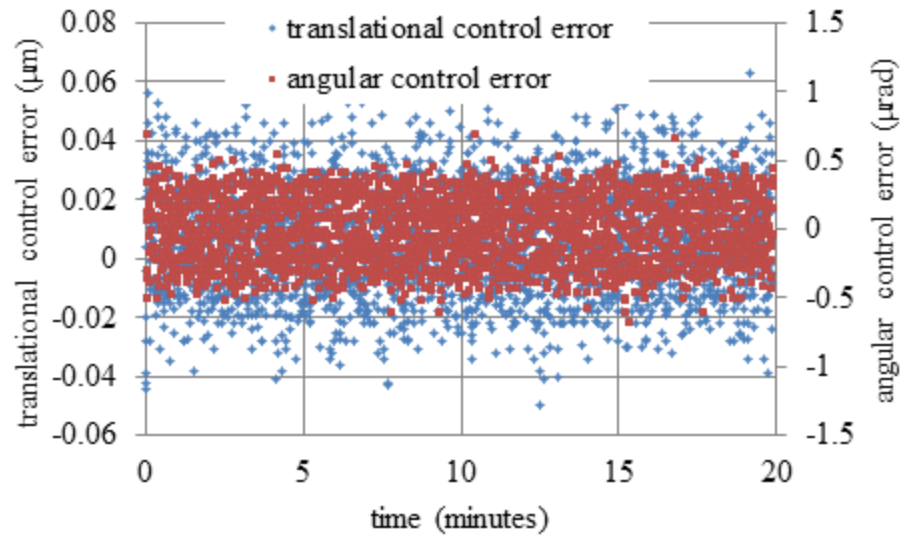


Figure 4-6: Plot of translation and angular tilt control error of the z -axis workpiece stage for the high-power experimental facility.

4.5 Testing Procedure

As with section 3.6, the testing procedure for the high-power experimental facility is provided to explain how to use the facility and provide a guide for researchers who are continuing investigations into this process. Comparatively, the testing procedure for the high-power facility is simpler than its low-power counterpart. Single footprints are machined at a time, and the larger-scale tooling and in situ measurement system has made for easier probe-to-workpiece referencing. In addition, the significantly higher removal rates make footprints visible with the naked eye making them easier to find and measure using metrology equipment.

Setup parameters specific to this facility will be covered before outlining the test procedure. While the system is capable of utilizing machining probes from 100 to 500 μm in diameter, only 500 μm Molybdenum probes have been utilized in studies to date. The probes have been manufactured to a variety of lengths and integrated into the actuators.

As such, probes with 1st to 3rd mode frequencies from 100 Hz to 3 kHz have been used. The probes are oriented vertically, with the workpiece fastened to an angle plate at 45°. The probe is oscillated along the direction of the workpiece plane (i.e. not towards the workpiece surface). Only undoped, silicon <100> workpieces have been used to date. Unless otherwise mentioned, the polishing medium used for studies has been a mixture of 50% water and 50 nm colloidal Alumina slurry (Allied High Tech Products, model #180-30000).

4.5.1 Pre-experimental Preparation

As with the low-power facility, the workpiece is attached to the workpiece holder using a 5 minute epoxy prior to testing and allowed to cure for a minimum of 24 hours. The flexure actuator and probe assembly that will be used for the test is then mounted (using ¼-20 bolts) into the high-power system. The next step is to align the in situ measurements system to measure the probe oscillations. In general, this is best accomplished by first oscillating the probe at a low frequency while observing the photodiode voltage using an oscilloscope. By carefully adjusting the flexure actuator position, this signal can be maximized and then actuator bolts can be fully tightened locking it in place. Next, the probe resonance is located using a lock-in amplifier that references the driving signal and probe measurement signal. The probe resonant frequency is determined by its value when the magnitude on the lock-in is at a maximum.

4.5.2 Probe-to-Workpiece Referencing

After moving the workpiece near to the probe and locating the desired machining location, the workpiece holder is filled with polishing slurry. The resonant frequency of the probe in air that was found prior to this step is then readjusted until resonance in the

polishing slurry is reached. The resonant frequency in slurry is typically a few Hz below the original frequency.

In order to reference the probe-to-workpiece contact position, the lateral manual stage is first translated slowly, moving the workpiece towards the probe. When a large change in phase on the lock-in amplifier is noticed, contact is assumed and the stage direction is reversed to retract from contact. Next, the fine z -axis is used to slowly move the workpiece vertically towards the probe. By monitoring the lock-in phase, probe-to-workpiece contact can be detected to within a couple micrometers in repeatability. After this contact position is recorded, the probe is retracted to a set stand-off distance (often 20 μm) and machining commences.

4.5.3 Ending the Experiment

After machining for a set time (usually 30 minutes), the workpiece is lowered away from the probe. The workpiece holder is removed from the z -axis, slurry is disposed of, and the sample and workpiece are cleaned.

4.5.4 Post-Experimental Analysis

After the experiment, the z -axis vertical and angular control errors, probe magnitude, and probe phase are analyzed to investigate the test stability. Unlike the low-power system, the high-power facility is comparatively robust to environmental instabilities and thus is stable throughout most tests. The workpiece is removed from the holder and is measured using the SWLI. Due to the scale of the high-power footprints (typically several hundred micrometers in lateral dimensions) the SWLI has sufficient lateral resolution to get a sense of the roughness capability of the process.

CHAPTER 5: DATA ANALYSIS PACKAGE

In section 2.4, a literature review on filtering, parametric characterization, and volumetric integration was presented. This background was critical to understanding the methods of analysis used to characterize surfaces. In the summary of section 2.4.3, a discussion ensued on which specific algorithms for the extraction of surface topography information were applied to Vortex Machining. After the optimal algorithms were chosen, a Matlab data analysis package was designed, constructed, and implemented for use in analysis of Vortex Machining footprints, listed in Appendix H. In this chapter, specifics on features of this analysis package and how each feature was implemented will be presented. Many surface characterization parameters are provided without reference to the specific methods that were used to calculate them. Since these methods govern the results of the surface characterization, knowing the specifics of the algorithms and their implementation is of vital importance. By providing the reader with a background on this information, much greater insight will be provided into characterization parameters used to evaluate the Vortex Machining process.

5.1 Features

In order to convey the features of the data analysis package, an operational flowchart of the program is shown in Figure 5-1. The program can be divided into approximately seven subroutines, each shown as the diamond-shaped decision blocks in the figure. These main functions are listed as follows; plane fitting, lateral axis trim,

outlier removal, sectional data removal, profile plotting, profile filtering, and area filtering algorithm. As is shown in the flowchart, the program takes as input the area data that was measured using either the AFM or SWLI. The user can then select which algorithms to process the data. While not specifically shown in Figure 5-1, it is noted that most algorithms can usually be repeated if the initial result is not satisfactory. This allows the analysis parameters used to be refined without restarting the complete process. The left column in the flowchart is composed of all the steps used to refine the measurement data. The right column shows steps to isolate line profiles and perform filtering operations on line profiles and area data. With the main features summarized, the operational process of the data analysis package should be clear. The code for the program is provided in Appendix H. While this program was debugged and utilized for many analyses without apparent errors, it is not necessarily error free. Now that the operational flow of the complete program has been established, specifics of some of the algorithms will be detailed. Screenshots of the program are provided where relevant and this software has been used by other researchers having reasonable knowledge of Matlab code and surface topography measurement; however, this is not meant to be a user manual to the data analysis package.

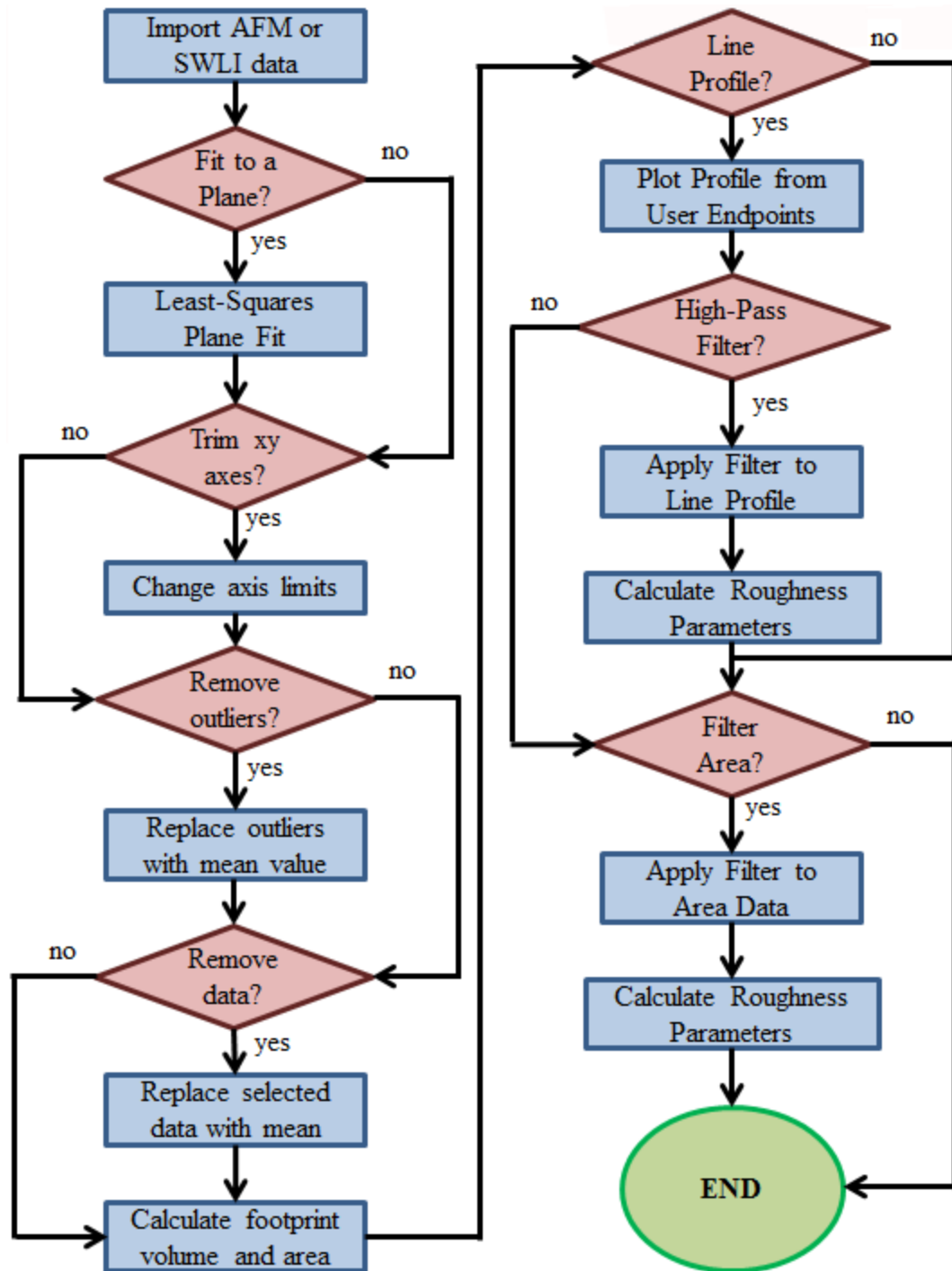


Figure 5-1: Flowchart diagram of data analysis package operation when analyzing Vortex Machining footprints.

5.1.1 Plane Fitting

In most surface measurement algorithms, a method is employed to fit the data to a nominal shape or geometry. The original measurement will usually be performed with the surface at some tilt or offset that should be removed for further analysis. While fitting to a nominal geometry aids with visualization of the data, it is not inherently necessary for many analyses, such as characterization of roughness, as the filtering operations will remove the long spatial-wavelength components. However, to calculate the footprint volume, of which was necessary these studies, a reference geometry is needed. Many data analysis packages allow fitting to spherical, cylindrical, and planar geometries. Since most Vortex Machining footprints were of small scale (less than 1 mm lateral scale) and produced on near atomically flat silicon substrates, a plane fitting routine was used.

A least square plane fitting routine was implemented to remove the angular and offset components from the surface. It was assumed that the surrounding, un-machined footprint represents a flat, nominal geometry. In its original form, all surface data points were used to perform the plane fit. However, it was quickly determined that irregular footprints would cause the fitting operation to leave angular deviations of the unmachined plane surface and also an offset in this un-machined portion of the surface. To remedy this, an interface in which the user could pick specific portions of the data to be used in the plane fit was added to the program. The user is prompted to decide how many rectangular areas to include in the fitting algorithm and then picks the diagonal corners of each of these areas using the cursor, see Figure 5-2. In this way, the user can define the un-machined surface data to use for the fitting routine thereby omitting irregular areas that would limit the algorithms effectiveness. An example of a surface polished use the

low-power Vortex Machining process before and after plane fitting is shown in Figure 5-3.

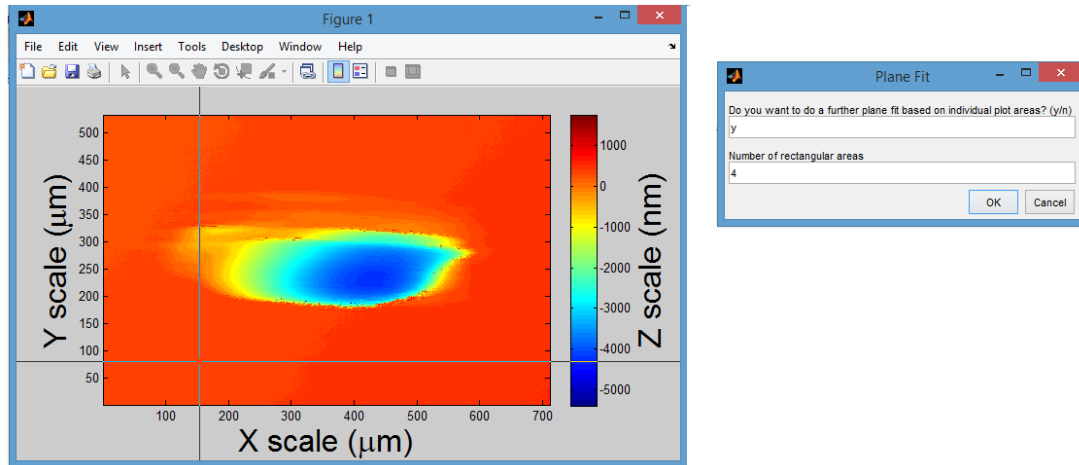


Figure 5-2: Screenshot showing user interface for plane fit algorithm. The user picks diagonal corners of rectangular areas using cursor marker.

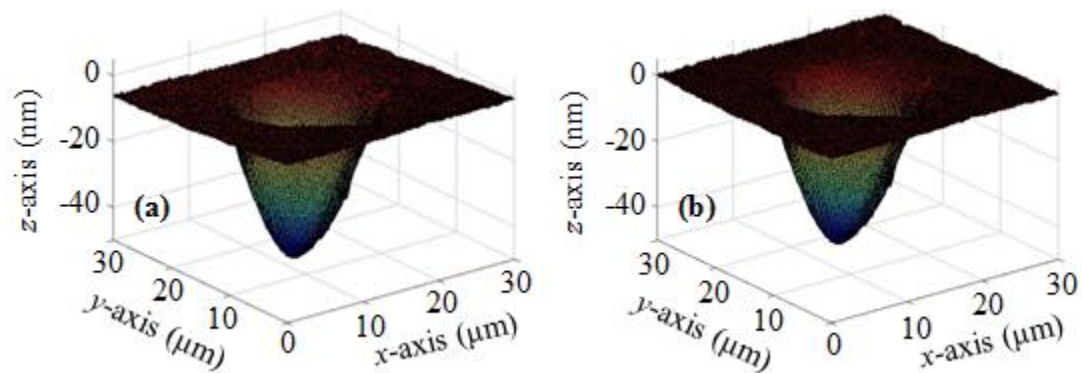


Figure 5-3: 3-D plot of low-power Vortex Machining footprint before (a) and after (b) plane fitting using outer, un-machined surface locations selected by the user.

5.1.2 Outlier Elimination

In common practice, surface measurements should always be critically examined. Artifacts attributable to instrumentation errors which are not representative of the surface being measured can show up in measurement data. As was mentioned in section 2.3.1,

care should be taken especially when using non-contact measurements as surface discontinuities and scattering of light can cause significant distortions to the raw data. In Vortex Machining, after polishing a footprint the surface was cleaned using tap water and unscented hand soap prior to measurement. However, some residual polishing particles are often left on the surface and cause large discontinuities (as large as 1 μm) during measurement with the SWLI. These large discontinuities caused problems in visualizing data since the scaling was often skewed and these large features also significantly impacted some of the parameter calculations. As a result, an algorithm was coded to enable the user to pick limits to which data outside of these values would be normalized to zero (average height of unmachined portions of measurement data), thereby limiting its impact on the analysis. This was accomplished by searching through the raw measurement data and replacing values outside of the user-selected limits. Outlier removals were performed seldomly and only when such features were clearly identified. In most instances, it was performed to enhance visualization of the data, in which an outlier would alter the optimal scaling ratio. A footprint with discontinuities in its edge in which an outlier removal operation is being performed is shown in Figure 5-4.

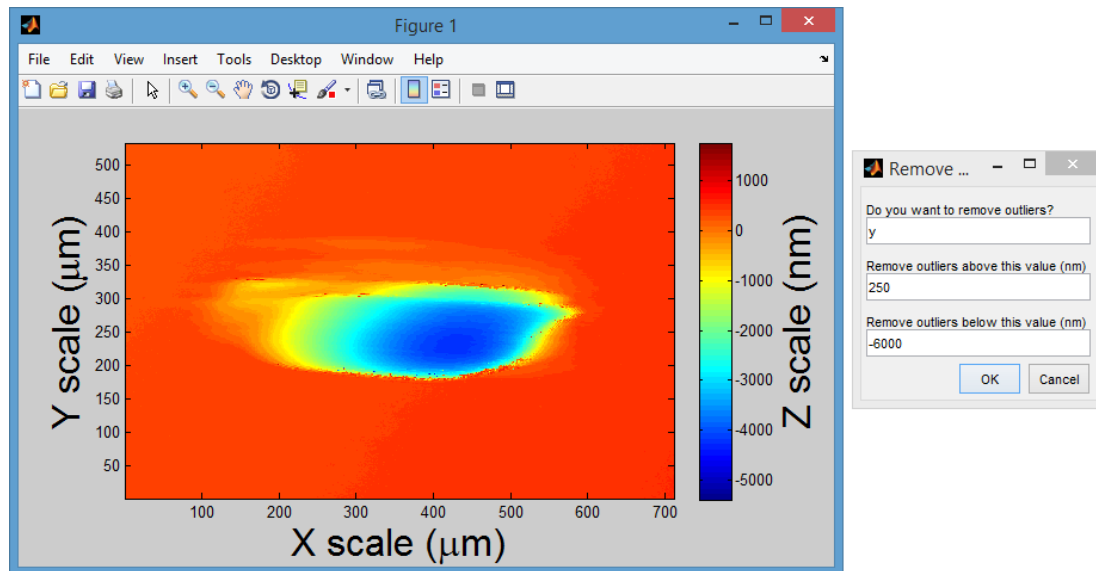


Figure 5-4: Screenshot of outlier removal interface. Footprint has peak discontinuities around its edges which should be removed for improved visualization and analysis. After picking the outlier removal range, the program will replace the outliers with a normalized surface height of the unmachined portion of the measurement data (i.e. zero).

5.1.3 Sectional Data Elimination

As with outlier elimination, the sectional data elimination algorithm was added to enable the user to remove obviously non-real artifacts that sometimes show up in raw measurement data. In some instances, raw data would show measurement artifacts in a corner or other small area. It was not always convenient to use the outlier removal algorithm to eliminate these sections. As a result, an algorithm was coded to allow the user to pick the rectangular sections of data to be removed. The user interface was identical to that used for the plane fitting routine as is shown in Figure 5-2. The program would replace each point in these rectangular areas with a value normalized to the unmachined surface height (i.e. zero). As with any outlier elimination, extreme care should be taken to eliminate personal bias when to avoid removal of relevant information. In practice, sectional data elimination was rarely, if ever, used for anything other than

removing ‘obviously erroneous’ portions of data to enhance visualization. In every instance of this, rigorous documentation was provided to appraise viewers of the footprint that this type of data manipulation had occurred.

5.1.4 Volumetric Removal Estimation

As discussed in sections 2.4.2 and 2.4.3, there are many algorithms that have been used to perform the sometimes complicated task of calculating footprint volumes. The most accurate methods are, not surprisingly, also computationally time intensive and sometimes difficult to setup experimentally. They also sometimes require the most operator judgement. For example, some of these algorithms require defining the footprint boundary using a series of slope and depth cut-offs that can change for different footprint geometries. Others require hardware for repeatably locating samples into measurement devices compare surfaces before and after they have been subjected to a process [56,57,58]. Since Vortex Machining is such a new process, it was determined that the ability to make reliable, but quick calculations using a standard approach of defining a reference plane would be adequate for the initial process verification and analysis. In this particular case, with a smooth and continuous profile deviating from a very flat reference it is not clear that these advanced routines will provide a significant improvement of the estimates. As a result, the linear approximation method was utilized for estimating footprint volumes.

The algorithm works by calculating any volumes from the nominal plane using trapezoidal rule integration. Due to this, the effectiveness of the plane fit is important to the accuracy of this method. Considering a two-dimensional matrix of depth values for the footprint (the measurement data), the algorithm will raster through and calculate an

average depth for each instance of four data values that are adjacent to each other. The lateral resolution of the measurement data is squared to calculate the lateral area of these adjacent data values. The area is then multiplied by the average depth to result in a rectangular volume estimate (i.e. a trapezoidal rule). This is repeated across all the data points to estimate a total footprint volume, see Figure 5-5 for a two dimensional representation of this algorithm. As mentioned previously, the accuracy of this calculation method depends significantly on the plane fitting since this reference plane sets the base, null or zero line for which all of the calculations are made. In practice, the user would be wise to trim the data window to the minimum size needed to capture the full footprint. While outliers or other artifacts will affect calculations, regular surface roughness or noise in the un-machined surface should in theory average and thus not affect the accuracy significantly. The algorithm, while simplistic, has proved to be a quick and repeatable method for calculating footprint volumes to date. Verifications of the algorithm will be given in section 5.2.1. However, it has been shown that when compared to other volume estimation methods such as a method utilizing averages of data points or Simpson's rule, the linear approximation method never deviates more than 2% [56]. This repeatability is significantly better than the current process repeatability of Vortex Machining (footprint volumes can deviate by 50% or more) making it adequate for studies presented in this thesis.

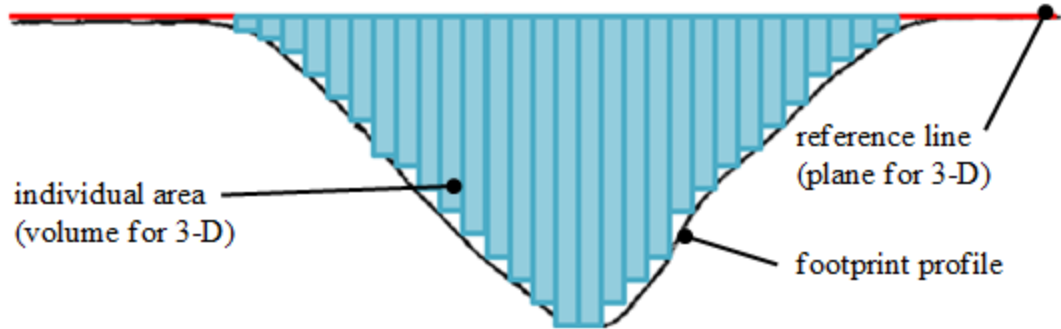


Figure 5-5: 2-D representation of volume estimation for footprint. Individual areas of fixed width (set by lateral resolution of measurement) and variable depth (average of two consecutive data points) are added to estimate total area of footprint (volume for 3-D measurement).

5.1.5 Filtering

In the initial iterations of the analysis package, many different types of filtering including recurse, non-recursive, digital RC, and double digital RC (with the second reversed for zero phase distortion) were investigated. After significant trials and a literature review into more modern filtering operations, the zero-order Gaussian regression filter was chosen for line and area filtering of Vortex Machining footprints as discussed in section 2.4.1.

After the initial phase of data manipulation culminating in estimation of the footprint volume, the user is given the option to look at and filter a line profile. By using the cursor interface as shown in Figure 5-2, the user can pick the end points of the line profile to be plotted. The user is then prompted to provide a cutoff frequency for the high-pass filter and the original footprint with line profile indicated, original profile, and roughness profile are plotted, see Figure 5-6.

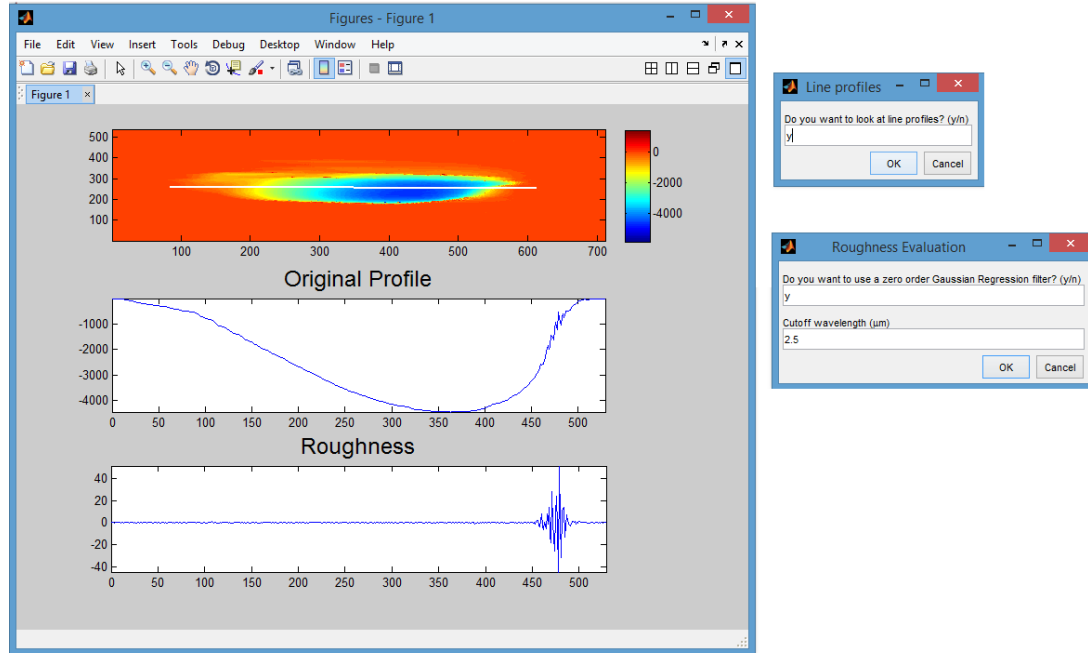


Figure 5-6: Screenshot of line profile plotting and profile roughness filtering on high-power Vortex Machining footprint using data analysis package. Location of line profile is indicated by white line across footprint contour plot.

Algorithmically, filtering is facilitated by first generating a Gaussian weighting function. This function is generated using the cut-off frequency supplied by the user and is convoluted with the line profile to produce the roughness data. For the zero-order Gaussian regression filter this weighting function is actually modified at the edges to limit edge effects due to the filtering process. For further information on specifics of implementation of this or other filters, consult [52].

In a similar fashion, the user can also choose to use the zero-order Gaussian regression filter on the area data. The filter is implemented by convoluting a two-dimensional weighting function with the measurement data to produce an area-based roughness plot that can be visualized using a contour plot in Matlab. While interesting, visualization and characterization of this type of roughness in general adds little to the

information content of individual line plots. Once again, [52] provides detailed discussions for understanding and implementing filters of this kind.

5.1.6 Parametric Characterization

With all other features of the data analysis package are implemented prior to this step, parametric characterization of the footprint represents an efficient approach for quantifying the performance of Vortex Machining and comparing it with related processes. In addition to calculating volume of the footprints, algorithms were implemented to identify the maximum footprint width and height (lateral lengths at perpendicular directions) as well as the width-to-height ratio. The algorithm for this is mathematically simple. A small offset value, for example 10 to 20 nm, was used to identify the footprint region in the measurement data. The maximum lateral lengths (x and y) were then used to calculate the width and height. It was speculated that some trends might emerge in these ratios for different frequencies and amplitudes being tested using the high-power machining center.

Mentioned in section 2.4.2.1, there are numerous parameters that have been established for characterization surface roughness. A small, but popular subset of these was coded into the data analysis package including; the arithmetic average (R_a), RMS roughness (R_q), maximum peak-to-valley (R_t), skewness (R_{sk}) and kurtosis (R_{ku}). As it turned out, R_q was used most significantly as the initial investigations into Vortex Machining have focused on increased repeatability of the process with some interest into simple parameterization of surface roughness. Also, it should be noted that the same parameters were coded for area roughness parameterization as well.

5.2 Program Verification

In practice, many measurement systems incorporate proprietary analysis software. This proprietary software is often powerful, but it was not used as the specific algorithms and implementation methods are unknown. By building a custom software package, the author is not only able to fully understand each analysis method, but also provide information to those who are interested with a more detailed understanding of the reported parameters. In addition, there is the opportunity to independently verify the accuracy and uncertainties of the data analysis package. In some instances these uncertainties could even be made traceable to a National Institute of Science and Technology (NIST) algorithm testing system. Verification of the volumetric, filtering, and parameterization algorithms will be discussed.

5.2.1 Volumetric Estimation Algorithm

In order to verify the volumetric estimation algorithm, a series of square and semi-spherical geometries were generated in Matlab, see Figure 5-7. These pseudo-footprints were then processed through the software, generating volume estimations. As was expected, the square geometries with infinitely steep sides resulted in estimations that converged exactly to the analytically calculated volumes. The largest deviations, on the order of 0.026%, occurred between the analytically calculated and estimated semi-spherical geometries' volumes. These deviations, while small, were investigated and determined to be caused by the linear approximation of the radial geometries. As a result of these studies, it was determined that the volumetric removal algorithm was of sufficient accuracy for analysis of Vortex Machining footprints.

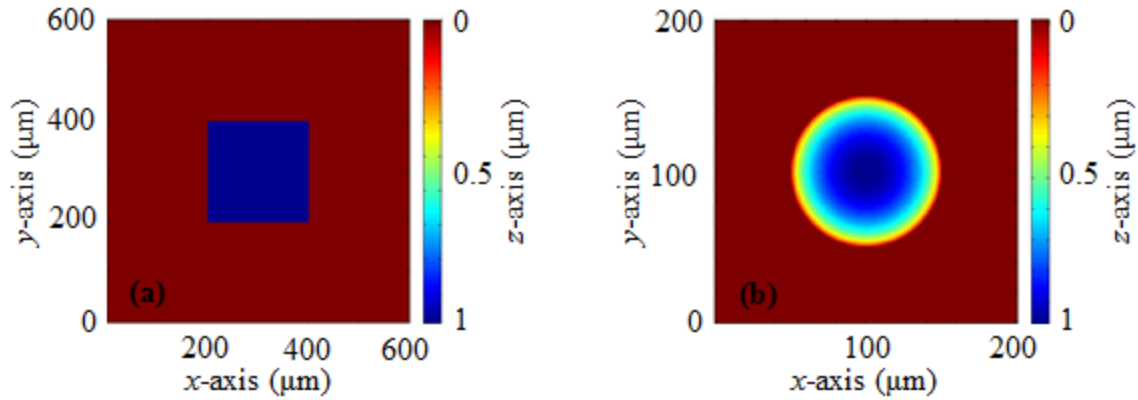


Figure 5-7: Contour plots of square (a) and semi-spherical (b) test geometries for verifying volumetric estimation algorithm.

5.2.2 Filtering

Due to the large number of measurement systems with proprietary analysis software, NIST has generated an internet-based surface metrology algorithm testing system (SMATS) [69]. SMATS can be used to verify a number of algorithms such as filtering, parameter calculation, least squares fitting, and more. Scientists interested in surface metrology would be advised to visit the website for verification of programs or for analysis using online tools.

Unfortunately, in addition to the zero-order Gaussian regression filter not being referenced in any standards, the SMATS also does not offer any verification techniques. However, it does have a Gaussian regression filter. This filter was programmed into Matlab using similar techniques to the zero-order filter, and the calculated R_q of a filtered profile were compared against the online system. The results showed convergence to the fourth decimal point. To sum this up, while the zero-order Gaussian regression filter could not be directly verified, a similar filter was verified showing strong evidence that the functionality of this algorithm is sufficient. Note that online the two-dimensional

filtering was verified using the SMATS as this was by far used the most in analysis of Vortex Machining.

5.2.3 Parameters

Line profile parameters including the arithmetic average (R_a), RMS (R_q), maximum profile height (R_t), skewness (R_{sk}) and kurtosis (R_{ku}) were also verified using SMATS. As a description for the reader, a randomized line profile was opened and analysed on the website and also downloaded to be investigated using the data analysis package. Once again, the results showed convergence to the fourth decimal point, verifying the algorithm for calculation of surface roughness parameters. As with the filtering verification, only two-dimensional profiles were verified using SMATS, although the system also offers the ability to check the algorithm for calculation area-based parameters as well.

CHAPTER 6: RESULTS AND DISCUSSION

Results of experimental studies using both the low-power and high-power experimental facilities are discussed in this chapter. Initial studies focused on stabilization of the low-power process. However, some initial investigations into the effect of machining time and footprint roughness are presented. Following these early results, a Master's student (Jeffrey Hunt) took over the experimental program using this facility and this work is expected to be completed in 2014. While the high-power facility has been in use for less time (less than 1.5 years), many preliminary results into process parameters such as probe-to-workpiece standoff distance, probe frequency, slurry concentration, and even effect of probe-to-workpiece abrasive mode machining have been achieved and some preliminary results from these studies are presented.

For the low-power facility, all footprints that will be presented have been machined using standard setup parameters except when noted specifically in the text. Probes were inclined at 45° with a <100> silicon workpiece. The slurry was a mixture of 50% 0.05 μm Alumina and 50% water. Most later tests utilized 30 minute testing periods.

Standard setup parameters were used with the high-power facility as well. Only 500 μm diameter probes were used to machine <100> silicon workpieces angled 45° relative to the probe. These 'standard' parameters were used mainly as they generated positive results early into research and were a benchmark for improving process repeatability and performance.

6.1 Low-Power Experimental Facility

In its initial conception, Vortex Machining was tested by placing a tool into a shallow stream of slurry and machining for periods of nearly 24 hours. No metrology system or feedback was present, and it was noticed that the tool position could change significantly between start and end of the experiment. Despite this, the apparatus was sufficient for verifying that the process was capable of producing material removal footprints with lateral dimensions in the tens to hundreds of micrometers and depths measured in tens of nanometers, see Figure 6-1. However, multiple footprints would often be produced in a single machining cycle and there was low repeatability between subsequent tests. This was attributed to a lack of control of both the polishing medium and position of the probe [1].

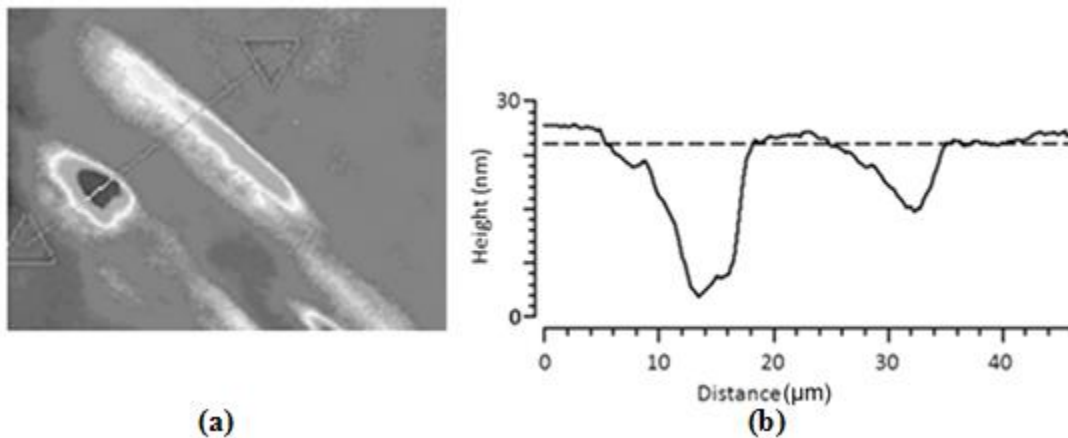


Figure 6-1: Contour (a) and line profile (b) plots of Vortex Machining footprint machined in initial verification tests. Modified from [1].

6.1.1 Footprint Volume and Machining Time

Utilizing the same tooling and methodology, a new experimental facility was developed to improve the repeatability of the process, see Chapter 3. In its first form, the facility

offered probe-to-workpiece position stabilities with less than 10 μm control error in each axis. Interestingly, although the translation control error was below 10 μm the footprint could be scattered by as much as 300 μm , see Figure 6-2(c and d). This test and others were at the time conducted over 3 hour time periods. In subsequent testing operations, it was discovered that by decreasing the machining time to 1 hour (or less), the footprints started to exhibit more uniformity and less scattering, see Figure 6-2(a and b). As shown in the figures, which are representative of many machining studies, the footprint scattering was reduced from over 300 μm to 50 μm or less by simply reducing the testing period from three hours to one hour. Currently, most testing using <100> silicon workpieces is conducted over 30 minute time periods. However, before making the shift to shorter machining periods, some trends were noticed. While the footprints were scattered significantly (and geometry was non-uniform), there were linear trends between volumetric removal and machining time, see Figure 6-3.

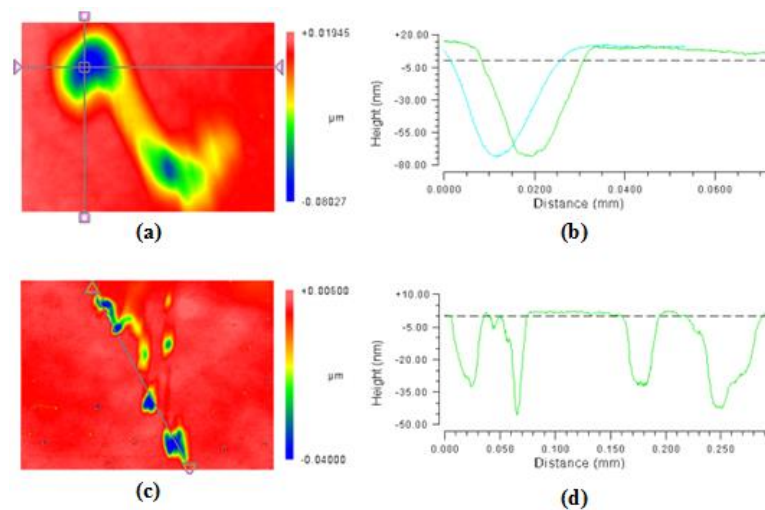


Figure 6-2: Contour and line profile plots of Vortex Machining footprints. (a) is 50 by 70 μm contour of single test conducted over 1 hour. (b) shows corresponding line profiles of top left footprint. (c) is 360 by 270 μm contour of single test conducted over 3 hours. (d) shows corresponding line profile. Modified from [5].

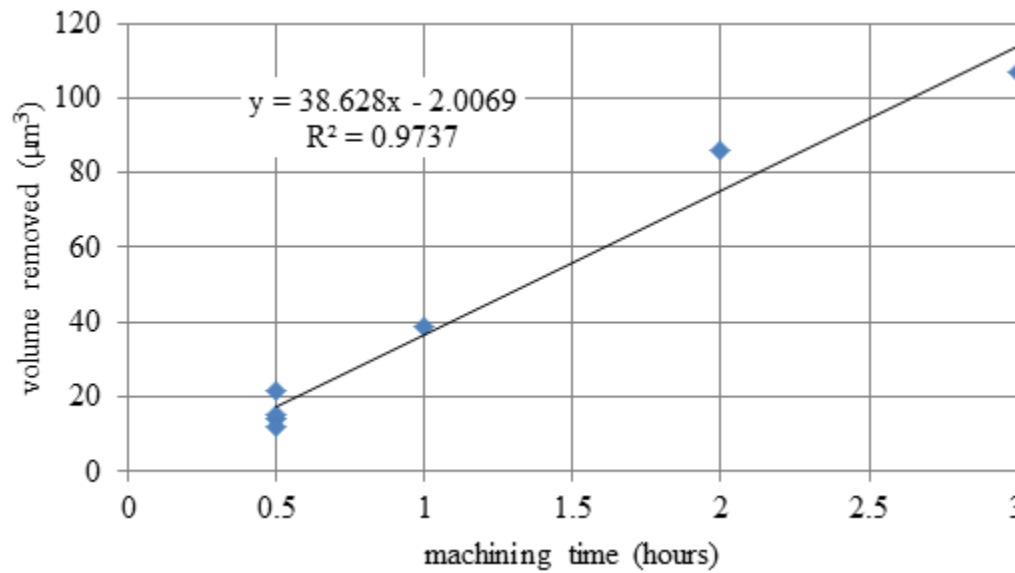


Figure 6-3: Plot of low-power Vortex Machining material removal against time. Four out of the seven data points are from tests at the 30 minute time period.

6.1.2 Footprint Volume and Probe Amplitude

Even with shortened machining times, increased uniformity in footprints was desired. Material removal rates could deviate by more than $7.5 \mu\text{m}^3 \cdot \text{hr}^{-1}$. Through high-magnification imaging of the machining location, it was noticed that the likely culprit for instabilities in the low-power facility was slurry evaporation. As the slurry depth decreased over time (approximately $200 \mu\text{m}$ per hour), the position of the meniscus on the probe would change significantly. This would cause the probe resonance to change in frequency (by several Hz) causing the probe amplitude to deviate by 50% or more. This likely caused significant variations in the resulting slurry flow energies. The meniscal force could also cause the probe move laterally as its position changed, and therefore position of the force along the axis of the probe fiber, with evaporation. Due to these instabilities, the low-power testing facility was substantially re-developed to provide

increased positional stability, real-time probe dynamic controls, and a compensation system for stabilizing the slurry depth during testing. The shorter testing period (30 minutes) also helped prevent long-term degradation of polishing fluids (mainly settling of particulates from the fluid). Subsequent tests showed that this second generation system was capable of polishing footprints with regular, near rotationally symmetric Gaussian geometries, even when using probes of different amplitudes, see Figure 6-4. While tests have indicated that higher amplitudes result in faster material removal (as shown in Figure 6-4), a full correlation of the effect of probe amplitude has not been undertaken to date.

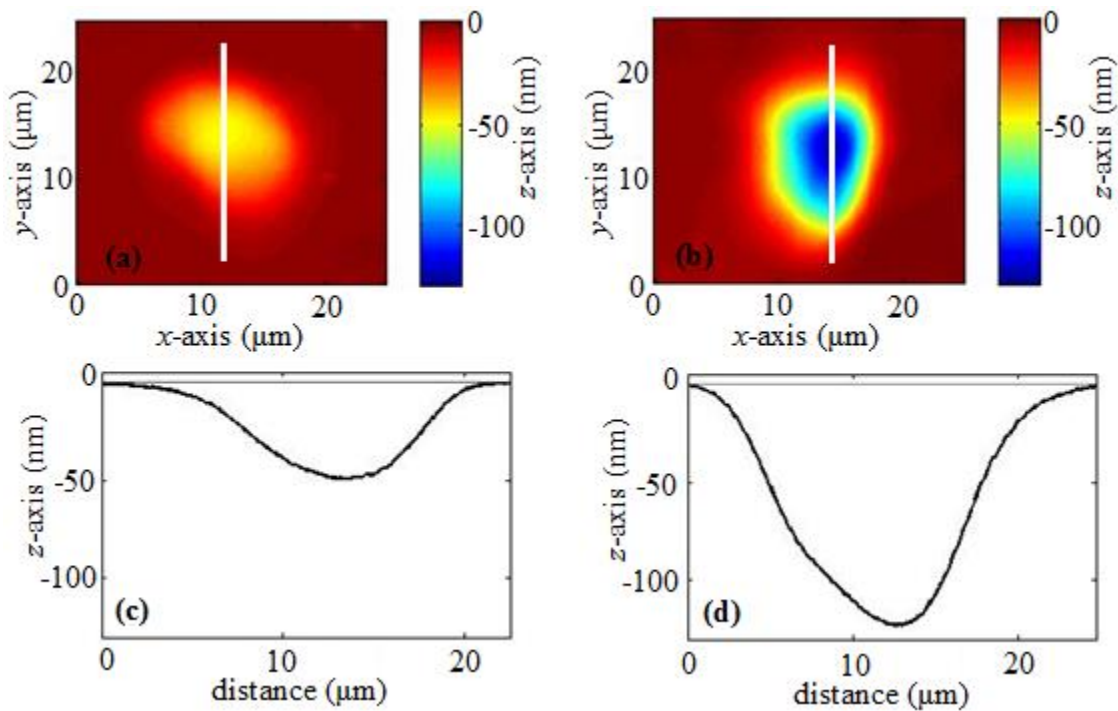


Figure 6-4: Contour and line profile of $5 \mu\text{m}^3$ footprint machined using probe with $25 \mu\text{m}$ amplitude ((a) and (c)) and $10 \mu\text{m}^3$ footprint machined using a different probe with $40 \mu\text{m}$ amplitude ((b) and (d)). Both probes were inclined at 45° relative to the workpiece in a slurry of 50% $0.05 \mu\text{m}$ Alumina and 50% water.

6.1.3 Evaluation of Footprint Roughness

In addition, preliminary studies into the effects of the process on roughness of the workpiece surface have been investigated. As shown in Figure 6-5, the roughness of low and high removal footprints are comparable, with an apparent measured increase for the higher removal volume footprint. However, at these levels it is difficult to ascribe the significance of this data given the different profiles that, while filtered, will also have contribute to the roughness values. Results also indicate that the outer, un-machined portions of the workpiece exhibit significantly less roughness. Taking into account similar studies of other footprints, no noticeable roughness difference for low and high removal footprints can be claimed, but roughness inside the footprints is consistently higher than outside. RMS footprint roughnesses of 0.5 nm and workpiece roughnesses of 0.25 nm are common, indicating the process produces produces surfaces with degraded roughness when polishing atomically flat surfaces.

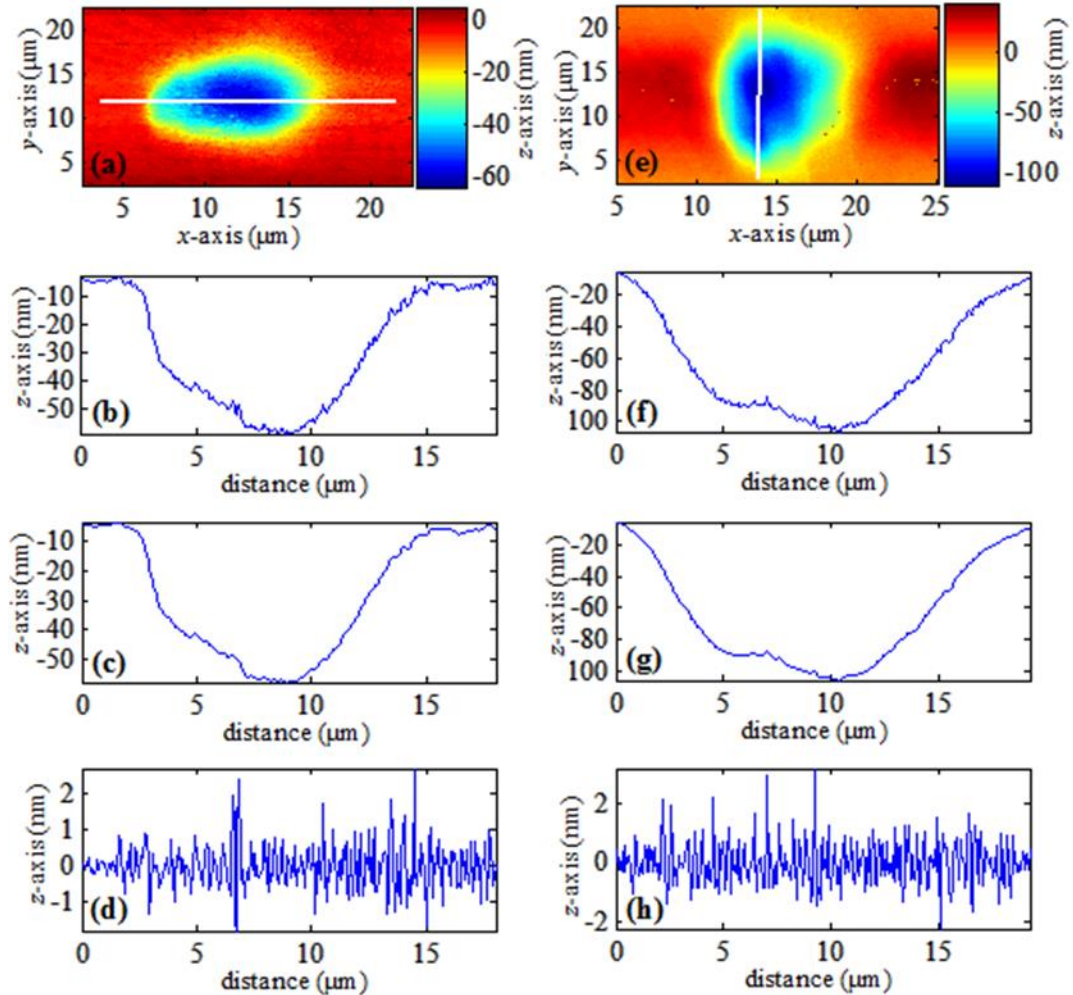


Figure 6-5: Roughness analysis of of low removal ($5 \mu\text{m}^3$; (a) through (d)) and high removal ($10 \mu\text{m}^3$; (e) through (h)) footprints machined in 50% 0.05 μm Alumina slurry. Footprints were measured with the AFM. (a) and (e) show contour, (b) and (f) show profile, (c) and (g) show form, and (d) and (h) show roughness. Line filtering was performed using zero order Gaussian regression filter with 0.5 μm cutoff. Low removal (d) and high removal (h) RMS roughness is 0.574 nm and 0.702 nm, respectively. RMS roughness outer, un-machined surface of low (a) and high (b) removal workpieces is 0.392 nm and 0.238 nm.

6.1.4 Process Automation

After integration of CNC-based automation, batches of 8 to 16 footprints at a time were being produced in square arrays, see Figure 6-6. This represents a major leap forward from the single footprint testing with scattered, unrepeatable results that were

common in the initial studies. The low-power facility has been developed to a point where it is now a platform for more quantifiable investigations into Vortex Machining. Studies of process variables such as probe amplitude, stand-off distance, dwell-time, workpiece material, and slurry composition are now more viable. However, it should be noted that instabilities still exist. While more repeatable in producing regular geometries, the volumetric removal to standard deviation is still around 4-to-1 for an average batch of results. This offers plenty of room for further improvement. Instabilities in probe manufacturing, probe sensitivity to environment, and slurry degradation (precipitation of slurry particles throughout testing) are seen as potential sources for further improvement and were also a part of the follow-up project to experimentally evaluate this machining process.

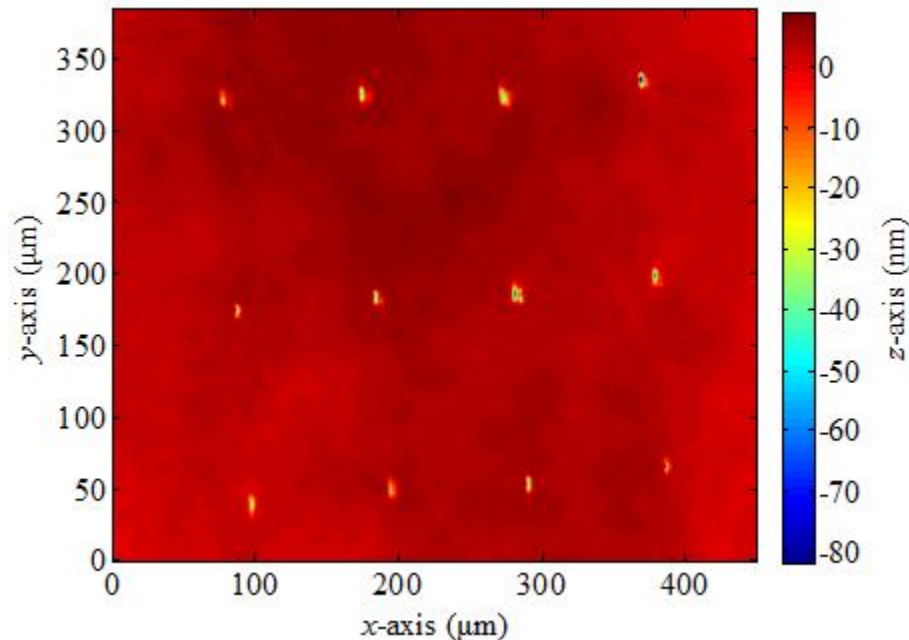


Figure 6-6: Array of footprints machined using low-power facility after integration of CNC-based automation software [3]. Footprints were machined using a 20 μm amplitude probe and had average removal rates of $7.5 \mu\text{m}^3 \cdot \text{hr}^{-1}$ with a standard deviation of $2 \mu\text{m}^3 \cdot \text{hr}^{-1}$.

6.2 High-Power Experimental Facility

In comparison with its lower power counterpart, the high-power experimental facility has had much less time in development and thus experimental results are preliminary. In addition, a similar facility has been produced and used for experimental investigations of streaming flows in fluids resulting from probe oscillations. Regardless of this, the facility's larger scale probes enabled investigations of more process parameters due to its robustness against instabilities such as slurry meniscal effects and environmental disturbances. As a note, all testing to date has used 500 μm diameter molybdenum probes. Depending on frequency and amplitude, the footprint removal volumes can vary drastically. However, they in general exhibit oval geometries with Gaussian-like edge transitions, see Figure 6-7.

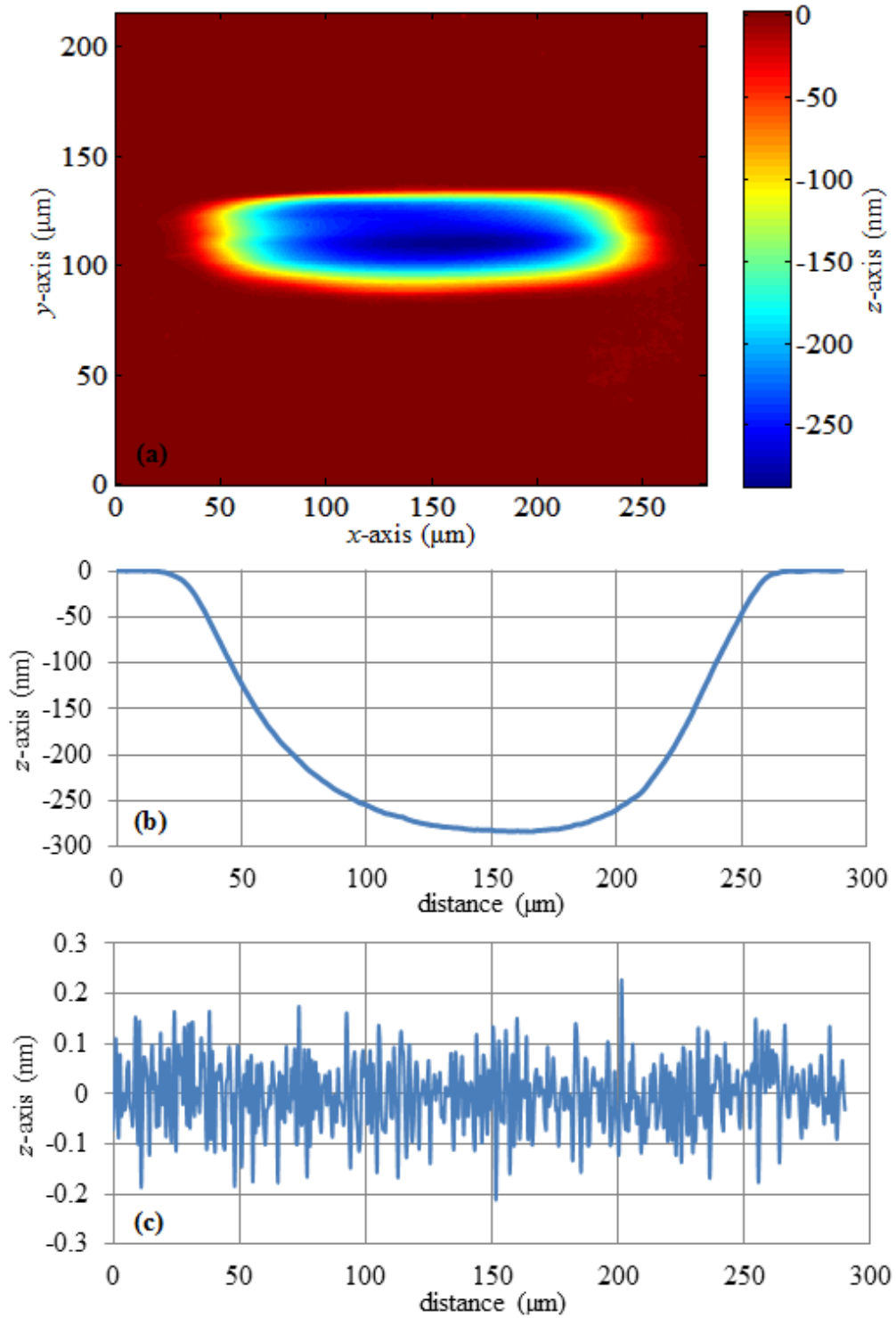


Figure 6-7: Footprint representative of high-power Vortex Machining process (machined using 500 μm diameter probe, 300 μm amplitude, 270 Hz). Contour (a), line profile (b), and filtered roughness (c) are shown. Roughness profile ($R_q = 0.069$ nm) filtered using zero order Gaussian regression filter with 2.5 μm cutoff. Volumetric removal rate is approximately $600 \mu\text{m}^3 \cdot \text{hr}^{-1}$ [33].

6.2.1 Material Removal Rate and Stand-off Distance

In an early test, a 270 Hz, 1st mode natural frequency probe with an amplitude of 600 μm was used to machine a sample when submersed in a non-drying slurry medium (Unicol 7530; colloidal Silica, pH 8.5 – 10.5, average particle size 65 – 80 nm). Stand-off distance showed no clear effect on material removal until reaching a critical distance, see Figure 6-8. Each footprint had similar geometry and surface roughness (<1 nm RMS). While not fully understood, it is theorized that this critical distance is actually the point where the probe begins to make physical contact with the workpiece. This is best explained by noting how the probe stand-off distance was referenced. In order to set the stand-off distance, the probe first has to be referenced in its vertical height to the workpiece surface. This contact position (see section 4.5.2) is established by moving the workpiece towards the probe until the probe phase exhibits a sharp change. Since this procedure was conducted with the probe immersed in the polishing medium, it was not initially clear if the probe had come into contact with the workpiece (or past the initial contact) at this point. This reference merely provided a standard that could be repeated with consecutive tests.

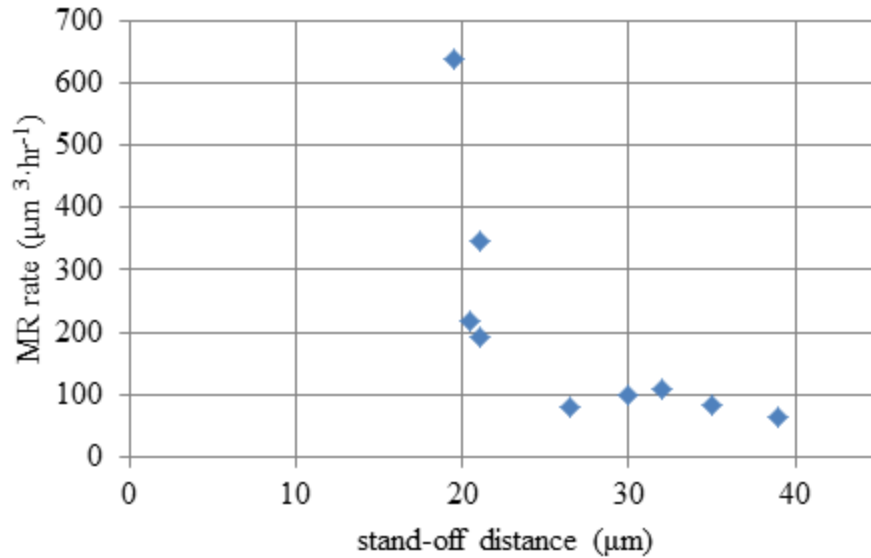


Figure 6-8: Material removal rate versus standoff distance for footprints machined using high-power facility. Tests were run with a 500 μm diameter probe at 270 Hz in a Unicol 7530 (colloidal Silica) slurry.

6.2.2 Material Removal Mechanism

There was a presumption in Vortex Machining that the process would remove material through accelerating a slurry across a workpiece, and not through direct contact of the tool as in traditional polishing methods. In order to clarify whether probe-to-workpiece contact was occurring or not (at specific stand-off distances), testing was conducted using three polishing mediums: pure distilled water, a pH 4 solution (mixture of citric acid and distilled water), and the standard 50% mixture of 0.05 μm Alumina slurry and 50% water. If removal occurred with the water solution, contact abrasion removal would be verified. Removal with the pH 4 solution would indicate a potential chemical component. Using a 2nd mode 2030 Hz probe, 30 minute machining tests were undertaken in each of these solutions. The results, see Figure 6-9, show that while each sample exhibited two scratches (from the probe-to-workpiece reference procedure), only

the test in 50% 0.05 μm Alumina slurry showed a footprint (center wear scar in Figure 6-9(a)). These tests were repeated two more times with similar results. These results verified that removal was occurring through through acceleration of polishing slurry across the surface and not through probe-to-workpiece abrasion. Testing using the high frequency, second mode probe resulted in significantly higher material removal rates (compared to lower frequency, first mode probes) with a high repeatability, see Figure 6-10 and Figure 6-11.

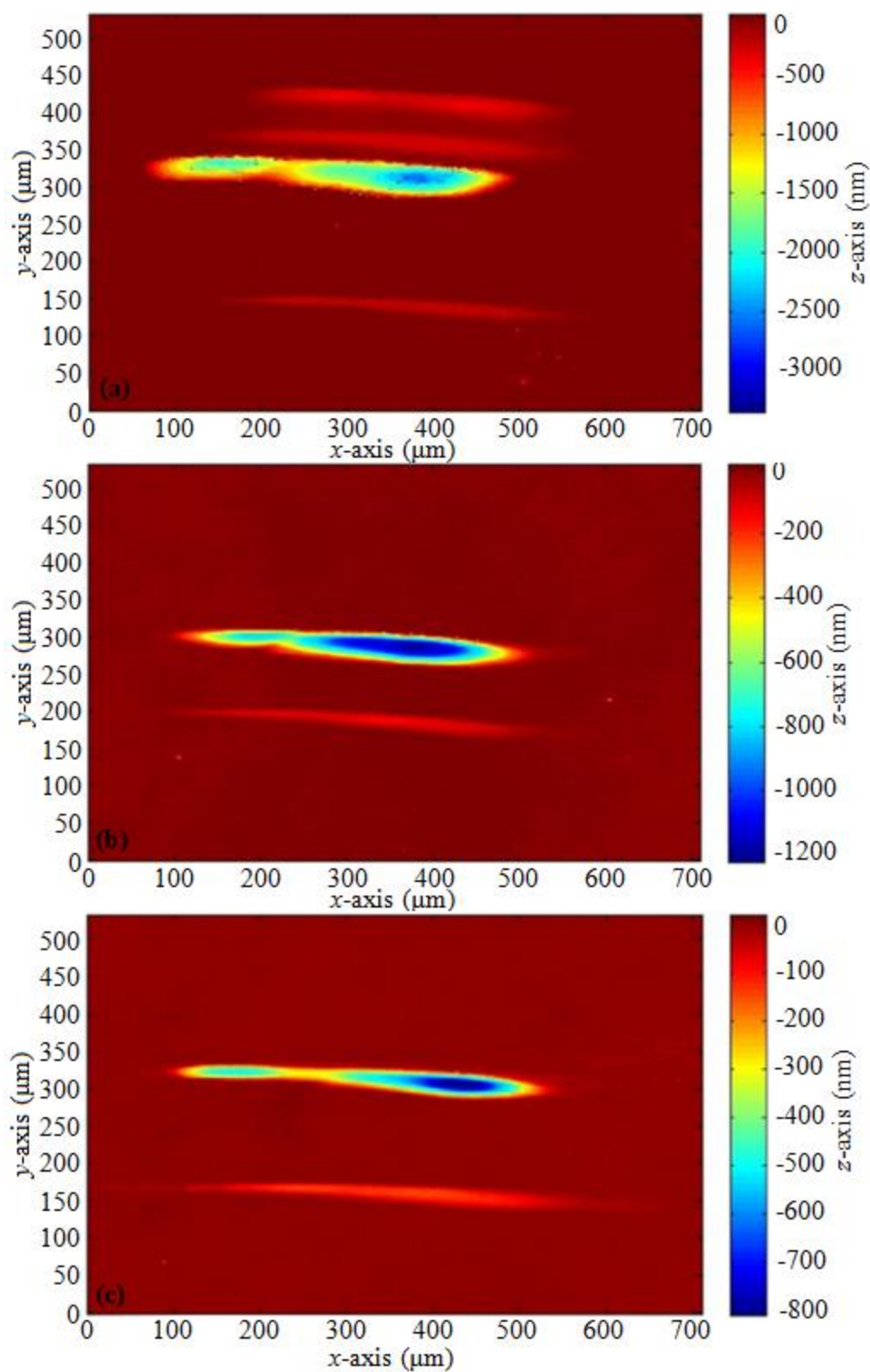


Figure 6-9: Footprints machined with 2nd mode, 2030 Hz probe over 30 minutes in (a) 50% 0.05 μm Alumina, (b) pH 4 solution (citric acid mixture), and (c) distilled water.

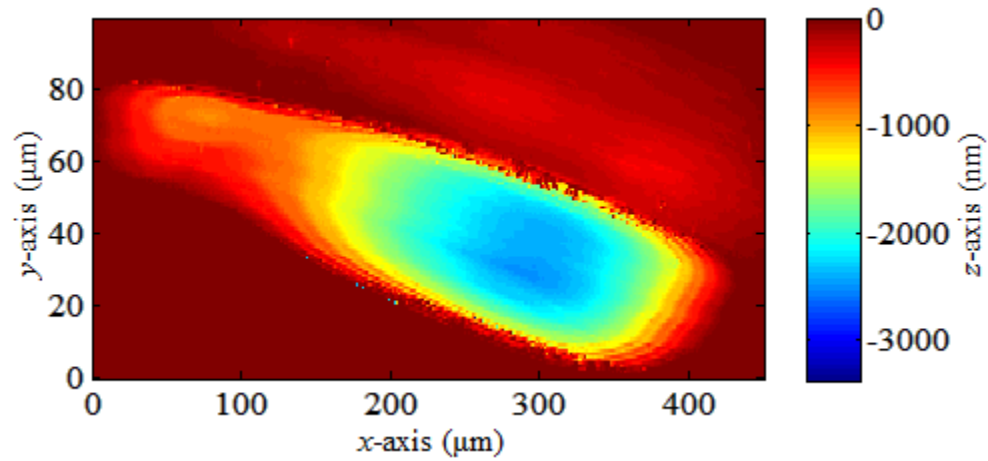


Figure 6-10: Footprint machined over 30 minute period in non-contact regime with 2nd mode, 2030 Hz probe in 50% mixture of 0.05 μm Alumina slurry. Material removal rate is $46608 \mu\text{m}^3 \cdot \text{hr}^{-1}$. Footprint had sub-nanometer roughness of similar scale to outer, un-machined workpiece.

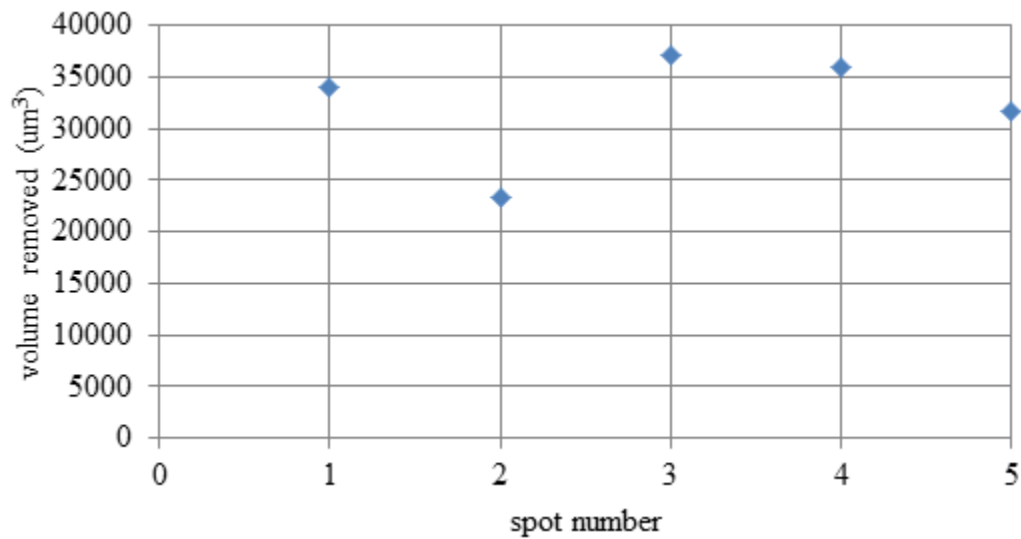


Figure 6-11: Graph of volume removed for 30 minute machining of footprints using 2nd mode, 2030 Hz probe in 50% mixture of 0.05 μm Alumina slurry. Spot 2 (representative of footprint geometries) is shown in Figure 6-7. Mean volume removed is $32407 \mu\text{m}^3$ and standard deviation is $5504 \mu\text{m}^3$.

6.2.3 Forced Contact Machining Mode

In a change with convention, it was also possible to purposely force a probe into contact with the workpiece with repeatable changes in probe dynamics by monitoring phase. This in theory results in reproducible contact forces between the probe and workpiece, allowing investigations into probe-to-workpiece abrasive removal. In practice, footprints machined in this manner were visually rougher (25 nm RMS), but test to test repeatability was high, see Figure 6-12 and Figure 6-13. With a comparison of a footprint machined in the non-contact regime using similar tooling (1st mode, 270 Hz, 300 μm amplitude, 0.5 mm diameter probe) shown in Figure 6-7, material removal rate is ten times the rate when machining in the abrasive regime.

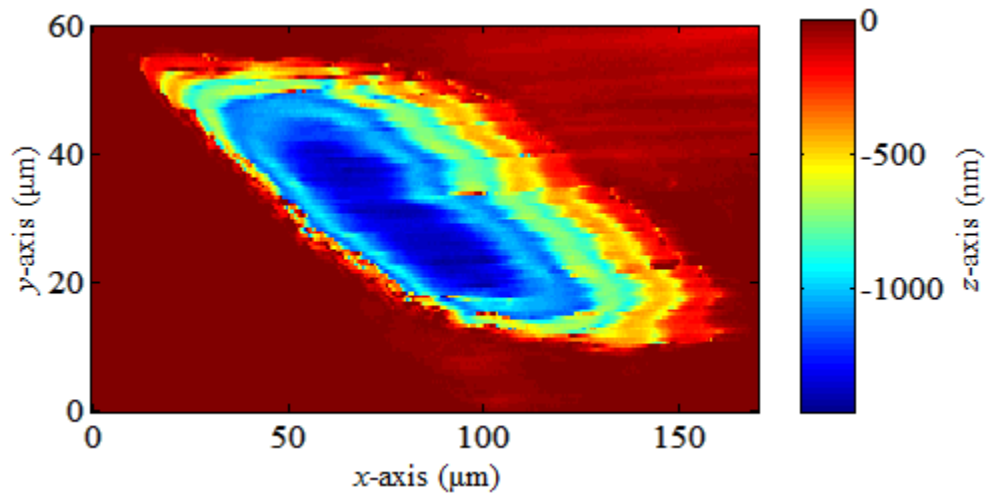


Figure 6-12: Footprint machined over 30 minutes using high-power facility. A 1st mode, 270 Hz probe was utilized making contact with the workpiece surface. Volumetric removal rate is approximately $6126 \mu\text{m}\cdot\text{hr}^{-1}$.

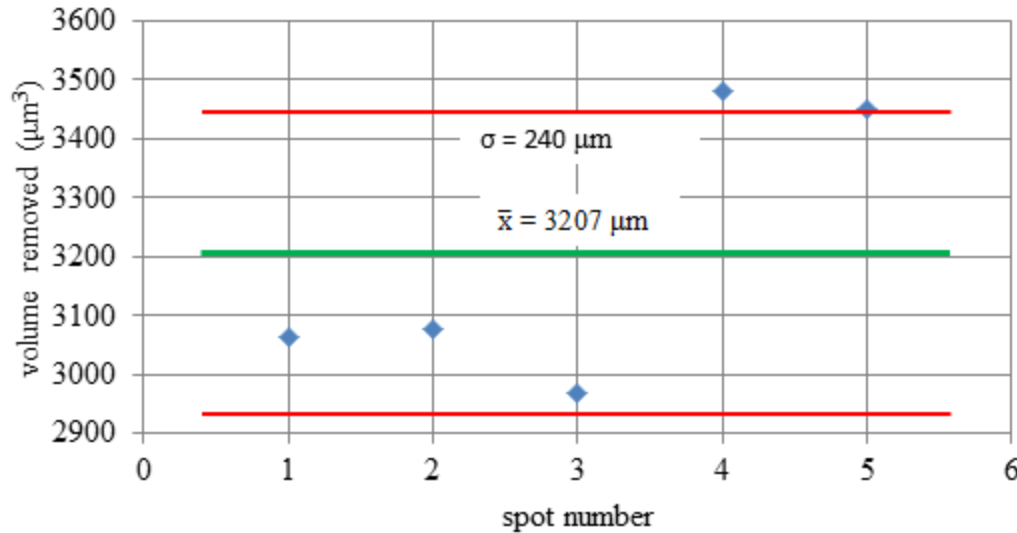


Figure 6-13: Comparison of five footprint removal volumes over 30 minute time periods (see Figure 6-11 for spot 2). The mean (\bar{x} , green line) and one standard deviation uncertainty (σ , orange lines) are $3207 \mu\text{m}$ and $3207 \pm 240 \mu\text{m}$, respectively.

6.2.4 Material Removal Rate and Slurry Concentration

While some tests proved highly variable, investigations were undertaken to investigate the effect of slurry concentration on removal rate. Using a 2nd mode, 2030 Hz probe, seven tests each at slurry concentrations from 2.5% to 50% were conducted. As shown in the plot in Figure 6-14, there is no clear trend in the data. However, it does seem that footprints with higher material removal were produced when using lower concentrations of slurry. The ratio of material removal rate to standard deviation of each test (a measure of variability), seems to suggest that repeatability is not clearly defined but was worst at 2.5% and best at 5% slurry mixtures. The theoretical relationship between energy density and process parameters (Equation 2-8) suggests that the energy density of the slurry will decrease in inverse proportion to the increase in slurry viscosity, whereby the higher concentration slurries have (visually) higher viscosity. This seems to agree in general with the initial experimental findings.

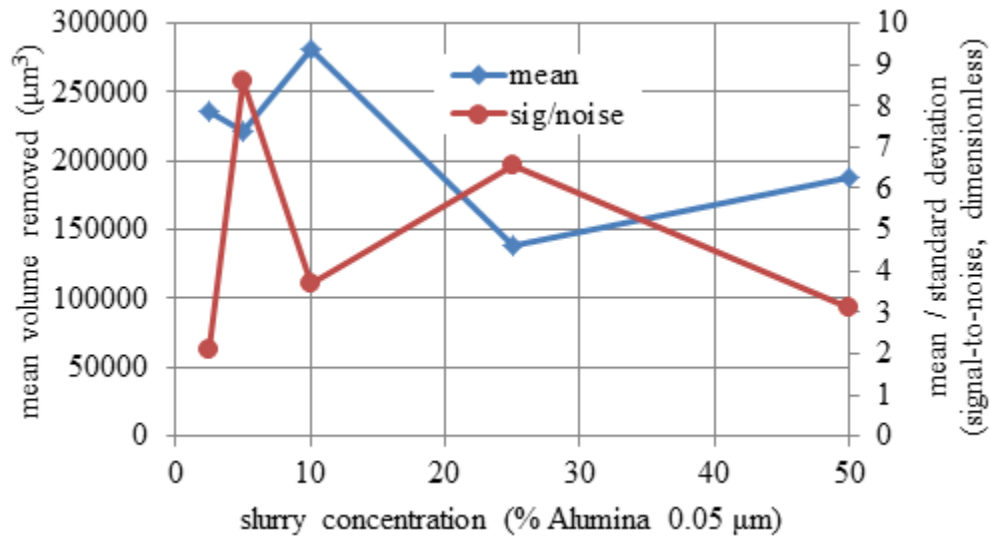


Figure 6-14: Plot of results from slurry concentration studies showing mean volume removed and mean-to-standard deviation ratio for concentrations of 0.05 μm Alumina slurry from 2.5% to 50%.

6.2.5 Evaluation of Process Roughness

The roughness of machined footprints was briefly investigated similar to investigations using the low-power system. As shown in Figure 6-7, footprints machined in the non-contact regime tend to show roughness values the same or slightly less than the outer, un-machined workpiece (approximately 0.1 nm). This trend remains true when using both high and low-frequency probes. In contrast, roughness of footprints machined in the contact regime tend to be rougher (see Figure 6-12), averaging RMS 25 nm or more depending on the lay of the line profile used. It should be noted that due to the larger scaling, a higher cutoff wavelength (2.5 μm) was employed for analyzing roughness of the high-power footprints than for the low-power (0.5 μm). Additionally, the SWLI measurements (0.5 μm lateral resolution) were used to measure the high-power footprints while AFM measurements (nanometer lateral resolution) were used for

roughness analysis of low-power footprints. Due to this, the results from each system are not directly comparable.

6.3 Conclusions of Preliminary Results

In conclusion, footprints machined using the high-power facility have material removal rates from 100 times – for low-frequency, non-contact machining – to 100,000 times – for high-frequency, non-contact machining – the rate of the low-power counterpart. Preliminary results show that increasing frequency substantially increases the material removal of the process. While not as conclusive, similar trends have been noticed when operating the probes at higher amplitudes. With all other process parameters kept constant, machining in an abrasive mode with the probe and workpiece in contact produces significantly higher removal rates. This comes at the price of significant surface roughening when compared to the virgin, un-processed outer workpiece surface. In contrast, machining in non-contact mode has resulted in reductions in roughness from the already smooth workpiece surface.

CHAPTER 7: CONCLUSIONS

In this chapter the major achievements and implications of research into Vortex Machining are reviewed. Throughout this dissertation, implementation of two experimental facilities, a custom data analysis package, and in-depth research studies have been presented. With this comes a host of new information about the process and its implications in the world of sub-aperture polishing. However, further work will be required to move the process from these initial studies to become a commercially viable process.

7.1 Experimental Implementation

In its inception, Vortex Machining was a process in which an oscillating probe was placed into a stream of slurry with no control or feedback into the process. When footprints were found, they often exhibited significantly variant geometries and removal volumes. This variability prevented in-depth analyses of the process and the effect or sensitivity of its parameters. A low-power facility employing a tuning fork based probe was first employed in an attempt to create a more repeatable process. After a series of developments, this facility now features x , y , and z -axis stages for relative positioning of the probe and workpiece with control error standard deviations less than $0.4\text{ }\mu\text{m}$ under long-term machining operations. Dynamic control of the probe response has been implemented through integration of FPGA-based lock-in and phase-locked loop, and the slurry depth variations have also been compensated from evaporative losses of over 200

$\mu\text{m}\cdot\text{hr}^{-1}$ to less than $10\text{ }\mu\text{m}$ deviation throughout machining tests. A summary of these control parameters is given in Table 7-1.

Table 7-1: Summary of process parameters for low-power experimental facility.

Process Parameter	Measure	Controller Error Deviation	Figures
Position	probe height x position y position	$< 0.1\mu\text{m}$ $< 0.1\mu\text{m}$ $< 0.4\mu\text{m}$	Figure 3-12
Probe	magnitude phase frequency	0.2 V 0.1° (air), 2.5° (slurry) 0.25 Hz	Figure 3-11
Slurry Height Control	$< 0.1\mu\text{m}$	Within $10\text{ }\mu\text{m}$ throughout machining	Figure 3-15

In order to investigate additional process parameters such as the affect of probe stand-off distance, frequency, and amplitude, a high-power facility featuring a broad-bandwidth (up to 10 kHz), large scale probe that was less sensitive to instabilities such as slurry meniscal effects and environmental variations was developed. This second facility featured a sturdy, robust frame; a manual xy -axis; and a z -axis with vertical and angular control errors stabilized to below one standard deviation uncertainty of 20 nm and 250 nrad . The high-power actuator has the ability to oscillate probes with diameters from $100\text{ }\mu\text{m}$ to $500\text{ }\mu\text{m}$ to frequencies of nearly 10 kHz with amplitudes of $500\text{ }\mu\text{m}$ or more at resonance. A summary of control parameters for the high-power facility are given in Table 7-2.

Table 7-2: Summary of process parameters for high-power experimental facility.

Process Parameter	Measure	Value	Figures
Position	vertical position (z) angular position (θ)	< 20 nm (control error) < 250 nrad (control error)	Figure 4-6
Probe	diameter frequency amplitude	100 μm – 500 μm DC – 10 kHz (bandwidth) 0 – 500 μm	Figure 4-3

Lastly, a custom data analysis package was designed and programmed specifically for analysis of Vortex Machining footprints. The program features plane fitting compensation with mechanisms for fitting around footprint geometries; outlier removal; axis trimming; volumetric estimation; as well as linear and area based filtering using zero order Gaussian regression filters. Each analysis feature was carefully researched and designed to best suit the specific needs for these investigations. The program's accuracy was also verified against NIST-based online data (SMATS).

7.2 Material Removal Mechanisms

The primary reason for developing more stable experimental facilities and analysis procedures was to enable repeatable investigations into Vortex Machining; and ultimately to investigate and develop an understanding of the material removal mechanisms of the process. The development of the facilities led to more reproducible testing and was a start towards deterministic analysis of process parameters. While much work remains to satisfy this latter goal, some general trends have been noted.

For the low-power system, preliminary results suggest some correlation between probe amplitude and removal rate. Tests have shown by nearly doubling the amplitude of

the probe in air, the footprint is machined at twice the removal rate, see Figure 6-4. However, these tests when repeated with different parameters or probes often produce variable results, so a more precise relationship cannot be determined with any reasonable certainty. Preliminary machining tests have also indicated that the material removal process is approximately linear with time. These results indicate that given constant process parameters, the process machining rate is consistent throughout time. Increasing the probe energy (amplitude) should correlate to higher energy flows and more slurry particles incident on the workpiece surface. This relationship between the number of particles being accelerated towards the workpiece surface and removal rate is reminiscent of other material removal processes such as EEM and FJP. This could indicate a combined chemical-mechanical removal model (EEM) or a purely abrasive model in which material is removed through shear-stress of workpiece atoms (FJP). Due to the low energy density of flow involved, low-power Vortex Machining likely is closer to the EEM removal mechanisms (chemical removal). Preliminary results consistently produce footprints with higher roughness value than that measured on the outer, un-machined workpiece (atomically smooth silicon wafer).

Using the high-power facility, investigations indicate increasing frequency of the probe can increase the material removal rate significantly (over 100 times for 270 Hz and 2030 Hz probe comparison). Studies of the effect of slurry concentration have yielded mixed results, but with some indication that lower concentrations may actually result in higher material removal rates. This creates conflicting theories. One theory is that increasing probe frequency (and thereby energy) results in higher fluidic energies and more particles incident on the workpiece causing higher material removal. The other

suggests high particle densities can actually be a detriment to the material removal rate. In EEM, a process in which material removal is generally attributed to chemical affects, the process increases removal rates with an increase in surface area of particles incident on the workpiece [19]. This is in contrast with initial findings on the relationship between slurry concentration and Vortex Machining. However, these seemingly contradictory findings are not dissimilar to findings in FJP (which has a mechanical erosion model) where concentration increases with removal rate linearly until a critical limit. Particle-to-particle interaction is then theorized to neutralize their independent kinetic energies [23]. This similarity with the FJP and its abrasive removal model is also present in other results. Footprints machined with the high-power facility showed removal rates varied little with stand-off distance (over 20 to 30 μm in range, see Figure 6-8) until a strong transition in which the removal rate went up over 500%. This transition may represent a change from machining purely with slurry flows (non-contact regime) to machining in which the probe and workpiece are touching (contact regime). It also may indicate a change from a chemical removal model to a mechanical removal model, which should be investigated further. With all other variables the same, machining in the contact regime has yielded nearly ten times the material removal with sufficiently high repeatability (similar to non-contact regime). However, the surface roughness is significantly degraded in comparison with the surrounding workpiece material (25 nm vs. 0.1 nm RMS). In contrast with the low-power process, non-contact machining using the high-power facility has yielded footprints with roughness consistently lower than the un-machined workpiece surface and comparable to that of other polishing processes.

7.3 Process Viability

Throughout the course of this research, the Vortex Machining process and results from investigations have been presented in numerous conference meetings [5,33,34,35] and a journal [3]. The primary response has been of interest into the process, although some concern of its limitations has also been expressed. Due its small scale probing, the principle use of the low-power process has been envisaged to include; finishing of edge effects on optics such as telescope mirrors, micro-lens arrays, diesel injector nozzles, and microfluidic devices, see Figure 7-1. The small diameter, high-aspect ratio probe has the potential to reach into difficult and complex geometries such as small holes and deep channels; or any other surface with steep geometries. This ability is not represented by the current set of sub-aperture processes that are available. CNC-based automation implemented in this research has shown viability for more complex finishing capabilities. In addition, the dual-use of the probe as a contact sensor could lead to in situ measurement and correction. Figure 7-1(c) shows an InsituTec MicroTouch probe being used to measure the diameter of a diesel injector nozzle. However, instabilities due to environmental disturbances and slurry effects currently limit the reproducibility of the process. Another concern has been the slow material removal rate.

Many of these concerns can potentially be alleviated using the high-power system. Utilizing the same methodology, a fully dynamic, controllable process can be used to create features of small scale with variable removal rates. The process is less susceptible to environmental instabilities, and can potentially remove bulk amounts of material allowing it to be used in more than just finishing operations. Other implementations could include arrays of probing for a sort of ‘carpet sweeper’ removal tool in large scale finishing of surfaces. The possibilities and implementations are wide-

ranging, indicating that the methodologies in Vortex Machining may prove useful in real-world applications.

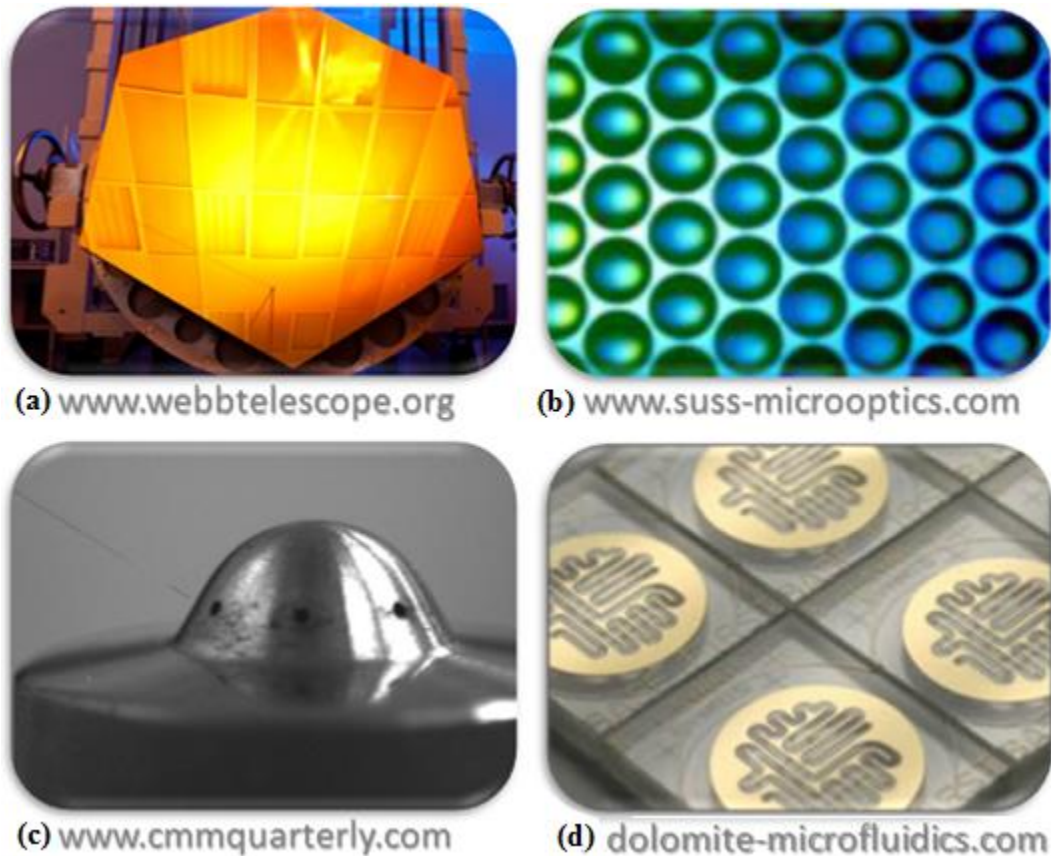


Figure 7-1: Images of hexagonal telescope mirror (a), micro-lens array (b), diesel injector nozzle (c), and micro-fluidic devices (d).

7.4 Future Work

While the potential array of applications are encouraging, there is still much development that is needed to further stabilize the process. For the low-power facility, a more consistent way for manufacturing probes, and a systematic method for post-quantification will be required for both higher repeatability in investigations and wide-scale commercial use. Currently, probes are made manually one-by-one by gluing them

together and carefully trimming the fiber length to attain an appropriate resonance. This results in variable dynamic responses, with probe resonant frequencies varying as much as 20 Hz, maximum tip amplitudes varying by as much as 50 μm , and also variable oscillation trajectories (in-plane and elliptical). Machining with different probes has thus produced inconsistent results thus far. Additionally, while studies into probe wear and degradation have been initiated by a Masters student (Jeffrey Hunt), further work is needed to quantify this and to develop methods for cleaning probes post-process for greater longevity. Another item that may increase probe stability is addition of a ‘magnitude-lock loop’ into the current controls. The system would conceptually work by both adjusting frequency and amplitude of the probe signal to keep the measured phase and magnitude consistent throughout tests. Subsequent to these advances, increases in the experimental facility’s positional control may allow finishing of more complex geometries such as channels and holes.

In the author’s opinion, the high-power facility has more potential for wide-scale use as the dynamic, high-energy actuator is capable of variable, but ultimately significantly larger scale removal. Three-axis positional control of this second process was never integrated, but would be a wise addition in order to automate the setup process. Additional compensation of slurry height (similar to the low-power process) may also increase footprint reproducibility. Hysteresis losses in the actuator result in heat generation so that the high-power actuator also requires an additional cooling mechanism to oscillate probes at frequencies higher than around 5 kHz for extended periods. Probe wear should also be investigated, especially for contact-based removal regimes.

However, possibly the most important advancement that is required for both facilities is an improved technique for probe-to-workpiece referencing. The current method is semi-qualitative and therefore the probe-to-workpiece ‘contact’ position can vary with different operators. Though a skilled operator can often perform this procedure quite repeatably (with 1 – 2 μm), this is not sufficient for an in-depth quantification of the process or its wide-scale use. Some form of the automated referencing system (see section 3.4.3) may be sufficient, however further development is required.

In addition to these improvements, a more complete understanding of the process will only be gained through further investigations of the effects of slurry composition and concentration, workpiece materials, probe energy, and probe-to-workpiece orientation. From the experience of the author and the results of this research, the proposed advancements in Vortex Machining should be achievable through successive developments of experimental facilities and in-depth testing and analysis of the process. In closing, it should be noted that, as shown in Table 2-1, most processes historically require decades – if not longer – of development to be sufficiently deterministic for commercial viability. With only three years since development was initiated on the low-power facility, Vortex Machining shows the potential to be a new alternative to current sub-aperture polishing processes.

REFERENCES

- [1] B. K. Nowakowski, S. T. Smith, B. A. Mullany and S. C. Woody, "Vortex machining: Localized surface modification using an oscillating fiber probe," *Machining Science and Technology*, 13 (4), pp. 561-570, 2010.
- [2] J. Holtsmark, I. Johnsen, T. Sikkeland and S. Skavlem, "Boundary Layer Flow Near a Cylindrical Obstacle in an Oscillating, Incompressible Fluid," *The Journal of the Acoustical Society of America*, 26(1), pp. 1-14, 1954.
- [3] **S. C. Howard**, J. W. Chesna, S. T. Smith and B. A. Mullany, "On the Development of an Experimental Testing Platform for the Vortex Machining Process," *Manufacturing Science and Engineering*, 135(5), 051005, ISSN 1087-1357.
- [4] Andrade, "On the Circulations Caused by the Vibration of Air in a Tube," *Proceedings of the Royal Society of London*, pp. 445-470, 1931.
- [5] **S. C. Howard**, J. W. Chesna, B. A. Mullany and S. T. Smith, "Subcomponent Developments for a Vortex Machining Test Facility," *Proceedings of ASPE conference*, 2011.
- [6] S. T. Smith, R. Keanini and S. Woody, "Energetics of a Particle Captured in a Stationary Vortex Flow," Charlotte, 2010.
- [7] B. E. Gillman and F. Tinker, "Fun Facts about Pitch and the Pitfalls of Ignorance," *SPIE Conference on Optical Manufacturing and Testing III*, vol. 3782, pp. 72-79, 1999.
- [8] N. J. Brown, "Optical Polishing Pitch," *Optical Society of America Workshop on Optical Fabrication and Testing*, 1977.
- [9] A. B. Shorey, S. D. Jacobs, W. I. Kordonski and R. F. Gans, "Experiments and observations regarding the mechanisms of glass removal in magnetorheological finishing," *Applied Optics*, vol. 40, no. 1, pp. 20-33, 2001.
- [10] S. D. Jacobs, D. Golini, Y. Hsu, B. E. Puchebner, D. Strafford, W. I. Kordonski, I. V. Prokhorov, E. Fess, D. Pietrowski and V. W. Kordonski, "Magnetorheological Finishing: A Deterministic Process for Optics Manufacturing," *SPIE*, vol. 2576, pp. 372-382, 1995.
- [11] M. Tricard, W. I. Kordonski and A. B. Shorey, "Magnetorheological Jet Finishing of Conformal, Freeform and Steep Concave Optics," *Annals of the CIRP*, vol. 55, no. 1, 2006.
- [12] S. D. Jacobs, "International Innovations in Optical Finishing," *Proceedings of SPIE*, vol. 5532, 2004.

- [13] C. J. Evans, E. Paul, D. Dornfeld, D. A. Lucca, G. Byrne, M. Tricard, F. Klocke, O. Dambon and B. A. Mullany, "Material Removal Mechanisms in Lapping and Polishing," *CIRP Annals*, vol. 52, no. 2, pp. 611-633, 2003.
- [14] F. W. Preston, "The theory and design of plate glass polishing machines," *Society of Glass Technology*, vol. 11, pp. 214-256, 1927.
- [15] M. Ando, M. Negishi, M. Takimoto, A. Deguchi and N. Nakamura, "Super-smooth polishing on aspherical surfaces," *Nanotechnology*, vol. 6, pp. 111-120, 1995.
- [16] M. Kanaoka, H. Takino, K. Nomura, Y. Mori, H. Mimura and K. Yamauchi, "Removal properties of low-thermal-expansion materials with rotating-sphere elastic emission machining," *Science and Technology of Advanced Materials*, vol. 8, pp. 170-172, 2007.
- [17] A. Kubota, H. Mimura, K. Inagaki, K. Arima, Y. Mori and K. Yamauchi, "Preparation of Ultrasmooth and Defect-Free 4H-SiC(0001) Surfaces by Elastic Emission Machining," *Electronic Materials*, vol. 34, no. 4, pp. 439-443, 2005.
- [18] K. Yamauchi, K. Hirose, H. Goto, K. Sugiyama, K. Inagaki, K. Yamamura, Y. Sano and Y. Mori, "First-principles simulations of removal process in EEM," *Computation Materials Science*, vol. 14, pp. 232-235, 1999.
- [19] A. Kubota, H. Mimura, K. Inagaki, Y. Mori and K. Yamauchi, "Effect of Particle Morphology on Removal Rate and Surface Topography in Elastic Emission Machining," *The Electrochemical Society*, vol. 153, no. 9, pp. 874-878, 2006.
- [20] Y. T. Su, S.-Y. Wang, P.-Y. Chao, Y.-D. Hwang and J.-S. Hsaiu, "Investigation of elastic emission machining process: lubrication effects," *Precision Engineering*, vol. 17, pp. 164-172, 1995.
- [21] M. Kanaoka, C. Liu, K. Nomura, M. Ando, H. Takino, Y. Fukuda, Y. Mori, H. Mimura and K. Yamauchi, "Processing efficiency of elastic emission machining for low-thermal-expansion material," *Surface and Interface Analysis*, vol. 40, pp. 1002-1006, 2008.
- [22] H. Fang, P. Guo and J. Yu, "Surface roughness and material removal in fluid jet polishing," *Applied Optics*, vol. 45, no. 17, pp. 4012-4019, 2006.
- [23] O. W. Fahnle, H. v. Brug and H. J. Frankena, "Fluid jet polishing of optical surfaces," *Applied Optics*, vol. 37, no. 28, pp. 6771-6773, 1998.
- [24] H. Liu, J. Want and H. C. Z, "Abrasive liquid jet as a flexible polishing tool," *Materials and Product Technology*, vol. 31, no. 1, pp. 2-13, 2008.
- [25] S. M. Booij, H. van Brug, J. J. M. Braat and O. W. Fahnle, "Nanometer deep shaping with fluid jet polishing," *Optical Engineering*, vol. 41, no. 8, pp. 1926-1931, 2002.

- [26] S. M. Booij, O. W. Fahnle and J. J. M. Braat, "Shaping with fluid jet polishing by footprint optimization," *Applied Optics*, vol. 43, no. 1, pp. 67-69, 2004.
- [27] S. R. Wilson, D. W. Reicher and J. R. McNeil, "Surface figuring using neutral ion beams," *SPIE Advances in Fabrication and Metrology for Optics and Large Optics*, vol. 966, pp. 74-81, 1988.
- [28] S. R. Wilson and J. R. McNeil, "Neutral ion beam figuring of large optical surfaces," *SPIE Current Developments in Optical Engineering II*, vol 818, pp. 320-324, 1987.
- [29] P. Gailly, K. Fleury-Frenette, J.-H. Lecat, J.-P. Collette and J.-M. Defise, "Ion beam figuring for precision optics," *SPIE*, 2008.
- [30] T. Arnold, G. Bohm, R. Fechner, J. Meister, A. Nickel, F. Frost, T. Hansel and A. Schindler, "Ultra-precision surface finishing by ion beam and plasma jet techniques - status and outlook," *Nuclear Instruments and Methods in Physics Research A*, vol. 616, pp. 147-156, 2010.
- [31] M. Weiser, "Ion beam figuring for lithography optics," *Nuclear Instruments and Methods in Physics Research B*, vol. 267, pp. 1390-1393, 2009.
- [32] P. Shore, C. Cunningham, D. DeBra, C. Evans, J. Hough, R. Gilmozzi, H. Kunzmann, P. Morantz and X. Tonnellier, "Precision engineering for astronomy and gravity science," *CIRP Annals - Manufacturing Technology*, vol. 596, pp. 1-23, 2010.
- [33] **S. Howard**, B. Mullany. and S. T. Smith, "Design and Implementation of a High-Power Machining Facility for Investigations in Vortex Machining," *Proceedings of 13th International Conference of euspen*, ISBN 13: 978-0-9566790-2-4, 2013.
- [34] **S. C. Howard**, J. W. Chesna, B. A. Mullany and S. T. Smith, "Preliminary Characterization of Vortex Machining," *Proceedings of 12th euspen International Conference*, ISBN 13: 978-0-9566790-0-0, 2012.
- [35] **S. Howard**, J. W. Chesna, B. Mullany and S. T. Smith, "Observations During Vortex Machining Process Development," *Proceedings of the ASME International Manufacturing Science and Engineering Conference*,. ISBN 978-0-7918-5499-0, 2012.
- [36] M. Stedman, "Basis for comparing the performance of surface-measuring machines," *Precision Engineering*, vol. 9, pp. 149-152, 1987.
- [37] T. R. Thomas, *Rough Surfaces*, London: Imperial College Press, 1999.
- [38] C. Evans, "MEGR 8284 Lecture Notes, Lecture 2," Charlotte, September 2011.

- [39] F. Gao, R. K. Leach, J. Petzing and J. M. Coupland, "Surface Measurement Errors using Commercial Scanning White Light Interferometers," *Measurement Science and Technology*, pp. 1-13, 2008.
- [40] R. E. Reason, "Surface finish and its measurement," *Journal of Industrial and Production Engineers*, vol. 23, pp. 347-372, 1944.
- [41] E. J. Abbott, S. Bousky and D. E. Williamson, "The Profilometer," *Mechanical Engineering*, vol. 60, pp. 205-216, 1938.
- [42] E. J. Abbott and F. A. Firestone, "Specifying surface quality," *Mechanical Engineering*, vol. 1933, pp. 569-572, 1933.
- [43] R. Leach and H. Haitjema, "Bandwidth characteristics and comparisons of surface texture measuring instruments," *Measurement Science and Technology*, pp. 1-9, 2010.
- [44] T. V. Vorburger, H. G. Rhee, T. B. Renegar, J. F. Song and A. Zheng, "Comparison of optical and stylus methods for measurement of surface texture," *Advanced Manufacturing Technology*, pp. 110-118, 2007.
- [45] E. Meyer, "Atomic Force Microscopy," *Progress in Surface Science*, vol. 41, pp. 3-49, 1992.
- [46] F. Lin and D. J. Meier, "Atomic-Scale Resolution in Atomic Force Microscopy," *American Chemical Society*, pp. 1660-1662, 1994.
- [47] C. Y. Poon and B. Bhushan, "Comparison of surface roughness measurements by stylus profiler, AFM and non-contact optical profiler," *Wear*, pp. 76-88, 1995.
- [48] D. J. Whitehouse, *Handbook of Surface Metrology*, Bristol, UK: Institute of Physics Publishing, 1994.
- [49] F. T. Farago, *Handbook of dimensional measurement*, New York: Industrial Press, 1982.
- [50] J. Raja, B. Muralikrishnan and F. Shengyu, "Recent advances in separation of roughness, waviness, and form," *Precision Engineering*, pp. 222-235, 2001.
- [51] M. P. Krystek, "ISO Filters in Precision Engineering and Production Measurement," *submitted to Measurement Science and Technology*, pp. 1-39, 2010.
- [52] B. Muralikrishnan and J. Raja, *Computational Surface and Roundness Metrology*, London: Springer, 2009.
- [53] International Standard, "ISO 4287," 1997.
- [54] International Standard, "ISO 13565 Part 1," 1996.

- [55] D. J. Whitehouse, "The parameter rash - is there a cure?," *Wear*, vol. 83, pp. 75-78, 1982.
- [56] J. W. McBride, K. J. Cross and S. M. A. Sharkh, "The Evaluation of Arc Erosion on Electrical Contacts Using Three-Dimensional Surface Profiles," *IEEE Transactions on Components, Packaging, and Manufacturing Technology*, pp. 87-97, 1996.
- [57] J. Jiang, F. H. Stott and M. M. Stack, "Characterization of wear scar surfaces using combined three-dimensional topographic analysis and contact resistance measurements," *Tribology International*, pp. 517-526, 1997.
- [58] J. Shöfer and E. Santner, "Quantitative wear analysis using atomic force microscopy," *Wear*, pp. 74-83, 1998.
- [59] B. K. Nowakowski, "Micromechanical systems for assembly, measurement and modification at micro and nanometer scale," UNC Charlotte, PhD Dissertation, Charlotte, 2010.
- [60] M. B. Bauza, "Development of Instrumentation Systems for Macro-to Micro-Scale Dimentsional Metrology," UNC Charlotte, PhD Dissertation, Charlotte, 2005.
- [61] R. J. Hocken and P. H. Pereira, *Coordinate Measuring Machinines and Systems*, Boca Raton: CRC Press, 2012.
- [62] H. Qi, "High speed motion generated by an oscillating microfiber, Master's Thesis," Department of Engineering at Brown University, Providence, Rhode Island, 2008.
- [63] J. B. Hunt, **S. C. Howard**, B. A. Mullany, and S. T. Smith, 2013 Investigation of tooling effects, slurry composition, and workpiece materials in vortex machining, *Proc. ASPE.*, **56**, 545 – 549.
- [64] S. T. Smith, *Flexures*, Boca Raton: CRC Press, 2000.
- [65] S. T. Smith and D. G. Chetwynd, *Foundatons of Ultraprecision Mechanism Design*, Boca Raton: CRC Press, 1992.
- [66] J. Phillips, *Freedom in Machinery*, Cambridge: Cambridge University Press, 2006.
- [67] Lin F., Elliott K.E., Parker W., Chakraborty, N., Teo C-S., Smith S.T., Elliott G.E., Moyer P.J., 2009, "Confocal and Force Probe Imaging System for Simultaneous Three Dimensional Optical and Mechanical Spectroscopic Evaluation of Biological Samples," *Rev. Sci. Instrum.*, *80*(5), 055110 (7 pages).
- [68] D. S. Batchelder, "Analysis and design of high-resolution capacitance probes for use in a precision motion control stage," UNCC Master's Thesis, Charlotte, 1994.

- [69] NIST, "About the Internet-based Surface Metrology Algorithm Testing System," NIST, 22 October 2012. [Online]. Available: <http://physics.nist.gov/VSC/jsp/About.jsp>. [Accessed 13 December 2013].

* References [3], [5], [33], [34], and [35] are publications by the dissertation author that provide more context to research in Vortex Machining.

APPENDIX A: LIST OF PAPERS AND CONFERENCE PROCEEDINGS
FROM THESE STUDIES

S. C. Howard, J. W. Chesna, S. T. Smith and B. A. Mullany, "On the Development of an Experimental Testing Platform for the Vortex Machining Process," *Manufacturing Science and Engineering*, 135(5), 051005, ISSN 1087-1357.

S. Howard, B. Mullany. and S. T. Smith, "Design and Implementation of a High-Power Machining Facility for Investigations in Vortex Machining," *Proceedings of 13th International Conference of euspen*, ISBN 13: 978-0-9566790-2-4, 2013.

S. C. Howard, J. W. Chesna, B. A. Mullany and S. T. Smith, "Preliminary Characterization of Vortex Machining," *Proceedings of 12th euspen International Conference*, ISBN 13: 978-0-9566790-0-0, 2012.

S. Howard, J. W. Chesna, B. Mullany and S. T. Smith, "Observations During Vortex Machining Process Development," *Proceedings of the ASME International Manufacturing Science and Engineering Conference*,. ISBN 978-0-7918-5499-0, 2012.

S. C. Howard, J. W. Chesna, B. A. Mullany and S. T. Smith, "Subcomponent Developments for a Vortex Machining Test Facility," *Proceedings of ASPE conference*, 2011.

APPENDIX B: MATLAB CODE FOR FLUID STREAMING SOLUTION

%coded by help of Dr's Phanindra Tallapragga, Bethany Woody, Stuart T
%Smith; used to plot streamlines and energy density of fluid flow based
%on solutions by Holtzmark and others

```
clear all
clc
%
a=250e-6; % radius of cylinder in m
A=0.0508;
Amp=1000e-6; %in m
Frequency=3000; % Frequency in Hz
omega=2*pi*Frequency; % Oscillation frequency in 1/sec
Uo=Amp*omega; % Velocity Amplitude of oscillation of cylinder in m/sec
eta=1.0e-6; % kinematic viscosity of fluid in m^2 per s. water = 1 x
%10-6

%%%% approximate parameters in Holtzmark paper %%%
%{
%a=1.1*1e-3; % radius of cylinder in m
%A=a*20;
%Amp=6.366197723675814e-005; %in m
%Frequency=200; % Frequency in Hz
%omega=2*pi*Frequency; % Oscillation frequency in 1/sec
%Uo=Amp*omega; % Velocity Amplitude of oscillation of cylinder in m/sec
%eta=1.5e-5; % kinematic viscosity of fluid in m^2 per s. water = 1 x
%10-6
%}

RTOL=1.0e-12; % relative tolerance in integration
time_period = 0.2*(2*pi/omega);
tblock = time_period;
r_step = 0.9*a;
% r = a:r_step/10:2*a;
% r = [r(1:end-1), 1.2*a:r_step/5:1.5*a];
% r = [r(1:end-1), 1.5*a:r_step/50*a];
% r = r';

r = a:r_step/50:3*a;
r = r';

theta_step = (1/100)*(pi/2);
t_step = tblock/100;
max_row = length(r);%round(1+(5*a-a)/r_step);
max_col = 1+ round((pi-0)/theta_step);
max_tdim = round(0+ (tblock)/t_step);
psi_01 = zeros(max_row,max_col,max_tdim);%array of zeros with
%dimensions max_row, max_col, max_tdim
psi_02 = zeros(max_row,max_col,max_tdim);
%psi_1 = zeros(max_row,max_col,max_tdim);
fr = zeros(max_row,1); %complex(zeros(max_row,1), zeros(max_row,1));
%gr = complex(zeros(max_row,1), zeros(max_row,1));
psi = zeros(max_row,max_col,max_tdim);
```

```

v0_radial = zeros(max_row,max_col,max_tdim);
v0_theta = zeros(max_row,max_col,max_tdim);
v1_s_radial = zeros(max_row,max_col);

temp_exp0 = complex(zeros(max_tdim,1));
temp_exp1 = complex(zeros(max_tdim,1));
temp_sin = zeros(max_col,1);
temp_sin2 = zeros(max_col,1);
temp_var = complex(zeros(max_row,max_tdim));
temp_var1 = complex(zeros(max_row,max_col));
temp_var2 = complex(zeros(max_row,max_col));

eps=sqrt(i*omega/eta); % Hankel function parameter
C=besselh(2,1,eps*a)/besselh(0,1,eps*a); % C coefficient in
%calculations for velocity components
Cc=conj(C);
Cr = real(C);
Ci = imag(C);

P=(omega*Uo*Uo/(4*eta*eta));%coefficient see p.29 Holtsmark
H_0_1 = besselh(0,1,eps*a);

X = besselh(0,1,eps*r)/H_0_1;
Y = besselh(1,1,eps*r)/H_0_1;
Z = besselh(2,1,eps*r)/H_0_1;
Xr = real(X);
Xi = imag(X);
Yr = real(Y);
Yi = imag(Y);
Zr = real(Z);
Zi = imag(Z);

rho_x = @(x)P*(-2)*imag( besselh(2,1,eps*x)/H_0_1 +
(a*a./(x.*x)).*C.*conj(besselh(0,1,eps*x)/H_0_1) +
2*(besselh(0,1,eps*x)/H_0_1).*conj(besselh(2,1,eps*x)/H_0_1) );
%{
%f1_x = @(x) (1./x).*rho_x(x);
%f2_x = @(x) x.*rho_x(x);
%f3_x = @(x) x.*x.*x.*rho_x(x);
%f4_x = @(x) x.*x.*x.*x.*rho_x(x);
%}
%
f1_x = @(x) P*(-2)*(1./x).*imag( besselh(2,1,eps*x)/H_0_1 +
(a*a./(x.*x))*C.*conj(besselh(0,1,eps*x)/H_0_1) +
2*(besselh(0,1,eps*x)/H_0_1).*conj(besselh(2,1,eps*x)/H_0_1) );
f2_x = @(x) P*(-2)*x.*imag( besselh(2,1,eps*x)/H_0_1 +
(a*a./(x.*x))*C.*conj(besselh(0,1,eps*x)/H_0_1) +
2*(besselh(0,1,eps*x)/H_0_1).*conj(besselh(2,1,eps*x)/H_0_1) );
f3_x = @(x) P*(-2)*x.*x.*x.*imag( besselh(2,1,eps*x)/H_0_1 +
(a*a./(x.*x))*C.*conj(besselh(0,1,eps*x)/H_0_1) +
2*(besselh(0,1,eps*x)/H_0_1).*conj(besselh(2,1,eps*x)/H_0_1) );
f4_x = @(x) P*(-2)*x.*x.*x.*x.*x.*imag( besselh(2,1,eps*x)/H_0_1 +
(a*a./(x.*x))*C.*conj(besselh(0,1,eps*x)/H_0_1) +
2*(besselh(0,1,eps*x)/H_0_1).*conj(besselh(2,1,eps*x)/H_0_1) );
%}

```

```

K = (1/48) *quadgk(f1_x,a, A, 'RelTol', RTOL, 'AbsTol', 0);
L = (-1/16) *quadgk(f2_x,a, A, 'RelTol', RTOL, 'AbsTol', 0);
M = (1/16) *quadgk(f3_x,a, A, 'RelTol', RTOL, 'AbsTol', 0);
N = (-1/48) *quadgk(f4_x,a, A, 'RelTol', RTOL, 'AbsTol', 0);
c1 = ((-A^6*K)+(3*A^4*a^2*K)+(A^2*(2*a^2*L+M))+(a^2*M)+(2*N))/(A^2-a^2)^3;
c2 = -
((A^6*L)+(A^4*(6*a^4*K+a^2*L+2*M))+(A^2*(4*a^4*L+2*M*a^2+3*N))+(2*a^4*M+3*a^2*N))/(A^2-a^2)^3;
c3 =
(a^2*((A^6*(3*a^2*K+2*L))+(A^4*(3*a^4*K+2*a^2*L+4*M))+(A^2*(2*a^4*L+a^2*M+6*N))+(a^4*M))/(A^2-a^2)^3;
c4 = (a^4*((-A^6*(2*a^2*K+L))- (A^4*(a^2*L+2*M))- (3*A^2*N)+(a^2*N))/(A^2-a^2)^3;
%}
f_x = @(x) x.^4.*( (1/48)*quadgk(f1_x, a, x, 'RelTol', RTOL, 'AbsTol', 0) + c1) + x.*x.*( ( (-1/16)*quadgk(f2_x, a, x, 'RelTol', RTOL, 'AbsTol', 0) + c2)) + ...
(1/16)*quadgk(f3_x, a, x, 'RelTol', RTOL, 'AbsTol', 0) + c3 + (1./(x.*x)).*((-1/48)*quadgk(f4_x, a, x, 'RelTol', RTOL, 'AbsTol', 0) + c4);
%
f11 = @(x) quadgk(f1_x, a, x, 'RelTol', RTOL, 'AbsTol', 0) ;
f22 = @(x) quadgk(f2_x, a, x, 'RelTol', RTOL, 'AbsTol', 0) ;
f33 = @(x) quadgk(f3_x, a, x, 'RelTol', RTOL, 'AbsTol', 0);
f44 = @(x) quadgk(f4_x, a, x, 'RelTol', RTOL, 'AbsTol', 0) ;
for row = 1:length(r)
    Q1(row,1) = (1/48)*f11(r(row)) + c1;
    Q2(row,1) = (-1/16)*f22(r(row)) + c2;
    Q3(row,1) = (1/16)*f33(r(row)) + c3;
    Q4(row,1) = (-1/48)*f44(r(row)) + c4;
    fr(row,1) = r(row)^4*Q1(row) + r(row)^2*Q2(row) + Q3(row) + (1/(r(row)^2))*Q4(row);
    d_fr(row,1) = 4*r(row)^3*Q1(row) + 2*r(row)*Q2(row) - 2*(1/r(row)^3)*Q4(row);
    d_ft(row,1) = (fr(row,1))/row;%partial derivative of psi wrt theta
    %plus a division by r, used for calculation of v_radial
end
%}
%{
%big_omega_x = @(x) i*P*(besselh(2,1,eps*x)/H_0_1 -
%(a*a/(x.*x))*C*besselh(0,1,eps*x)/H_0_1);
%g1_x = @(x)i*P*(1./x).*(besselh(2,1,eps*x)/H_0_1 -
%(a*a/(x.*x))*C.*besselh(0,1,eps*x)/H_0_1);
%g2_x = @(x)i*P*x.*x.*(besselh(2,1,eps*x)/H_0_1 -
%(a*a/(x.*x))*C.*besselh(0,1,eps*x)/H_0_1);
%g3_x = @(x)i*P*x.*besselh(2,2,
%eps*x*sqrt(2)).*(besselh(2,1,eps*x)/H_0_1 -
%(a*a/(x.*x))*C.*besselh(0,1,eps*x)/H_0_1);
%g4_x = @(x)i*P*x.*besselh(2,1,eps*x*sqrt(2)).*(
%besselh(2,1,eps*x)/H_0_1 - (a*a/(x.*x))*C.*besselh(0,1,eps*x)/H_0_1);
%fun_k2_x =
%@(x)x*besselh(2,2,eps*x*sqrt(2))*i*P*(besselh(2,1,eps*x)/H_0_1 -
%(a*a/(x.*x))*C*besselh(0,1,eps*x)/H_0_1);

%k1 = (i*eta/(8*omega))*quadgk(g1_x, a, 100*A, 'RelTol', RTOL,
%'AbsTol', 0);

```

```

    %k3 = (pi*eta/(8*omega))*quadgk(g3_x, a, 10*A, 'RelTol', RTOL,
    %'AbsTol', 0);
    %k2 = ((-4*a*i/pi)*k3 +
    %eps*sqrt(2)*a^4*besselh(3,2,eps*a*sqrt(2))*k1)/(eps*sqrt(2)*besselh(1,
    %2,eps*a*sqrt(2))) ;
    % k4 = (4*a*k1 +
    %eps*sqrt(2)*besselh(2,1,eps*a*sqrt(2))*k3)/(eps*sqrt(2)*besselh(1,2,ep
    %s*a*sqrt(2)));

    %g_x = @(x)x.*x.*( (-i*eta/(8*omega))*quadgk(g1_x, a, x, 'RelTol',
    %RTOL, 'AbsTol', 0) + k1) + ...
    % (1./(x.*x))*( i*eta/(8*omega))*quadgk(g2_x, a, x,
    %'RelTol', RTOL, 'AbsTol', 0) + k2)+ ...
    %besselh(2,1,eps*x*sqrt(2)).*((pi*eta/(8*omega))*quadgk(g3_x, a, x,
    %'RelTol', RTOL, 'AbsTol', 0) + k3) + ...
    % besselh(2,2,eps*x*sqrt(2)).*((pi*eta/(8*omega))*quadgk(g4_x,
    %a, x, 'RelTol', RTOL, 'AbsTol', 0) + k4);
    %}
    %{
    %for row = 1:length(r)
        %fr(row,1) = f_x(r(row));
        %{
        %fr1(row,1) = r^4*( (1/48)*f11(r) + c1);
        %fr2(row,1) = r*r*( -(1/16)*f22(r)+c2);
        %fr3(row,1) = ((1/16)*f33(r)+ c3);
        %fr4(row,1) = (1/(r*r))*( (-1/48)*f44(r)+c4);
        %}
        %gr(row,1) = g_x(r);
    %end
    %}

theta = 0:theta_step:pi/2;
theta = theta';
temp_sin = sin(theta);
temp_sin2 = sin(2*theta);
temp_cos = cos(theta);
temp_cos2 = cos(2*theta);

temp_var1 = -0.5*Uo*a*(r/a + (a./r).*C)*temp_sin';
temp_var2 = (1/eps)*Uo*(besselh(1,1,eps*r)/H_0_1)*temp_sin';

psi_1s = fr*temp_sin2';

v1_s_theta = d_fr*temp_sin2';
v1_s_radial = -2*d_ft*temp_cos2';

energydensity = (v1_s_theta).^2 + (v1_s_radial).^2;
logED = log(energydensity);

```

```

%temp_var = 2*real(gr*temp_exp1');
xgrid = zeros(max_row, max_col);
ygrid = zeros(max_row, max_col);

xgrid= r*cos(theta)';
ygrid = r*sin(theta)';

xgridNormal=xgrid./a;
ygridNormal=ygrid./a;
%
save xgrid xgrid;
save ygrid ygrid;
save psi_stationary psi_1s;

%contour(xgrid,ygrid, psi_1s,100);%plots stationary component streams

hold on

%figure (1), contourf(xgrid,ygrid, energydensity,100) %plots energy
%density contour
figure (1), contourf(xgridNormal,ygridNormal, energydensity,100) %plots
%energy density contour

contour(xgridNormal,ygridNormal, energydensity, 100)%plots regular
%contour overlay to get rid of black lines

xlabel('Normalized radius (r/a)', 'FontSize', 12)

ylabel('Normalized radius (r/a)', 'FontSize', 12)

title('Energy Density Plot', 'FontSize', 16, 'Fontweight','b')

colorbar('EastOutside')

h=colorbar;

set(get(h, 'ylabel'), 'String', 'Energy Density (m^2/s^2)', 'FontSize',
12)

hold off

figure (2), contour(xgridNormal,ygridNormal, psi_1s,40);%plots
%stationary component streams

xlabel('Normalized radius (r/a)', 'FontSize', 12)

ylabel('Normalized radius (r/a)', 'FontSize', 12)

title('Streamline Plot', 'FontSize', 16, 'Fontweight','b')

hold off

```

```

%contour(xgrid,ygrid, logED,10)

%}
% for tcount = 1:5
%     t_row =0;
%
%     init_time = (tcount-1)*tblock;
%     final_time = tcount*tblock - t_step;
%
%     t= init_time:t_step:final_time;
%     t=t';
%     temp_exp0 = exp(-i*omega*t);
%     temp_exp1 = exp(-2*i*omega*t);
%
% for t = init_time : t_step : final_time
%     t_row = t_row+1;
%     psi_01(:, :, t_row) = 2* real(temp_var1*temp_exp0(t_row));
%     psi_02(:, :, t_row) = 2*real(temp_var2*temp_exp0(t_row));
% end
% psi_0 = psi_01 +psi_02;
% file_psi_01 = strcat('psi_01_t',sprintf('%02d',tcount));
% file_psi_02 = strcat('psi_02_t',sprintf('%02d',tcount));
% %
% save(file_psi_01, 'psi_01');
% save(file_psi_02, 'psi_02');
% %}
% end
% %}

```

APPENDIX C: PRELIMINARY VALIDATION OF FLUID FLOW THEORY

To date, preliminary studies have been initiated in an attempt to provide validation to the flow field theory [2] as well as assumptions upon which the theory is based. As discussed in section 2.1.1, many assumptions are not realistic such as those prescribing an infinitely large reservoir and infinitely long tool. However, another concern was the assumption that the tool was oscillating in a linear trajectory which is often difficult to achieve in practice. Due to this, a study was initiated to investigate the high-power probe trajectory at different frequencies within its frequency response.

Figure C-1 shows a schematic diagram and photograph of the experimental facility used to conduct the probe tracking studies. While for the presented results a fluid reservoir was not used, probe tracking in a fluid medium is possible and should be considered for future experiments. A horizontally positioned high-magnification camera (Sony, model #XCD-SX910CR) is used to image the oscillations of a rod through reflection of a turning mirror, see Figure C-1. By taking a series of images of the rod as it is oscillated, its trajectory can be mapped. One issue that arose early into the study was camera speeds. While a high-speed, high-magnification was used, it was still not fast enough to capture enough images of the rod motion at the frequencies we were interested (200 Hz – 10 kHz) in which anywhere from 10 to 100 frames per cycle were required. This is due to limits on how quickly data can be streamed from the camera to the host computer. However, images could be captured at very low exposure times (down to 9 μ s), but not fast enough consecutively. As a result, a plan was proposed to use aliasing techniques enabling pseudo-tracking of high-frequency rod motions. This technique relies on the assumption that the probe undergoes a harmonic motion and is repeatable between

cycles. The aliasing methodology is displayed graphically in Figure C-2. By assuming that the probe position varies regularly in a repeatable pattern, even high frequency probe oscillations can be captured by grabbing consecutive image frames at integer multiples of the time period of the probe oscillation plus a specified time step. This methodology is further clarified in the following equation,

$$\Delta t_{loop} = m t_{period} + \frac{t_{period}}{n} \quad \text{Equation C-1}$$

where

Δt_{loop} , loop interval for capturing images

m , multiple of probe oscillation time periods between consecutive image capture

t_{period} , period of oscillation for probe

n , number of image captures per cycle

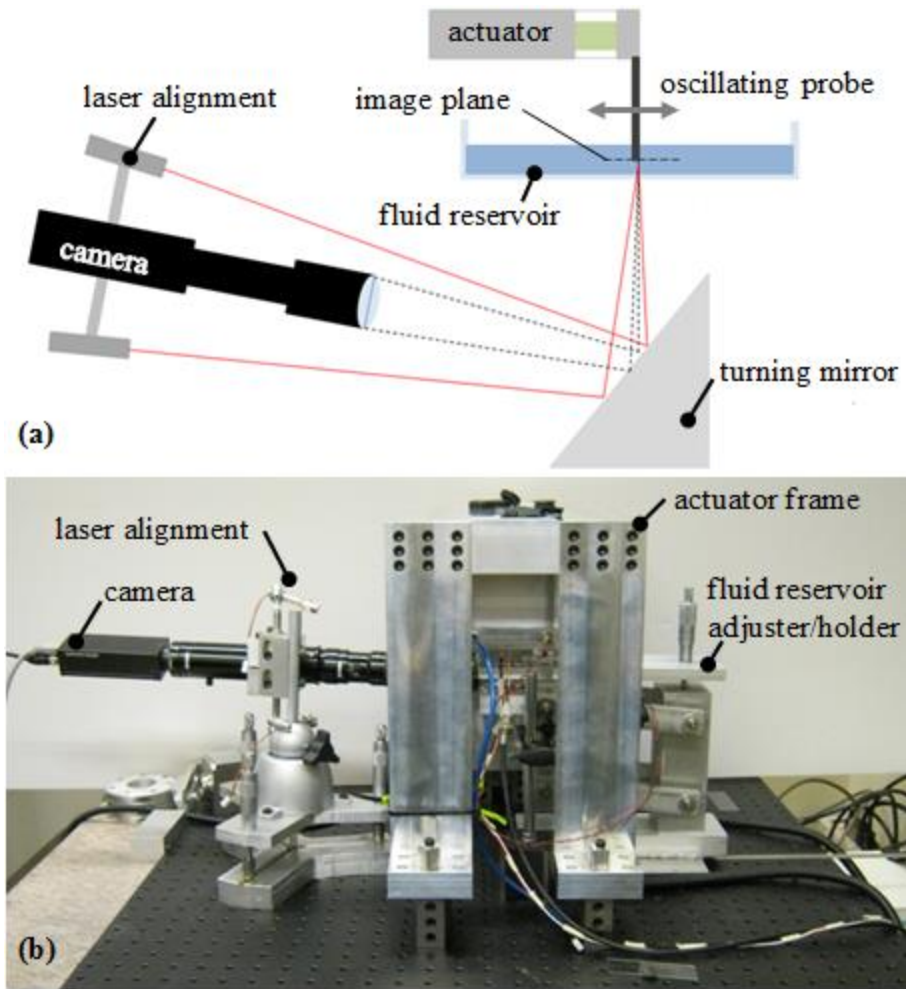


Figure C-1: Schematic diagram (a) and physical implementation (b) of experimental setup used for particle tracking studies. Probe trajectory tracking used same setup except without fluid reservoir.

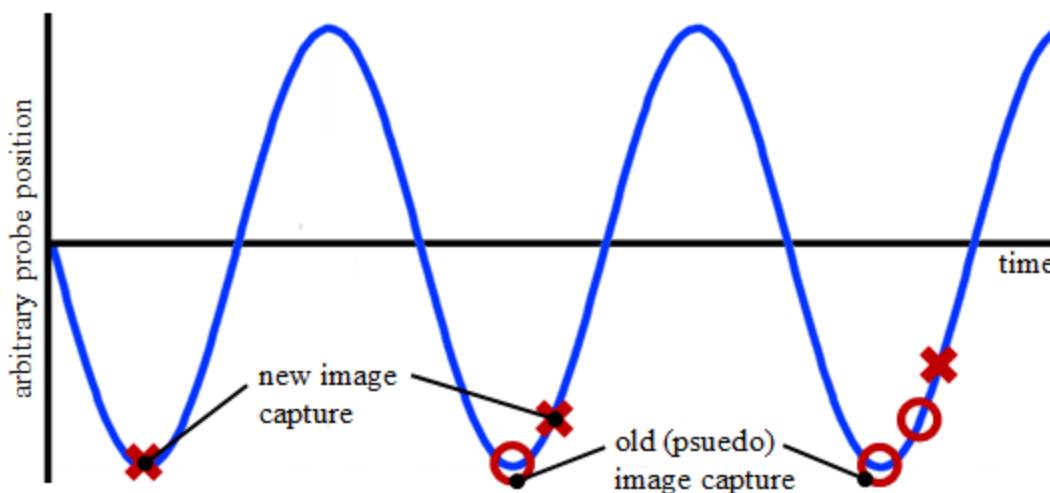


Figure C-2: Diagram depicting aliasing technique used in probe tracking studies. If the positional variation of the probe is considered linear and repeatable (sinusoidal for example), then a complete cycle can be captured by imaging at integer multiple intervals of the time period of the probe variation plus a specified time step.

Using Equation C-1, a Microsoft ExcelTM spreadsheet was designed in which optimum loop intervals could be calculated given specific probe frequencies. These loop intervals could then be programmed into National Instruments LabVIEWTM software on a computer control system consisting of real-time hardware. As shown in Figure C-2, images are recorded of the probe end by using a turning mirror. These images, once recorded, are then loaded into a MatlabTM script that was designed to calibrate the length scale of the images (using the probe diameter as a reference) and then to record the xy position of the centroid of the probe. This positional data was then put together into graphs to visualize the rod trajectory. A control test was undertaken in which a probe was tracked using the aliasing methodology at 1 Hz of oscillation, see Figure C-3. As can be seen from the figure, the probe has an approximately linear, sinusoidal time-variant trajectory. The secondary axis shows some deviations from the ideal but much of this is likely measurement noise due to the resolution of the camera and the post-processing

analysis effectiveness of locating the probe centroid position. While notable, Vortex Machining requires much higher frequency probe oscillations and to increase the amplitude to a level where enough energy is imparted into the slurry, the probe often needs to be oscillated at or near resonance. While studies at higher frequencies showed similar results to those in Figure C-3 – further validating the aliasing techniques – studies of probe trajectories at frequencies near resonance began to show significant deviations from the ideal. As the probe approached resonance, the primary axis amplitude would increase rapidly. However, simultaneously the secondary axis would show significant increases in amplitude as the probe would begin to exhibit an elliptical oscillation trajectory. Also, the primary axis directionality would begin rotating slightly about the desired trajectory of motion as the probe was oscillated through its resonance. This trend of rotation was relatively constant in the frequency domain, starting a few Hz before and ending a few Hz after resonance, after which the trajectory rotated back to its driven direction. This behavior has been noted to appear similar to observation of a frequency sweep through resonance of a system when viewing the sweep in XY-mode. The maximum rotation identified during the studies was approximately 30 degrees from the ideal (i.e. driven) oscillation direction. Figure C-4 shows the elliptical trajectory of a probe near resonance. Since these original probe tracking experiments, it has been noted that the elliptical behavior and rotation near resonance is reduced significantly when the rod is inserted into a fluid medium, although no quantitative data has been recorded of this phenomenon yet.

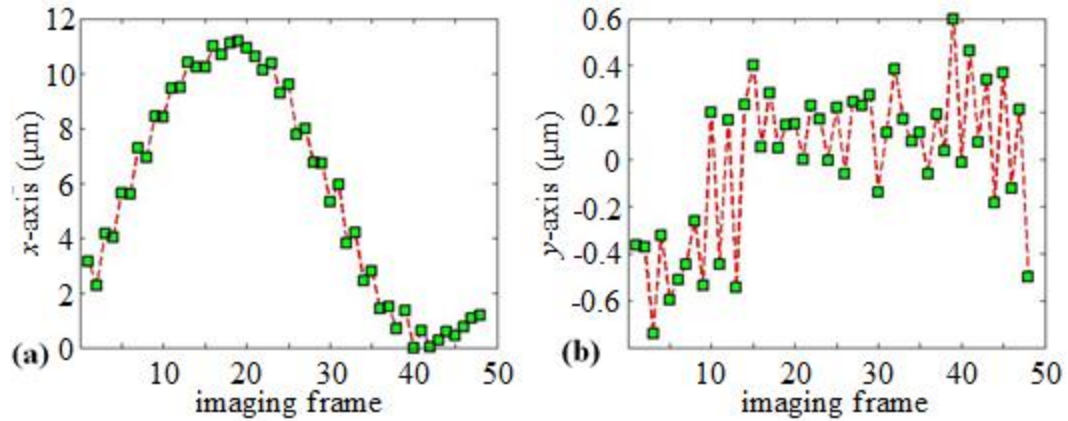


Figure C-3: Resultant plots from probe tracking study using 500 μm diameter probe oscillating at 1 Hz. One cycle is depicted in which 48 data points were collected. The primary direction of oscillation is shown in (a) and the secondary direction is shown in (b).

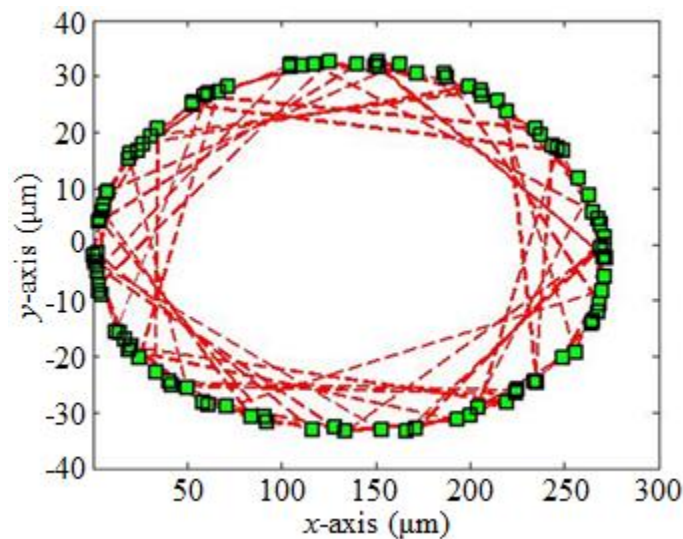


Figure C-4: Resultant plot from probe tracking study using 500 μm diameter probe oscillating near 1st mode resonance at 270 Hz. Several cycles have been collected and plotted on an xy graph.

After preliminary investigations into tracking the probe trajectory, the next step was to initiate studies of particle trajectories in a fluid medium in response to probe oscillations. While much of these investigations relate to Vortex Machining, they were

funded mainly through a separate NSF grant entitled *Collaborative Research: Manipulation of Suspended Microparticles via Localized Fluid Boundary Dynamics: Modeling, Simulation, and Experiments*, in which the author led experimental design and studies from 2010 to 2012. The experimental setup shown in Figure C-1 was used to conduct the particle tracking studies. Most investigations to date have used a mixture of water and 10 μm diameter, silver coated hollow glass spheres (Dantec Dynamics model #S-HGS-10) with a concentration of approximately 0.1 grains of spheres per 20 mL of water. As a note for future investigations, these solutions were often mixed just prior to running the experiment as the spheres would settle to the bottom of the solution within minutes. This is due to the fact that the spheres have a specific density of approximately 1.4. Subsequent investigators are now examining the use of more neutrally buoyant particulates.

While these studies need more work, a large amount of data has been collected and some general trends can be mentioned. At frequencies less than 250 Hz no noticeable streaming of the particles was identified. Even at frequencies above 250 Hz the probe needed to be within a few Hz of resonance (corresponding to over 50 μm in amplitude) before any streaming could be resolved. It was also noticed that when the rod trajectory was significantly elliptical a rotational pattern of particle flow seemed to develop following the rotation of the rod trajectory. Linear trajectories tended to cause vortices more closely corresponding to the flow patterns predicted by the Holtmark theory [2]. Movies of these experiments have been recorded and stored in a database for future reference. However, it was found useful to view the data by layering consecutive images on top of each other thereby showing the evolution of particle trajectories over time. As

shown in Figure C-5, a four quadrant vortex pattern similar to that predicted in theory was produced using a 500 μm rod oscillating near 270 Hz. Also noticeable is the particles seem to move over time into ‘trapping spots’ at the center of the vortices. The data was also processed through Dantec Dynamics software to produce the streamlines shown in Figure C-6. While visualization of particle trajectories seems to suggest convergence between theory and experimental investigations, more work is needed to compare measured particle paths to those expected by theory using specific setup parameters.

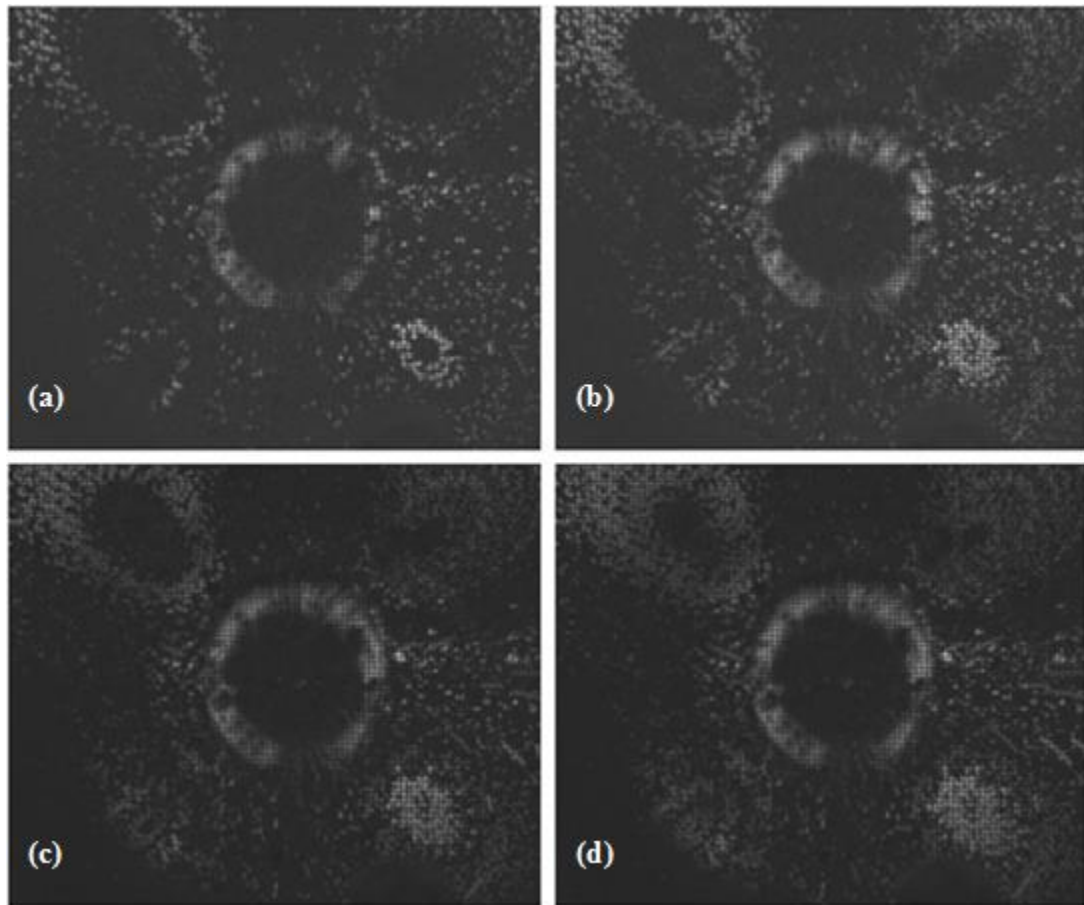


Figure C-5: Images showing particles (light-colored spots) layered over 50 (a), 100 (b), 150 (c), and 200 (d) frames. Note four major vortices and particle trajectories converging towards the center of these vortices. Particle streaming was produced by oscillating a 500 μm diameter rod at 270 Hz at an amplitude of 100 μm .

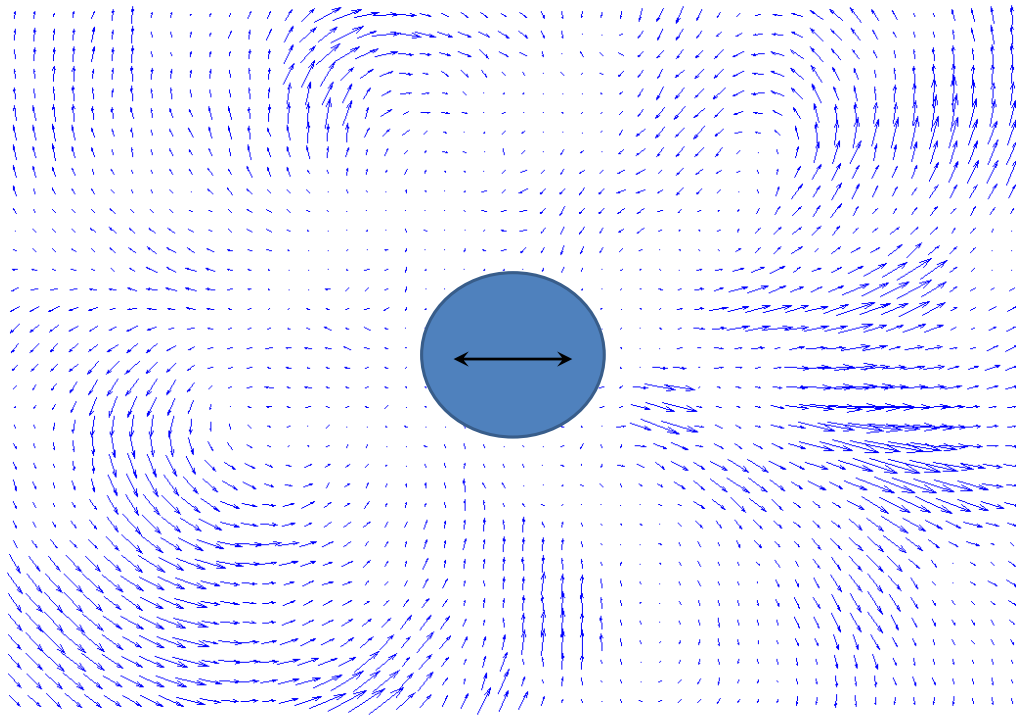


Figure C-6: Particle image velocimetry (PIV) map created using Dantec Dynamics software and images captured from experiment depicted in Figure C-5.

APPENDIX D: ZYGO NEWVIEW 5000 SPECIFICATIONS

NewView 5000™ General Specifications:**Technical Performance**

Vertical (Z) Scan Range:	≤ 5 mm
Vertical (Z) Scan Rate:	≤ 10 μm/sec
Vertical (Z) Resolution:	≥ 0.1 nm
Lateral (X, Y) Resolution Range:	0.45 – 11.8 μm
Field of View Range:	0.04 – 17.5 mm; larger areas can be imaged with field stitching capability
Step Height Accuracy:	≤ 0.75% (Model 5032)
Step Height Repeatability:	≤ 0.1% (Model 5032)

System

Standard Platforms:	Models 5010, 5022, 5032; each platform is modular and upgradeable
Image Zoom:	Standard; variable with six indexed positions: 0.4X, 0.5X, 0.8X, 1.0X, 1.3X, and 2X
Imaging Objectives:	Standard: 1X, 2.5X, 5X, 10X, 20X, 50X, and 100X Super Long Working Distance: 2X, 5X, and 10X
Objective Mounting:	Single quick-mount adapter, manual, or automated 5-position indexing turret
Sample Positioning:	Manual or automated stages available
Computer:	Latest generation Dell Optiplex PC with R/W CD-ROM, floppy drive, and 19-inch color monitor; optional printers available
Software:	Zygo MetroPro™ comprehensive metrology package with advanced graphical display, data analysis, and scripting capabilities

Zygo TeraOptix
Westborough, MA USA

Zygo TeraAutomation
Delray, FL USA

Zygo Automation
Longmont, CO USA

Zygo Western Regional
Sunnyvale CA USA

Zygo Central Region
Northbrook, IL USA

ZygoLOT
Germany

Zygo KK
Japan

Zygo Asia
Singapore

Discover the power of 3D surface metrology and get a **New View** of your parts. See for yourself why leading manufacturers worldwide have taken a **New View** of their processes and benefited from ZYGO's metrology and yield improvement solutions. Contact us today to arrange for a demonstration.



ZYGO CORPORATION
LAUREL BROOK ROAD
MIDDLEFIELD, CT 06455
VOICE: 860 347-8506
FAX: 860 348-4188

WWW.ZYGO.COM
EMAIL: inquire@zygo.com

Covered by one or more of the following US patents: 5,402,234, 5,398,113, and 5,558,004.
Other US and foreign patents pending.

Data subject to change without notice.
©2001 Zygo Corporation. Zygo Corporation and the Zygo logo are registered trademarks of Zygo Corporation.

SB-0323 4/01 2M

APPENDIX E: VEECO AFM SPECIFICATIONS

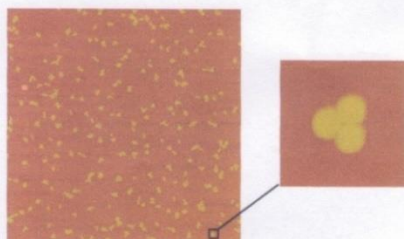


Figure 8: Example of x-y positioning accuracy: real-time zoom and offset to a 2µm area (right) at the lower right corner of a 50µm area (left).

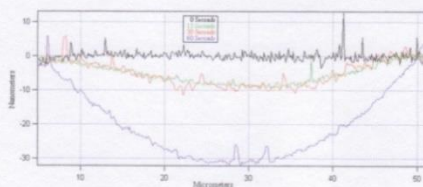
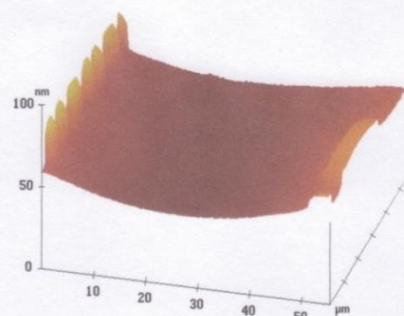


Figure 9: Four cross-sections, taken at the same location on four different SRAM wafers. In the 3D image, the SRAM is on the left edge and an isolated structure is on the right. The dielectric film is flat before CMP, but develops dishing after 15, 30, and 60 seconds of CMP.

Specifications

- **Scan size:**
x-y imaging area 65µm x 65µm; z range 6µm
- **X,Y Integral Linearity:**
0.1% measured on 3µm-pitch VLSI standard with Calibrator Pro™ software
- **Z Differential Linearity:**
1% (based on 180nm measurement)
- **Orthogonality:**
<0.2° x,y
- **Static Repeatability:**
x,y pitch: 3nm (1σ) measured on 3µm pitch VLSI standard with Calibrator Pro software
z: 0.5nm (1σ) measured with 180nm stepheight VLSI standard
- **Noise Level:**
<0.9Å RMS in vertical (z) dimension in acoustic environment of 75dbc white noise. <0.6Å RMS in low vibration, low noise environments (Test condition: surface tracking servo gain set to repeatably resolve 10nm-scale texture on polished silicon wafer surface at scan size of 1µm and scan rate of 2.5Hz)
- **Flatness of x,y plane over 65µm on a level surface:**
x: 10nm
y: 10nm
- **Sidewall angle:**
<86 degrees using FIB probe
- **Full 16-bit resolution on all axes for all scan sizes**

di Digital
Instruments

Veeco
Metrology Group

112 Robin Hill Road
Santa Barbara, California 93117
T: (800) 873-9750
T: (805) 967-1400
F: (805) 967-7717
Email: info@di.com
www.di.com, www.veeco.com

Distributors World Wide

DS12 Rev 2/01

NanoScope is a registered trademark of Veeco Instruments, Inc.
Dimension and TappingMode are trademarks of Veeco Instruments, Inc.
Calibrator Pro software is a trademark of Advanced Surface Microscopy, Indianapolis, IN, USA.

Bob Tench, 03:59 PM 10/1/2003 -0400, Re: Metrology head

To: Bob Tench <Bob.Tench@veeco.com>
 From: Jimmie Miller <jamiller@uncc.edu>
 Subject: Re: Metrology head
 Cc: John Janzer <JJanzer@veeco.com>, mafiddy@uncc.edu, hocken@uncc.edu
 Bcc:
 Attached:

Bob,

Based on our discussions and email, it is apparent that the upgraded system still meets the specifications outlined in the original request for bid and also gives additional capabilities. Therefore I thank you and Veeco for giving us the choice to remain at the cutting edge of dimensional metrology in the scanned probe arena. We willingly accept your offer to install the upgraded head at no additional expense to us.

Thanks again,
 -jimmie

At 12:42 PM 10/1/2003 -0700, you wrote:
 Dear Jim,

Thank you for taking the time to talk with us today. I am glad you are considering letting us upgrade you for free to our newest style Metrology head. As discussed, you will send official confirmation of acceptance in response to this email.

Points of comparison between the old style head that you ordered and the new one we would like to provide.

XY capabilities match for both heads to the specifications you have.

Z range is increased from 8 microns to 15 microns (nominal maximums).
 Z sensor resolution increases by a factor of 2.5. The z sensor is monitored by a 14 bit DAC as you asked about on the second phone call. (not the 16 bit that I mistakenly mentioned on the first.) Resolution = 25 micron / 14 bits.
 Z scanner resolution is controllable to sub-nanometer resolution with the 3 DACs controlling the Z voltage.

At the end of the conversation you asked about how we calibrate the Z sensor. This is done through a two step process. First we use a heterodyne interferometer to set the sensitivity and then we use the microscope and measure and fine tune against a VLSI step-height standard.

I hope this answers all your questions.

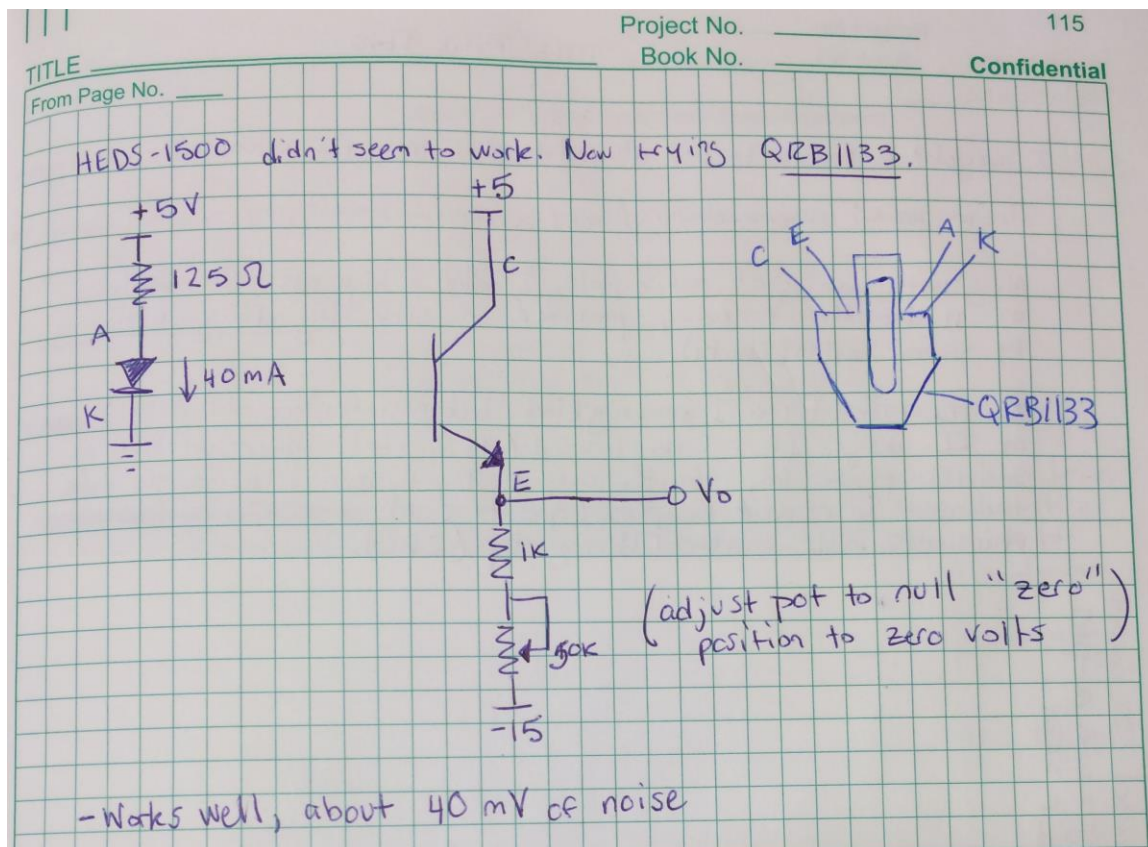
Regards,

BOB

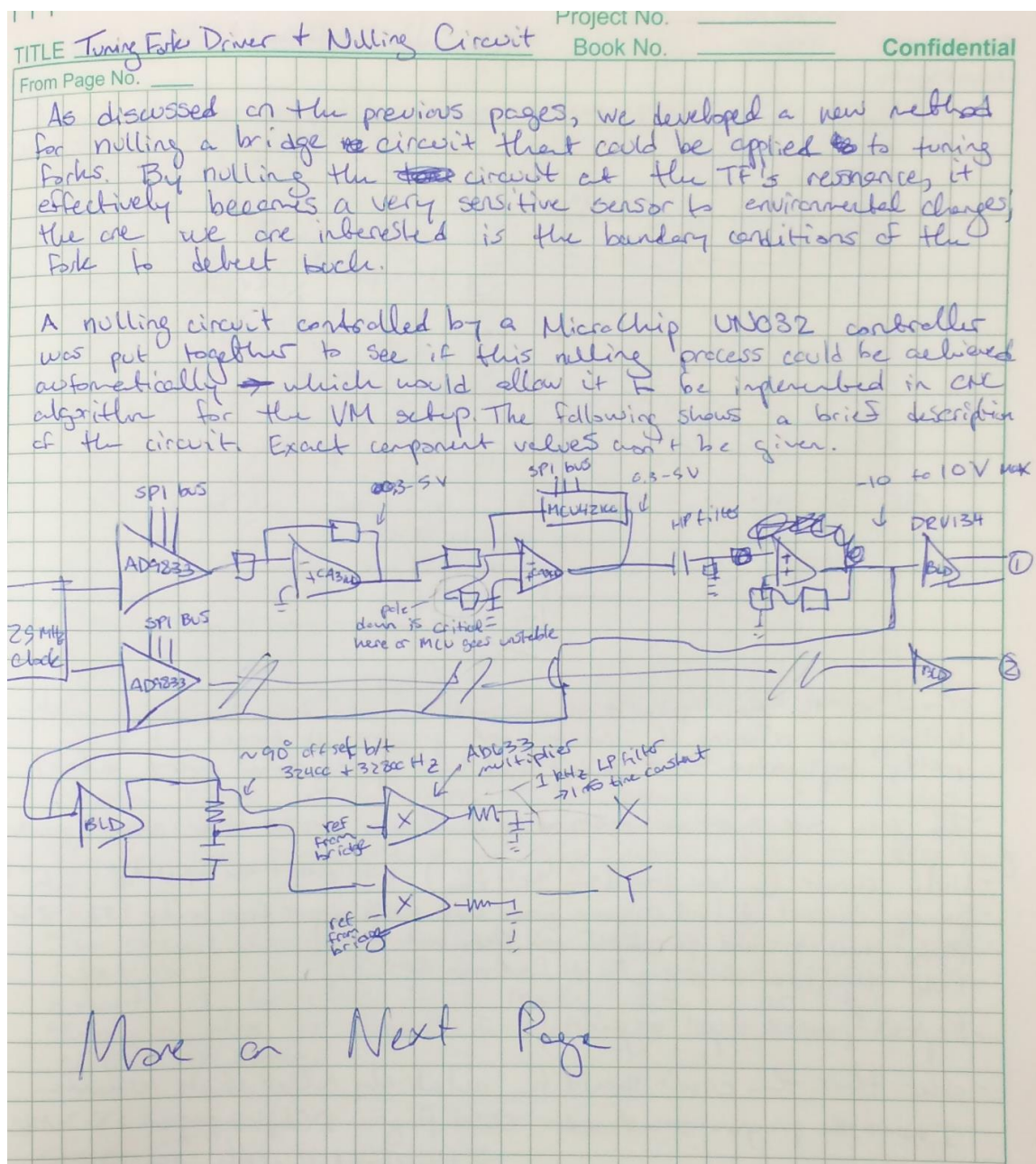
Dr. jimmie miller <http://personal.uncc.edu/jamiller>
 Chief Engineer
 Center for Precision Metrology: www.uncc.edu/cpm
 Cameron Applied Research Center Room 132
 9201 University City Blvd
 UNC Charlotte

APPENDIX F: CIRCUIT DIAGRAMS

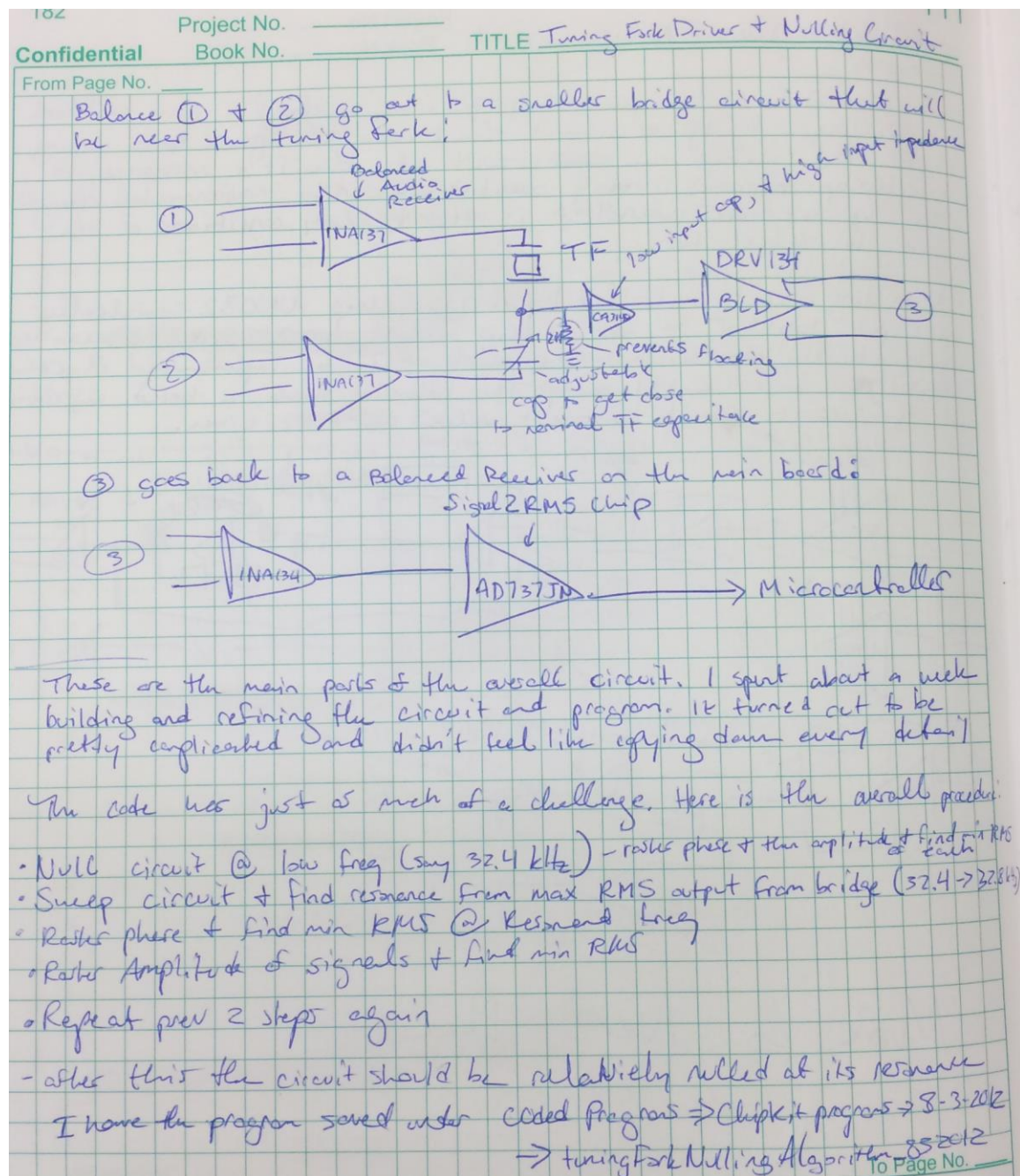
Slurry Depth Measurement Sensor Circuit Diagram: Sheet 1 of 1



Probe-to-workpiece Automated Referencing Circuit Diagram: Sheet 1 of 3

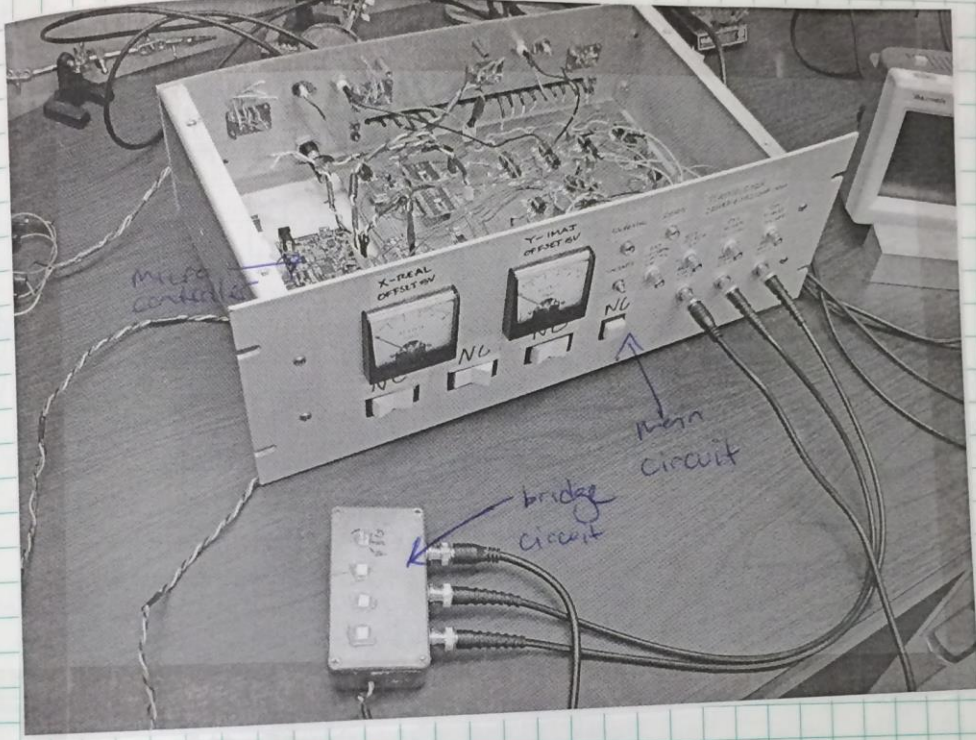


Probe-to-workpiece Automated Referencing Circuit Diagram: Sheet 2 of 3



Probe-to-workpiece Automated Referencing Circuit Diagram: Sheet 3 of 3

TITLE Tuning Fork Driver + Nulling Circuit Project No. 183
 From Page No. Book No. Confidential

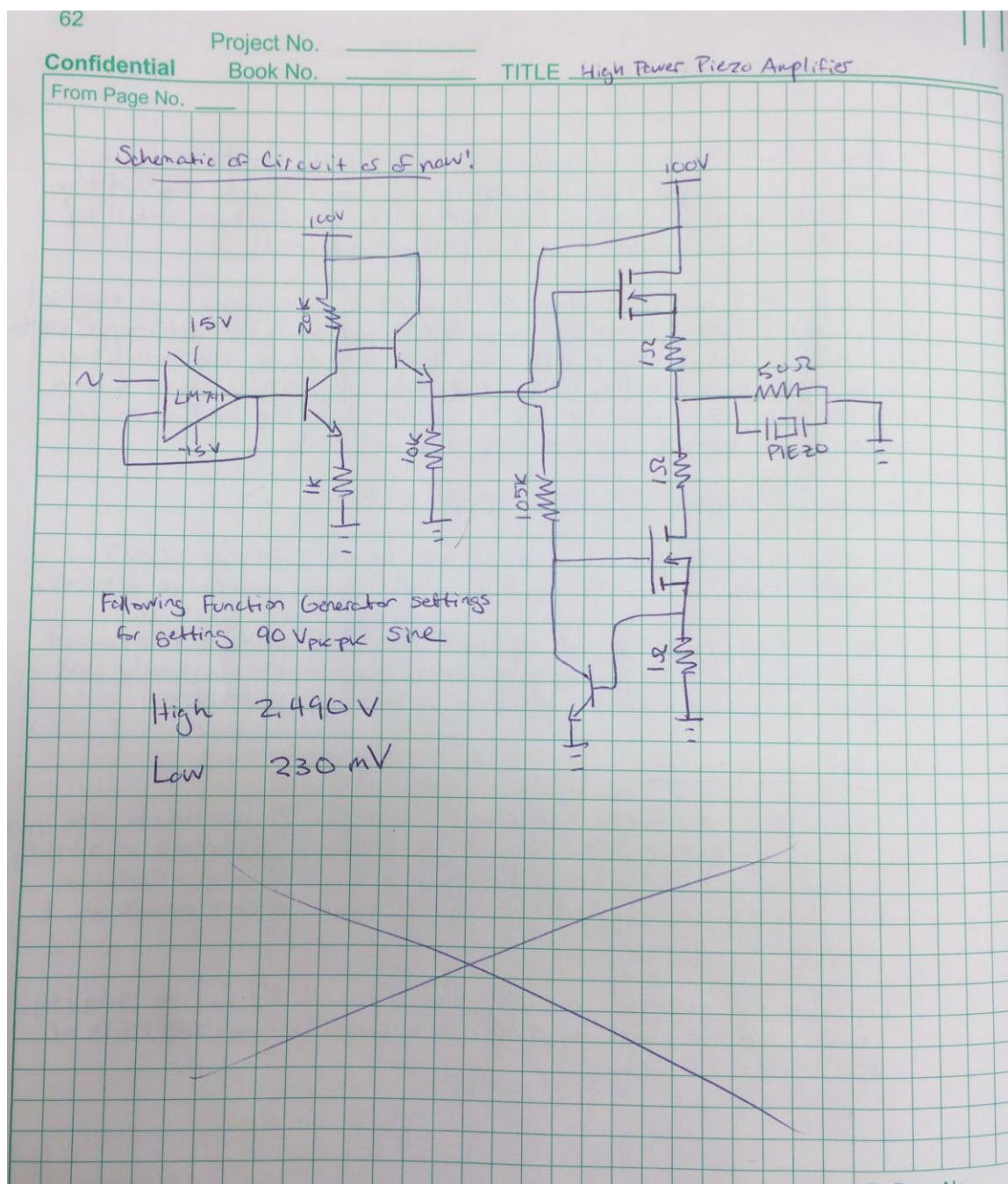


Shown above is an image of the main circuit + bridge circuit discussed on the previous two pages. The box was scrap + came w/ gauges which I used for displaying X + Y.

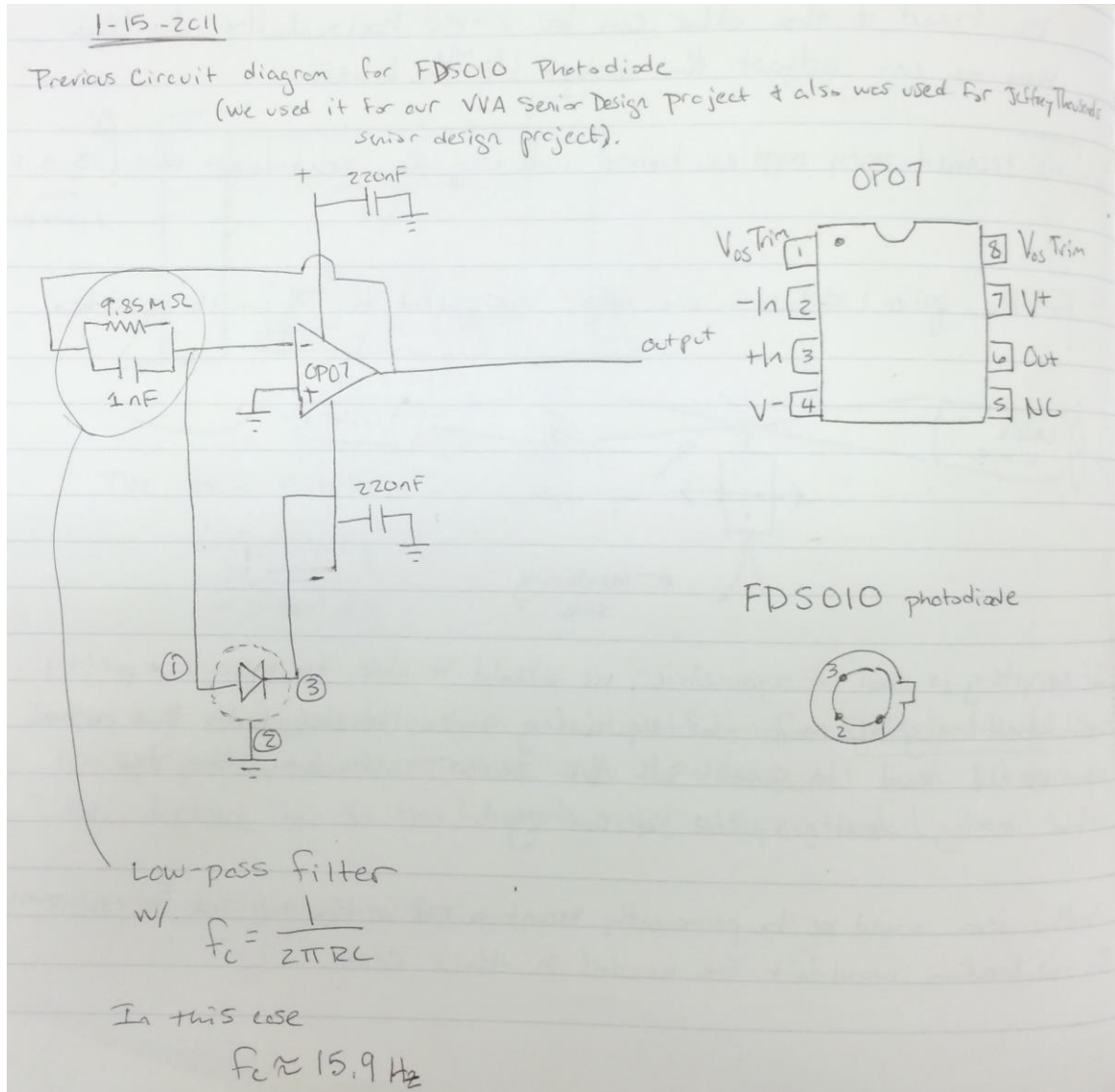
The circuit can be controlled manually or through a digital input it has an LED for when it is calibrating (nulling the circuit) + for when it is ready (done w/ nulling). There is also an output for letting a host know when the circuit is done.

To Page No.

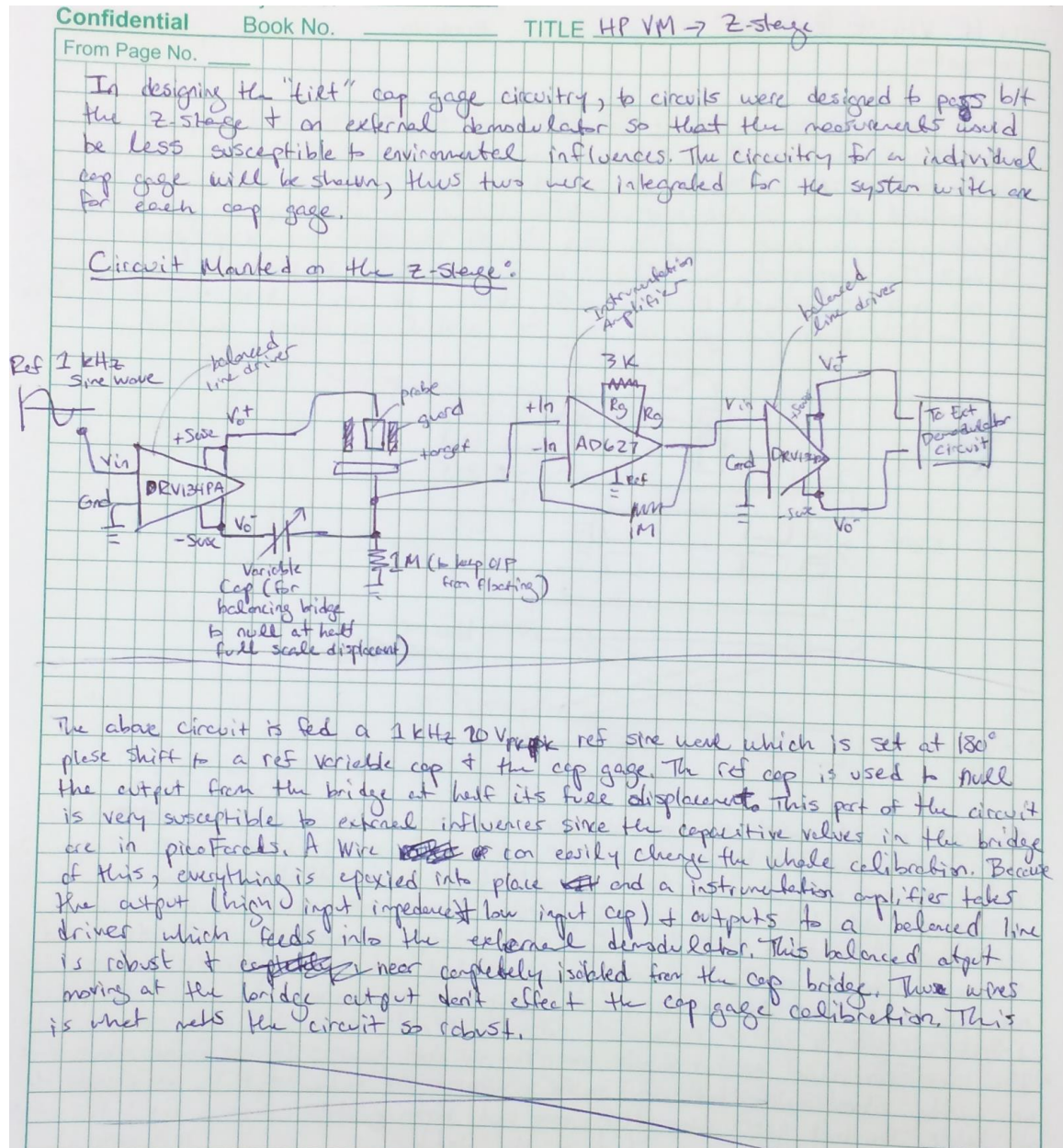
High-Power Capacitive Amplifier Circuit Diagram: Sheet 1 of 1



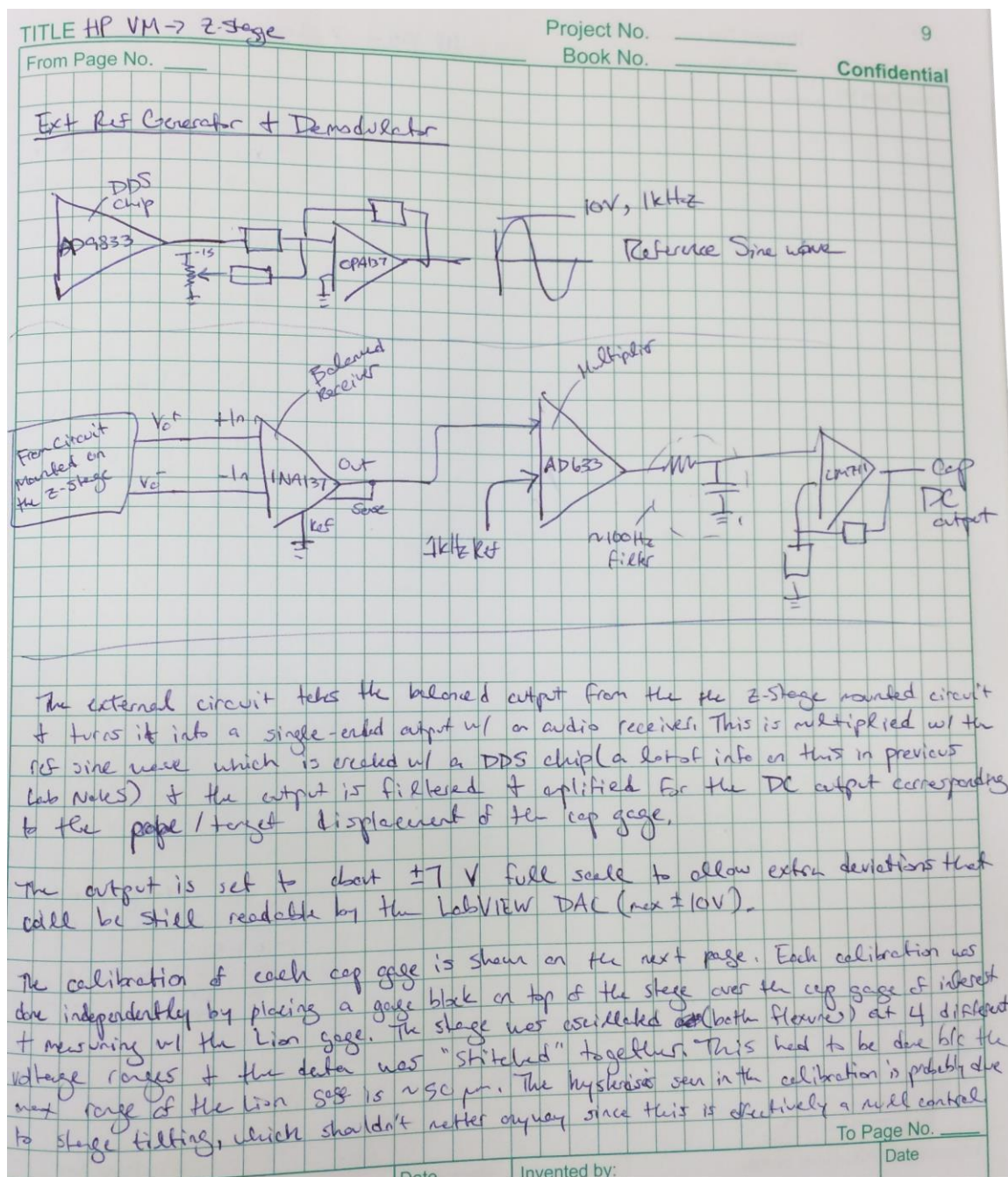
Photodetector Circuit Diagram (for in situ tool measurement system): Sheet 1 of 1



Capacitance Gage Driver and Demodulator Circuit Diagram: Sheet 1 of 2



Capacitance Gage Driver and Demodulator Circuit Diagram: Sheet 2 of 2



APPENDIX G: VORTEX MACHINING OPERATIONAL GUIDELINES

Vortex Machining Guideline for Running an Experiment
Stephen Howard; 12-23-2012

Introduction

This document will provide a general procedure for running a Vortex Machining test on the low-power system located in Duke 140. It is not fully comprehensive, but through revisions should become more helpful in addressing common problems for a first user of the system. I welcome any changes to this document. Whenever a substantial change is made, it would be advisable to update the document, author(s), and date. In this way we can keep track of updates and operational procedures for any future engineers using the system.

Procedure

1. The first step is to turn on all components needed to perform a test. Check to make sure that the host computer and real-time computer are turned on and operating correctly, see Figure 1. The host computer should show the Windows environment operating correctly on the two flat screens located on the workspace desk, and the real-time computer should show no errors on the command screen displayed on the CRT located on the floor to the right of the desk, see Figure 2.

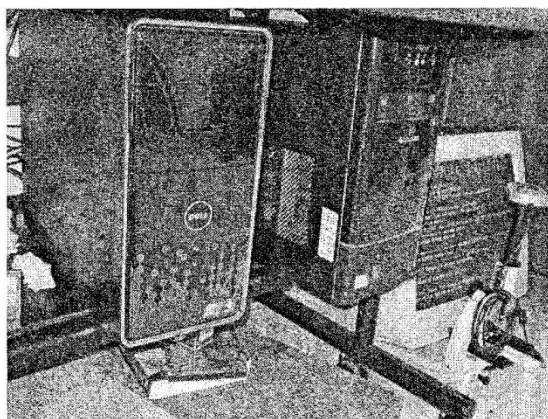


Figure 1: Host on left, real-time on right.

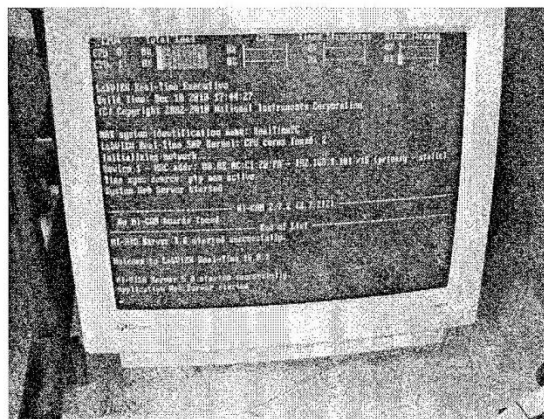


Figure 2: Real-time command screen.

Vortex Machining Guideline for Running an Experiment
Stephen Howard; 12-23-2012

Next check that the PXI (FPGA) system and the two servo motor controllers for the XY stage are turned on. The FPGA should show a green/yellow light next to “power” and “link” labels, see Figure 3. The controllers should show a blinking red message on their display screen, as shown in Figure 4.

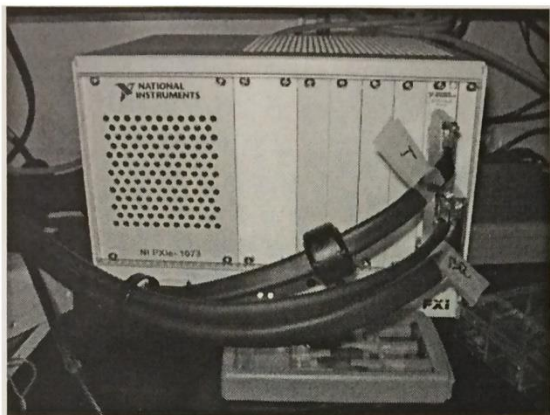


Figure 3: PXI system with green lights.

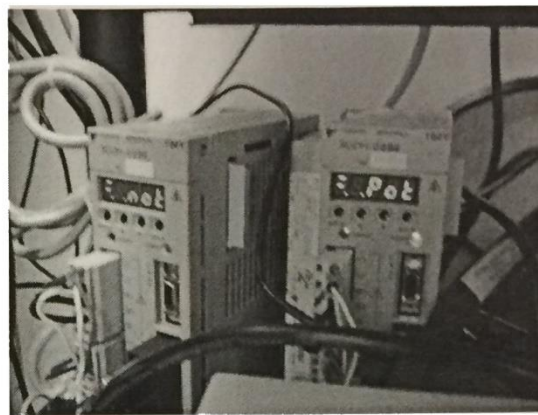


Figure 4: XY stage controllers with LED message.

Next ensure the 3-axis piezo (PZT) controller and Z stage stepper motor controller are turned on. The PZT controller will show green numbers in the display screens for all 3 axes and the stepper controller will show a light on the power button and a number in the display screen, see Figure 5.

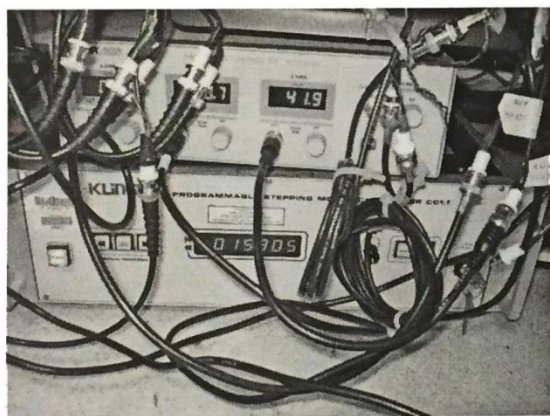


Figure 5: PZT controller with numbers in display screens shown on top. Z axis stepper controller with light on power button and number in display screen on bottom.

Lastly, check that the two AAK power supplies are powered on, the EFD Ultimus unit is powered on, and that there is fluid in the auto syringe. The AAK power supplies have switches that should be in the upward position and should show a red indicator light when powered on, see Figure 6. The EFD Ultimus should show a display screen with operating parameters when powered on, see Figure 7.

Vortex Machining Guideline for Running an Experiment
 Stephen Howard; 12-23-2012

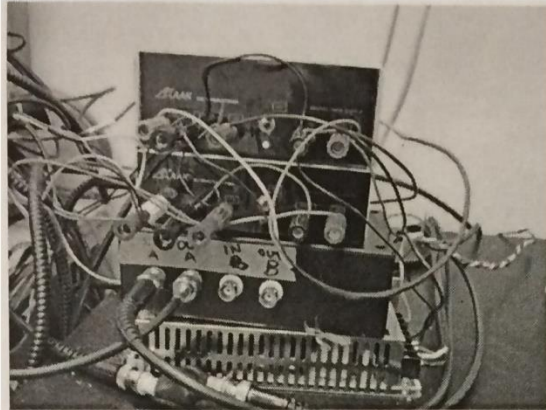


Figure 6: AAK power supplies that are ON.



Figure 7: EFD Ultimus powered on, see display.

2. After all components are turned on, we now need to boot up the software interface designed to run a Vortex Machining test. The first step is to ensure that the computer “sees” the Klinger Z-axis stepper controller (which is connected via a USB-GPIB connection). To do this, open Measurement & Automation Explorer (MAX) on the host desktop. Under “My System” on the project tree located on the left of the MAX window, click to expand the “Devices and Interfaces” tab. Then click on the “GPIB0 (GPIB-USB-HS)” icon. On the middle-right of the MAX window will be a toolbar. Click on “Scan for Instruments” tab once or twice and make sure the instrument shows up at the bottom of the screen. “Identification” under the instrument listing should show the same number as printed on the front of the Klinger Motor Controller, refer to Figures 5 and 8.

Vortex Machining Guideline for Running an Experiment

Stephen Howard; 12-23-2012

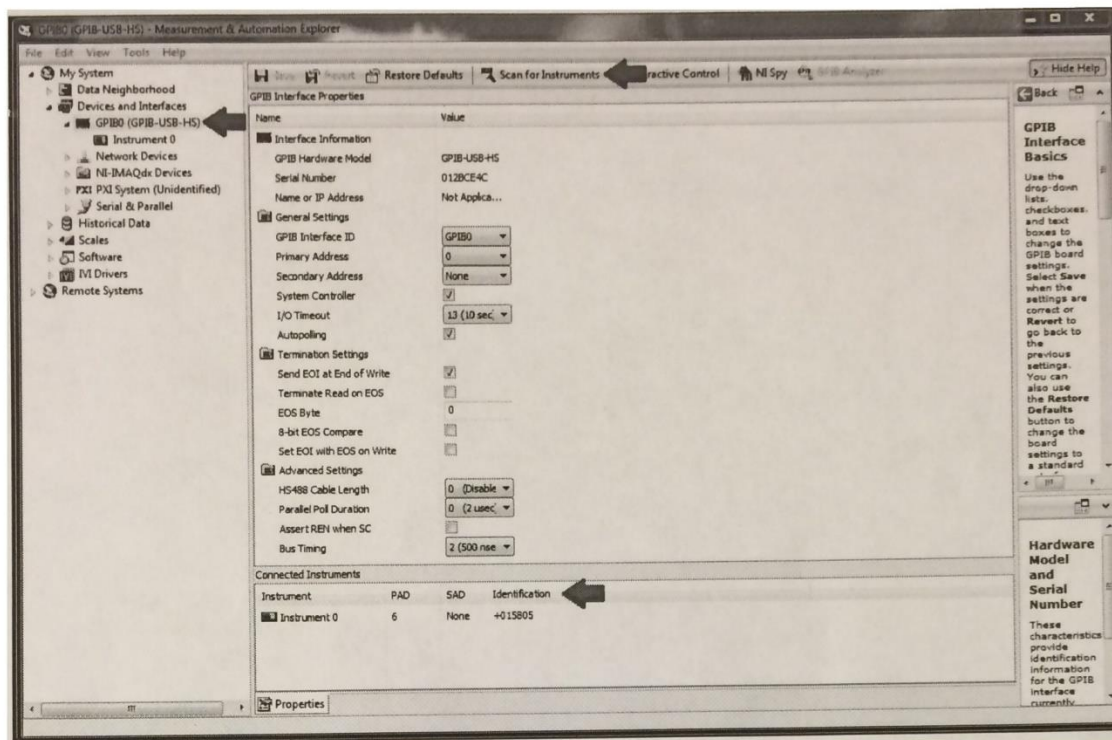


Figure 8: Shows MAX window and arrows associated with making sure the host computer is communicating with the Klinger Motor Controller.

Next open up LabVIEW 2010 SP1 using the shortcut located on the desktop. Go to File >> Open Project >> Local Disk (C:) >> Vortex Machining >> LabVIEW >> Projects >> VortexProject >> VortexMachining.lvproj. This will open up the LabVIEW realtime project associated with running a Vortex Machining test. The "Project Explorer" window should now be on the host computer screen. For both "RealTimePC (192.168.1.101)" and "ECDCrioTest2 (192.168.1.104)" icons in the tree, right click the icons and left click "Connect", see Figure 9. The "RealTimePC" (which is the real-time computer) should deploy within a couple seconds. The "ECDCrioTest2" (which is the compact RIO used to read the eddy-current, z displacement gauge) may take up to a minute to connect. If the real-time computer fails to connect, make sure that it is turned on and showing no error on the display screen, and make sure that the Ethernet cable from the real-time to host computer is secured on both ends. If the compact RIO fails to connect, make sure it is on (it should be at all times, you can see a yellow-green ON light next to a number 1 indicating power on the device) or try pressing the reset with a pencil or pen. Then check that the Ethernet cable between it and the host computer is secure on both ends (this seems to always be the issue when it fails to connect). When both devices are connected, you should see a little green indicator on the "Project Explorer" turn a shade brighter; Figure 9 shows this with the real-time connected and the compact RIO not connected.

Vortex Machining Guideline for Running an Experiment
 Stephen Howard; 12-23-2012

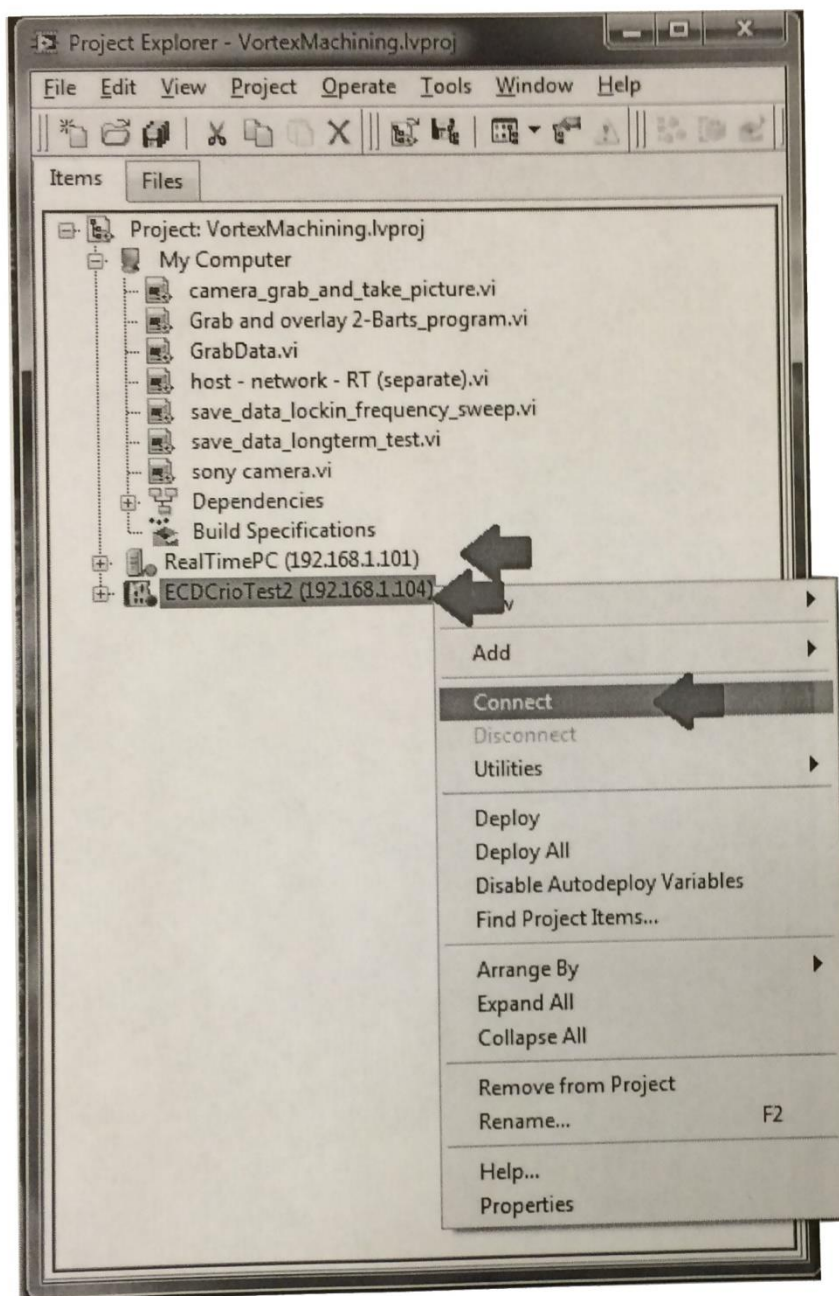


Figure 9: Showing icons to click in "Project Explorer" to make sure both the real-time computer and compact RIO are connected to the host computer.

The next step is to setup and run the software for the eddy current gage. In the "Project Explorer" under the "ECDRIOTest2 (192.168.1.104)" icon, expand "Chassis (cRIO-9111)" then "FPGA Target (RIO0, cRIO-9111)" and double click the VI entitled "ECD14x Clock and FIFO.vi". Once the VI is opened, run the

Vortex Machining Guideline for Running an Experiment
Stephen Howard; 12-23-2012

program by clicking the arrow button. Once the program is running, you can close and exit the program (by clicking the red X) because it will continue to run on the FPGA architecture. Then the VI "ECD14x Basic Demo.vi" (located under the "Chassis (cRIO-9111)" classification) can be open and run. Do not close this program, just minimize it. Once this has been done, the eddy current gage should be being read by the compact RIO. See Figure 10 for images of the locations of the VI's previously described.

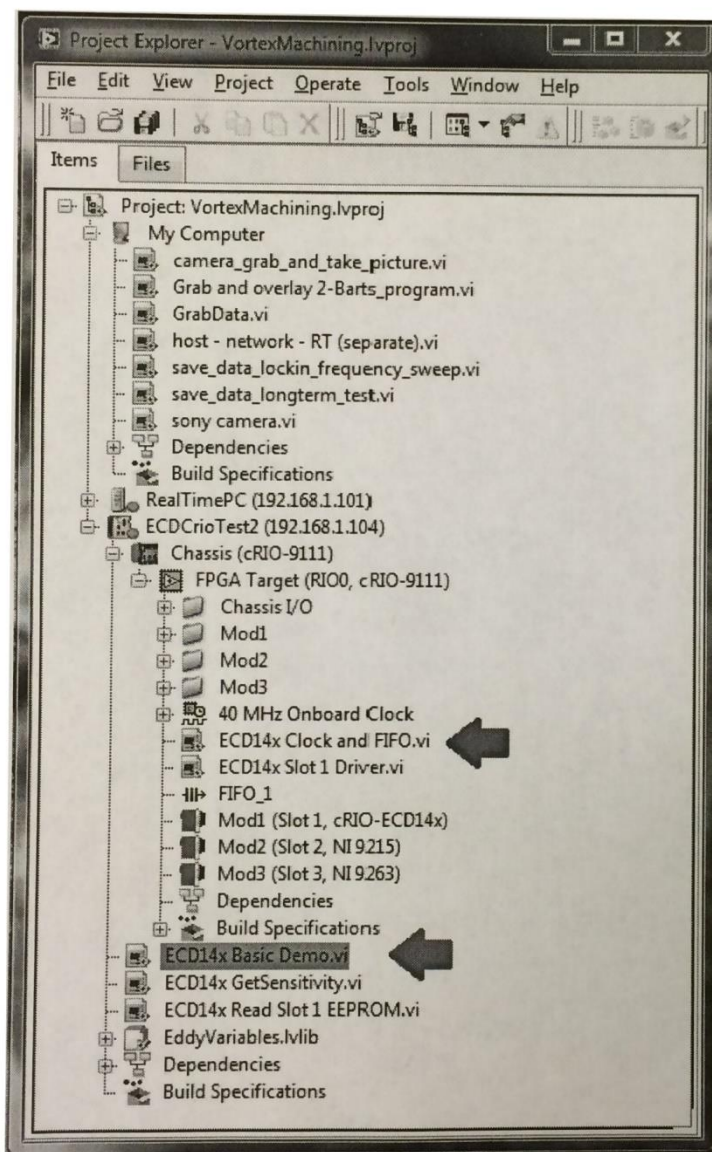


Figure 10: Shows locations of ECD14x Clock and FIFO.vi and ECD14x Basic Demo.vi under "Project Explorer."

Vortex Machining Guideline for Running an Experiment
Stephen Howard; 12-23-2012

Next, open the FPGA program that controls the inputs/outputs from the R-series card in the PXI. Under the "Project Explorer" expand "RealTimePC (192.168.1.101)", then "FPGA Target 2 (RIO0, PXI-7851R)", and then open and run "FPGA_lockin_rev5.vi", see Figure 11. This will allow all the digital and analog inputs and outputs to be read by the FPGA computer, and will also run the lock-in/demodulation routine which is used for analyzing and phase-locking to the tuning fork probes. Once this program is run you can exit out as it will keep running since it is on the FPGA.

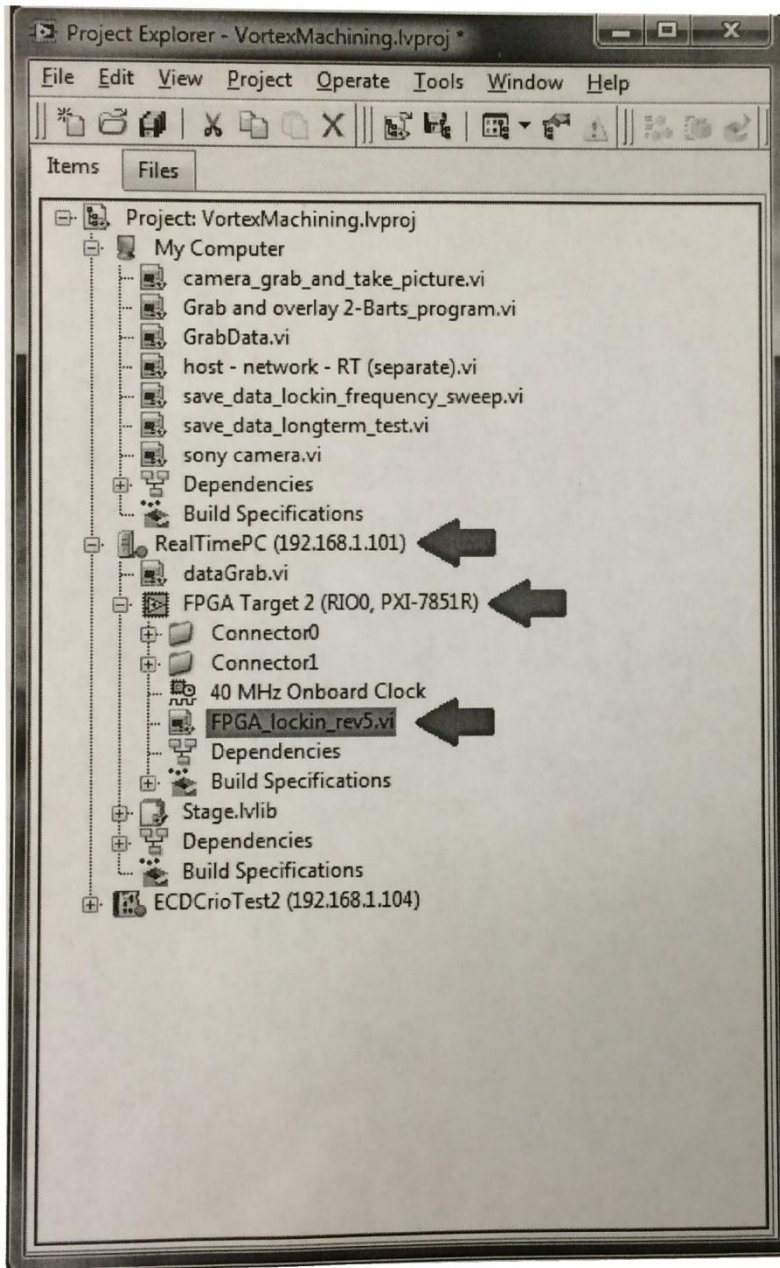
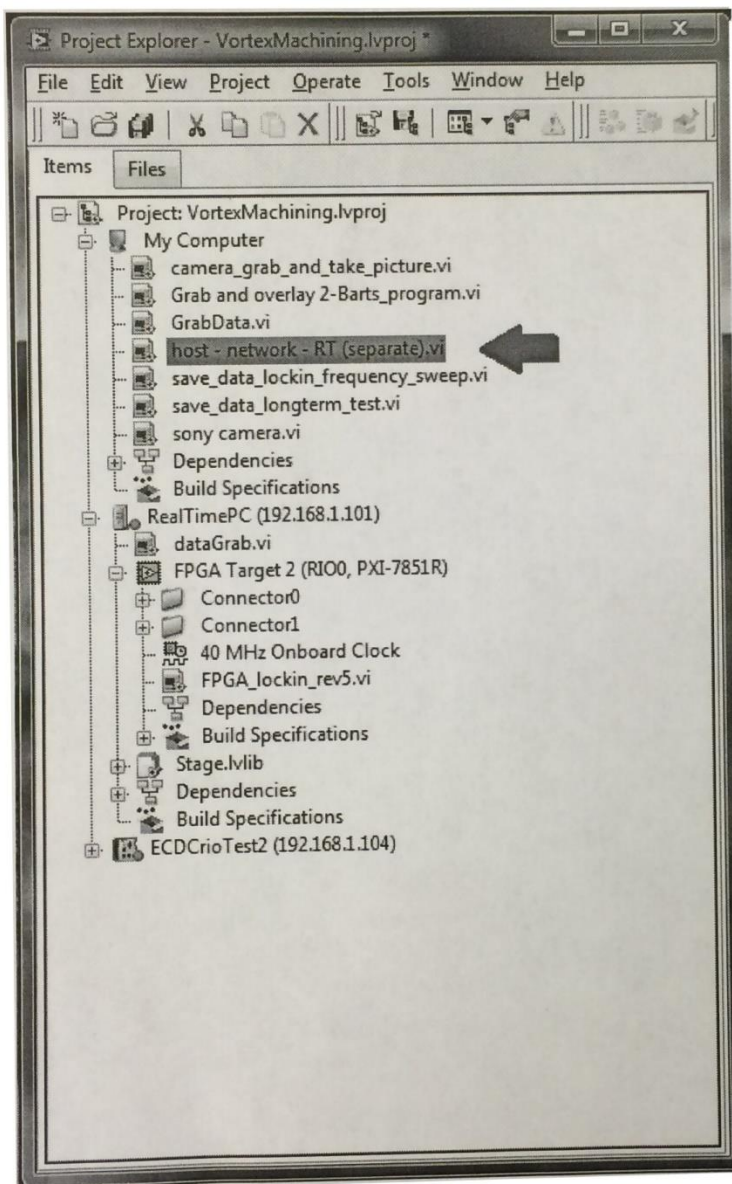


Figure 11: Shows location of FPGA program within "Project Explorer."

Vortex Machining Guideline for Running an Experiment
Stephen Howard; 12-23-2012

The next step is to open a program on the host computer that will relay the Eddy Current Gage reading, CNC toolpath, and communication with the Klinger Motor Controller to the real-time computer for control. Under the "Project Explorer", expand "My Computer" and then open "host - network - RT (separate).vi", see Figure 12. When you run the program, it will first prompt you to open a file relating to the CNC toolpath. Since we have not yet identified locations where we want to machine, it doesn't really matter which file you pick. However, I usually pick an old toolpath file to avoid confusing the program. The toolpath file will be a tab delimited text file saved from the Excel master sheet entitled "CNC_Excel_template" which is located on the host computer desktop. Do not exit out of the "host - network - RT (separate).vi" program, just minimize.



Vortex Machining Guideline for Running an Experiment
Stephen Howard; 12-23-2012

Figure 12: Location of "host – network – RT (separate).vi"

Finally, we now open the main Vortex Machining control program that is compiled and run on the real-time computer. Under the "Project Explorer" expand "RealTimePC (192.168.1.101)" then "Stage.lvlib" then "Stage Control", then open "Stage.vi", see Figure 13. For some reason, in order for this program to startup and run for the first time, a program parameter must be reset in the LabVIEW block diagram so the program can re-save and compile. I usually just go to a "constant number" box and re-type in the same number that it originally had in the box, see Figure 14. Now run the program. Do not exit out of this program, this will be the main program used to control the Vortex Machining process.

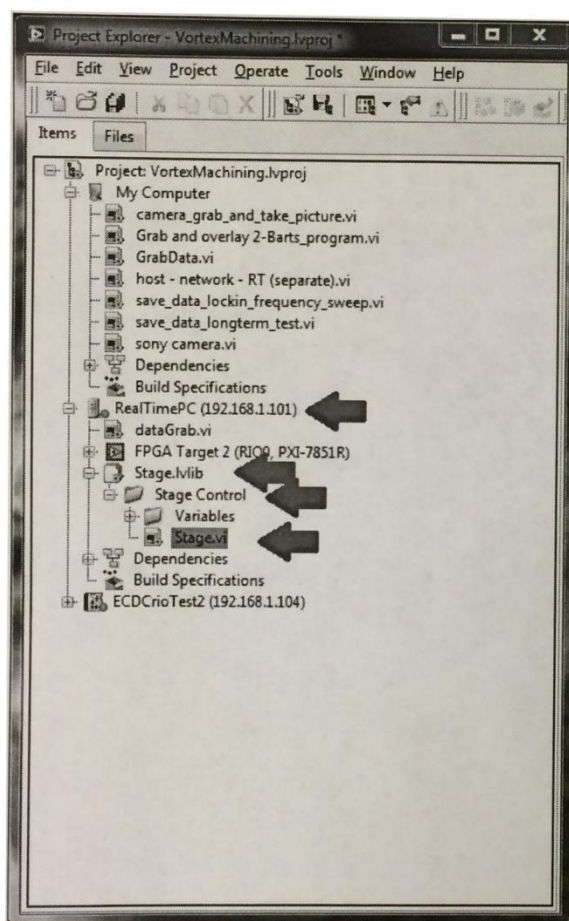


Figure 13: Location of "stage.vi"

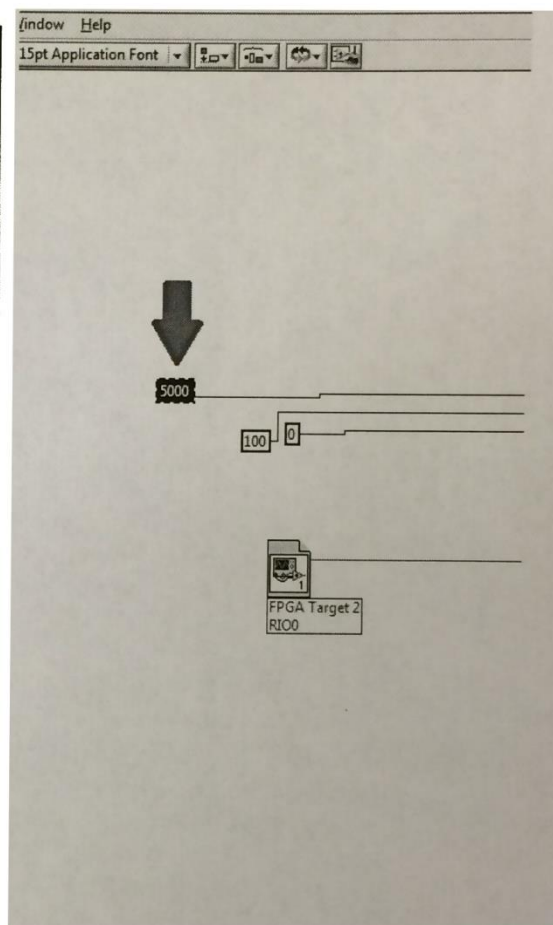


Figure 14: Re-set number box.

Vortex Machining Guideline for Running an Experiment
Stephen Howard; 12-23-2012

3. Now that the system is fully running, it is time to set everything up for a test. It is assumed at this point that the operator/engineer will be running a machining test on multiple spots on a silicon workpiece, but the overall setup strategy can be used for other configurations as well. Note that if needed, the operator should first measure the probe under a microscope and save any data before setting it up for a test. When the probe is in position and used to set up a test, it should not be removed until after the test is finished. Figure 15 shows the positions of the probe, workpiece, workpiece holder, auto syringe, and reflective sensor. All of these components, except for the workpiece and auto syringe, are kinematically mounted so notice their positions as the image shows where they are meant to be placed. The auto syringe position is less critical, however, the position shown works well as of this writing. The workpiece should be bonded to a glass stack in the workpiece holder in three positions with 5 minute epoxy and should be allowed to dry for at least 2 hours before any test or test setup is attempted. I find it most convenient to go ahead and bond the workpiece directly after a test is finished so it will be ready for the next experiment. I usually check the position of the probe fiber relative to the workpiece first, then bond it in place thereby ensuring that there is enough room to machine multiple spots in a single test (i.e. glue sample so that fiber is has at least 2 by 2 mm region to move along the workpiece).

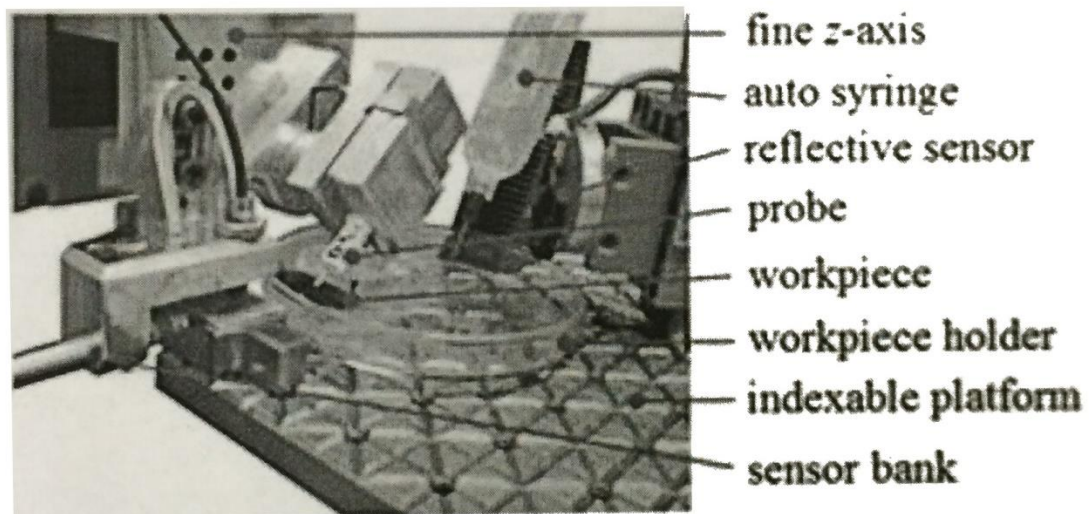


Figure 15: Location of hardware for Vortex Machining test.

The next step is to decide on the xy toolpath for the multiple machining locations and record this in the Test Records Template, see the appendix. Now in the main control program, "Stage.vi", set x and y desired positions to the start position you decided on. Set the z desired position to some spot safely above the silicon surface. Then turn on the PID for x, y, and z. Once the system has arrived at the start position with a low control error (less than 1 μm), find the frequency pertaining to the resonance of the probe.

Vortex Machining Guideline for Running an Experiment
Stephen Howard; 12-23-2012

Turn on the program entitle "sony camera.vi" which is located under the "My Computer" tab in the "Project Explorer." Running this program allows you to see the image captured by the sony camera. Turn on the cold lights and arrange them so that the end of the fiber is imaged. Oscillating the probe at its resonance, slowly translate the probe towards the sample. When it touches, you should be able to visibly see instability with a repeatability of $\pm 1 \mu\text{m}$. I usually repeat this touch process several times to ensure that I found the touch position with a high level of confidence. Record this touch position on the Test Records Template. Now raise the probe 3 to 6 μm , and translate the system to the next position. Repeat this process finding the touch position for each position where the operator intends to machine. After finding the last touch position, I would bring the system back to the start position and check the touch position again to make sure that touch at the start position is the same as when you found it before.

After verifying all the z touch positions and recording them, decide on machining positions (for example 20 μm above the touch position) and dwell times (for example 30 minutes) and record these into the test records template. Open the "CNC_Excel_template" on the desktop and using this template, enter in the CNC toolpath (x,y, z positions, and dwell times). Save as a tab delimited text file to the desktop to be used for running the experiment.

Stop the "Stage.vi" and "host – network – RT (separate).vi" programs. Now restart the "host – network – RT (separate).vi" program and pick the new CNC file you just created when the dialog box comes up (see previous paragraph). Now restart the "Stage.vi" program.

Make sure that the x and y PID is on and that the desired position corresponds to the start position in the CNC toolpath file you just uploaded. Make the desired z position approximately 1200 – 1300 μm above the z touch point for the start position and turn on the PID for the z axis.

After the system has settled at the x, y, and z position previously set, go to the lock-in tab in the main control program and run a frequency sweep around where you know the resonance frequency to be (I usually run the sweep 50 Hz before and 50 Hz after the resonant frequency). Open up "save_data_lockin_frequency_sweep.vi" under "My Computer" in the "Project Explorer." Run the program to save the frequency sweep of the probe in air, before the machining test.

The next step is to add slurry to the petri dish (or workpiece holder). Using a pipet, slowly add slurry (making sure to "wet" areas around the workpiece) until the slurry fills over the workpiece. Lower the z-axis until the probe fiber makes contact with the slurry, and record this position. The goal here is to fill the slurry to approximately 1200 (± 100) μm above the workpiece surface. Now lower the z-axis to the start machining position that was indicated in the CNC worksheet (for example 20 μm above the start touch position).

Record and save another frequency sweep, as indicated two paragraphs previous to this, but this time in slurry and before the test. Find the resonant frequency, or more importantly the phase at the probe's resonance, and input this phase into the PLL sections "Desired Theta" under the Lock-In tab in the main control program. Turn the PLL switch to the upward position (turn PLL on).

Vortex Machining Guideline for Running an Experiment
Stephen Howard; 12-23-2012

The next step is to setup the slurry depth sensor, which should already be in place over the petri dish (it is important to do this before so you don't move the workpiece after already recording all the machining positions). Make sure that the cold light is turned off as this will interfere with the fluid height sensor. Under the Fluid Height Controls tab in the main control program, enter "3" as the desired height. Carefully turn the micrometer screw on the sensor assembly until the graph on the screen reads close to 3 V. Now turn the Slurry Height Control switch up (turn on) to initiate the control algorithm.

Now everything should be ready to begin the test. In fact, you are already machining in the 1st position, which is why we generally through this data point out in the end. Open the program "save_data_longterm_test.vi" under "My Computer" in the "Project Explorer." Run this program. This will start the reference time used to run the CNC algorithm. After waiting 5 to 10 seconds to make sure this program started successfully, go to the main control program ("Stage.vi") and under the CNC tab turn on the CNC algorithm. The test should now initiate and will run through all the positions that were input into the CNC spreadsheet. When the test ends, a green indicator light will turn on under the CNC tab, and the z-axis will move up about 200 um.

4. After a test has ended, there is generally some additional data that should be collected. The "save_data_longterm_test.vi" should be stopped and this long-term data should be saved as a record in the appropriate location. A frequency sweep should be run with the probe in slurry and in air after the test. Additionally, it would be a good idea to measure the probe visually after the test, to see how much the fiber amplitude has changed.

All programs can then be stopped and the user should exit LabVIEW. The petri dish should be cleaned out, and the sample carefully removed from the workpiece holder. A new sample should be bonded in place for a future test.

Vortex Machining Test Records Template

Operator(s): Stephen Howard, Jeffrey Hunt Date: 12-23-2012

Machining locations, stand-off, dwell time:

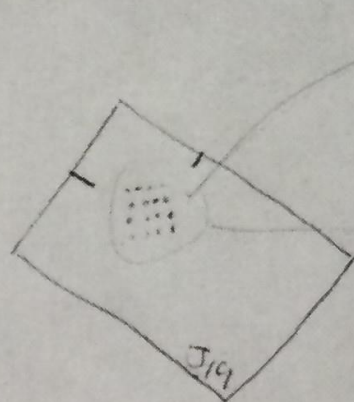
Spot Number	X position (μm)	Y position (μm)	Z contact position (μm)	Z machining position (μm)	Dwell Time (minutes)
1	-300	-200	376.5	396.5	30
2	-200	-200	376.5	396.5	
3	-100	-200	376	396	
4	0	-200	375.5	395.5	
5	0	-100	377	397	
6	-100	-100	378	398	
7	-200	-100	378	398	
8	-300	-100	378	398	
9	-300	0	379	399	
10	-200	0	381	401	
11	-100	0	381	401	
12	0	0	380.5	400.5	
13	0	100	380.5	400.5	
14	-100	100	382	402	
15	-200	100	382	402	
16	-300	100	382	402	

Sample identifier:

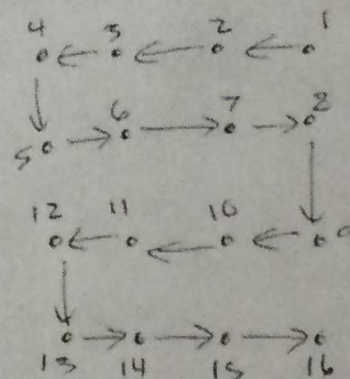
J19

Sample description:

Sample sketch:



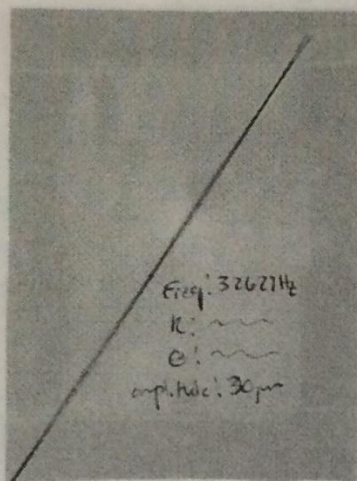
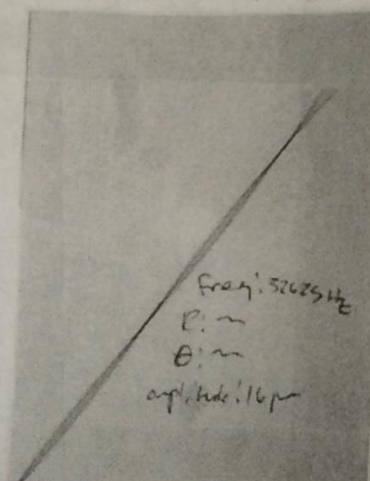
Individual spot orientation:



Vortex Machining Test Records Template

Operator(s): Stephen Howard, Jeffrey HuntDate: 12-23-2012Workpiece material: Silicon <100>Slurry composition: Mixture of 50% 0.05 μ m colloidal Alumina (Allied High-Tech Products, Lot: 124027612DA) + water from reverse filtration, mixed on 12-15-102.Probe identifier: D6

Probe description:

Before image, amplitude, frequency, R, θ :After test image, amplitude, frequency, R, θ :EFD setup parameters (when unit is not provided impulse): 0.002 ^{first} shot, (6.2 psi)
0.0 mH₂O (vacuum), 21 gauge (purple) syring tipEFD null voltage (default 3 V when using 0.05 Alumina): 3 V

Slurry surface (measured with tip of probe fiber):

Before test: 1640 μ mAfter test: 1500 μ m

Resonance in slurry, at initial machining position, before beginning test:

Frequency: 32622Magnitude (R): 2.22Phase (θ): 52°

Vortex Machining Test Records Template

Operator(s): Stephen Huest, Jeffrey HartDate: 12-23-2012Probe phase-locked to: 52°Started running test: 12:13 PMEnded test: 8:13 PM

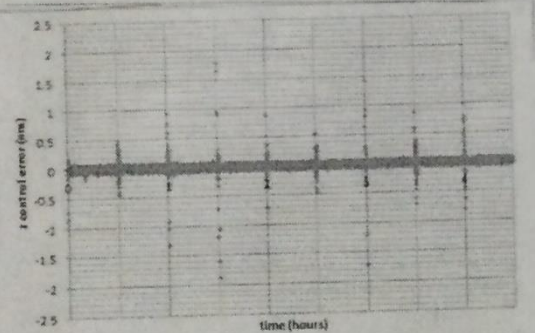
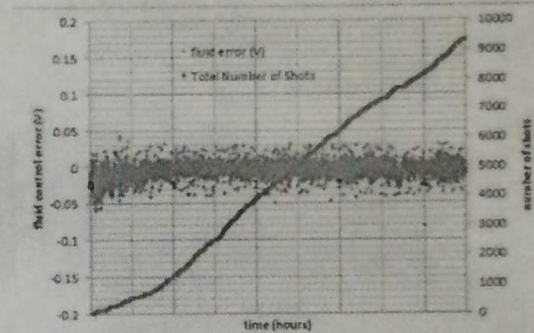
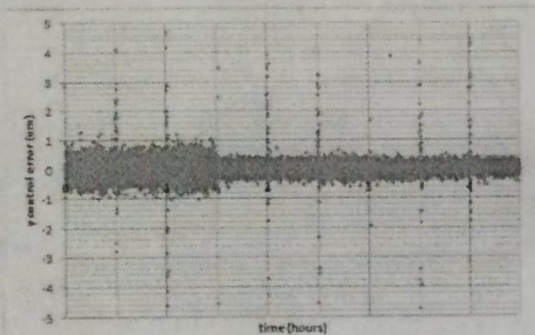
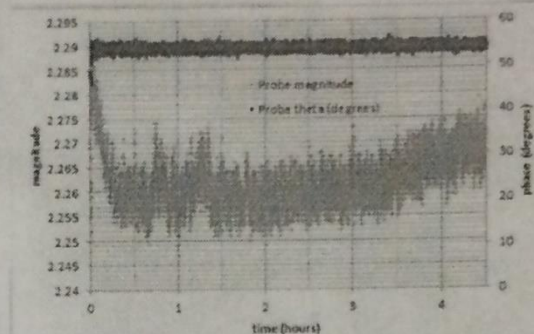
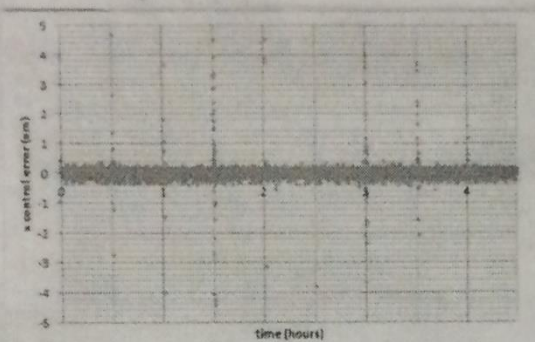
Additional notes:

- slurry compensation overshoot in beginning of test
- took about 5 min to set up at spot 1, might throw this data point out
- noticed aggregation of slurry @ 4:30 pm
- did not shake up slurry before adding to petri dish; there was aggregates at bottom & we thought less would precipitate during test if we didn't shake up

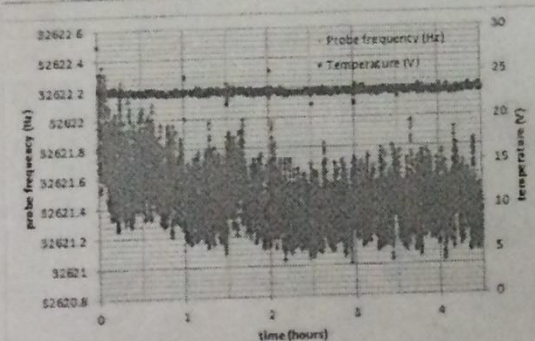
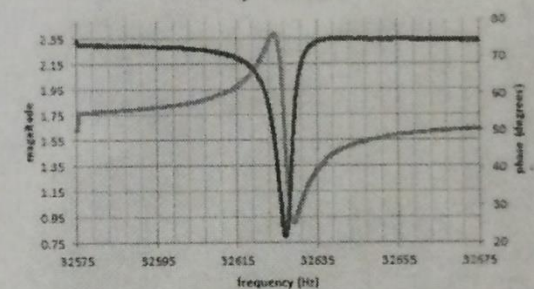
Vortex Machining Test Records Template

Operator(s): Sebastian, Jeffrey HuntDate: 12-23-2012

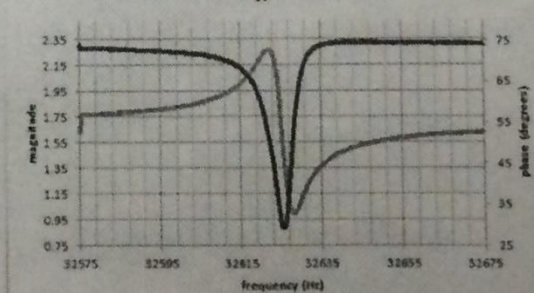
Testing data (x, y, and z control error; probe frequency, magnitude, and phase; fluid control error and total number of impulses; temperature; probe frequency sweeps before and after testing, in slurry and in air):



In Air, After Test



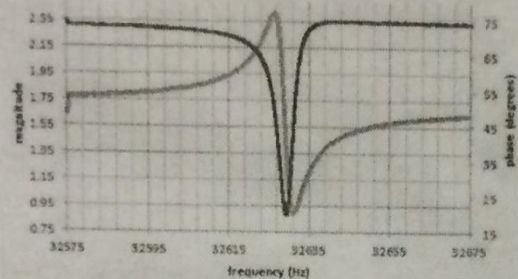
In slurry, after test



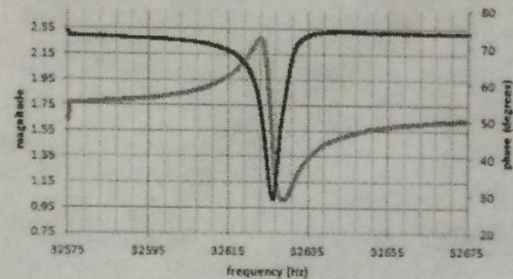
Vortex Machining Test Records Template

Operator(s): Stephen Howard, Jeffrey HuntDate: 12-23-2012

In air, before test



In slurry, before test



APPENDIX H: MATLAB CODE FOR DATA ANALYSIS PACKAGE

```
% Program designed to conduct surface metrology of Vortex Machining
% footprints. Designed to work with both NewView 5000 SWLI dat files and
% XYZ data from Veeco AFM.
```

```
% Created by Stephen Howard, last revised January 2012
```

```
close all; clear all; clc %clear memory, figures
```

```
% % Program dialogue box for measurement type.
```

```
prompt={'What type of measurement file would you like to analyze?
(SWLI/AFM)'};
```

```
name='Type of Measurement File';
```

```
numlines=1;
```

```
defaultanswer={'swli'};%default answers
```

```
options.Resize='on';
```

```
options.WindowStyle='normal';
```

```
options.Interpreter='tex';
```

```
answer=inputdlg(prompt,name,numlines,defaultanswer,options); %read in
%answers
```

```
%naming and converting answers into appropriate data type
```

```
measurementtype=char(answer(1,1));%converting filename into a string
```

```
condmeasurementtype=strcmpi(measurementtype,'SWLI');
```

```
if condmeasurementtype==1
```

```
% % Program dialogue box for inputting SWLI parameters.
```

```
prompt={'Filename with extension (has to be .dat)'};
```

```
name='SWLI File Information';
```

```
numlines=1;
```

```
defaultanswer={'sample_E_spot_2_50x_2xZoom.dat'};%default answers
```

```
options.Resize='on';
```

```
options.WindowStyle='normal';
```

```
options.Interpreter='tex';
```

```
answer=inputdlg(prompt,name,numlines,defaultanswer,options); %read in
%answers
```

```
%naming and converting answers into appropriate data type
```

```
filename=char(answer(1,1));%converting filename into a string
```

```
%%%%%%Read full sized map, read in data file in .dat format. References
%%%%%%file ReadMetroProFile that was provided by Dr. Evans.
```

```

lError=0;
%DatInFileName=strcat(filename, '.dat');
DatInFileName=filename;

[lError,
InfoHeader, IntensityMap, PhaseMap]=ReadMetroProFile(DatInFileName);%read
PhaseMap=PhaseMap.*10^9; %in nm

% converts NaN's in PhaseMap matrix to zeros;
PhaseMap(isnan(PhaseMap))=0;

xpxl=double(InfoHeader.PhaseWidth);% retrieving number of x pixels from
%.dat file

ypxl=double(InfoHeader.PhaseHeight);%retrieving number of y pixels from
%.dat file

%% This section of code is commented out on purpose. It was made to
%% test the accuracy of the volumetric integral algorithm by making a
test
%% square.%watch out for loop below that replaces NaN's with average
of Z.
%% This can cause errors
%%
% PhaseMap=0.5*ones(600,600);
%
% for incr1=201:400
%
%     for incr2=201:400
%
%         PhaseMap(incr1,incr2)=-0.5;
%
%     end
%
% end
%
% xpxl=600;
% ypxl=600;
% %objective=1;
% %zoom=12;
% xfov=600;
% yfov=600;
% pixelspacing = 1;
%
% % Test code

%% This section of code is commented out on purpose. It was made to
%test
%% the accuracy of the volumetric integral algorithm by making a test

```

```

% % hemisphere. The program replaces any complex numbers calculated in
%the
% % algorithm with zeros. The loop below that replaces zeros with
%avgzcalc
% % and the xfov and yfov calculations should be commented out when
%running
% % this or the square hole validation routine.
%
% PhaseMap=zeros(600,600);
%
% for incr1=201:400
%
%     for incr2=201:400
%
%         PhaseMap(incr1,incr2)=-1000*sqrt(2500-((incr1-300)^2)-
%((incr2-300)^2));
%
%         checkreality=isreal(PhaseMap(incr1,incr2));
%
%         if checkreality==0
%
%             PhaseMap(incr1,incr2)=0;
%
%         else
%
%             PhaseMap(incr1,incr2)=PhaseMap(incr1,incr2);
%
%         end
%
%     end
%
% end
%
% xpxl=600;
% ypxl=600;
% objective=1;
% zoom=12;
% xfov=600;
% yfov=600;
%
% % Test Code

```

```

pixelspacing=InfoHeader.CameraRes*10^6; %pixel spacing in micrometers
%from .dat opening program

```

```

xfov=xpxl*pixelspacing;
yfov=ypxl*pixelspacing;

```

```

else

```

```

    % % Program dialogue box for inputting AFM parameters.

```

```

prompt={'Filename with extension (probably .txt)', 'Data resolution
(128, 256, 512)', 'Scan size (in \mum)'};
name='AFM File Information';
numlines=1;
defaultanswer={'sample_E_spot_2_50x_2xZoom.txt', '512',
'28.5'};%default answers
options.Resize='on';
options.WindowStyle='normal';
options.Interpreter='tex';

answer=inputdlg(prompt,name,numlines,defaultanswer,options); %read in
%answers

%naming and converting answers into appropriate data type

afmfilename=char(answer(1,1));%converting filename into a string

datares=char(answer(2,1));
datares=str2num(datares);%converting data resolution to a number

scansize=char(answer(3,1));
scansize=str2num(scansize);%converting scan size to a number

PhaseMap=dlmread(afmfilename);%only calling phasemap to match up with
%rest of program which was originally meant only for swli

% converts NaN's in PhaseMap matrix to zeros;
PhaseMap(isnan(PhaseMap))=0;

xfov=scansize;
yfov=xfov;

xpxl=datares;

ypxl=xpxl;

end

% The loop will build x, y, and z 1 X N matrices (xcalc,ycalc,zcalc). I
% initialize a matrix for zcalc,xcalc, and ycalc so it will run faster
% (preallocating for speed).

zcalc=zeros(1,(xpxl*ypxl));
xcalc=zeros(1,(xpxl*ypxl));
ycalc=zeros(1,(xpxl*ypxl));

for yindex=1:ypxl

    for xindex=1:xpxl

```

```

        zcalc(xindex+xp*1*(yindex-1))=PhaseMap(yindex,xindex);%for some
%reason the .dat file lists y as rows and x and columns
        xcalc(xindex+xp*1*(yindex-1))=xindex;
        ycalc(xindex+xp*1*(yindex-1))=yindex;

    end

end

zcalc=zcalc';%transposing matrix zcalc

avgzcalc=mean(zcalc);%finding the average of zcalc

%loop that will replace any zeros in the zcalc matrix (formerly NaN's)
%with the average of the zcalc matrix.

for incr=1:length(zcalc)

    if zcalc(incr)==0

        zcalc(incr)=avgzcalc;

    else

        zcalc(incr)=zcalc(incr);

    end

end

end

xcalc=xcalc';%transposing xcalc
ycalc=ycalc';%transposing ycalc

%equations below will do an initial least squares fit on the data to
%take slope out and normalize to zero.

A=[xcalc, ycalc, ones(length(xcalc),1)];

B=[zcalc];

ATA=A'*A;
ATB=A'*B;

corrections=inv(ATA)*ATB; %x and y slope and z intercept

zcalc=zcalc-corrections(1,1)*xcalc-corrections(2,1)*ycalc;%taking out
%slope
zcalc=zcalc-corrections(3,1);%normalizing

```

```

%loop will build the z matrix back into a rectangular matrix for
%contour plotting--called NewPhaseMap. Preallocating NewPhaseMap for
%speed.

NewPhaseMap=zeros (ypxl,xpxl);

for yindex=1:ypxl

    for xindex=1:xpxl

        NewPhaseMap(yindex,xindex)=zcalc(xindex+xpxl*(yindex-1));

    end

end

%setting up initial plot with plane fit of complete data set (including
%MR footprint

xstart=1;
ystart=1;
xend=xpxl;
yend=ypxl;

xrange=xstart:xend;
yrange=ystart:yend;

xrange=xrange.*(xfov/xpxl);
yrange=yrange.*(yfov/ypxl);

NewZ=NewPhaseMap;

%setting up image plot

scrsz = get(0,'ScreenSize');%figures out screen resolution on the
%computer
figure('Position',[1 ((scrsz(4)/2)-75) scrsz(3)/2
((scrsz(4)/2))] );%sets position and size of figure (left, bottom,
%width, height)

xstartum=1;
xendum=xrange;
ystartum=1;
yendum=yrange;

imagesc([xstartum xendum],[ystartum yendum],NewZ)

axis xy

```

```

%setting up xlabel, ylabel, title, and colorbar text and fonts.

xlabel('X scale (\mum)', 'FontSize', 24)

ylabel('Y scale (\mum)', 'FontSize', 24)

colorbar('EastOutside')

g=colorbar;

set(get(g,'ylabel'),'String','Z scale (nm)', 'FontSize', 24)


%plane fit prompt

prompt={'Do you want to do a further plane fit based on individual plot  
areas? (y/n)', 'Number of rectangular areas'};
name='Plane Fit';
numlines=1;
defaultanswer={'n', '4'};%default answers
options.Resize='on';
options.WindowStyle='normal';
options.Interpreter='tex';

answer=inputdlg(prompt,name,numlines,defaultanswer,options); %read in
%answers

planeFit=char(answer(1,1));%converting y/n answer into a string

crectangularareas=char(answer(2,1));
rectangularareas = str2num(crectangularareas);%converting rectangular
%areas into a number


%loop below does a plane fit on areas selected with the mouse cursor.
%The first if statement decides whether the user wishes to do the plane
%fit. If so, it collects points provided by the mouse cursor (ginput
%command). For this algorithm to work the user should provide points at
%opposing corners.

condition0=strcmpi(planeFit, 'y');

if condition0==1

    [xplaneFit,yplaneFit]=ginput(rectangularareas*2);

    %rounds the collected values to a specific pixel

    xplaneFitValues=zeros(1,(rectangularareas*2)); %Preallocating for
%speed

```

```

for rnd=1:(rectangularareas*2)

    xplanefitvalues(rnd)=round(xplanefit(rnd).*(xpxl/xfov));
    yplanefitvalues(rnd)=round(yplanefit(rnd).*(ypxl/yfov));

    if xplanefitvalues(rnd)<0 || xplanefitvalues(rnd)>xpxl ||
    yplanefitvalues(rnd)<0 ||yplanefitvalues(rnd)>ypxl

        h=errordlg('You have picked a value outside of the data range.
Program cannot continue.');
        end

    end

xplanefitvalues1=xplanefitvalues;
yplanefitvalues1=yplanefitvalues;

for i=1:2:(2*rectangularareas)

    if xplanefitvalues(i)>xplanefitvalues(i+1)

        xplanefitvalues(i)=xplanefitvalues1(i+1);
        xplanefitvalues(i+1)=xplanefitvalues1(i);

    elseif yplanefitvalues(i)>yplanefitvalues(i+1)

        yplanefitvalues(i)=yplanefitvalues1(i+1);
        yplanefitvalues(i+1)=yplanefitvalues1(i);

    elseif xplanefitvalues(i)>xplanefitvalues(i+1) ||
    yplanefitvalues(i)>yplanefitvalues(i+1)

        xplanefitvalues(i)=xplanefitvalues1(i+1);
        xplanefitvalues(i+1)=xplanefitvalues1(i);

        yplanefitvalues(i)=yplanefitvalues1(i+1);
        yplanefitvalues(i+1)=yplanefitvalues1(i);

    else

        xplanefitvalues(i)=xplanefitvalues(i);
        xplanefitvalues(i+1)=xplanefitvalues(i+1);

        yplanefitvalues(i)=yplanefitvalues(i);
        yplanefitvalues(i+1)=yplanefitvalues(i+1);

    end

end
end

```

```

i=-1;
xplanefitarray=[];
yplanefitarray=[];
zplanefitarray=[];

for iter=1:(rectangularareas)

    i=i+2;
    xlength=length(xplanefitvalues(i+1)-xplanefitvalues(i));
    ylength=length(yplanefitvalues(i+1)-yplanefitvalues(i));

    for iter1=yplanefitvalues(i):yplanefitvalues(i+1)

        for iter2=xplanefitvalues(i):xplanefitvalues(i+1)

            xplanefitarray=[xplanefitarray iter2];
            yplanefitarray=[yplanefitarray iter1];
            zplanefitarray=[zplanefitarray NewZ(iter1,iter2)];

        end

    end

end

%equations below will do an initial least squares fit on the data to
%take slope out and normalize to zero.

xplanefitarray=xplanefitarray';
yplanefitarray=yplanefitarray';
zplanefitarray=zplanefitarray';

A=[xplanefitarray, yplanefitarray, ones(length(xplanefitarray),1)];

B=[zplanefitarray];

ATA=A'*A;
ATB=A'*B;

corrections=inv(ATA)*ATB; %x and y slope and z intercept

zcalc=zcalc-corrections(1,1)*xcalc-corrections(2,1)*ycalc;%taking out
%slope
zcalc=zcalc-corrections(3,1);%normalizing

%loop will build the z matrix back into a rectangular matrix for
%contour plotting--called NewZ.

for yindex=1:ypxl

```

```

    for x1index=1:xpxl

        NewZ(y1index,x1index)=zcalc(x1index+xpxl*(y1index-1));

    end

end

%setting up initial plot with plane fit of complete data set (including
%MR footprint

xrange=1:xpxl;
yrange=1:ypxl;

xrange=xrange.*(xfov/xpxl);
yrange=yrange.*(yfov/ypxl);

NewZ=NewZ(1:ypxl,1:xpxl);

%setting up image

close all;

figure('Position',[1 ((scrsz(4)/2)-75) scrsz(3)/2
((scrsz(4)/2))] );%sets position and size of figure (left, bottom,
%width, height)

imagesc([0 xrange],[0 yrange], NewZ)

axis xy

%setting up xlabel, ylabel, title, and colorbar text and fonts.

xlabel('X scale (\mum)', 'FontSize', 24)

ylabel('Y scale (\mum)', 'FontSize', 24)

colorbar('EastOutside')

g=colorbar;

set(get(g,'ylabel'),'String','Z scale (nm)', 'FontSize', 24)

end

```

```

% Dialogue box for trimming axes.

prompt={'Do you want to trim axes? (y/n)', 'Trim x-axis from left
(\mum)', 'Trim x-axis from right (\mum)', 'Trim y-axis from bottom
(\mum)', 'Trim y-axis from top (\mum)'};
name='Trim Axes';
numlines=1;
defaultanswer={'n', '0', '70', '0', '50'};%default answers
options.Resize='on';
options.WindowStyle='normal';
options.Interpreter='tex';

answer=inputdlg(prompt,name,numlines,defaultanswer,options); %read in
%answers

%naming and converting answers into appropriate data type

trim=char(answer(1,1));%converting answer to 'Trim axes?' into a string
%(y/n)

cxlefttrim=char(answer(2,1));
xlefttrim=str2num(cxlefttrim);%converting x-axis trim from left to a
%number

cxrighttrim=char(answer(3,1));
xrighttrim=str2num(cxrighttrim);%converting x-axis trim from right to a
%number

cybottomtrim=char(answer(4,1));
ybottomtrim=str2num(cybottomtrim);%converting y-axis trim from bottom
%to a number

cytoptrim=char(answer(5,1));
ytoptrim=str2num(cytoptrim);%converting y-axis trim from top to a
%number

% The if statement written below is used to determine the trimming
% conditions of the x and y axes. If adequate values are inputted to
%the program, the program will trim the data to only show values
%between xstart, xend, ystart, and yend. The if statement will not trim
%if a 'y' is not inputted into the program dialogue box (see strcmpi
%command directly below). It also has safeguards in case any of the
%inputted parameters are out of bound of the data. For example, if all
%parameters are in bounds except for xstart, xstart will default to the
%initial value. Another example, if all the parameters are out of

```

%bounds, all parameters will default to initial values. The xstart, %xend, ystart, and yend values are rounded to the closes integer % (pixel) from the user inputted bounds in micrometers.

```

xstart=round(xlefttrim.*(xpxl/xfov));
xend=round(xrighttrim.*(xpxl/xfov));

ystart=round(ybottomtrim.*(ypxl/yfov));
yend=round(ytoptrim.*(ypxl/yfov));

condition=strcmpi(trim,'y');

if condition==1 && xstart>0 && xstart<xpxl && xstart<xend && ystart>0
&& ystart<ypxl && ystart<yend && xend<=xpxl && xend>0 && yend<=ypxl &&
yend>0

    xstart=xstart;
    xend=xend;

    ystart=ystart;
    yend=yend;

elseif condition==1 && xstart<=0 && ystart>0 && ystart<ypxl &&
ystart<yend && xend<=xpxl && xend>0 && yend<=ypxl && yend>0

    xstart=1;
    xend=xend;

    ystart=ystart;
    yend=yend;

elseif condition==1 && xstart>0 && xstart<xpxl && xstart<xend &&
ystart<=0 && xend<=xpxl && xend>0 && yend<=ypxl && yend>0

    xstart=xstart;
    xend=xend;

    ystart=1;
    yend=yend;

elseif condition==1 && xstart<=0 && ystart<=0 && xend<=xpxl && xend>0
&& yend<=ypxl && yend>0

    xstart=1;
    xend=xend;

    ystart=1;
    yend=yend;

elseif condition==1 && xstart>0 && xstart<xpxl && xstart<xend &&
ystart>0 && ystart<ypxl && ystart<yend && xend>xpxl && yend<=ypxl &&
yend>0

```

```

        xstart=xstart;
        xend=xpxl;

        ystart=ystart;
        yend=yend;

elseif condition==1 && xstart>0 && xstart<xpxl && xstart<xend &&
ystart>0 && ystart<ypxl && ystart<yend && xend<=xpxl && xend>0 &&
yend>ypxl

        xstart=xstart;
        xend=xend;

        ystart=ystart;
        yend=xpxl;

elseif condition==1 && xstart>0 && xstart<xpxl && xstart<xend &&
ystart>0 && ystart<ypxl && ystart<yend && xend>xpxl && yend>yxpl

        xstart=xstart;
        xend=xpxl;

        ystart=ystart;
        yend=yxpl;

elseif condition==1 && xstart<=0 && ystart>0 && ystart<ypxl &&
ystart<yend && xend>xpxl && yend<=ypxl && yend>0

        xstart=1;
        xend=xpxl;

        ystart=ystart;
        yend=yend;

elseif condition==1 && xstart>0 && xstart<xpxl && xstart<xend &&
ystart<=0 && xend<=xpxl && xend>0 && yend>ypxl

        xstart=xstart;
        xend=xend;

        ystart=1;
        yend=yxpl;

elseif condition==1 && xstart<=0 && ystart>0 && ystart<ypxl &&
ystart<yend && xend<=xpxl && xend>0 && yend>yxpl

        xstart=1;
        xend=xend;

        ystart=ystart;
        yend=yxpl;

```

```

elseif condition==1 && xstart>0 && xstart<xp1 && xstart<xend &&
ystart<=0 && xend<xp1 && yend<=yp1 && yend>0

    xstart=xstart;
    xend=xp1;

    ystart=1;
    yend=yend;

elseif condition==1 && xstart<=0 && ystart<=0 && xend>xp1 &&
yend<=yp1 && yend>0

    xstart=1;
    xend=xp1;

    ystart=1;
    yend=yend;

elseif condition==1 && xstart<=0 && ystart>0 && ystart<yp1 &&
ystart<yend && xend>xp1 && yend>yp1

    xstart=1;
    xend=xp1;

    ystart=ystart;
    yend=yp1;

elseif condition==1 && xstart<=0 && ystart<=0 && xend<=xp1 && xend>0
&& yend>yp1

    xstart=1;
    xend=xend;

    ystart=1;
    yend=yp1;

elseif condition==1 && xstart>0 && xstart<xp1 && xstart<xend &&
ystart<=0 && xend>xp1 && yend>yp1

    xstart=xstart;
    xend=xp1;

    ystart=1;
    yend=yp1;

elseif condition==1 && xstart<=0 && ystart<=0 && xend>xp1 && yend>yp1

    xstart=1;
    xend=xp1;

    ystart=1;
    yend=yp1;

```

```

else

    xstart=1;
    xend=xpxl;
    ystart=1;
    yend=ypxl;

end

if condition==1 %if user decided to trim axes it will replot inside the
%if statement

% Setting up a grid of x and y values with ranges based on the user
% inputted bounds referenced earlier. Also defining NewZ, which is the
%new Z matrix based on these bounds.

xrange=xstart:xend;
yrange=ystart:yend;

xrange=xrange.*(xfov/xpxl);
yrange=yrange.*(yfov/ypxl);

OldZ=NewZ;%holding onto full range of data in case of re-trim

NewZ=OldZ(ystart:yend,xstart:xend);

xstartum=xstart*(xfov/xpxl);
xendum=xend*(xfov/xpxl);
ystartum=ystart*(yfov/ypxl);
yendum=yend*(yfov/ypxl);

%setting up contourf plot with no black lines

close all;

figure('Position',[1 ((scrsz(4)/2)-75) scrsz(3)/2
((scrsz(4)/2))] );%sets position and size of figure (left, bottom,
%width, height)

imagesc([0 (xendum-xstartum)], [0 (yendum-ystartum)], NewZ)

axis xy

%setting up xlabel, ylabel, title, and colorbar text and fonts.

xlabel('X scale (\mum)', 'FontSize', 24)

ylabel('Y scale (\mum)', 'FontSize', 24)

colorbar('EastOutside')

g=colorbar;

```

```

set(get(g, 'ylabel'), 'String', 'Z scale (nm)', 'FontSize', 24)

% Dialogue box for retrimming axes.

prompt={'Do you want to re-trim axes? (y/n)', 'Trim x-axis from left (\num)', 'Trim x-axis from right (\num)', 'Trim y-axis from bottom (\num)', 'Trim y-axis from top (\num)'};
name='Re-trim Axes';
numlines=1;
defaultanswer={'n', '0', '70', '0', '50'};%default answers
options.Resize='on';
options.WindowStyle='normal';
options.Interpreter='tex';

answer=inputdlg(prompt, name, numlines, defaultanswer, options); %read in
%answers

%naming and converting answers into appropriate data type

trim=char(answer(1,1));%converting answer to 'Trim axes?' into a string
% (y/n)

cxlefttrim=char(answer(2,1));
xlefttrim=str2num(cxlefttrim);%converting x-axis trim from left to a
%number

cxrighttrim=char(answer(3,1));
xrighttrim=str2num(cxrighttrim);%converting x-axis trim from right to a
%number

cybottomtrim=char(answer(4,1));
ybottomtrim=str2num(cybottomtrim);%converting y-axis trim from bottom
%to a number

cytoptrim=char(answer(5,1));
ytoptrim=str2num(cytoptrim);%converting y-axis trim from top to a
%number

condition1=strcmpi(trim, 'y');

else

    condition1=0;

end

% setting up if and while loop to determine how many times the user
%wishes to retrim the axes

if condition1==1

    condition2=1;

```

```

while condition2==1

% The if statement written below is used to determine the trimming
% conditions of the x and y axes. If adequate values are inputted to
%the program, the program will trim the data to only show values
%between xstart, xend, ystart, and yend. The if statement will not trim
%if a 'y' is not inputted into the program dialogue box (see strcmpi
%command directly below). It also has safeguards in case any of the
%inputted parameters are out of bound of the data. For example, if all
%parameters are in bounds except for xstart, xstart will default to the
%initial value. Another example, if all the parameters are out of
%bounds, all parameters will default to initial values. The xstart,
%xend, ystart, and yend values are rounded to the closes integer
%(pixel) from the user inputted bounds in micrometers.

xstart=round(xlefttrim.*(xpxl/xfov));
xend=round(xrighttrim.*(xpxl/xfov));

ystart=round(ybottomtrim.*(ypxl/yfov));
yend=round(ytoptrim.*(ypxl/yfov));

if xstart>0 && xstart<xpxl && xstart<xend && ystart>0 && ystart<ypxl &&
ystart<yend && xend<=xpxl && xend>0 && yend<=ypxl && yend>0

    xstart=xstart;
    xend=xend;

    ystart=ystart;
    yend=yend;

elseif xstart<=0 && ystart>0 && ystart<ypxl && ystart<yend &&
xend<=xpxl && xend>0 && yend<=ypxl && yend>0

    xstart=1;
    xend=xend;

    ystart=ystart;
    yend=yend;

elseif xstart>0 && xstart<xpxl && xstart<xend && ystart<=0 &&
xend<=xpxl && xend>0 && yend<=ypxl && yend>0

    xstart=xstart;
    xend=xend;

    ystart=1;
    yend=yend;

elseif xstart<=0 && ystart<=0 && xend<=xpxl && xend>0 && yend<=ypxl &&
yend>0

```

```

        xstart=1;
        xend=xend;

        ystart=1;
        yend=yend;

elseif xstart>0 && xstart<xp1 && xstart<xend && ystart>0 &&
ystart<yp1 && ystart<yend && xend>xp1 && yend<=yp1 && yend>0

        xstart=xstart;
        xend=xp1;

        ystart=ystart;
        yend=yend;

elseif xstart>0 && xstart<xp1 && xstart<xend && ystart>0 &&
ystart<yp1 && ystart<yend && xend<=xp1 && xend>0 && yend>yp1

        xstart=xstart;
        xend=xend;

        ystart=ystart;
        yend=yp1;

elseif xstart>0 && xstart<xp1 && xstart<xend && ystart>0 &&
ystart<yp1 && ystart<yend && xend>xp1 && yend>yp1

        xstart=xstart;
        xend=xp1;

        ystart=ystart;
        yend=yp1;

elseif xstart<=0 && ystart>0 && ystart<yp1 && ystart<yend && xend>xp1
&& yend<=yp1 && yend>0

        xstart=1;
        xend=xp1;

        ystart=ystart;
        yend=yend;

elseif xstart>0 && xstart<xp1 && xstart<xend && ystart<=0 &&
xend<=xp1 && xend>0 && yend>yp1

        xstart=xstart;
        xend=xend;

        ystart=1;
        yend=yp1;

```

```

elseif xstart<=0 && ystart>0 && ystart<ypxl && ystart<yend &&
xend<=xpxl && xend>0 && yend>ypxl

    xstart=1;
    xend=xend;

    ystart=ystart;
    yend=ypxl;

elseif xstart>0 && xstart<xpxl && xstart<xend && ystart<=0 && xend<xpxl
&& yend<=ypxl && yend>0

    xstart=xstart;
    xend=xpxl;

    ystart=1;
    yend=yend;

elseif xstart<=0 && ystart<=0 && xend>xpxl && yend<=ypxl && yend>0

    xstart=1;
    xend=xpxl;

    ystart=1;
    yend=yend;

elseif xstart<=0 && ystart>0 && ystart<ypxl && ystart<yend && xend>xpxl
&& yend>ypxl

    xstart=1;
    xend=xpxl;

    ystart=ystart;
    yend=ypxl;

elseif xstart<=0 && ystart<=0 && xend<=xpxl && xend>0 && yend>ypxl

    xstart=1;
    xend=xend;

    ystart=1;
    yend=ypxl;

elseif xstart>0 && xstart<xpxl && xstart<xend && ystart<=0 && xend>xpxl
&& yend>ypxl

    xstart=xstart;
    xend=xpxl;

    ystart=1;
    yend=ypxl;

elseif xstart<=0 && ystart<=0 && xend>xpxl && yend>ypxl

```

```

        xstart=1;
        xend=xpxl;

        ystart=1;
        yend=ypxl;

    else

        xstart=1;
        xend=xpxl;
        ystart=1;
        yend=ypxl;

    end

    % Setting up a grid of x and y values with ranges based on the user
    % inputted bounds referenced earlier. Also defining NewZ, which is the
    % new Z matrix based on these bounds.

    xrange=xstart:xend;
    yrange=ystart:yend;

    xrange=xrange.*(xfov/xpxl);
    yrange=yrange.*(yfov/ypxl);

    NewZ=OldZ(ystart:yend,xstart:xend);

    xstartum=xstart*(xfov/xpxl);
    xendum=xend*(xfov/xpxl);
    ystartum=ystart*(yfov/ypxl);
    yendum=yend*(yfov/ypxl);

    %setting up image plot

    close all;

    figure('Position',[1 ((scrsz(4)/2)-75) scrsz(3)/2
        ((scrsz(4)/2))]);%sets position and size of figure (left, bottom,
    %width, height)

    imagesc([xstartum xendum],[ystartum yendum], NewZ)

    axis xy

    %setting up xlabel, ylabel, title, and colorbar text and fonts.

    xlabel('X scale (\mu m)', 'FontSize', 24)

```

```

ylabel('Y scale (\mum)', 'FontSize', 24)

colorbar('EastOutside')

g=colorbar;

set(get(g,'ylabel'),'String','Z scale (nm)', 'FontSize', 24)

% Dialogue box for retrimming axes.

prompt={'Do you want to re-trim axes? (y/n)', 'Trim x-axis from left (\mum)', 'Trim x-axis from right (\mum)', 'Trim y-axis from bottom (\mum)', 'Trim y-axis from top (\mum)'};
name='Re-trim Axes';
numlines=1;
defaultanswer={'n', '0', '70', '0', '50'};%default answers
options.Resize='on';
options.WindowStyle='normal';
options.Interpreter='tex';

answer=inputdlg(prompt,name,numlines,defaultanswer,options); %read in
%answers

%naming and converting answers into appropriate data type

trim=char(answer(1,1));%converting answer to 'Trim axes?' into a string
% (y/n)

cxlefttrim=char(answer(2,1));
xlefttrim=str2num(cxlefttrim);%converting x-axis trim from left to a
%number

cxrighttrim=char(answer(3,1));
xrighttrim=str2num(cxrighttrim);%converting x-axis trim from right to a
%number

cybottomtrim=char(answer(4,1));
ybottomtrim=str2num(cybottomtrim);%converting y-axis trim from bottom
%to a number

cytoptrim=char(answer(5,1));
ytoptrim=str2num(cytoptrim);%converting y-axis trim from top to a
%number

condition2=strcmpi(trim,'y');

    end

end

%Dialog box for filtering outliers

```

```

prompt={'Do you want to remove outliers?','Remove outliers above this
value (nm)','Remove outliers below this value (nm)'};
name='Remove Outliers';
numlines=1;
defaultanswer={'n','1','-1',};%default answers
options.Resize='on';
options.WindowStyle='normal';
options.Interpreter='tex';

answer=inputdlg(prompt,name,numlines,defaultanswer,options); %read in
%answers

%naming and converting answers into appropriate data type

outliers=char(answer(1,1));%converting answer to 'Do you want to filter
%outliers?' into a string (y/n)

coutlierhigh=char(answer(2,1));
outlierhigh=str2num(coutlierhigh);%converting high outliers to a number

coutlierlow=char(answer(3,1));
outlierlow=str2num(coutlierlow);%converting low outliers to a number

condoutliers=strcmpi(outliers,'y');

if condoutliers==1

    condoutliers1=1;%condition for re-assessing outliers

    while condoutliers1==1 && outlierhigh>outlierlow % will break out
%of loop if user decides not to re-assess outliers or if user inputs
%incorrect data -- outlierhigh<=outlierlow

        OldZ=NewZ;%setting new matrix of OldZ to range of NewZ
%determined by trim. Resets back to NewZ after every while loop
%allowing user to change outlier range on virgin Z data

        lengthx=length(xstart:xend);
        lengthy=length(ystart:yend);

        for xincr=1:lengthx

            for yincr=1:lengthy

                if NewZ(yincr,xincr)>outlierhigh ||
NewZ(yincr,xincr)<outlierlow

                    OldZ(yincr,xincr)=0; %setting value to 0

                end

            end

        end
end

```

```

end

%setting up image plot

close all;

figure('Position',[1 ((scrsz(4)/2)-75) scrsz(3)/2
((scrsz(4)/2))] );%sets position and size of figure (left, bottom,
%width, height)

imagesc([0 (xendum-xstartum)], [0 (yendum-ystartum)], OldZ)

axis xy

%setting up xlabel, ylabel, title, and colorbar text and fonts.

xlabel('X scale (\mum)', 'FontSize', 24)

ylabel('Y scale (\mum)', 'FontSize', 24)

colorbar('EastOutside')

g=colorbar;

set(get(g, 'ylabel'), 'String', 'Z scale (nm)', 'FontSize', 24)

%Dialog box for filtering outliers

prompt={'Do you want to re-assess outlier range?', 'Remove outliers
above this value (nm)', 'Remove outliers below this value (nm)'};
name='Re-assess Outliers';
numlines=1;
defaultanswer={'n', '1', '-1', }; %default answers
options.Resize='on';
options.WindowStyle='normal';
options.Interpreter='tex';

answer=inputdlg(prompt, name, numlines, defaultanswer, options); %read in
%answers

%naming and converting answers into appropriate data type

outliers=char(answer(1,1)); %converting answer to 'Do you want to filter
%outliers?' into a string (y/n)

coutlierhigh=char(answer(2,1));
outlierhigh=str2num(coutlierhigh); %converting high outliers to a number

coutlierlow=char(answer(3,1));
outlierlow=str2num(coutlierlow); %converting low outliers to a number

condoutliers1=strcmpi(outliers, 'y');

```

```

end %end to 'Re assessing outliers' statement

NewZ=OldZ; %setting NewZ to filtered outlier data, OldZ

end %end to 'Do you want to filter outliers?' statement

%Dialog box picking and removing sections of data

prompt={'Do you want to pick and remove sections of data? (y/n)', 'How
many areas of data do you want to remove?'};
name='Remove Data';
numlines=1;
defaultanswer={'n', '1'};%default answers
options.Resize='on';
options.WindowStyle='normal';
options.Interpreter='tex';

answer=inputdlg(prompt,name,numlines,defaultanswer,options); %read in
%answers

%naming and converting answers into appropriate data type

removedata=char(answer(1,1));%converting answer to 'Do you want to pick
%and remove sections of data?' into a string (y/n)

crectangularareas=char(answer(2,1));
rectangularareas=str2num(crectangularareas);

condremovedata=strcmpi(removedata,'y');

if condremovedata==1

    condremovedata1=1;%condition for re-assessing outliers

    while condremovedata1==1 % will break out of loop if user decides
    %not to re-assess removing data

        %loop below picks out areas of data selected with the mouse cursor.

        [xarea,yarea]=ginput(rectangularareas*2);

        %rounds the collected values to a specific pixel

        xvalues=zeros(1,(rectangularareas*2)); %Preallocating for speed
        yvalues=zeros(1,(rectangularareas*2)); %Preallocating for speed

        for rnd=1:(rectangularareas*2)

            xvalues(rnd)=round(xarea(rnd).*(xpxl/xfov));
            yvalues(rnd)=round(yarea(rnd).*(ypxl/yfov));

```

```

    if xvalues(rnd)<xstart || xvalues(rnd)>xend || yvalues(rnd)<ystart
    ||yvalues(rnd)>yend

        h=errordlg('You have picked a value outside of the data range.
Program cannot continue.');
```

end

end

```

xvalues1=xvalues;
yvalues1=yvalues;

for i=1:2:(2*rectangularareas)

    if xvalues(i)>xvalues(i+1) && yvalues(i)>yvalues(i+1)

        xvalues(i)=xvalues1(i+1);
        xvalues(i+1)=xvalues1(i);

        yvalues(i)=yvalues1(i+1);
        yvalues(i+1)=yvalues1(i);

    elseif xvalues(i)>xvalues(i+1)

        xvalues(i)=xvalues1(i+1);
        xvalues(i+1)=xvalues1(i);

    elseif yvalues(i)>yvalues(i+1)

        yvalues(i)=yvalues1(i+1);
        yvalues(i+1)=yvalues1(i);

    else

        xvalues(i)=xvalues(i);
        xvalues(i+1)=xvalues(i+1);

        yvalues(i)=yvalues(i);
        yvalues(i+1)=yvalues(i+1);

    end

    for xincr=xvalues(i):xvalues(i+1)

        for yincr=yvalues(i):yvalues(i+1)

            NewZ((yincr-ystart),(xincr-xstart))=0;%ystart and xstart
%are subtracted from yincr and xincr because the position of the matrix
%needs to be compensated for previous trimming

            end

```

```

end

end

%setting up image plot

close all;

figure('Position',[1 ((scrsz(4)/2)-75) scrsz(3)/2
((scrsz(4)/2))] );%sets position and size of figure (left, bottom,
%width, height)

imagesc([xstartum xendum],[ystartum yendum],NewZ)

axis xy

%setting up xlabel, ylabel, title, and colorbar text and fonts.

xlabel('X scale (\mum)', 'FontSize', 24)

ylabel('Y scale (\mum)', 'FontSize', 24)

colorbar('EastOutside')

g=colorbar;

set(get(g,'ylabel'),'String','Z scale (nm)', 'FontSize', 24)

%Dialog box for removing more data

prompt={'Do you want to remove more data? (y/n)', 'How many areas of
data do you want to remove?'};
name='Remove more data';
numlines=1;
defaultanswer={'n','1'};%default answers
options.Resize='on';
options.WindowStyle='normal';
options.Interpreter='tex';

answer=inputdlg(prompt,name,numlines,defaultanswer,options); %read in
%answers

%naming and converting answers into appropriate data type

removedata=char(answer(1,1));%converting answer to 'Do you want to
%remove more data?' into a string (y/n)

condremovedata1=strcmpi(removedata,'y');

crectangularareas=char(answer(2,1));
rectangularareas=str2num(crectangularareas);

```

```

end %end to 'Remove more data' statement

end %end to 'Remove data' statement


%loop for depth using rectangular sections in each
%pixel-- averaging z across each x by y pixel

depth=0;

SizeofNewZ=size(NewZ);

lengthx=SizeofNewZ(2);

lengthy=SizeofNewZ(1);

for xincr=1:(lengthx-1)

    for yincr=1:(lengthy-1)

depth=depth+( (NewZ(yincr,xincr)+NewZ(yincr+1,xincr)+NewZ(yincr,xincr+1)
+NewZ(yincr+1,xincr+1))/4);

    end

end

% Volumetric removal calculation finished by converting depth to um and
% then multiplying by the x and y lengths.

material_removed=-depth*(xfov/xpxl)*(yfov/ypxl)/1000;%should be in um^3

%Surface area calculation algorithm with threshold value to determine
"What is a footprint?"

surfaceArea=0; %initializing surface area variable

depthThreshold=-50;%initializing threshold at -50 nm

unitSurfArea=pixelspacing*pixelspacing; %sets each unit of surface area
%as area of one pixel

for xincr=1:(lengthx-1)

    for yincr=1:(lengthy-1)

        if (NewZ(yincr,xincr)< depthThreshold)

```

```

        surfaceArea=surfaceArea + unitSurfArea;

    end

end

end

surfaceArea=num2str(surfaceArea);

%end surface area calculation

%major and minor length calculations

columnlength=zeros(1,lengthx);

for xincr=1:(lengthx-1)

    for yincr=1:(lengthy-1)

        if (NewZ(yincr,xincr)< depthThreshold)

            columnlength(1,xincr)=columnlength(1,xincr)+pixelspacing;

        end

    end

end

end

maxFootprintHeight=num2str(max(columnlength));

rowlength=zeros(1,lengthy);

for yincr=1:(lengthy-1)

    for xincr=1:(lengthx-1)

        if (NewZ(yincr,xincr)< depthThreshold)

            rowlength(1,yincr)=rowlength(1,yincr)+pixelspacing;

        end

    end

end

end

maxFootprintWidth=num2str(max(rowlength));

```

```

widthToHeightRatio=num2str(max(rowlength)/max(columnlength));

% end major and minor length calculations


%setting up image plot

close all; %close previous figures

figure('Position',[1 ((scrsz(4)/2)-75) scrsz(3)/2
((scrsz(4)/2))]);%sets position and size of figure (left, bottom,
%width, height)

imagesc([xstartum xendum],[ystartum yendum],NewZ)

axis xy

%setting up title that will include the volumetric removal results

mr=num2str(material_removed);

%titlestring=strcat({'Volumetric Removal: '},mr,{' \mum^3'});

msgbox({'Calculated parameters:', ' ', 'Volume Removed = ',mr, ' ', 'Max
Footprint Width = ',maxFootprintWidth, ' ', 'Max Footprint Height =
',maxFootprintHeight, ' ', 'Width-to-Height Ratio = ',
widthToHeightRatio, ' ', 'Surface Area = ',surfaceArea},'Surface
Results')

%setting up xlabel, ylabel, title, and colorbar text and fonts.

xlabel('X scale (\mum)', 'FontSize', 24)

ylabel('Y scale (\mum)', 'FontSize', 24)

%title(titlestring, 'FontSize', 24, 'Fontweight','b')

colorbar('EastOutside')

g=colorbar;

set(get(g,'ylabel'),'String','Z scale (nm)', 'FontSize', 24)


% % algorithm for looking at line profiles in data

prompt={'Do you want to look at line profiles? (y/n)'};
name='Line profiles';

```

```

numlines=1;
defaultanswer={'n'};%default answers
options.Resize='on';
options.WindowStyle='normal';
options.Interpreter='tex';

answer=inputdlg(prompt,name,numlines,defaultanswer,options); %read in
%answers

%naming and converting answers into appropriate data type

lineprofile=char(answer(1,1));%converting answer to 'Do you want to
%look at line profiles?' into a string (y/n)

condlineprofile=strcmpi(lineprofile,'y');

while condlineprofile==1

    profile=0; %re-initializing values in case another profile is
%initiated
    form=0;
    roughness=0;

    [x,y]=ginput(2);

    xumlength=abs(x(2)-x(1));
    yumlength=abs(y(2)-y(1));

    if xumlength>yumlength

        if x(1)>x(2)

            x1=x(1);
            x2=x(2);
            y1=y(1);
            y2=y(2);

            x(1)=x2;
            x(2)=x1;
            y(1)=y2;
            y(2)=y1;

        end

        x1um=x(1);
        x2um=x(2);

        y1um=y(1);
        y2um=y(2);

        x1=(x(1)-xstartum)*(xpxl/xfov);
        x2=(x(2)-xstartum)*(xpxl/xfov);

```

```

y1=(y(1)-ystartum)*(ypxl/yfov);
y2=(y(2)-ystartum)*(ypxl/yfov);

lengthpxl=round(sqrt((x2-x1)^2+(y2-y1)^2));
lengthum=lengthpxl*xfov/ypxl;
slope=(y2-y1)/(x2-x1);

number=lengthpxl+1;

profile=zeros(lengthpxl+1);

for i=0:lengthpxl

    x=x1+((i*(x2-x1))/lengthpxl);
    y=y1+((i*(y2-y1))/lengthpxl)*slope;

    xlow=floor(x);%round down
    xhigh=ceil(x);%round up

    ylow=floor(y);
    yhigh=ceil(y);

    % Bilinear interpolation algorithm

    fx1=((xhigh-x)/(xhigh-xlow))*NewZ(ylow,xlow)+((x-xlow)/(xhigh-
xlow))*NewZ(ylow,xhigh);
    fx2=((xhigh-x)/(xhigh-xlow))*NewZ(yhigh,xlow)+((x-xlow)/(xhigh-
xlow))*NewZ(yhigh,xhigh);
    profile(i+1)=((yhigh-y)/(yhigh-ylow))*fx1+((y-ylow)/(yhigh-
ylow))*fx2;

    % Bilinear interpolation algorithm

end

else

    if y(1)>y(2)

        x1=x(1);
        x2=x(2);
        y1=y(1);
        y2=y(2);

        x(1)=x2;
        x(2)=x1;
        y(1)=y2;
        y(2)=y1;

    end

    x1um=x(1);
    x2um=x(2);

```

```

y1um=y(1);
y2um=y(2);

x1=(x(1)-xstartum)*(xpxl/xfov);
x2=(x(2)-xstartum)*(xpxl/xfov);

y1=(y(1)-ystartum)*(ypxl/yfov);
y2=(y(2)-ystartum)*(ypxl/yfov);

lengthpxl=round(sqrt((x2-x1)^2+(y2-y1)^2));
lengthum=lengthpxl*xfov/xpxl;
slope=(x2-x1)/(y2-y1);

number=lengthpxl+1;

profile=zeros((lengthpxl+1),1);

for i=0:lengthpxl

    y=y1+((i*(y2-y1))/lengthpxl);
    x=x1+((i*(x2-x1))/lengthpxl)*slope;

    xlow=floor(x);%round down
    xhigh=ceil(x);%round up

    ylow=floor(y);
    yhigh=ceil(y);

    % Bilinear interpolation algorithm

    fy1=((yhigh-y)/(yhigh-ylow))*NewZ(ylow,xlow)+((y-ylow)/(yhigh-
ylow))*NewZ(ylow,xhigh);
    fy2=((yhigh-y)/(yhigh-ylow))*NewZ(yhigh,xlow)+((y-ylow)/(yhigh-
ylow))*NewZ(yhigh,xhigh);
    profile(i+1)=((xhigh-x)/(xhigh-xlow))*fy1+((x-xlow)/(xhigh-
xlow))*fy2;

    % Bilinear interpolation algorithm

end

end

close all;

figure('Position',[1 ((scrsz(4)/2)-275) scrsz(3)/2
((scrsz(4)/2)+200)]);%sets position and size of figure (left, bottom,
%width, height)

subplot(2,1,1),imagesc([xstartum xendum],[ystartum yendum],NewZ);

```

```

axis xy %sets lower left hand corner as origin

line([x1um x2um],[y1um y2um], 'Color','w','linewidth',2)%draw a line
%where I specified

%setting up title that will include the volumetric removal results

titlestring=strcat({'Volumetric Removal: '},mr,{' \mum^3'});

%setting up xlabel, ylabel, title, and colorbar text and fonts.

xlabel('X scale (\mum)', 'FontSize', 24)

ylabel('Y scale (\mum)', 'FontSize', 24)

title(titlestring, 'FontSize', 24, 'Fontweight','b')

colorbar('EastOutside')

g=colorbar;

set(get(g,'ylabel'),'String','Z scale (nm)', 'FontSize', 24)

profilex=(0:(lengthum/lengthpxl):lengthum);%used to define x axis in
%profile plot

subplot(2,1,2),plot(profilex,profile);

axis tight;

xlabel('X scale (\mum)', 'FontSize', 24)

ylabel('Y scale (\mum)', 'FontSize', 24)

%fitdata=polyfit(profilex,profile,2)

% % algorithm to decide whether to do a polynomial fit to data

prompt={'Do you want to use a zero order Gaussian Regression filter?
(y/n)', 'Cutoff wavelength (\mum)'};
name='Roughness Evaluation';
numlines=1;
defaultanswer={'y','1'};%default answers
options.Resize='on';
options.WindowStyle='normal';
options.Interpreter='tex';

answer=inputdlg(prompt,name,numlines,defaultanswer,options); %read in
%answers

```

```

%naming and converting answers into appropriate data type

filterprofile=char(answer(1,1));%converting answer to 'Do you want to
%look at line profiles?' into a string (y/n)

cprofilecutoff=char(answer(2,1));
profilecutoff=(str2double(answer(2,1)));

condfilterprofile=strcmpi(filterprofile,'y');

if condfilterprofile==1

% % The following is code based largely on p.71 out of Computational
% surface metrology for a zero order gaussian regression filter
profile=profile(:,1);
n=length(profile);%number of points
dx=max(profilex)/n;%spacing of points in micrometers
x=(0:1:n-1)*dx; %generate x data

lambdac=profilecutoff;
xg=(-lambdac:dx:lambdac)'; % x axis for generating filter -cutoff to
% cutoff
alpha=0.4697; %constant

S=(1/(alpha*lambdac)).*exp(-pi*(xg/(alpha*lambdac)).^2);%Gaussian
%filter
S=S/sum(S); %normalize filter sum to unity

w1=conv(S,profile); %convolution of filter with profile
trimlength=(length(xg)-1)/2;
w1=w1(trimlength:(length(w1)-trimlength),1); %extract relevant data

%ZERO order gaussian regression

const=sqrt(log(2)/2/pi/pi);
for k=1:n
    p=(1:1:n)'; %for each position k (center of filter), generate the
    %filter over entire profile length

    S1=(1/sqrt(2*pi)/const/lambdac).*exp(-0.5*((k-
    p)*dx/const/lambdac).^2); %generate weighting function
    SMOD=S1/sum(S1); %normalize filter to unit sum
    form(k,1)=sum(SMOD.*profile);% sum of products (this step replaces
    %the convolution)

end

roughness=profile-form; %create roughness profile

```

```

r_a=num2str(sum(abs(roughness))/n);
r_mean = num2str(mean(roughness));
r_q=sqrt(sum(roughness.^2)/n);
r_rms = num2str(r_q);
r_std = num2str(std(roughness));
r_peak = max(roughness);
r_valley = min(roughness);
r_pv = num2str(r_peak - r_valley);
r_skew = num2str((1/(n*r_q^3))*sum(roughness.^3));
r_kurt = num2str((1/(n*r_q^4))*sum(roughness.^4));

    close all;

figure('Position',[1 ((scrsz(4)/2)-575) scrsz(3)/2
((scrsz(4)/2)+500)]);%sets position and size of figure (left, bottom,
%width, height)

subplot(4,1,1),imagesc([xstartum xendum],[ystartum yendum],NewZ);

axis xy %sets lower left hand corner as origin

line([xlum x2um],[ylum y2um],'Color','w','linewidth',2)%draw a line
%where I specified

%setting up title that will include the volumetric removal results

titlestring=strcat({'Volumetric Removal: '},mr,{' \mum^3'});

%setting up xlabel, ylabel, title, and colorbar text and fonts.

xlabel('X scale (\mum)', 'FontSize', 18)

ylabel('Y scale (\mum)', 'FontSize', 18)

title(titlestring, 'FontSize', 18, 'Fontweight','b')

colorbar('EastOutside')

g=colorbar;

set(get(g,'ylabel'),'String','Z scale (nm)', 'FontSize', 24)

profilex=0:(lengthum/lengthpxl):lengthum;%used to define x axis in
%profile plot

subplot(4,1,2),plot(profilex,profile);

title('Original Profile','FontSize',18)

axis tight;

subplot(4,1,3),plot(profilex,form)

```

```

title('Form','FontSize',18)

axis tight;

subplot(4,1,4),plot(profilex,roughness)

title('Roughness','FontSize',18)

axis tight;

msgbox({'Parameters for the Zero Order Gaussian Regression Filter
are:', ' ', 'Ra = ', r_a, ' ', 'Rq = ', r_rms, ' ', 'Rt = ', r_pv, ' ', 'Rsk = ', ' ',
'r_skew, ' ', 'Rku = ', ' ', r_kurt},'Surface Results')

end

pause(3);%pause program for 3 seconds

% Ask user if he wants to look at another profile

prompt={'Do you want to look at another line profiles? (y/n)'};
name='Line profiles';
numlines=1;
defaultanswer={'n'};%default answers
options.Resize='on';
options.WindowStyle='normal';
options.Interpreter='tex';

answer=inputdlg(prompt,name,numlines,defaultanswer,options); %read in
%answers

%naming and converting answers into appropriate data type

lineprofile=char(answer(1,1));%converting answer to 'Do you want to
%look at line profiles?' into a string (y/n)

condlineprofile=strcmpi(lineprofile,'y');

end

% % algorithm to decide whether to do a 3-D Gaussian Regression filter

prompt={'Do you want to use a 3-D Gaussian filter? (y/n)', 'Cutoff
wavelength (\mum)'};

```

```

name='3-D Roughness Evaluation';
numlines=1;
defaultanswer={'n','1'};%default answers
options.Resize='on';
options.WindowStyle='normal';
options.Interpreter='tex';

answer=inputdlg(prompt,name,numlines,defaultanswer,options); %read in
%answers

%naming and converting answers into appropriate data type

filterarea=char(answer(1,1));%converting answer to filter area into a
%string (y/n)

cxcutoff=char(answer(2,1));
xcutoff=(str2double(answer(2,1)));

condfilterarea=strcmpi(filterarea,'y');

if condfilterarea==1

while condfilterarea==1
% % The following is code based largely on p.56 out of Computational
% surface metrology for 3-d gaussian filter

dx=xfov/xpxl; %spacing in um
dy=yfov/ypxl; %spacing in um

nx=(xend-xstart)+1;
ny=(yend-ystart)+1; %number of points

alpha=sqrt(log(2)/pi);
lambdacX=xcutoff; %wavelenght cutoff
lambdacY=xcutoff;

x=(-lambdacX:dx:lambdacX-dx)'; %generate x array
y=(-lambdacY:dy:lambdacY-dy)';%generate y array

mx=size(x,1); %number of points along x
my=size(y,1);%number of points along y
for i=1:mx
    for j=1:my
        S(j,i)=(1/(alpha^2*lambdacX*lambdacY))*exp(-
pi*(x(i)/alpha/lambdacX)^2-pi*(y(j)/alpha/lambdacY)^2);

    end
end

S=S/sum(sum(S));%normalize to zero sum

C=conv2(NewZ,S); %2d convolution
form3d=C(my/2+1:ny+my/2,mx/2+1:nx+mx/2); %extract central portions of
%the surface

```

```

roughness3d=NewZ-form3d;

close all;

figure('Position',[1 ((scrsz(4)/2)-575) scrsz(3)/2
((scrsz(4)/2)+500)]);%sets position and size of figure (left, bottom,
%width, height)

subplot(3,1,1),imagesc([xstartum xendum],[ystartum yendum],NewZ);

axis xy %sets lower left hand corner as origin

%setting up title that will include the volumetric removal results

titlestring=strcat({'Volumetric Removal: '},mr,{' \mum^3'});

%setting up xlabel, ylabel, title, and colorbar text and fonts.

xlabel('X scale (\mum)', 'FontSize', 18)

ylabel('Y scale (\mum)', 'FontSize', 18)

title(titlestring, 'FontSize', 18, 'Fontweight','b')

colorbar('EastOutside')

g=colorbar;

set(get(g,'ylabel'),'String','Z scale (nm)', 'FontSize', 24)

subplot(3,1,2),imagesc([xstartum xendum],[ystartum yendum],C);

axis xy %sets lower left hand corner as origin

%setting up xlabel, ylabel, title, and colorbar text and fonts.

xlabel('X scale (\mum)', 'FontSize', 18)

ylabel('Y scale (\mum)', 'FontSize', 18)

title('Form', 'FontSize', 18, 'Fontweight','b')

colorbar('EastOutside')

g=colorbar;

set(get(g,'ylabel'),'String','Z scale (nm)', 'FontSize', 24)

subplot(3,1,3),imagesc([xstartum xendum],[ystartum
yendum],roughness3d);

```

```

axis xy %sets lower left hand corner as origin

%setting up xlabel, ylabel, title, and colorbar text and fonts.

xlabel('X scale (\mum)', 'FontSize', 18)

ylabel('Y scale (\mum)', 'FontSize', 18)

title('Roughness', 'FontSize', 18, 'Fontweight','b')

colorbar('EastOutside')

g=colorbar;

set(get(g,'ylabel'),'String','Z scale (nm)', 'FontSize', 24)

n=nx*ny; %number of total points
Sa=num2str(sum(sum(abs(roughness3d)))/nx/ny);
Sq=sqrt(sum(sum(roughness3d.^2))/n);
Sq=num2str(Sq);
Sp=max(max(roughness3d));
Sv=min(min(roughness3d));
St=num2str(Sp-Sv);
Ssk = num2str((1/(nx*ny*Sqn^3))*sum(sum(roughness3d.^3)));
Sku = num2str((1/(nx*ny*Sqn^4))*sum(sum(roughness3d.^4)));

msgbox({'Parameters for the 3-D filtered roughness profile are:',
', 'Sa = ', Sa, ', ', 'Sq = ', Sq, ', ', 'St = ', St, ', ', 'Ssk = ', ' ', 'Ssk, '
', 'Sku = ', ' ', 'Sku}', '3-D Surface Results')

prompt={'Do you want to 3-D filter again? (y/n)', 'X Cutoff wavelength
(\mum)', 'Y Cutoff wavelength (\mum)'};
name='3-D Roughness Evaluation';
numlines=1;
defaultanswer={'y', '1', '1'};%default answers
options.Resize='on';
options.WindowStyle='normal';
options.Interpreter='tex';

answer=inputdlg(prompt,name,numlines,defaultanswer,options); %read in
%answers

%naming and converting answers into appropriate data type

filterarea=char(answer(1,1));%converting answer to filter area into a
%string (y/n)

xcutoff=char(answer(2,1));
xcutoff=(str2double(answer(2,1)));

cycutoff=char(answer(3,1));
ycutoff=(str2double(answer(3,1)));

```

```
condfilterarea=strcmpi(filterarea,'y');  
end  
end
```